Study of Internal Poiseuille Flows of Nano Fluids

By

Nasir Shehzad

Reg. No. 40-FBAS/PHDMA/F13

Department of Mathematics and Statistics

Faculty of Basic and Applied Sciences

International Islamic University, Islamabad, Pakistan

2019

Pipe - Fluid dynamics
Fluid dynamics
Mathematics

Study of Internal Poiseuille Flows of Nano Fluids

By

Nasir Shehzad

Reg. No. 40-FBAS/PHDMA/F13

Supervised by

Dr. Ahmed Zeeshan

Co-supervised by

Dr. Rahmat Ellahi

Department of Mathematics and Statistics
Faculty of Basic and Applied Sciences
International Islamic University, Islamabad,
Pakistan

2019

Study of Internal Poiseuille Flows of Nano Fluids

By

Nasir Shehzad

A Thesis
Submitted in the Partial Fulfillment of the
Requirements for the Degree of

DOCTOR OF PHILOSOPHY
IN
MATHEMATICS

Supervised by
Dr. Ahmed Zeeshan

Co-supervised by
Dr. Rahmat Ellahi

Department of Mathematics and Statistics
Faculty of Basic and Applied Sciences
International Islamic University, Islamabad,
Pakistan
2019

Author's Declaration

I, **Nasir Shehzad** Reg. No. **40-FBAS/PHDMA/F13** hereby state that my Ph.D. thesis titled: **Study of Internal Poiseuille Flows of Nano Fluids** is my own work and has not been submitted previously by me for taking any degree from this university, **International Islamic University, Sector H-10, Islamabad, Pakistan** or anywhere else in the country/world.

At any time if my statement is found to be incorrect even after my Graduation the university has the right to withdraw my Ph.D. degree.

Name of Student: ***(Nasir Shehzad)***
Reg. No. **40-FBAS/PHDMA/F13**
Dated: **13/11/2019**

Plagiarism Undertaking

I solemnly declare that research work presented in the thesis titled: **Study of Internal Poiseuille Flows of Nano Fluids** is solely my research work with no significant contribution from any other person. Small contribution/help wherever taken has been duly acknowledged and that complete thesis has been written by me.

I understand the zero tolerance policy of the HEC and University, **International Islamic University, Sector H-10, Islamabad, Pakistan** towards plagiarism. Therefore, I as an Author of the above titled thesis declare that no portion of my thesis has been plagiarized and any material used as reference is properly referred/cited.

I undertake that if I am found guilty of any formal plagiarism in the above titled thesis even after award of Ph.D. degree, the university reserves the rights to withdraw/revoke my Ph.D. degree and that HEC and the University has the right to publish my name on the HEC/University Website on which names of students are placed who submitted plagiarized thesis.

Student/Author Signature: ______________

Name: **(Nasir Shehzad)**

Certificate of Approval

This is to certify that the research work presented in this thesis, entitled: **Study of Internal Poiseuille Flows of Nano Fluids** was conducted by **Mr. Nasir Shehzad**, Reg. No. **40-FBAS/PHDMA/F13** under the supervision of **Dr. Ahmed Zeeshan** no part of this thesis has been submitted anywhere else for any other degree. This thesis is submitted to the **Department of Mathematics & Statistics, FBAS, IIU, Islamabad** in partial fulfillment of the requirements for the degree of **Doctor of Philosophy in Mathematics, Department of Mathematics & Statistics, Faculty of Basic & Applied Science, International Islamic University, Sector H-10, Islamabad, Pakistan.**

Student Name: Nasir Shehzad **Signature:** ____________

Examination Committee:

a) **External Examiner 1:**
Name/Designation/Office Address **Signature:** ____________
Prof. Dr. Saleem Asghar
Professor of Mathematics,
Department of Mathematics,
COMSATS, IIT, Park Road, Chak Shahzad,
Islamabad.

b) **External Examiner 2:**
Name/Designation/Office Address) **Signature:** ____________
Prof. Dr. Muhammad Ayub
Professor of Mathematics,
Department of Mathematics,
Hitech University, Taxilla.

c) **Internal Examiner:**
Name/Designation/Office Address) **Signature:** ____________
Dr. Nasir Ali
Associate Professor

Supervisor Name:
Dr. Ahmed Zeeshan **Signature:** ____________

Co-Supervisor Name:
Dr. Rahmat Ellahi **Signature:** ____________

Name of Dean/HOD:
Prof. Dr. Muhammad Sajid, T.I **Signature:** ____________

Acknowledgement

All praise for **ALLAH RAB-UL-IZZAT**, the creator, the glorious and the merciful Lord, who guides me in darkness, helps me in difficulties and enables me to view stumbling blocks as stepping stones to the stars to reach the ultimate stage with courage. I am nothing without my **ALLAH** but I can achieve everything with HIS assistance. All of my veneration and devotion goes to our beloved **Prophet Hazrat MUHAMMAD (SALLALLAHU ALAYHI WA SALAAM)** the source of humanity, kindness, guidance for the whole creatures and who declared it an obligatory duty of every Muslim to seek and acquire knowledge. My **ALLAH RAB-UL-IZZAT** shower HIS countless blessing upon **Prophet Hazrat MUHAMMAD (SALLALLAHU ALAYHI WA SALAAM)** and companions.

I owe a great debt of sincerest gramercy to my respected, affectionate, benevolent and devoted supervisor **Dr. Ahmed Zeeshan**, who helped me throughout my research time. His inspiring guidance, valuable suggestions, kind attitude and encouragement enabled me to complete my research work. I wish to express my profound appreciation and sincerest thanks to my worthy co-supervisor **Prof. Dr. Rahmat Ellahi**, for his unsurpassed, inexhaustible inspiration, selfless guidance, dedication and greatest support all the way of my research work. Despite of his engaging and hectic schedule, he always welcomed me for guidance and assistance in my work. His tremendous enthusiasm and insight will continue to influence me throughout my career as a Mathematician.

I am also very grateful to **Prof. Dr. Muhammad Sajid (T.I)** chairman of the department of mathematics and statistics, International Islamic university Islamabad for providing facilities that enabled the successful completion of this research work.

Salute to my Father, Mother (late) and Siblings, who did a lot for my thesis, financially and miscellaneous matters. I owe my heartiest gratitude for their assistance and never ending prayers for my success. I have no words to express millions of thanks to my Wife for her part, which may never ever be compared or replaced with any reward.

My sincere thanks to all my respected teachers in my career; whom teachings, instructions, knowledge and experiences made it possible. I enact my heartiest thanks to all my friends, colleagues and well-wishers for the constructive, productive, fruitful and moral support throughout this whole journey.

Nasir Shehzad

Dedication

I dedicate this thesis

To

My Father,

My Family,

My Wife,

My Children,

And

Especially

My Mother (Late).

Preface

The internal flows such as heating and cooling fluids, chemical processes, petrol in an engine of car, blood in an artery or vein environmental control and energy conservation technologies are very significant because they have a vast range of applications. The flows extended the concept of boundary layer to a fully developed flow. These flows are usually induced by either movement of a wall or change in pressure. The class of flows that occurs due to pressure gradient is called Poiseuille flow. They incorporate laminar and incompressible internal flows. Many heat-transfer devices employ Poiseuille internal flow to add to/remove heat from the system. For the purpose, a good heat transmitting liquid is filled in pipe and transmitted. Few more examples of such devices are heat systems and automobile coolant, refrigerator and cooling rods in nuclear reactor.

One of the efficient heat convection fluids such as nanofluids gained importance. The mixture of nanosized particles in low conductive and inert liquids enhances the thermal conductivity unpredictably. The particles (1-100nm) having different shapes such as spherical, cylindrical or platelet, etc., produce amazingly different results from the large particles with huge surface region to volume proportions properties due to inhabitance of an extensive of iotas on the limits which makes it stable in suspension.

The two main models namely Buongiorno and Tiwari & Das models have an extensive mathematical use to express the behaviour of such liquid. This thesis discusses the internal Poiseuille flow through channel with flat and wavy plates saturated by nanofluid under the influence of different body forces. It comprises seven chapters. The details are:

Chapter one is based on literature review, some basic concepts, thermophysical properties of nanofluids, fundamental equations and analytical schemes.

Chapter two addresses convective radiative plane Poiseuille flow of nanofluid through porous medium with slip. Novel features regarding thermophoresis and Brownian motion are taken into consideration. The purpose of this chapter is to explore the effect of second-order velocity slip on magnetohydrodynamics (MHD) plane Poiseuille flow of nanofluid through two-fold parallel horizontal plates with viscous and Ohmic dissipations. Stefan blowing factor at the lower wall for injection along with the concentration of nanoparticles and thermal radiation is considered. The analytical solution of formidable governing equations is achieved by homotopy analysis method. The effectual reliability of obtained solutions is first verified through $\hbar$-curves and later warranted by means of residual errors norms in each case. The effects of physical elements along with convergence analysis have also been offered. The contents of this chapter are **published in "Journal of Molecular Liquids, 273 (2019) 292–304"**.

Chapter three discusses the structural impact of kerosene-Alumina (Al_2O_3) a nanofluid on MHD Poiseuille flow having variable thermal conductivity with application of cooling process. In this chapter, the Alumina has been manufactured for application as a kerosene-based nanofluid to assess its potential heat-transfer application in thrust chamber cooling of liquid rocket engine. The proposed study with impact of inclined uniform magnetic field, variable thermal conductivity, heat generation and heat flux on steady plane Poiseuille flow is discussed. The systems of coupled nonlinear equations are solved analytically by homotopy analysis method. This study is **published in "Journal of Molecular Liquids, 264 (2018) 607–615"**.

Chapter four presents the analysis of activation energy in Couette-Poiseuille flow of nanofluid in presence of chemical reaction and convective boundary conditions. In this chapter a Couette – Poiseuille nanofluid flow through two parallel straight walls with convective boundary heat and mass conditions are studied. The main aim of this chapter is to scrutinize the mutual influence of chemical reaction with activation energy and manufacturing extrusion thermal system in the presence of radiation effects. For this analysis, appropriate transformations on the partial differential equations have been used. The governing systems of nonlinear coupled ordinary, differential equations are tackled analytically with the advantages of homotopy analysis method. The findings of this chapter are **published in "Results in Physics, 8 (2018) 502–512"**.

Chapter five deals with the convective Poiseuille flow of Al_2O_3-Ethylene glycol a nanofluid in a porous-wavy channel with thermal radiation. The electro-magnetohydrodynamics (EMHD) flow in a wavy channel with porous media has been discussed. The emphases are given to investigate the simultaneous effects of porosity and electro-magnetohydrodynamics flow of heat-transfer with the existence of thermal radiations and uniform wall temperatures. The homotopy analysis method is used to obtain the analytical solutions of coupled thermal boundary layer equations. The investigations of this chapter are **published in "Neural Computing and Applications, 30 (2018) 3371–3382"**.

Chapter six consists of a study of internal energy loss due to entropy generation for non-Darcy Poiseuille flow of silver-water nanofluid. In this chapter, separate non-Darcy porous media irreversibility is discussed in a wavy channel for the first time. The purpose is to indicate the key factors that can be use to control energy loss (entropy) in the said phenomenon. Also, this chapter offers a significant attempt to present an adequate theoretical estimate for low-cost purification of drinking water by silver nanoparticles with very low energy loss in an industrial process. More specifically, this chapter concentrates on MHD mixed convection Poiseuille with different pressure gradient flow of fluid with silver (Ag) nanoparticles passing through the porous wavy channel. The phenomena of coupled nonlinear differential equations are tackled by the homotopy method. These observations have been **published in "Entropy, 20(11) (2018) 851"**.

Chapter seven illustrates the effects of radiative electro-magnetohydrodynamics diminishing internal energy of pressure-driven flow of titanium dioxide-water nanofluid due to entropy generation. The effective influences of electro-magnetohydrodynamics (EMHD) and entropy generation with nanoparticles through a wavy channel on Poiseuille flow synthesis have been studied. In addition, the simultaneous impact of electro-hydrodynamics (EHD) and thermal radiation are examined. The average entropy generation with buoyancy force yielded a nonlinear coupled relationship. To achieve a formidable and reliable solution of such a nonlinear flow problem, the homotopy analysis method is used. These observations have been **published in "Entropy, 21(3) (2019) 236"**.

Nomenclature

$\mathbf{V}$	Dimensional nanofluid velocity
T	Dimensional nanofluid temperature
C	Dimensional nanoparticle concentration
$T*$	Reference temperature
$\bar{u}$	Dimensional components of velocity along $\bar{x}$
$\bar{v}$	Dimensional components of velocity along $\bar{y}$
$-a/a$	Lower / upper walls of flat channel
$\bar{p}$	Dimensional pressure
$\mathbf{B}$	Magnetic field strength
u	Dimensionless components of velocity along x - axis
v	Dimensionless components of velocity along y - axis
K_1	Porous medium permeability coefficient
S	Stefan mass blowing/suction parameter
$2a$	Width of channel
k	Thermal conductivity
B_0	Uniform transverse magnetic field
D_T	Thermophoretic diffusion coefficient
D_B	Brownian diffusion coefficient
K_r^2	Reaction rate
h_f	Heat transfer coefficient
Da	Darcy parameter
S_1	Fluid suction/injection parameter
$m*$	Temperature scale
$k*$	Mean absorption coefficient
P	Constant pressure gradient
Ra	Rayleigh number
M	Magnetic field parameter
$\bar{M}$	Inclined Magnetic field parameter
Rd	Radiation parameter
Nb	Brownian motion parameter
h_f	Heat transfer coefficient
Nr	Buoyancy ratio

g	Gravitational acceleration
T_1	Temperature at lower wall
T_2	Upper wall temperature
∇	Vector differential operator
V_0	Suction/injection velocity
C_1	Concentration at lower wall
C_2	Concentration at upper wall
$U*$	Constant wall velocity
U_m	Mean velocity
Q_0	Dimensional heat source/sink coefficient
Q	Non-dimensional heat source/sink coefficient
k^{ε}	Variable thermal conductivity
Le	Lewis number
$\mathbf{J}$	Joule current
Φ	Viscous dissipation
$C*$	Reference concentration
q_r	Radiative heat flux
E_a	Dimensional Activation energy
n_1	Fitted rate constant
h_s	Mass transfer coefficient
κ_B	Boltzmann constant
$n*$	Concentration scale
p	Dimensionless pressure
Pr	Prandtl number
Ec	Eckert number
Nt	Thermophoresis parameter
Sc	Schmidt number
Bi	Biot number
Nj	Convection diffusion parameter
Cr	Reaction rate
E	Dimensionless Activation energy
Re	Reynolds number

E_1	Electric field parameter	Br	Brinkman number
C_p	Heat capacity	Sh	Sherwood number
C_f	Skin friction coefficient	Nu	Nusselt number

Greek Symbols

μ	Dynamic Viscosity	ν	Kinematic viscosity
$(\rho C_p)_f$	Heat capacity of the base fluid	θ	Dimensionless temperature
ε	Momentum accommodation coefficient	ϕ	Dimensionless nanoparticles volume fraction
α	Thermal diffusivity	σ^*	Stefan Boltzman constant
β	Volumetric volume expansion coefficient	σ	Electrical conductivity
$(\rho C_p)_p$	Heat capacity of the nanoparticle material	Ω	Temperature difference parameter
δ	Non-dimensional wave number	ρ	Density
λ	Wavelength	δ_1	Molecular mean free path

Subscripts

f	Base fluids	s	Nanoparticle material

Contents

Chapter 1

1 Introduction

This chapter deliver two major themes, namely, motivation and preliminaries. The motivation contains a detail literature survey and background of problems under consideration. The preliminaries include the basics of fluid mechanics with its fundamental laws, nanofluid with their thermophysical properties and few most relevant definitions for a better understanding of present work.

1.1 Motivation

The flow which is bounded by walls is known as internal flow. These flows are very important and represent a simple geometry for heating and cooling fluids, chemical processes environmental control and energy conservation technologies. Also, flow of petrol in engine of car, or flow of blood in artery or vein are example of internal flows. Applications of internal flows are wide ranged almost all the fluid devices use internal flows. The flows extended the concept of boundary layer to fully developed flow. The flow usually induced by either movement of wall or change in pressure. The class of flows which occurs due to pressure gradient is Poiseuille flow. Firstly, the jean Poiseuille was experimentally studied Poiseuille flow in 1838. These incorporate laminar and incompressible internal flows. Many heat transfer devices employ Poiseuille internal flow to add/remove heat from the system. For the purpose, a good heat transmitting liquid is filled in pipe and transmitted. Some good examples of such devices are heat systems, pulse combustor for both civil and military uses, automobile coolant, refrigerator and cooling rods in nuclear reactor. The characteristics of

Poiseuille flow and related convection heat transfer remained the focus of attention for several year as it had many manifestation in daily life. Internal Poiseuille flows extensive application in engineering [1-5] and medical sciences [6-10] is the motivation behind this.

Convectional heat transfer liquids in many industrial sectors like acetone, ethylene glycol, water and kerosene, etc., play an important role in various chemical productions, air-conditioning, microelectronics and transportation. However, owing to transfer of heat these liquids do not cause very high level of thermal conductivity. Various processes have been implemented to speed up heat transfer. Process to control this barrier and enhance heat properties in liquids via suspensions of nanoparticles in liquids is new developments in this field that is very effective for heat transfer performance. The subsequent combination of the base fluid and nanoparticles having exclusive chemical a physical premises is known as a nanofluid and word "nanofluid" was carried in 1995 by Choi [11]. Furthermore, a liquid blend involving nanometer (1nm–100nm) estimate particles or strands is known as nanofluid. Contrasted with micrometer particles, nanoparticles have a high surface region to volume proportion because of the inhabitance of an extensive figure of iotas on limits, allows them to be in a stable condition in suspensions. Therefore, nanoparticles suspension indicates greater amount of conductivity conceivably because of upgraded convection between the strong molecule and fluid surfaces. The base fluids are commonly used for nanofluids are water, propylene glycol, bio-fluids, kerosene, polymeric solution, lubricants and organic liquids (refrigerant, ethylene, etc.) [12-17]. Metals (Ag, Au, Cu, TiO_2, Al_2O_3), carbides (Tic, Sic), nitrides (SiN, AlN) and non-metals (carbon nanotubes, graphite, diamond) are the most common nanoparticles used in nanofluids. Thereafter, a noteworthy work has been studied on nanofluids due to its vast applications.

Convection in saturated permeable is a popular field of study among researchers nowadays due to its numerous applications in painting filtration, microelectronic heat transfer, soil sciences, thermal insulation, petroleum industries, nuclear waste disposal, geothermal systems, chemical catalytic beds, fuel cells, solid matrix heat exchangers, grain storage, etc. Darcy's law [18] is mathematically expressed by the following relationship

$$-\nabla \bar{p} = \eta_1 \bar{u} . \tag{1.1}$$

It is understood that equation (1.1) is insufficient to discuss high rate of flow in permeable medium because, low Reynolds number Re depend on mean pore diameter exceeds 1 to 10. As a matter of fact, when the Re increases to a critical value or when inertial forces dominate, then validity of equation (1.1) is not more and it come to be nonlinear. Whereas, the structure of nonlinear Darcy's law illustrates a mechanism of viscous flow under different geometric and physical conditions. To overcome this deficiency, Forchheimer [19] proposed nonlinear correction of Darcy's law by the following universal decree

$$-\nabla \bar{p} = \eta_1 \bar{u} + \eta_2 \bar{u}^2 , \tag{1.2}$$

where $\nabla \bar{p}$ is a pressure gradient, $\eta_1 = \mu_{nf} / K_1$, η_2 is an empirical constant in second-order shape related to resistance which represents porosity and pore size [20-23]. Eastman et al. [24] have examined that thermal conductivity of fluid enhance 40% when 0.3% nanosized copper are mixed in ethylene glycol. According to Pak and Cho [25], they have examined that convective energy transfer coefficient enhances by 75% when 2.78% of Al_2O_3 particle concentration with a constant Reynolds number suspended in fluid. Rocket engine thrust chamber experiences very high temperature due to the combustion product. Various cooling methods are used to protect thrust chamber wall from the high-temperature combustion gases. In one of the methods, propellant is allowed to flow beside the outer surface of the nozzle wall through the cooling channels. The cooling efficiency of such system depends upon the thermophysical property and flow velocity of the liquid medium. Higher flow velocity in the coolant channel results in an increased pressure drop in the system and in turn increases the requirement of pumping power. In semi-cryogenic engine rocket system, kerosene, the fuel, is being used as a coolant. Kerosene has very low thermal conductivity and is not a good candidate for convective transfer of heat. Therefore, a step to raised thermal property of kerosene by suspending rare amount of nano-size particles in it. In nanofluid preparation, two methods are give, one of them: single-step and another one: two-step method. Agarwal et al. [26] employed a two-step technique for manufacturing of nanofluid with nano-size aluminum dioxide Al_2O_3 particles in kerosene. Surfactants, pH methods and ultra-sonication process are used to maintain the stability of the kerosene-Al_2O_3 nanofluid at a certain temperature and Malvern-Zeta size procedure was adopted to calculate size of particles. The authors discussed the significant results of kerosene-Al_2O_3 nanofluid when the nanofluid color of from white to gray in the ultra-sonication process.

In particular, silver nanoparticle is a very effective agent, as seen by its applications in agriculture (fruits, vegetables), medicine (devices, burn treatment, infections [27]), and industry (solar energy absorption, cosmetics, clothing, chemical catalysis, water purification). Silver particles in ionic form exhibit antibacterial action, they are able to break down bacteria such as Escherichia coli and Staphylococcus aureus. Silver nano colloid in a concentration of 0.8–1.2 ppm removes Escherichia coli bacteria from groundwater. Ceramic water filter devices can eliminate waterborne pathogens. Ceramic water filters are also reported to be very helpful to removing protozoa more than 99% and bacteria 90–99.99% from drinking water [28, 29]. It is noted that nanoparticle preparations are very effective in relation to Helicobacter pylori. Silver ions also act synergistically with benzyl penicillin, erythromycin, amoxicillin, and clindamycin [30]. Godson et al. [31] calculated the effects for different factors for example temperature (between 323 K and 363 K) and concentration (0.3, 0.6, and 0.9% volume concentration) on thermal conductivity of Ag-deionized water nanofluid by using uniform nanosized silver particles. The outcomes described that thermal characteristics increased by 27% to 80% with increase in temperature and concentration of particles from 0.3% to 0.9%. Silver water used in investigations contained antibacterial "silver water" from Nanoco. It was found that exposure of the investigated food material on the activity of the sprayed nanosilver particles could almost double their microbiological and sensorial stability.

The collision of particles "Brownian motion" and energy transfer "thermophoresis" contribute vital part in flow of nanofluid. Radiation as well as diffusion of particles effects in nanofluid flow at on permeable wall have successfully investigated in [32]. Autors determined that behavior of φ, Nt and Nb don't go hand in hand while the magnitude of fluid highly varies for Williamson fluid parameter and porosity parameter.

Xu et al. [33] used Buongiorno mathematical model in vertical channel to discuss the analysis of natural convection nanofluid flow. Authors investigated that characteristic of heat transfer can be enhanced if the suitable nanofluid used. The Arrhenius activation energy with the inclusion of chemical reaction has a significant application in chemical industries, such as to maintain the temperature of nuclear reactors up to certain degree, extraction of oil and geothermal reservoirs in mass transfer. In vertical porous pipe the combine influence of Arrhenius activation energy along the addition of chemical reaction are considered first time by Bestman [34].The author bring in to use perturbation method as an analytical technique to estimate a solution.

Study of magnetohydrodynamics (MHD) is an important application in industrial equipment, physics, chemistry and engineering fields. In industrial fields, like MHD pimps, MHD generators and ball bearing, etc. The impact of MHD nanofluid in porous cavity under the action of forced convection is discussed by Sheikholeslami [35]. The author gives important results about platelet shaped nanosized particles, which contribute major role to enhance heat transfer activity in fluid flow. Bhatti et al. [36] investigated the entropy generation with combined under act of chemical reaction along thermal radiation on MHD boundary layer flow above on a moving surface. Rashidi et al. [37] estimated entropy of flow in three different types of nanoparticles, like Cu, CuO and Al_2O_3 with influences of MHD over porous disk. The authors obtained the major results about minimization of entropy for flow over a disk. Sheikholeslami and Bhatti [38] also discussed the minimization of entropy in magnetic environment in a porous semi-annulus.

The energy losses due to entropy generation analysis have diverse utilizations in the physical sciences. For example, the characteristics of energy loss for radiative mixed convection flow passing through the vertical channel was reported by Mahmud and Fraser [39]. The effects of MHD and the group parameter illustrated subdue behavior on entropy generation, as compared to the mixed convection and radiation parameter. Another study Rashidi et al. [40] have designed the entropy generation of magnetically developing a nanofluid flow for a spinning porous disk. It is noted that a continuous reduction was noted in the average entropy generation for larger value of the nanoparticle volume fraction, while increasing values of MHDl parameter produced an escalation in the average entropy generation number. Approximate survey on entropy generation on nanofluid containing nanoparticles, like Cu, Al_2O_3 and TiO_3 in pure water between wavy walls, was implemented by Cho et al. [41]. They testified that for a given nanofluid, total energy loss could be diminished and the mean heat transfer number exploited through a suitable adjustment of the wavy surface geometry parameters. Ranjit and Shit [42] carried out the results of entropy generation on electro-osmotic flow with magnetic and Joule heating. They perceived that entropy generation near the channel wall rapidly improved with rise of the joule heating parameter. A few remarkable contributions on entropy generation with diverse studies can be explored in references [43-45].

Motivated from the above literature major aim of present thesis is to study the internal Poiseuille nanofluid in different flow configurations under different effects. Significant modeling is presented with the help of dimensionless parameters and using long wavelength approximations. The governing systems of highly nonlinear coupled ordinary, differential equations are tackled analytically with the advantages of homotopy analysis method (HAM) [46-49]. The HAM has following superiority for results estimations: (i) It is useful in providing flexibility in the developing equation of linear functions of solutions. (ii) It gives us a way to verify the convergence of the developed series solutions. (iii) HAM is independent of small or large numerical value of parameters involved in problem. On the other hand it may take unnecessary long computational time and some time for complex problems solution could not achieved desired convergences as computers may not have sufficient internal memory. Physical clarification of results is interpreted by means of graphs and tables. This thesis contains seven chapters that are authors own work which is published in international reputed journals.

1.2 Preliminaries

In this section, some fundamental concept used in subsequent chapters, has been given briefly. It includes basic definitions, terminologies, the dimensionless numbers of physical importance and the governing equations, etc.

1.2.1 Fluid

There are three states of matter namely, liquid, solid and gas, among which the gas and liquid both are fluids. A fluid is a substance (gas or liquid) which modifies its shape continuously under the action of external forces or any material that deforms continuously. The fluid flow is a universal phenomenon which occurs frequently in our everyday life. On the other hand, a solid always gives the opposing effects on deforming force and can't move easily [50, 51].

Fluids have been further sub-categorized into ideal and viscous fluids. In ideal or inviscid fluids the most effective internal force is the pressure, which acts in such a way that the fluid flows from high stress to low. In viscous fluids, shear rate and viscosity are independent to each other. Moreover, these are the fluids which satisfies Newton's law about viscosity "the shear stress is directly and linearly related to the shear rate".

1.2.2 Fluid mechanics

It concerns with prediction, and controlling nature of fluids. Fluid mechanics is one of the engineering sciences that forms the basis for all forms of engineering [52]. This subject branches out into various specialties such as aerodynamics, hydraulic engineering, marine engineering, gas dynamics, and manufacturing processes. It includes the statics, kinematics and dynamics of fluids. Fluid mechanics studies the dynamic properties (e.g. motion) of fluid.

1.2.3 Heat transfer phenomenon

Heat transfer processes assume a key part in many natural, industrial and biological systems. Transition of heat is actually the transport of energy owing to temperature differences. Conduction, radiation and convection are the three types of heat transfer as presented in figure 1.1.

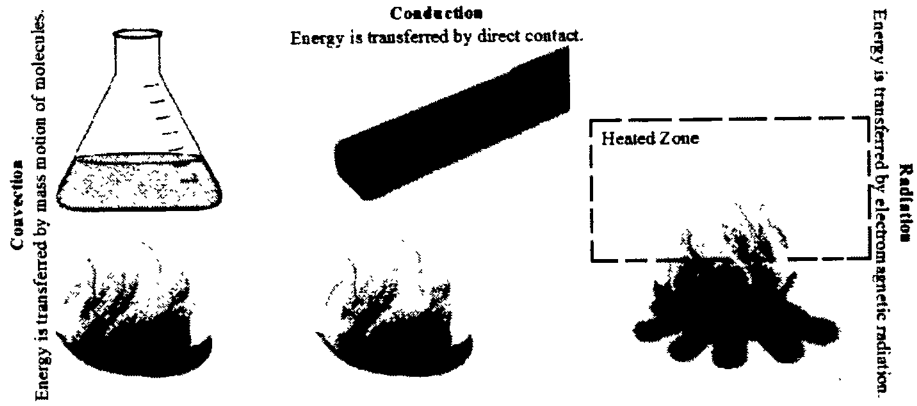

Figure 1.1: Classifications of energy transfer.

Conductive heat transfer takes place in solids via molecular energetic movement due to the temperature gradient within a medium. In Radiation, thermal energy is transferred between two or more bodies without any defined medium by electromagnetic waves. Convection is an energy transfer through liquids and gases or fluids in general moving near the surface. Natural convection flow is caused by density variance in different sections of the fluid. This density change, along with the influence of the gravity, generates a buoyancy force, due to which the heavier fluid travels downwards and the lighter fluid moves upwards, generating buoyancy-driven flow. The density variance in natural convection flows may result from a temperature variance or from the changes in the concentration of chemical species. The most common buoyant flows may be seen as air flows around our rooms and other engineering applications [53, 54]. When these two phenomena of heat transfer (forced and natural convection) are occurring at the same time the situation is commonly known as mixed convection.

1.2.4 Nanofluid

In 1881, Maxwell [55] succeeded in exploring that energy transfer can be augmented by mixing micro-sized particles in base fluid. After Maxwell, it was observed that although addition of micro-sized material particles in the base fluid do result in some enhancement in rate of heat transfer but the major issues are clogging, erosion, and pressure drop, produced due to these particles, retained the technology away from the practical usage of this strategy for a long time.

Table 1.1: Potential usage of the nanomaterials [56].

Nanomaterial	General applications
Ag	Microelectronic industry, antibacterial and disinfecting agent, anti-corrosive coating, catalysis.
TiO_2	Solar cells, photo-catalysis, antibacterial and disinfecting agent, cosmetics, air purification, semiconductors, UV resistors, astronautics.
Al, Al_2O_3	Heat transfer fluid, catalyst support, water-proof material, wear-resistant additive, cosmetic filler.
SiO_2	Construction industry, production of glass, sensitive optical fiber, ceramics, food and pharmaceutical applications.
Cu, CuO	Superconductors, antibacterial and disinfecting agent, catalysis, gas sensors, thermo-electronics, microelectronic industry.
Fe, Fe_2O_3, Fe_3O_4	Biomedical applications, environment remediation, magnetic data storage, semiconductor, microwave devices.

Masuda et al. [57] firstly conveyed that influence of nanoparticles improves thermal conductivity of base fluid. Particles are of different types such as metals, non-metals, metallic oxides and non- metallic oxides, etc. Water, oils and ethylene glycol are frequently use base fluids. In industries, normally used nanoparticles are TiO_2, Fe_3O_4, SiO_2, Al_2O_3, CuO in compound form and Au, Cu, Fe, Ag in elemental form. Some important applications of nanomaterial are given in Table 1.1.

1.2.5 Thermophysical characteristic of nanofluid

Thermophysical features of nanofluid strongly affect solution of the considered flow problems. There are different models for the description of thermophysical properties of nanofluid which are derived by various scientist. Thermophysical properties for example viscosity, density, thermal conductivity, electrical conductivity and specific heat are calculated by employing the formulas [58], which are adopted as empirical relationships among the base fluid and nanoparticles.

1.2.5.1 Viscosity

Engineers and scientists utilize different models for dynamic viscosity of nanofluid. Einstein [59] defined viscosity of solid spherical particles suspended very low amount (less than 2%) volume fraction. Later-on, Brinkman [60] presented a new relation by modifying Einstein's equation of viscosity correlation with particle volume fraction less than 4%. Viscosity of the nanofluid can be computed by the simple mixture theory [61] and is expressed as

$$\mu_{nf} = \frac{\mu_f}{(1-\varphi)^{2.5}}. \tag{1.3}$$

A new relation between effective viscosity and φ at very low (0.3, 0.6, and 0.9% volume concentration) along temperature between 323 K and 363 K was proposed by Godson et al. [62] in the following form

$$\mu_{nf} = \left(1.005 + 0.497\varphi - 0.1149\varphi^2\right)\mu_f. \tag{1.4}$$

An experiment is performed to collect data from correlation between TiO_2–water nanofluid viscosity and volume fractions φ from 0.2% to 2% by Duangthongsuk and Wongwises [63]. The objective of the following correlations are to estimate effective nanofluid viscosity at three different temperature scenario

$$\left.\begin{aligned}\mu_{nf} &= \left(1.0226 + 0.0477\varphi - 0.0112\varphi^2\right)\mu_f; & T &= 15^{\circ}C\\ \mu_{nf} &= \left(1.013 + 0.092\varphi - 0.015\varphi^2\right)\mu_f; & T &= 25^{\circ}C\\ \mu_{nf} &= \left(1.018 + 0.112\varphi - 0.0177\varphi^2\right)\mu_f; & T &= 35^{\circ}C\end{aligned}\right\}. \tag{1.5}$$

1.2.5.2 Thermal conductivity

The suspension of solid particles are the reason to rise in thermal conductivity of liquid. A classical formula defined for thermal conductivity [64] as

$$\frac{k_{nf}}{k_f} = \frac{2k_f + k_p - 2\varphi\left(k_f - k_p\right)}{2k_f + k_p + \varphi\left(k_f - k_p\right)}. \tag{1.6}$$

Godson et al. [65] proposed relation for thermal conductivity at low volume fraction as

$$k_{nf} = \left(0.9692\varphi + 0.9508\right)k_f. \tag{1.7}$$

The expressions of nanofluid thermal conductivity for three different temperature conditions are also discussed by Duangthongsuk and Wongwises [66] as

$$\left.\begin{aligned}k_{nf} &= \left(1.0225 + 0.0272\varphi\right)k_f; & T &= 15^{\circ}C\\ k_{nf} &= \left(1.0204 + 0.0249\varphi\right)k_f; & T &= 25^{\circ}C\\ k_{nf} &= \left(1.0139 + 0.0250\phi\right)k_f; & T &= 35^{\circ}C\end{aligned}\right\}. \tag{1.8}$$

1.2.5.3 Density

Using the physical principle of the mixture law, density of nanofluid may be calculated analytically. Using this law measuring weight and volume of amalgamation density of nanofluid can be determined. The φ can be assessed by knowing the densities of both components and nanofluid density [67] can be described as

$$\rho_{nf} = \left(1 - \varphi\right)\rho_f + \varphi\rho_p. \tag{1.9}$$

1.2.5.4 Electrical conductivity

The electrical conductivity of nanofluid rises with rise in concentration and temperature of particle. Electrical conductivity is detected to be higher for smaller sized particles in

1.3 Governing equations

The fundamental dynamic equations for nanofluid flow are the same as they are for the pure fluid which are well known as (i) Continuity equation (conservation of mass), (ii) Momentum equation (conservation of momentum) and (iii) Energy equation (conservation of energy). However, the consideration of nanofluid does modify these equations to some extent. Since we intend to use the two famous nanofluid models, namely, Buongiorno model [73] and Tiwari and Das model [74]. Therefore, the modification in the governing laws shall be mentioned with regard to these two models.

1.3.1 Equation of continuity

Principle of mass conservation for fluid flow also known as the continuity equation, in vector notation it is written as follows

$$\frac{1}{\rho_f}\frac{D\rho_f}{Dt}+\nabla.\mathbf{V}=0. \tag{1.13}$$

Equation (1.13) is valid for pure fluid and nanofluid[1]. In which, material derivative D/Dt is defined as

$$\frac{D(\;)}{Dt}=\frac{\partial(\;)}{\partial t}+\mathbf{V}.\nabla(\;), \tag{1.14}$$

where $\partial/\partial t$ represents local time derivative, in steady case local time derivative term is neglected and $\mathbf{V}.\nabla$ denotes convective derivative. Equation (1.14) for fluid density ρ_f described as follow

$$\frac{D\rho_f}{Dt}=\frac{\partial\rho_f}{\partial t}+\left(u\frac{\partial}{\partial x}+v\frac{\partial}{\partial y}+w\frac{\partial}{\partial z}\right)\rho_f. \tag{1.15}$$

---

[1] For Tiwari and Das model, ρ_f has been replaced by ρ_{nf}

Constant density of fluid represents incompressible fluids. Mathematically it is expressed as

$$\frac{D\rho_f}{Dt}=0. \tag{1.16}$$

Hence, the equation (1.13) takes the form

$$\nabla.\mathbf{V}=0, \tag{1.17}$$

or

$$\frac{\partial \bar{u}}{\partial \bar{x}}+\frac{\partial \bar{v}}{\partial \bar{y}}+\frac{\partial \bar{w}}{\partial \bar{z}}=0. \tag{1.18}$$

1.3.2 Momentum equation

The principle of momentum conservation for an incompressible viscous fluid reads as

$$\rho_f\left[\frac{\partial \mathbf{V}}{\partial t}+(\mathbf{V}.\nabla)\mathbf{V}\right]=-\nabla\bar{p}+\mu_f\nabla^2\mathbf{V}+\mathbf{F}. \tag{1.19}$$

In equation (1.19), $\mathbf{F}$ denotes the body forces and in view of the problems considered in this dissertation the expected body forces are define as

$$\mathbf{F}=\mathbf{F}_L+\mathbf{F}_P+\mathbf{F}_B. \tag{1.20}$$

1.3.2.1 Magnetic force

The Lorentz force caused because of the application of wall-normal magnetic field and is defined as

$$\mathbf{F}_L=\mathbf{J}\times\mathbf{B}, \tag{1.21}$$

In equation (1.21), current density $\mathbf{J}$ defined via Ohm's law

$$\mathbf{J}=\sigma_f\left[\mathbf{E}+(\mathbf{V}\times\mathbf{B})\right]. \tag{1.22}$$

Equation (1.22) is valid for both pure fluid and nanofluid[2]. The flow area is depended under the action of magnetic fields $\mathbf{B}=[0,B_0,0]$ and uniformly applied electric field $\mathbf{E}=[0,0,-E_0]$, thus $\mathbf{J}\times\mathbf{B}=\sigma_{nf}\left[E_0B_0-B_0^2\bar{u},0,0\right]$. The boundary layer flow is always stabilized [75] with the influence of magnetic & electric fields. For moderate strength of magnetic & electric fields fulfill Ohm's law as well as Maxwell's equations

$$\nabla\times\mathbf{E}=0 \text{ and } \nabla.\mathbf{B}=0. \tag{1.23}$$

1.3.2.2 Darcy and non-Darcy porous media

The Poiseuille flow developed in between two parallel walls which are away from each other with defined distance occurred by an average pressure gradient $\nabla\bar{p}$. The parabolic shape of velocity profile generated when inertial forces are lesser as compared to viscous forces. It reflects the famous Darcy law, i.e., a linear relationship between average velocity [76] and pressure gradient.

$$\nabla\bar{p}=-\frac{\mu_f}{K_1}\mathbf{V}. \tag{1.24}$$

It is understood that Darcy's law is inadequate to describe the high rate of flow in porous media because low Re depended on the average diameter of pore extends 1 to 10. As a matter of fact, when the Re increases to a critical value or when inertial forces dominate, then equation (1.24) is not valid anymore and it becomes nonlinear, whereas the structure of nonlinear Darcy's law illustrates the mechanism of viscous flow under different geometric and physical conditions. To overcome this deficiency, Forchheimer proposed a nonlinear correction of Darcy's law by the following universal decree

$$\nabla\bar{p}=-\frac{\mu_f}{K}\mathbf{V}-\rho_f F_c|\mathbf{V}|\mathbf{V}, \tag{1.25}$$

---

[2] For Tiwari and Das model, σ_f has been replaced by σ_{nf}.

where, F_c is the dimensionless inertial resistance (coefficient) or Forchheimer correction. Equation (1.25) is also known as non-Darcy Forchheimer correction. Hence

$$\mathbf{F}_P = -\frac{\mu_f}{K}\mathbf{V} - \rho_f F_c |\mathbf{V}| \mathbf{V}. \tag{1.26}$$

1.3.2.3 Buoyancy force

In natural convection flow addition of $\rho_{nf}\mathbf{g}$ in equation (1.19) represents the gravitational force, this force applied as per volume unit of liquid. In thermal convection, density should be the function of temperature. The simplest equation of state is written as

$$\rho_{nf} = \rho_{nf}^{*}\left(1 - \beta\left(\bar{T} - T^{*}\right)\right), \tag{1.27}$$

where ρ_{nf}^{*} is nanofluid density at reference temperature T^{*}. Hence the buoyancy force is given by

$$\mathbf{F}_B = \rho_{nf}\mathbf{g}. \tag{1.28}$$

The nanofluid density ρ_{nf} at very low concentration of nanoparticles is taken to be approximated with base-fluid density ρ_f, then Boussinesq's approximation applied and buoyancy term converted to given expansion

$$\begin{aligned} \rho_{nf}\mathbf{g} &\cong \left[C\rho_p + (1-C)\left\{\rho_f\left(1-\beta\left(\bar{T}-T^{*}\right)\right)\right\}\right]\mathbf{g} \\ &\cong \left[(1-C^{*})\rho_f \beta g\left(T-T^{*}\right) - \left(\rho_p - \rho_f\right) g\left(C-C^{*}\right)\right]. \end{aligned} \tag{1.29}$$

1.3.3 Concentration equation

The convective processes 'usually' and 'often' go along with the mass transfer. Therefore, transport of materials that act as components (constituents, species) in the fluid mixture. Mathematically, this phenomena about conservation equation for nanoparticles along presence of chemical reaction with activation energy can be inscribed as

$$\frac{\partial C}{\partial t}+(\mathbf{V}.\nabla)C=-\frac{1}{\rho_p}\nabla.\mathbf{j}_p-K_r^2\left(\frac{T}{T*}\right)^{n_1}(C-C*)\exp\left(\frac{-E_a}{\kappa_B T}\right). \tag{1.30}$$

In the above equation, C is concentration of nanoparticle, $K_r^2(T/T*)^{n_1}\exp(-E_a/\kappa_B T)$ is the modified Arrhenius function [77]. The diffusion mass flux $\mathbf{j}_p$ express as Brownian $\mathbf{j}_{p,B}$ and thermophoresis $\mathbf{j}_{p,T}$ diffusion

$$\mathbf{j}_p=\mathbf{j}_{p,B}+\mathbf{j}_{p,T}=-\rho_p D_B\nabla C-\rho_p D_T\frac{\nabla T}{T*}. \tag{1.31}$$

Here D_B defined by the Einstein-Stokes equation as

$$D_B=\frac{k_B T}{3\pi\mu_f d_p} \tag{1.32}$$

and thermophoretic velocity $\mathbf{V}_T$ is defined as

$$\mathbf{V}_T=-\tilde{\beta}\frac{\mu_f}{\rho_f}\frac{\nabla T}{T*}, \tag{1.33}$$

the proportionality factor $\tilde{\beta}$ is given by

$$\tilde{\beta}=0.26\frac{k_f}{2k_f+k_p}. \tag{1.34}$$

The thermophoretic diffusion defined as

$$\mathbf{j}_{p,T}=\rho_p C\mathbf{V}_T=-\rho_p D_T\frac{\nabla T}{T*}, \tag{1.35}$$

where D_T is amount of thermophoretic diffusion, which is

$$D_t=\tilde{\beta}\frac{\mu_f}{\rho_f}C. \tag{1.36}$$

1.3.3.1 Brownian motion

The random movement of suspended particles in gas and liquid is due to the collisions of surrounding molecules in base fluid, called Brownian motion. The rise in temperature are due to diffusion of small particles in fluid and also cause to enhance thermal conductivity as governed by Fick's law as revealed in figure 1.2. Therefore, Brownian motion is an important feature in the thermal augmentation of nanofluid.

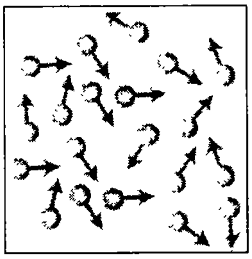

Figure 1.2: Particles Brownian motion.

1.3.3.2 Thermophoresis

Thermophoresis is a force which arises due to the temperature gradient. This phenomenon is termed as thermophoresis. Heat transfer is basically can be explained as shift of thermal energy form the higher temperature zone (region) to a lower temperature zone, as elaborate in figure 1.3. The transfer of heat is always from high to low temperature region until both regions reach the same temperature.

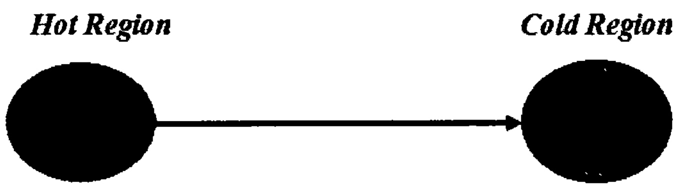

Figure 1.3: Schematic of the thermophoresis phenomenon.

Now, using equation (1.32) in equation (1.31) then the conservation equation take the form

$$\frac{\partial C}{\partial t}+\mathbf{V}.\nabla C = D_B\nabla^2 C+\frac{D_T}{T^*}\nabla^2 T+\text{Chemical reaction with activation energy.} \quad (1.37)$$

1.3.4 Energy equation

The thermal energy equation (principle of energy conservation) for a viscous incompressible nanofluid with the existence of heat source/sink and dissipation in energy can be written by Buongiorno's as

$$\left(\rho C_p\right)_f\left[\frac{\partial T}{\partial t}+(\mathbf{V}.\nabla)T\right]=-\nabla.\mathbf{q}+h_p\nabla.\mathbf{j}_p+q^*+D_{Dissipation}. \tag{1.38}$$

In equation (1.38), h_p is enthalpy, energy flux $\mathbf{q}$ can be calculated as the sum of heat flux conduction ($k_f\nabla T$), heat flux by nanoparticle diffusion ($h_p\mathbf{j}_p$) and heat flux by radiation ($\mathbf{q}_r$). Therefore, we get energy flux as

$$\mathbf{q}=-k_f\nabla T+h_p\mathbf{j}_p+\mathbf{q}_r \tag{1.39}$$

and

$$\nabla.\mathbf{q}=-\nabla.\left(k_f\nabla T\right)+\nabla.\left(h_p\mathbf{j}_p\right)+\nabla.\mathbf{q}_r. \tag{1.40}$$

If neglecting radiative heat flux, volumetric heat source/sink, dissipations and also consider diffusion mass flux for the nanoparticles $\mathbf{j}_p$ is equal to zero, then equation (1.45) becomes the familiar energy equation of pure fluid.

$$\nabla.\left(h_p\mathbf{j}_p\right)=h_p\nabla.\mathbf{j}_p+\mathbf{j}_p.\nabla h_p. \tag{1.41}$$

By using assumptions that base fluid and nanoparticles are in thermal equilibrium, so

$$\nabla h_p=c_p\nabla T, \tag{1.42}$$

and in view of the problems considered in this dissertation the expected dissipations are the viscous dissipation and Ohmic dissipation or Joule's heating[3].

---

[3] For Tiwari and Das model μ_f, σ_f have been replaced by μ_{nf}, σ_{nf} respectively.

$$D_{Dissipation} = D_{Viscous\ dissipation} + D_{Ohmic\ dissipation}, \tag{1.43}$$

where viscous dissipation for Newtonian fluid is

$$D_{Viscous\ dissipation} = \mu_f \left(\frac{\partial \bar{u}}{\partial y} \right)^2 \tag{1.44}$$

and Ohmic dissipation define as

$$D_{Ohmic\ dissipation} = \frac{1}{\sigma_f} \mathbf{J}.\mathbf{J} = \sigma_f \left(B_0 \bar{u} - E_0 \right)^2. \tag{1.45}$$

1.3.4.1 Heat source/sink

Volumetric heat source/sink q^* (W/m^3) can be written as

$$q^* = \begin{cases} Q_0 (T - T^*) & T \geq T^*, \\ 0 & T < T^*, \end{cases} \tag{1.46}$$

while the constant $Q_0 > 0$ or $Q_0 < 0$ represents the heat source/sink.

Substituting equations (1.31), (1.40), (1.41) and (1.42) in equation (1.38), the energy equation is found as

$$\begin{aligned} \left(\rho c_p\right)_f \left[\frac{\partial T}{\partial t} + (\mathbf{V}.\nabla) T \right] = k_f \nabla^2 T + \left(\rho c_p\right)_p \left[D_B \nabla C.\nabla T + D_T \frac{\nabla T.\nabla T}{T^*} \right] - \nabla.\mathbf{q}_r + \\ q^* + D_{Dissipation}. \end{aligned} \tag{1.47}$$

Equation (1.47) is valid for both pure fluid and nanofluid[4].

[4] For Tiwari and Das model k_f, $\left(\rho c_p\right)_f$ have been replaced by k_{nf}, $\left(\rho c_p\right)_{nf}$ respectively.

1.4 Surfaces

1.4.1 Flat surface

In this thesis, the chapters (2) to (4) are consist of viscous laminar incompressible nanofluid passing through a channel, contains two parallel flat walls. Concerned problems are considered in a Cartesian coordinate system, such that $\bar{x}$ – axis is taken along the channel wall, while $\bar{y}$ – axis is perpendicular to the channel which also indicates the contribution of g (i.e., gravity). The middle of channel taken at origin and the configuration of the walls (left and right) are at $\bar{y} = -a$ and $\bar{y} = a$ respectively as displayed in figure 1.4.

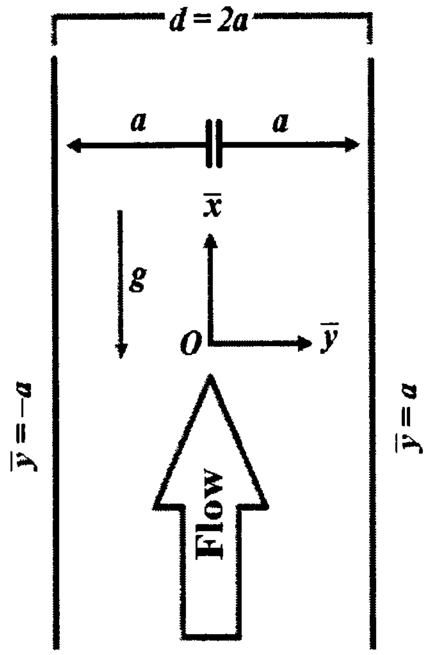

Figure 1.4: Schematic of the flat walls considered in this dissertation.

1.4.2 Wavy surface

In majority of the chapters of this dissertation, we shall be considering the viscous laminar incompressible nanofluid between two symmetric wavy walls. Concerned chapters consider in a Cartesian coordinate system, such that $\bar{x}$ – axis is taken along the channel wall, while $\bar{y}$ – axis is in transverse direction. The middle of channel taken at origin as indicate in figure 1.5 and the configuration of the walls (left and right) with amplitude a_1, width d and length L of the walls are defined as respectively

$$H_1 = -d - a_1 \cos\left(\frac{2\pi}{L}\bar{x}\right), \quad H_2 = d + a_1 \cos\left(\frac{2\pi}{L}\bar{x}\right). \tag{1.48}$$

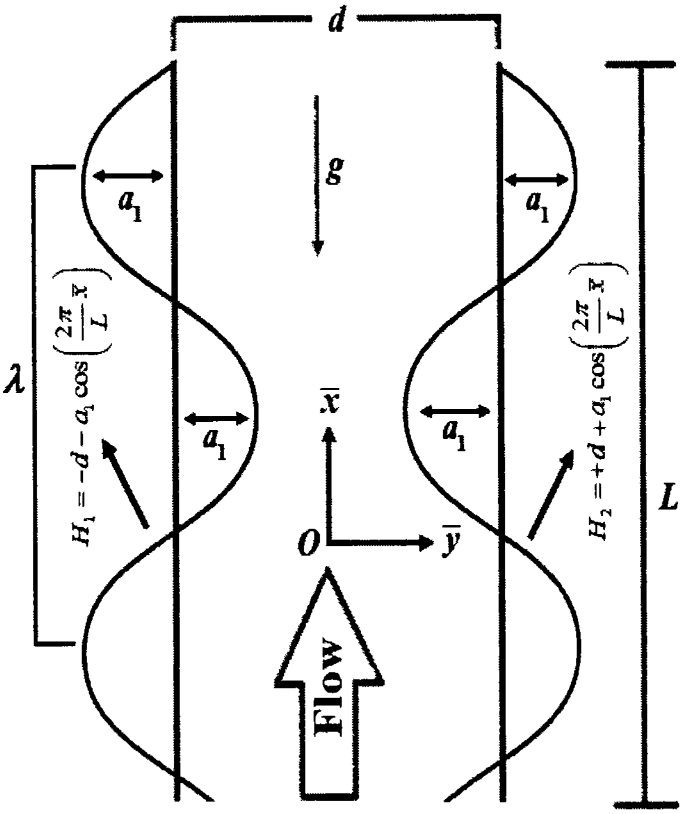

Figure 1.5: Schematic of the wavy walls considered in this dissertation.

1.5 Non-dimensional parameters

1.5.1 Prandtl number

Prandtl number ($\Pr$), named after a German scientist, Ludwig Prandtl, who has a dominant role in the research on viscous flow in the first half of the 20th century. $\Pr$ is the ratio of the coefficient of diffusion of momentum to the coefficient of diffusion of heat, i.e.,

$$\Pr = \frac{\nu_f}{\alpha_f} = \frac{\mu_f/\rho_f}{k_f/(\rho c_p)_f} = \frac{\mu_f c_p}{k_f}, \tag{1.49}$$

here α_f is thermal diffusivity of fluid.

1.5.2 Reynolds number

The Reynolds number (Re) named after the famous British fluid dynamicist of the late nineteenth century Osborne Reynolds, is ratio between inertial and viscous forces in flow, i.e.,

$$\mathrm{Re} = \frac{U_m l_1}{\nu_f} = \frac{\rho_f U_m l_1}{\mu_f}, \tag{1.50}$$

where U_m represents the reference velocity l_1 represents the characteristic length and ν_f is dynamic viscosity. The Reynolds number is used to characterize flow as turbulent or laminar.

1.5.3 Lewis number

For the combined studies of heat and mass transfer, Lewis number is an important physical quantity. It is a ratio between the characteristic lengths of diffusion of heat and diffusion of mass. Lewis number is also regarded as the ratio of thermal diffusivity to the mass diffusivity and is defined as

$$Le = \frac{\alpha_f}{D_B} = \frac{k_f/(\rho c_p)_f}{D_B}. \tag{1.51}$$

1.5.4 Schmidt number

For characterizing fluid flows in which there are simultaneous momentum and mass diffusion-convection processes occur. It is a ratio between the momentum diffusivity (kinematic viscosity) and diffusion of mass

$$Sc = \Pr Le = \frac{\nu_f}{D_B} = \frac{\mu_f}{\rho_f D_B}. \tag{1.52}$$

1.5.5 Grashof number

The dimensionless number which arises from the ratio of the buoyancy to the viscous forces is known as Grashof number. It is frequently used in study of natural or mixed convection flows. Mathematically,

$$Gr = \frac{\beta g \Delta T l_1^3}{\nu_f^2}. \tag{1.53}$$

where β is the coefficient of the volumetric change, ΔT is the temperature difference.

1.6 Physical quantities

1.6.1 Skin friction coefficient

The coefficient of skin friction at wavy surface in two-dimensional flow is defined as

$$C_f = \frac{\text{Shear stress on a surface}}{\text{Dynamic pressure}} = \frac{\tau_w}{\frac{1}{2}\rho U_m^2}, \tag{1.54}$$

where τ_w is wall shear stress, i.e.,

$$\tau_w = \mu_f \left(\nabla \bar{u} \bullet \hat{\boldsymbol{n}} \right) \text{ at surface}, \tag{1.55}$$

where $\hat{\boldsymbol{n}}$ is the unit vector normal to surface.

1.6.2 Nusselt number

Dimensionless heat transfer coefficient is known as Nusselt number which is an important physical parameter in the process of convective heat transfer. In convective heat transfer phenomena, the heat transfer rate is described as

$$Nu = \frac{\text{Convective heat transfer}}{\text{Conductive heat transfer}} = \frac{q_w}{k_f\left(T_1 - T^*\right)/l_1}, \tag{1.56}$$

where q_w is the wall heat flux which is given by

$$q_w = -k_f\left(\nabla T \cdot \hat{\boldsymbol{n}}\right) \text{ at surface.} \tag{1.57}$$

1.6.3 Sherwood number

This dimensionless number defines the rate transfer of convective mass. It is denoted as

$$Sh = \frac{\text{Convective mass transfer rate}}{\text{Diffusion rate}} = \frac{q_m}{D_B\left(C_1 - C^*\right)/l_1}, \tag{1.58}$$

where q_m is the wall mass flux which is given by

$$q_m = -D_B\left(\nabla C \cdot \hat{\boldsymbol{n}}\right) \text{ at surface.} \tag{1.59}$$

1.7 Methodology

The nonlinear differential equations, nonlinear boundary conditions, variable coefficient differential equations and coupled differential equations have little chance of getting exact solutions or even semi-analytical solutions that is why some numerical techniques have been developed, however analytical and semi-analytical solutions are still very important as they provide a stander for checking the accuracy of approximate solutions. Analytical solutions can also be used as a test to verify numerical schemes developed for the study of more complex problems. To find the analytical solutions of nonlinear governing equation, there are various methods available in the existing literature. Few of them are as follows

1. Homotopy analysis method
2. Bvph2.0 package

1.7.1 Homotopy analysis method

Most physical problems are inherited nonlinear in nature and cannot be solved by several traditional methods such as perturbation techniques [78] which are mostly based on small parameters either in governing equations or in boundary conditions, called perturbation quantities. The small parameter plays a very important role because it determines not only the accuracy of the perturbation approximations but also the validity of the perturbation method itself. In general, it is not guaranteed that a perturbation result is valid in the whole region for all physical parameters. Therefore, it is necessary to develop some new methods which are independent of small parameters because in physical situation there are many nonlinear problems which do not contain any small parameter, especially those having nonlinearity. To overcome the restrictions of perturbation techniques, some powerful mathematical methods have been recently introduced to eliminate the small parameter, such as artificial parameter method introduced by He [79], Tanh method [80], Jacobi elliptic function method [81] and Adomian decomposition method [82], etc. In principle, all of these methods are based on a so-called artificial parameter in which approximate solutions are expanded into a series of such kind of artificial parameter. This artificial parameter is often used in such a way that one can easily get approximation solutions efficiently for a given nonlinear equation. All these traditional methods cannot provide any guarantee for the convergence of approximation series. In 1992, Liao [83] is thought to be the first who calculated an analytical solution for nonlinear equations $N\left[f(\mathbf{r})\right]=0$ with help of zeroth-order deformation equation).

$$(1-\xi)\pounds\left[I(\mathbf{r};\xi)-f_0(\mathbf{r})\right]=qN\left[I(\mathbf{r};\xi)\right], \tag{1.60}$$

in which, N is nonlinear differential operator and $f(\mathbf{r})$ is the unknown function of the independent variable(s) $\mathbf{r}=\{r_1,r_2,r_3,...,r_n\}$, $\pounds$ is an auxiliary linear operator, $f_0(\mathbf{r})$ an initial approximation of $f(\mathbf{r})$, $\xi\in[0,\ 1]$ is the embedding parameter. The Taylor series of $I(\mathbf{r};\xi)$ w.r.t embedding parameter ξ can be written as

$$I(\mathbf{r};\xi)=f_o(\mathbf{r})+\sum_{l=1}^{\infty}f_l(\mathbf{r})\xi^l, \tag{1.61}$$

where

$$f_l(\mathbf{r})=\frac{1}{l!}\frac{\partial^l I(\mathbf{r};\xi)}{\partial\xi^l}\bigg|_{\xi=0}. \tag{1.62}$$

In above approach, a liability appears that Taylor series could be diverged at $\xi=1$, Liao [84] came with an idea to add nonzero auxiliary parameter $\hbar$, which sort out this disadvantage in method. He named this parameter as "Convergence-control" parameter

$$(1-\xi)\pounds\left[I(\mathbf{r};\xi)-f_0(\mathbf{r})\right]=\xi\hbar N\left[I(\mathbf{r};\xi)\right]. \tag{1.63}$$

Note that the solution $I(\mathbf{r};\xi)$ of the above equation is not only dependent upon the embedding parameter ξ but also the convergence-control parameter $\hbar$. So, the term $f_l(\mathbf{r})$ given by equation (1.62) is also dependent upon $\hbar$ and therefore the convergence region of the Taylor series equation (1.61) is influenced by $\hbar$. Thus, the auxiliary parameter $\hbar$ provides us a convenient way to ensure the convergence of the Taylor series equation (1.61) at $\xi=1$. For $\xi=0$ and $\xi=1$, we have

$$I(\mathbf{r};0) = f_o(\mathbf{r}),\ I(\mathbf{r};1) = f(\mathbf{r}), \tag{1.64}$$

$f(\mathbf{r})$ is a solution of given differential equation. Thus we can write it as

$$f(\mathbf{r}) = f_o(\mathbf{r}) + \sum_{l=1}^{\infty} f_l(\mathbf{r}). \tag{1.65}$$

1.7.2 Bvph2.0 package

In 2003, Liao [85] developed a homotopy analysis method based package "Bhvh2" that can tackle many systems of ordinary differential equations (ODEs). It can solve various sort of systems of ODEs, including a system of coupled ODEs infinite interval, a system of coupled ODEs in semi-infinite interval, a system of coupled ODEs with algebraic property at infinity, a system of ODEs with an unknown parameter to be determined and a system of ODEs in different intervals. For simplicity, the BVPh2.0 package will properly work, if best initial guess of governing equations which correspond to boundary conditions are satisfied with the help of linear operators. To run the package, need to define all the inputs of problem properly, except the convergence-control parameters. Usually, the optimal values of the convergence-control parameters are obtained by minimizing the squared residual error. To the accuracies of this package, compare the results of some problem of this thesis with results obtained by another analytical and numerical method and find good accuracy.

Chapter 2

2 Convective radiative plane Poiseuille flow of nanofluid through porous medium with slip: An application of Stefan blowing

Slip effects of 2^{nd} order slip on nanofluid through a space bounded by opposite two planes is studied in this chapter. Poiseuille nanofluid flow, further experiences the impact of Stefan blowing. The starring role of heat transfer, magnetic field and porosity are altogether taken into account. The mathematical modeling is performed via Buongiorno's model. The effectual reliability of analytical solutions derived by homotopy analysis method is verified through $\hbar$–curves as well as by means of residual errors norms in each case. Impact of physical factors is inspected by graphs along numerical tables. The slowing down effects of Stefan blowing are significantly seen for velocity as well as temperature profiles whereas opposite characteristic for the nanoparticle concentrations is noticed. Finally, the effects of high order slip on various field parameters are highlighted.

2.1 Problem formulation

2.1.1 Flow analysis

Consider steady two dimensional incompressible laminar flow of nanofluid passed through porous channel with the impact of second-order flow slip with Stefan blowing. The geometry of the problem consists two parallel straight walls as displayed in figure 2.1. The origin of coordinates is considered at midway of the channel such that the position of the channel at left and right walls are taken $\bar{y} = -a$ and $\bar{y} = a$, respectively.

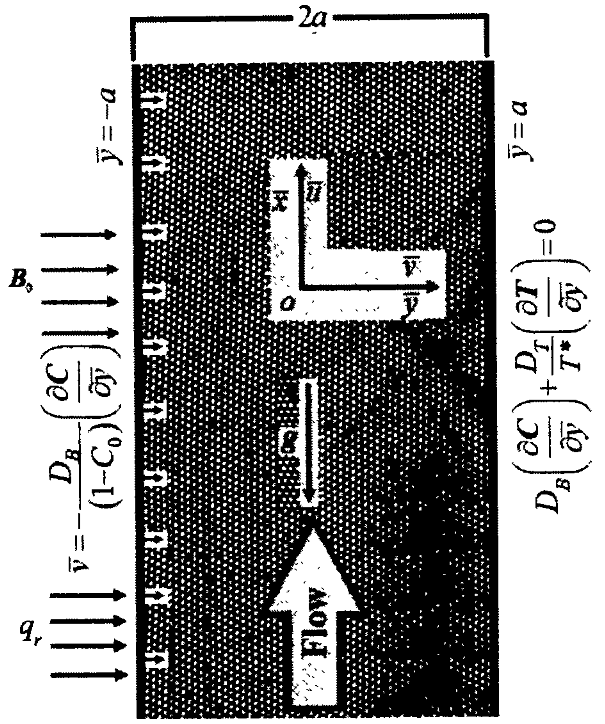

Figure 2.1: Configuration of the problem.

2.1.2 Governing equations (Buongiorno's model)

There are two famous homogenous nanofluid models, namely, Buongiorno and Tiwari and Das models. In this chapter, with existence of temperature gradient, the thermophoresis force produces a concentration gradient of nanoparticles in base fluid. In view of Buongiorno, thermophoresis and Brownian diffusion were found to be important for nanoparticle transport mechanism. Therefore, in view of equations (1.18), (1.19), (1.37) and (1.38) given in the previous chapter, for a steady state, incompressible nanofluid with influence of Lorentz magnetic force, buoyancy, radiative heat flux, viscous and Ohmic dissipations transporting through a porous medium is mathematically modeled with the application of Boussinesq's approximation as

$$\rho_f\left(\bar{v}\frac{\partial \bar{u}}{\partial \bar{y}}\right) = -\frac{\partial \bar{p}}{\partial \bar{x}} + \mu\left(\frac{\partial^2 \bar{u}}{\partial \bar{y}^2}\right) - \sigma B_0^2 \bar{u} - \frac{\mu}{K_1}\bar{u} + \left[(1-C^*)\rho_f \beta g(T-T^*) - (\rho_p - \rho_f) g(C-C^*)\right], \tag{2.1}$$

$$(\rho c_p)_f\left(\bar{v}\frac{\partial T}{\partial \bar{y}}\right)=k_f\left(\frac{\partial^2 T}{\partial \bar{y}^2}\right)+(\rho c_p)_p\left[D_B\left(\frac{\partial C}{\partial \bar{y}}\frac{\partial T}{\partial \bar{y}}\right)+\frac{D_T}{T^*}\left(\frac{\partial T}{\partial \bar{y}}\right)^2\right]-\frac{\partial q_r}{\partial \bar{y}}+ \mu_f\left(\frac{\partial \bar{u}}{\partial \bar{y}}\right)^2+\sigma_f B_0^2\bar{u}^2 \tag{2.2}$$

and

$$\bar{v}\frac{\partial C}{\partial \bar{y}}=D_B\left(\frac{\partial^2 C}{\partial \bar{y}^2}\right)+\frac{D_T}{T^*}\left(\frac{\partial^2 T}{\partial \bar{y}^2}\right). \tag{2.3}$$

Concerned boundary conditions [86-88] are

$$\left.\begin{aligned}&\bar{u}=-\bar{u}_{\text{Slip}},\ \bar{v}=-\frac{D_B}{(1-C_1)}\left(\frac{\partial C}{\partial \bar{y}}\right),\ T=T_1,\ C=C_1\ \text{at}\ \bar{y}=-a\\&\bar{u}=\bar{u}_{\text{Slip}},\quad T=T_2,\quad D_B\left(\frac{\partial C}{\partial \bar{y}}\right)+\frac{D_T}{T^*}\left(\frac{\partial T}{\partial \bar{y}}\right)=0\ \text{at}\ \bar{y}=a\end{aligned}\right\}, \tag{2.4}$$

and

$$\left.\begin{aligned}&\bar{u}_{\text{Slip}}=\frac{2}{3}\left(\frac{3-\varpi e^2}{\varpi}-\frac{3}{2}\frac{1-e^2}{\tilde{k}_n}\right)\delta_1\frac{\partial \bar{u}}{\partial \bar{y}}-\frac{1}{4}\left(e^4+\frac{2(1-e^2)}{\tilde{k}_n}\right)\delta_1^2\frac{\partial^2 \bar{u}}{\partial \bar{y}^2}\\&e=\min\left(\frac{1}{\tilde{k}_n},1\right)\end{aligned}\right\}, \tag{2.5}$$

here ϖ and e are defined as $0\le\varpi\le1$ and $0\le e\le1$ respectively. Gas flow in the channels for Knudsen number $\tilde{k}_n$ can be categorized into four cases: (i) for continuum flow, Knudsen number ≤ 0.001, (ii) for slip flow, this implies that $0.001 \le$ Knudsen number ≤ 0.1, (iii) for transition flow, Knudsen number lies between 0.1 to 10 and (iv) for free molecular flow, Knudsen number ≥ 10. Equation (2.5) is reported by many researchers [89-91] due to its vital and remarkable contribution.

Let us acquaint the following nondimensional quantities

$$\left.\begin{aligned} p=\frac{a^2\bar{p}}{\mu U_m},\ x=\frac{\bar{x}}{a},\ \theta=\frac{T-T^*}{T_1-T^*}, y=\frac{\bar{y}}{a},\ \phi=\frac{C-C^*}{C^*}, u=\frac{\bar{u}}{U_m}, \\ m^*=\frac{T_2-T^*}{T_1-T^*}, v=\frac{\bar{v}}{U_m},\ n^*=\frac{C_1-C^*}{C^*}=\frac{\Delta C}{C^*} \end{aligned}\right\}. \tag{2.6}$$

Subsequently when fluid is flowing due to fixed (constant) pressure gradient then reference velocity U_m will occur between two walls and as a matter of fact, it will be maximum velocity and defined as ($U_m=-\frac{a^2}{2\mu_f}\frac{\partial p}{\partial x}$). In this phenomenon consider the low Reynolds, therefore the induced magnetic field is ignored.

However, q_r [92] denoting the flux is denoted as

$$q_r=-\frac{4\sigma^*}{3k^*}\frac{\partial T^4}{\partial \bar{y}}. \tag{2.7}$$

Expending T^4 for reference temperature T^* by the Taylor series can be expressed [93, 94] as

$$T^4=T^{*4}+4T^{*3}\left(T-T^*\right)+6T^{*2}\left(T-T^*\right)^2+\dots . \tag{2.8}$$

In this case $\left(T-T^*\right)$ is considered to be very small, so the square and higher-order terms of $\left(T-T^*\right)$ can be neglected. Thus T^4 converted to

$$T^4\cong T^{*3}\left(4T-3T^*\right). \tag{2.9}$$

Therefore, the equation (2.7) becomes

$$q_r=-\frac{16T^{*3}\sigma^*}{3k^*}\frac{\partial T}{\partial \bar{y}}. \tag{2.10}$$

After incorporating the appropriate transform defined in equation (2.6), convert the equations (2.1) to (2.3) in dimensionless expressions which take the following form

$$\frac{\partial^2 u}{\partial y^2}+\mathrm{Re}\frac{S}{Sc}\frac{\partial u}{\partial y}\frac{\partial \phi}{\partial y}-\left(M^2+\frac{1}{Da}\right)u+\frac{Ra}{\mathrm{RePr}}\left(\theta-Nr\phi\right)-P=0, \tag{2.11}$$

$$\left(Rd+1\right)\frac{\partial^2\theta}{\partial y^2}+\left(Nb+\mathrm{RePr}\frac{S}{Sc}\right)\frac{\partial\theta}{\partial y}\frac{\partial\phi}{\partial y}+Ec\mathrm{Pr}\left(\frac{\partial u}{\partial y}\right)^2+Nt\left(\frac{\partial\theta}{\partial y}\right)^2+M^2\mathrm{Pr}Ecu^2=0, \quad (2.12)$$

$$\frac{\partial^2\phi}{\partial y^2}+\frac{Nt}{Nb}\left(\frac{\partial^2\theta}{\partial y^2}\right)+\mathrm{Re}\,S\left(\frac{\partial\phi}{\partial y}\right)^2=0. \quad (2.13)$$

Dimensionless second-order slip is

$$u_{\mathrm{Slip}}=A\frac{\partial u}{\partial y}+B\frac{\partial^2 u}{\partial y^2}, \quad (2.14)$$

where

$$A=\frac{2}{3}\left(\frac{3-\varpi e^2}{\varpi}-\frac{3}{2}\frac{1-e^2}{k_n}\right)\frac{\delta_1}{a},\quad B=-\frac{1}{4}\left(e^4+\frac{2\left(1-e^2\right)}{k_n}\right)\frac{\delta_1^2}{a^2}. \quad (2.15)$$

The corresponding dimensionless boundary conditions are

$$\left.\begin{aligned} &u_{\mathrm{Slip}}=-A\frac{\partial u}{\partial y}-B\frac{\partial^2 u}{\partial y^2}, v=-\frac{S}{Sc}\left(\frac{\partial\phi}{\partial y}\right), \theta=1, \phi=n^* \ \text{at}\ y=-1\\ &u_{\mathrm{Slip}}=A\frac{\partial u}{\partial y}+B\frac{\partial^2 u}{\partial y^2}, \theta=m^*, Nb\left(\frac{\partial\phi}{\partial y}\right)+Nt\left(\frac{\partial\theta}{\partial y}\right)=0\ \text{at}\ y=1\end{aligned}\right\}, \quad (2.16)$$

here

$$\left.\begin{aligned} &Ra=\frac{(1-C^*)(T_1-T^*)\beta g a^3}{\nu\alpha}, Nr=\frac{\left(\rho_p-\rho_f\right)C^*}{\rho_f\beta(T_1-T^*)(1-C^*)}, Nb=\frac{\tau D_B C^*}{\alpha_f},\\ &Nt=\frac{\tau D_T\left(T_1-T^*\right)}{T^*\alpha_f}, Le=\frac{\alpha_f}{D_B}, Ec=\frac{U_m^{\ 2}}{C_p\left(T_1-T^*\right)}, \mathrm{Re}=\frac{aU_m}{\nu_f}, \mathrm{Pr}=\frac{\nu_f}{\alpha_f},\\ &Sc=\mathrm{Pr}\,Le=\frac{\mu_f}{\rho D_B}, M^2=\frac{\sigma_f B_0^{\ 2}d^2}{\mu_f}, S=\frac{\Delta C}{\left(1-C_1\right)}, Da=\frac{K_1}{a^2}, Rd=\frac{16\sigma^* T^{*3}}{3k^* k_f}\end{aligned}\right\}. \quad (2.17)$$

Expression of coefficient of skin friction defined in equation (1.54), Nusselt number defined in equation (1.56) and Sherwood number defined in equation (1.58) are transformed in view of equation (2.6) as

$$\left.\begin{aligned} \operatorname{Re} C_f &= 2u'(y)\Big|_{y=-1,1} \\ Nu &= -\theta'(y)\Big|_{y=-1,1} \\ Sh &= -\phi'(y)\Big|_{y=-1,1} \end{aligned}\right\}. \tag{2.18}$$

2.2 Solution of the problem

Equations (2.11) to (2.13) are tackled by HAM procedure to seek analytical solution.

Zeroth-order solution

Consider, the following initial approximations $(u_0,\ \theta_0,\ \phi_0)$ which satisfy the linear operators $(\pounds_u,\ \pounds_\theta,\ \pounds_\phi)$ and associated boundaries

$$\left.\begin{aligned} u_0(y) &= \frac{-1+3A-2A^2+2By+y^2-Ay^2}{2(A-1)} \\ \theta_0(y) &= \frac{(1-y)+(1+y)m^*}{2} \\ \phi_0(y) &= \frac{2n^*Nb+(1+y)(1-m^*)Nt}{2Nb} \end{aligned}\right\} \tag{2.19}$$

and

$$\pounds_u = \frac{d}{dy}\left(\frac{du}{dy}\right),\quad \pounds_\theta = \frac{d}{dy}\left(\frac{d\theta}{dy}\right),\quad \pounds_\phi = \frac{d}{dy}\left(\frac{d\phi}{dy}\right). \tag{2.20}$$

The convergence control parameters $\hbar_u$, $\hbar_\theta$, $\hbar_\phi$ and nonlinear operators N_u, N_θ, N_ϕ of velocity, temperature, nanoparticle volume fraction with embedding parameter $\xi \in [0,\ 1]$ yields the following zeroth-order deformations respectively are

$$\left.\begin{aligned} (1-\xi)\pounds_u\left[u(y,\xi)-u_0(y)\right] &= \xi\hbar_u N_u\left[u(y,\xi),\theta(y,\xi),\phi(y,\xi)\right] \\ (1-\xi)\pounds_\theta\left[\theta(y,\xi)-\theta_0(y)\right] &= \xi\hbar_\theta N_\theta\left[u(y,\xi),\theta(y,\xi),\phi(y,\xi)\right] \\ (1-\xi)\pounds_\phi\left[\phi(y,\xi)-\phi_0(y)\right] &= \xi\hbar_\phi N_\phi\left[u(y,\xi),\theta(y,\xi),\phi(y,\xi)\right] \end{aligned}\right\}, \tag{2.21}$$

with associated boundary conditions

$$\left.\begin{array}{l} u(y,\xi)_{\text{Slip}} = -A\dfrac{\partial u(y,\xi)}{\partial y} - B\dfrac{\partial^2 u(y,\xi)}{\partial y^2}, v = -\dfrac{S}{Sc}\left(\dfrac{\partial \phi(y,\xi)}{\partial y}\right), \theta(y,\xi) = 1, \phi(y,\xi) = n^* \text{ at } y = -1 \\ u(y,\xi)_{\text{Slip}} = A\dfrac{\partial u(y,\xi)}{\partial y} + B\dfrac{\partial^2 u(y,\xi)}{\partial y^2}, \theta(y,\xi) = m^*, Nb\left(\dfrac{\partial \phi(y,\xi)}{\partial y}\right) + Nt\left(\dfrac{\partial \theta(y,\xi)}{\partial y}\right) = 0 \text{ at } y = 1 \end{array}\right\}, \quad (2.22)$$

here

$$\left.\begin{array}{l} N_u = -P + \dfrac{\partial^2 u(y,\xi)}{\partial y^2} + \text{Re}\dfrac{S}{S_c}\dfrac{\partial u(y,\xi)}{\partial y}\dfrac{\partial \phi(y,\xi)}{\partial y} - \left(M^2 + \dfrac{1}{Da}\right)u(y,\xi) + \dfrac{Ra}{\text{Re}\Pr}\left(\theta(y,\xi) - N_r\phi(y,\xi)\right) \\ N_\theta = (1+Rd)\dfrac{\partial^2 \theta(y,\xi)}{\partial y^2} + \left(\text{Re}\Pr\dfrac{S}{Sc} + Nb\right)\dfrac{\partial \phi(y,\xi)}{\partial y}\dfrac{\partial \theta(y,\xi)}{\partial y} + Nt\left(\dfrac{\partial \theta(y,\xi)}{\partial y}\right)^2 + Ec\Pr\left(\dfrac{\partial u(y,\xi)}{\partial y}\right)^2 + \\ \quad M^2 \Pr Ec\left(u(y,\xi)\right)^2 \\ N_\phi = \dfrac{\partial^2 \phi(y,\xi)}{\partial y^2} + \text{Re}\,S\left(\dfrac{\partial \phi(y,\xi)}{\partial y}\right)^2 + \dfrac{Nt}{Nb}\dfrac{\partial^2 \theta(y,\xi)}{\partial y^2} \end{array}\right\}. \quad (2.23)$$

$$\left.\begin{array}{llll} \text{For} & u(y,\xi) & \theta(y,\xi) & \phi(y,\xi) \\ \xi = 0 & u_0(y) & \theta_0(y) & \phi_0(y) \\ \xi = 1 & u(y) & \theta(y) & \phi(y) \end{array}\right\}. \quad (2.24)$$

When embedding parameter ζ diverges from 0 to 1, then $u(y,\ \zeta)$, $\theta(y,\ \zeta)$ and $\phi(y,\ \zeta)$ transform from initial $u_0(y)$, $\theta_0(y)$ and $\phi_0(y)$ to final solution $u(y)$, $\theta(y)$ and $\phi(y)$.

Let expand $u(y,\ \zeta)$, $\theta(y,\ \zeta)$ and $\phi(y,\ \zeta)$ in Taylor's series as

$$\left.\begin{array}{l} u(y,\zeta) = u_0(y) + \sum_{l=1}^{\infty} u_l(y)\zeta^l \\ \theta(y,\zeta) = \theta_0(y) + \sum_{l=1}^{\infty} \theta_l(y)\zeta^l \\ \phi(y,\zeta) = \phi_0(y) + \sum_{l=1}^{\infty} \phi_l(y)\zeta^l \end{array}\right\}, \quad (2.25)$$

where

$$u_l(y)=\frac{1}{l!}\frac{\partial^l u(y,\zeta)}{\partial\zeta^l}\bigg|_{\zeta=0},\ \theta_l(y)=\frac{1}{l!}\frac{\partial^l \theta(y,\zeta)}{\partial\zeta^l}\bigg|_{\zeta=0},\phi_l(y)=\frac{1}{l!}\frac{\partial^l \phi(y,\zeta)}{\partial\zeta^l}\bigg|_{\zeta=0}. \tag{2.26}$$

***l* th-order solution**

The l th-order deformation expression for $u_l(y)$, $\theta_l(y)$ and $\phi_l(y)$ as follow

$$\left.\begin{aligned}&\pounds_u\left[u_l(y)-\chi_l u_{l-1}(y)\right]=\hbar_u R_l^u(y)\\&\pounds_\theta\left[\theta_l(y)-\chi_l \theta_{l-1}(y)\right]=\hbar_\theta R_l^\theta(y)\\&\pounds_\phi\left[\phi_l(y)-\chi_l \phi_{l-1}(y)\right]=\hbar_\phi R_l^\phi(y)\end{aligned}\right\}. \tag{2.27}$$

$$\left.\begin{aligned}&u_l(y,\xi)_{\text{slip}}=-A\frac{\partial u_l(y,\xi)}{\partial y}-B\frac{\partial^2 u_l(y,\xi)}{\partial y^2},\theta_l(y,\xi)=1,v=-\frac{S}{Sc}\left(\frac{\partial\phi_l(y,\xi)}{\partial y}\right),\phi_l(y,\xi)=n^*\ \text{at}\ y=-1\\&u_l(y,\xi)_{\text{slip}}=A\frac{\partial u_l(y,\xi)}{\partial y}+B\frac{\partial^2 u_l(y,\xi)}{\partial y^2},\theta_l(y,\xi)=m^*,Nb\left(\frac{\partial\phi_l(y,\xi)}{\partial y}\right)+Nt\left(\frac{\partial\theta_l(y,\xi)}{\partial y}\right)=0\ \text{at}\ y=1\end{aligned}\right\}, \tag{2.28}$$

where

$$\chi_l=\begin{cases}0, & l\le 1,\\ 1, & l>1.\end{cases} \tag{2.29}$$

$$\left.\begin{aligned}&R_l^u(y)=-P+u_l''+\text{Re}\frac{S}{S_c}\sum_{k=0}^{l}u_k'\phi_{l-k}'-\left(M^2+\frac{1}{Da}\right)u_l+\frac{Ra}{\text{Re}\Pr}(\theta_l-N_r\phi_l)\\&R_l^\theta(y)=(1+Rd)\theta_l''+\left(\text{Re}\Pr\frac{S}{Sc}+Nb\right)\sum_{k=0}^{l}\phi_k'\theta_{l-k}'+Nt\sum_{k=0}^{l}\theta_k'\theta_{l-k}'+Ec\Pr\sum_{k=0}^{l}u_k'u_{l-k}'+M^2\Pr Ec\sum_{k=0}^{l}u_k u_{l-k}\\&R_l^\phi(y)=\phi_l''+\text{Re}\,S\sum_{k=0}^{l}\phi_k\phi_{l-k}'+\frac{Nt}{Nb}\theta_l''\end{aligned}\right\}. \tag{2.30}$$

The solution can be described as of l th-order

$$\left.\begin{aligned} u(y) &= u_0(y) + \sum_{k=1}^{l} u_k(y) \\ \theta(y) &= \theta_0(y) + \sum_{k=1}^{l} \theta_k(y) \\ \phi(y) &= \phi_0(y) + \sum_{k=1}^{l} \phi_k(y) \end{aligned}\right\}. \tag{2.31}$$

The analytical expressions for velocity, thermal and particles flux considering HAM-based Mathematica package BVPh2.0 are obtained as below

$$
u(y)=\frac{1}{(1-A)^4}\left(\begin{array}{l}
\frac{1}{2}-By-\frac{1}{2}y^2+\hbar_u\left(\begin{array}{l}\frac{565}{1632}+B^2\left(\frac{9}{4}-\frac{3}{40}y\right)+\frac{551}{4080}y-\frac{359}{816}y^2-\frac{551}{4080}y^3+\frac{3}{32}y^4+\\ B\left(-\frac{1051}{1360}-\frac{53}{408}y-\frac{3}{80}y^2+\frac{3}{8}y^3\right)\end{array}\right)+\\
A\left(\begin{array}{l}-3+3By+2y^2+\\ \hbar_u\left(\begin{array}{l}-\frac{205}{68}+B^2\left(-\frac{27}{4}+\frac{3}{20}y\right)-\frac{551}{680}y+\frac{1177}{408}y^2+\frac{551}{1020}y^3-\\ \frac{3}{8}y^4+B\left(\frac{4153}{1360}+\frac{461}{136}y+\frac{9}{80}y^2-\frac{9}{8}y^3\right)\end{array}\right)\end{array}\right)+\\
A^2\left(\begin{array}{l}-7-3By-3y^2+\\ \hbar_u\left(\begin{array}{l}-\frac{8851}{816}+B^2\left(\frac{27}{4}-\frac{3}{40}y\right)+\frac{551}{340}y-\frac{971}{136}y^2-\frac{551}{680}y^3+\\ \frac{9}{16}y^4+B\left(-\frac{6153}{1360}-\frac{1175}{136}y-\frac{9}{80}y^2+\frac{9}{8}y^3\right)\end{array}\right)\end{array}\right)+\\
A^3\left(\begin{array}{l}-8+By+2y^2+\\ \hbar_u\left(\begin{array}{l}-\frac{8227}{408}+\frac{9}{4}B^2-\frac{551}{408}y+\frac{434}{51}y^2+\frac{551}{1020}y^3-\frac{3}{8}y^4+\\ B\left(\frac{4051}{1360}+\frac{3113}{408}y+\frac{3}{80}y^2-\frac{3}{8}y^3\right)\end{array}\right)\end{array}\right)+\\
A^4\left(\frac{9}{2}-\frac{1}{2}y^2+\hbar_u\left(\begin{array}{l}\frac{11079}{544}-\frac{25}{34}B+\frac{551}{1360}y-\frac{9}{4}By-\frac{4031}{816}y^2-\\ \frac{551}{4080}y^3+\frac{3}{32}y^4\end{array}\right)\right)+\\
A^5\left(-1+\hbar_u\left(\frac{-4337}{408}+\frac{9}{8}y^2\right)\right)+\frac{9}{4}A^6\hbar_u
\end{array}\right), \qquad (2.32)
$$

$$\theta(y)=\frac{1}{(-1+A)^{8}}\left(\begin{array}{l}
\frac{1}{2}-\frac{1}{2}y+\hbar_{\theta}\left(\begin{array}{l}\frac{221}{4000}-\frac{17}{160}y^{2}+\frac{119}{2400}y^{4}+\frac{17}{12000}y^{6}+B^{2}\left(-\frac{17}{48}+\frac{17}{50}y^{2}+\frac{17}{1200}y^{4}\right)\\ +B\left(-\frac{1241}{6000}y+\frac{119}{600}y^{3}+\frac{17}{2000}y^{5}\right)\end{array}\right)+\\
A\left(-4+4y+\hbar_{\theta}\left(\begin{array}{l}-\frac{2227}{6000}+\frac{153}{200}y^{2}-\frac{153}{400}y^{4}-\frac{17}{1500}y^{6}+B^{2}\left(\frac{17}{8}-\frac{51}{25}y^{2}-\frac{17}{200}y^{4}\right)\\ +B\left(\frac{8347}{6000}y-\frac{799}{600}y^{3}-\frac{119}{2000}y^{5}\right)\end{array}\right)\right)+\\
A^{2}\left(14-14y+\hbar_{\theta}\left(\begin{array}{l}\frac{1343}{1500}-\frac{221}{100}y^{2}+\frac{51}{40}y^{4}+\frac{119}{3000}y^{6}+B^{2}\left(-\frac{85}{16}+\frac{51}{10}y^{2}+\frac{17}{80}y^{4}\right)\\ +B\left(-\frac{23681}{6000}y+\frac{2261}{600}y^{3}+\frac{357}{2000}y^{5}\right)\end{array}\right)\right)+\\
A^{3}\left(-28+28y+\hbar_{\theta}\left(\begin{array}{l}-\frac{323}{750}+\frac{289}{100}y^{2}-\frac{119}{50}y^{4}-\frac{119}{1500}y^{6}+B^{2}\left(\frac{85}{12}-\frac{34}{5}y^{2}-\frac{17}{60}y^{4}\right)\\ +B\left(\frac{7259}{1200}y-\frac{3451}{600}y^{3}-\frac{119}{400}y^{5}\right)\end{array}\right)\right)+\\
A^{4}\left(35-35y+\hbar_{\theta}\left(\begin{array}{l}\frac{119}{48}-\frac{119}{400}y^{2}+\frac{1071}{400}y^{4}+\frac{119}{1200}y^{6}+B^{2}\left(-\frac{85}{16}+\frac{51}{10}y^{2}+\frac{17}{80}y^{4}\right)\\ +B\left(-\frac{6307}{1200}y+\frac{119}{24}y^{3}+\frac{119}{400}y^{5}\right)\end{array}\right)\right)+\\
A^{5}\left(-28+28y+\hbar_{\theta}\left(\begin{array}{l}\frac{19873}{3000}-\frac{119}{25}y^{2}-\frac{357}{200}y^{4}-\frac{119}{1500}y^{6}+B^{2}\left(\frac{17}{8}-\frac{51}{25}y^{2}-\frac{17}{200}y^{4}\right)\\ +B\left(\frac{14161}{6000}y-\frac{1309}{600}y^{3}-\frac{357}{2000}y^{5}\right)\end{array}\right)\right)+\\
A^{6}\left(14-14y+\hbar_{\theta}\left(\begin{array}{l}-\frac{25109}{3000}+\frac{1547}{200}y^{2}+\frac{119}{200}y^{4}+\frac{119}{3000}y^{6}+B^{2}\left(-\frac{17}{48}+\frac{17}{50}y^{2}+\frac{17}{1200}y^{4}\right)\\ +B\left(-\frac{1547}{6000}y+\frac{119}{600}y^{3}+\frac{119}{2000}y^{5}\right)\end{array}\right)\right)+\\
A^{7}\left(-4+4y+\hbar_{\theta}\left(\frac{2363}{375}-\frac{1139}{6000}By-\frac{626}{100}y^{2}+\frac{119}{600}By^{3}-\frac{17}{2000}By^{5}-\frac{17}{1500}y^{6}\right)\right)+\\
A^{8}\left(-\frac{1}{2}-\frac{1}{2}y+\hbar_{\theta}\left(-\frac{34697}{12000}+\frac{17}{300}By+\frac{2363}{800}y^{2}-\frac{17}{300}By^{3}-\frac{51}{800}y^{4}+\frac{17}{12000}y^{6}\right)\right)+\\
A^{9}\hbar_{\theta}\left(\frac{901}{1200}-\frac{153}{200}y^{2}+\frac{17}{1200}y^{4}\right)+A^{10}\hbar_{\theta}\left(-\frac{17}{200}+\frac{17}{200}y^{2}\right)
\end{array}\right), \quad (2.33)$$

$$
\phi(y)=\frac{1}{(-1+A)^{6}}\left(\begin{aligned}
&\frac{1}{2}-\frac{9}{160}\hbar_{\phi}+\hbar_{\theta}\left(\frac{17}{3000}+B\left(-\frac{323}{750}-\frac{323}{750}y\right)+B^{2}\left(-\frac{221}{300}-\frac{221}{300}y\right)+\frac{17}{3000}y\right)+\frac{1}{2}y-\frac{3}{80}\hbar_{\phi}y+\frac{3}{160}\hbar_{\phi}y^{2}+\\
&A\left(-3-3y+\hbar_{\phi}\left(\frac{27}{80}+\frac{9}{40}y-\frac{9}{80}y^{2}\right)+\hbar_{\theta}\left(\frac{119}{1500}+\frac{119}{1500}y+B\left(\frac{51}{25}+\frac{51}{25}y\right)+B^{2}\left(\frac{221}{75}+\frac{221}{75}y\right)\right)\right)+\\
&A^{2}\left(\frac{15}{2}+\hbar_{\theta}\left(-\frac{153}{200}+B\left(-\frac{187}{50}-\frac{187}{50}y\right)+B^{2}\left(-\frac{221}{50}-\frac{221}{50}y\right)-\frac{153}{200}y\right)+\frac{15}{2}y+\hbar_{\phi}\left(-\frac{27}{32}-\frac{9}{16}y+\frac{9}{32}y^{2}\right)\right)+\\
&A^{3}\left(-10-10y+\hbar_{\phi}\left(\frac{9}{8}+\frac{3}{4}y-\frac{3}{8}y^{2}\right)+\hbar_{\theta}\left(\frac{391}{150}+\frac{391}{150}y+B\left(\frac{238}{75}+\frac{238}{75}y\right)+B^{2}\left(\frac{221}{75}+\frac{221}{75}y\right)\right)\right)+\\
&A^{4}\left(\frac{15}{2}+\hbar_{\theta}\left(-\frac{2839}{600}+B\left(-\frac{51}{50}-\frac{51}{50}y\right)+B^{2}\left(-\frac{221}{300}-\frac{221}{300}y\right)-\frac{2839}{600}y\right)+\frac{15}{2}y+\hbar_{\phi}\left(-\frac{27}{32}-\frac{9}{16}y+\frac{9}{32}y^{2}\right)\right)+\\
&A^{5}\left(-3-3y+\hbar_{\theta}\left(\frac{2533}{500}+B\left(-\frac{17}{125}-\frac{17}{125}y\right)+\frac{2533}{500}y\right)+\hbar_{\phi}\left(\frac{27}{80}-\frac{9}{40}y-\frac{9}{80}y^{2}\right)\right)+\\
&A^{6}\left(\frac{1}{2}+\hbar_{\theta}\left(-\frac{9673}{3000}+B\left(\frac{17}{150}+\frac{17}{150}y\right)-\frac{9673}{30000}y\right)+\frac{1}{2}y+\hbar_{\phi}\left(-\frac{9}{160}-\frac{3}{80}y+\frac{3}{160}y^{2}\right)\right)+\\
&A^{7}\hbar_{\theta}\left(\frac{17}{15}+\frac{17}{15}y\right)+A^{8}\hbar_{\theta}\left(-\frac{17}{100}-\frac{17}{100}y\right)
\end{aligned}\right). \qquad (2.34)
$$

2.3 Discussion of results

2.3.1 Inspection of convergence

The solution obtained from equation (2.31) consists of $\hbar_u$, $\hbar_\theta$ and $\hbar_\phi$. Moreover, the convergence is accelerated by the auxiliary parameters $\hbar_u$, $\hbar_\theta$ and $\hbar_\phi$. The optimal values of these parameters are chosen with the help of $\hbar$–curves, which is showing in figures 2.2 at 20th–order approximations. The best range of $\hbar_u$, $\hbar_\theta$ and $\hbar_\phi$ are $-0.8 \le \hbar_u \le -0.2$, $-0.9 \le \hbar_\theta \le -0.1$ and $-0.9 \le \hbar_\phi \le -0.3$.

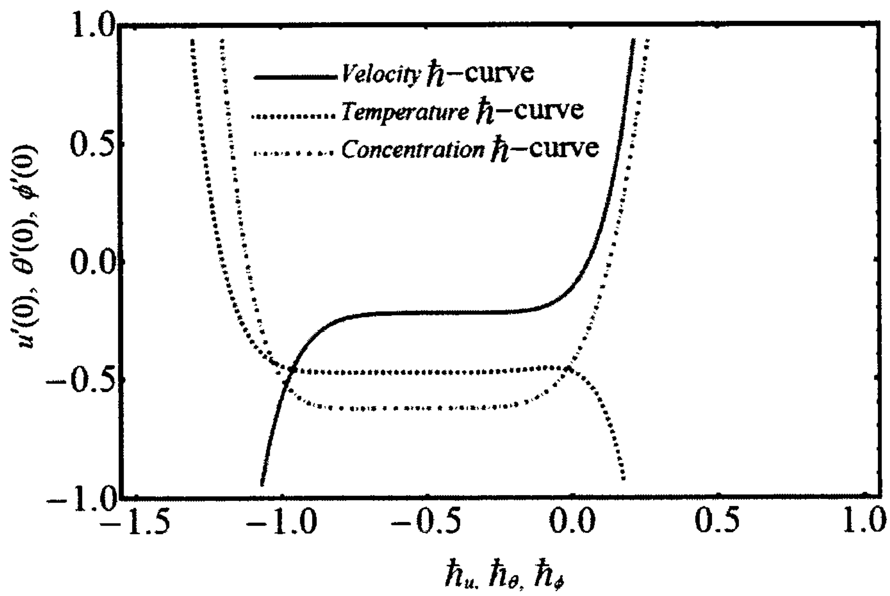

Figure 2.2: $\hbar$ –curves.

2.3.2 Residual error of norm 2

The optimized values of $\hbar_u$, $\hbar_\theta$ and $\hbar_\phi$ are very essential for solution. Therefore, the residual errors were computed up to 20th –order approximation over an embedding parameter $\xi \in [0,\ 1]$ of velocity E_u, temperature E_θ and nanoparticles concentration E_ϕ by the succeeding formulas

$$E_u = \sqrt{\frac{1}{21}\sum_{i=0}^{20}\left(u(i/20)\right)^2},\quad E_\theta = \sqrt{\frac{1}{21}\sum_{i=0}^{20}\left(\theta(i/20)\right)^2},\quad E_\phi = \sqrt{\frac{1}{21}\sum_{i=0}^{20}\left(\phi(i/20)\right)^2}. \qquad (2.35)$$

The above residual formulas give the minimum error for velocity at $\hbar_u = -0.6$, for temperature $\hbar_\theta = -0.4$ and for nanoparticle concentration $\hbar_\phi = -0.7$ which are shown clearly in figures 2.3, 2.4 and 2.5 respectively. Table 2.1 shows the error for the convergence series solution up to the 20th-order approximation.

Table 2.1: Residual error of analytic solutions when $m^* = n^* = 0$, $A = 0.1$, $B = -0.1$, $Sc = 1$, $Rd = 1$, $Nr = 0.5$, $Nt = 0.5$, $Nb = 0.5$, $Da = 0.5$, $S = 0.5$ and $M = 0.5$.

Order of approximation	Time	E_u	E_θ	E_ϕ
02	1.07793	3.2399×10^{-2}	5.2315×10^{-2}	7.2473×10^{-3}
06	3.4508	3.0496×10^{-2}	5.2259×10^{-2}	7.2272×10^{-3}
10	8.3315	2.9912×10^{-2}	5.1242×10^{-2}	7.0287×10^{-3}
14	15.3252	2.9899×10^{-2}	$5..0754\times10^{-2}$	6.9178×10^{-3}
20	30.8517	2.9879×10^{-2}	5.0739×10^{-2}	6.8912×10^{-3}

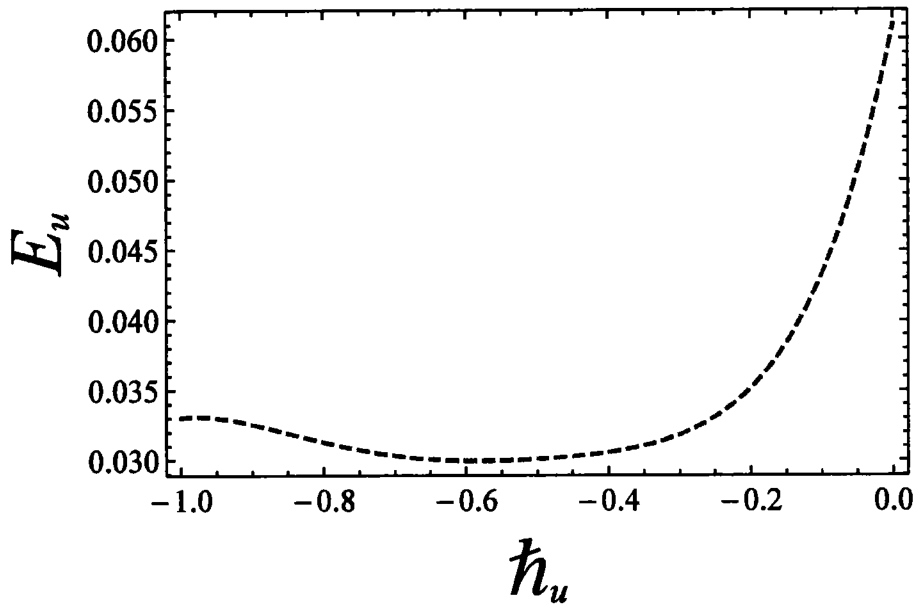

Figure 2.3: Residual error E_u −curve for velocity profile.

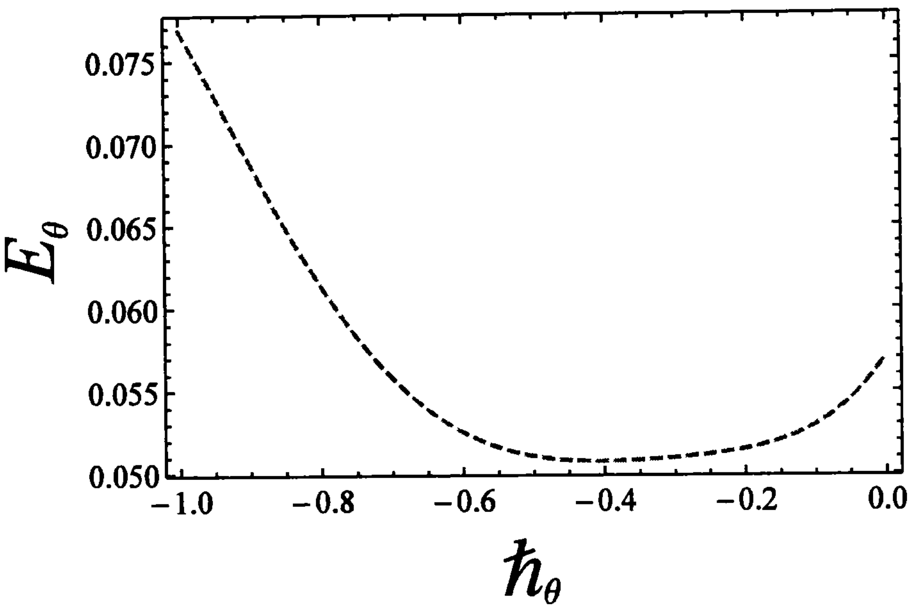

Figure 2.4: Residual error E_θ −curve for temperature profile.

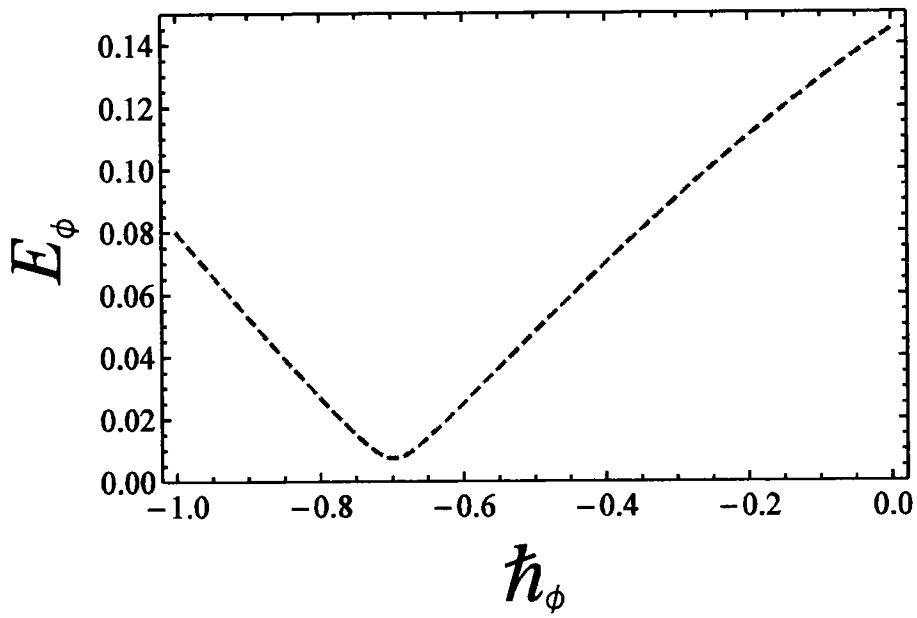

Figure 2.5: Residual error E_ϕ −curve for temperature profile.

2.3.3 Illustration of graphical results

To see the impact of key factors for numerous range of slip parameters the graphical representations are demonstrated from figures 2.6 to 2.14. The influences of zero, first, and second order velocity slip are shown throughout the figures. Figures 2.6(a), 2.6(b), and 2.6(c) demonstrate the combined impact of zero, first, and second-order velocity slips along with Stefan mass blowing/suction parameter S on velocity, temperature, and nanoparticle concentration distributions. In figure 2.6(a) it is found that in case of zero or no-slip $(A=0, B=0)$ velocity distribution for plentiful values of Stefan blowing/suction parameter $(S=-1, S=0 \text{ and } S=1)$ closer to the mid of channel decreases, while its boosts up in the neighborhood of walls. The velocity in case of strong blowing $(S=-1)$ is improved and it overshoots near the right wall for first-order slip $(A=0.2, B=0)$ and second-order slip$(A=0.2, B=-0.1)$. Also for the right wall case $(S=0 \text{ and } S=1)$ condition of overshoot still exists but it extinct at the left wall for blowing/suction cases$(S=-1, S=0 \text{ and } S=1)$. Figure 2.6(b) offerings the performance of temperature profile versus numerous values of Stefan blowing/suction parameter, i.e., $(S=-1, S=0 \text{ and } S=1)$. It is perceived that the temperature variations are very small in case of zero, first and second-order slips i.e., system is cooled so that the thickness of thermal boundary layer decreases with an enhancement in the first-order slip. Blowing is discussed to inspect the rise in temperature, while suction depicts the reverse trends to cools the system. Figure 2.6(c) reflects the nanoparticle concentration distribution for numerous values of S with zero, first and second-order flow slip. It is observed that the nanoparticle concentration function is slightly increased with increase of blowing/suction parameter in zero, first, and second-order flow slips cases. The velocity behavior via porosity parameter/Darcy number Da is exposed in figure 2.7 along with impacts of zero, first, and second-order velocity slips. It is found that in case of porosity parameter, velocity at the middle of channel falls down by increasing Da, while it accelerates in the neighborhood of walls. The flow is accelerated with a corresponding overshoot near the right wall in first-order slip $(A=0.2, B=0)$ and for the case of a second-order slip $(A=0.2, B=-0.1)$.

The effects of magnetic parameter M are depicted in figures 2.8(a) for velocity, 2.8(b) for temperature, and 2.8(c) for nanoparticle distribution along with the consideration of zero, first, and second-order velocity slips. Retardation occurs on velocity profile as shown in figure 2.8(a), because of the fact that MHD is acted normally to flow direction in the occurrence and absence of slip parameters. On the other hand, the velocity is accelerated with a very low exceed near the right wall in first and second-order velocity slips. Figure 2.8(b) depict the M on temperature profile is illustrated with zero, first, and second-order velocity slips. Here transverse magnetic field also effects the thermal boundary layer thickness, which resist the motion in correspondence increasing temperature. Figure 2.8(c) depicts the effects of zero, first, and second-order velocity slips with magnetic field parameter M on ϕ nanoparticle concentration distribution. Figure 2.9 signifies effect of buoyancy ratio Nr on velocity profile for the cases of zero, first, and second-order velocity slips. For the case of $Nr>0$, it is perceived that velocity decreases near the channel centerline by increasing Nr, while the opposite behavior can be seen near the walls. It is also observed that an exponential rise near the right wall occurs between first and second-order slip. The effects of Reynolds number Re is reflected in figures 2.10(a), 2.10(b), and 2.10(c) on velocity, temperature, and concentration profile respectively. In figure 2.10(a), velocity is increasing with the increase of Re in zero, first, and second-order flow slip cases. Here it is also be noted that velocity overshoot with the greater value of the second-order velocity slip parameter on the right wall and velocity is decreasing near the left wall in first-order linear flow slip. Temperature is gradually decreasing with the rise of Re in figure 2.10(b) and nanoparticle concentration also decrease with an enhancement of Re in figure 2.10(c) in all slip cases.

Figures 2.11(a), 2.11(b) and 2.11(c) reflects the influence of $\Pr$ on velocity, temperature and nanoparticles concentration profiles in the presence of zero, first, and second-order velocity slips. In figure 2.11(a), it is observed that how $\Pr$ contribute its effect on the flow. It is analyzed that velocity profiles increase rapidly by increasing $\Pr$. The decreasing effect of temperature distribution happens with the increase of $\Pr$ is exposed in figure 2.11(b). It is because of an increase in $\Pr$ means very slow rate of thermal diffusion thickness. The influence of $\Pr$ on nanofluid is decelerated in concentration distribution in the presence/absence of slip parameters as shown in figure 2.11(c). Thermal conductivity distributions and migration of nanoparticles are determined by the mutual effects of Nt and Nb. According to figures 2.12(a) and 2.12(b) both temperature and nanoparticles concentration profiles directly depend on thermophoresis parameter, thus rise in Nt is directly proportional to an improvement in both θ and ϕ. While, in figures 2.13(a) and 2.13(b) show the impact of Nb on temperature and nanoparticles concentration function. The small change is occurred in temperature distribution due to Brownian parameter in the presence of suction $(S > 0)$ is showed in figure 2.13(a) and figure 2.13(b) exposes the fluctuation in the trend of concentration corresponding to varying Nb. As a result, a variation of Brownian motion reduces thickness of boundary layer when compared with the concentration. Figure 2.14 displays result of Rd on θ. It is inspected that enhancement occur in θ profile is due to increase in Rd. Obviously, an improvement in the radiation delivers more heat to fluid which leads to enhance temperature and thermal properties.

The shear stress function $u'(-1)$ and $u'(1)$, heat transfer rate $\theta'(-1)$ and $\theta'(1)$, nanoparticle mass transfer rate $\phi'(-1)$ and $\phi'(1)$ at left and right wall are provided for no-slip, first-order, second-order slips in Tables 2.2–2.4. In Table 2.2, effects of S, M, Re and $\Pr$ are calculated. The value of shear stress function decreases for Stefan blowing/suction parameter and magnetic parameter with increase of first-order flow slip parameter A at left wall whereas, at right wall, it increases with decrease of second-order slip parameter B . Results of emerging parameters like S , $\Pr$, Re , Rd and Nb for heat transfer rate are seen in Table 2.3. Heat transfer rate decreases for Brownian motion and radiation in first-order velocity slip parameter A that rises at left wall and gives growing effects with decrease of second-order flow slip parameter B . Table 2.4 represents the mass transfer for evolving different parameters. It is found that the mass transfer rate decelerates with an increase of first-order velocity slip parameter A for Stefan blowing/suction parameter, Prandtl number and Reynolds number at the left wall, however, accelerate with the decrease of second-order slip parameter B at right wall.

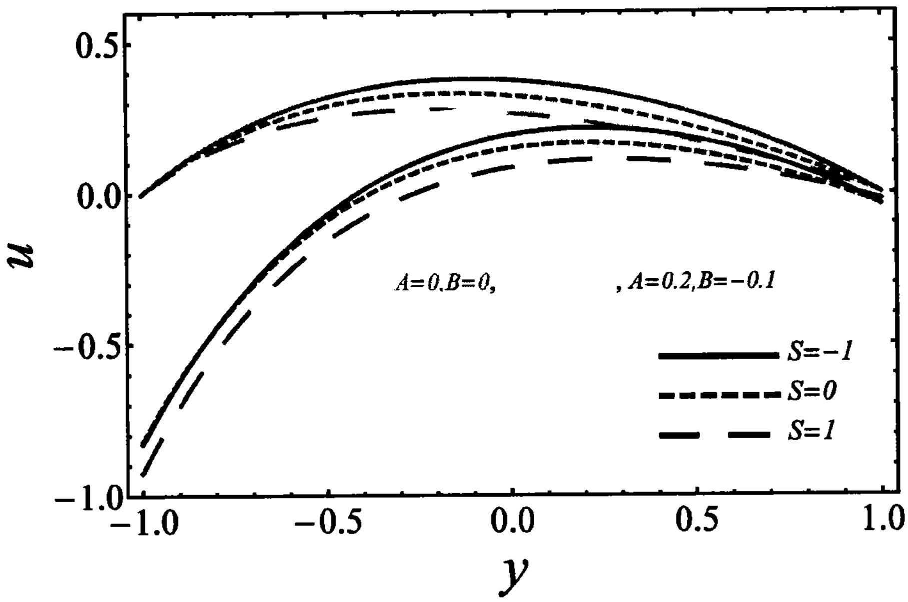

Figure 2.6(a): Impact of suction/injection at velocity.

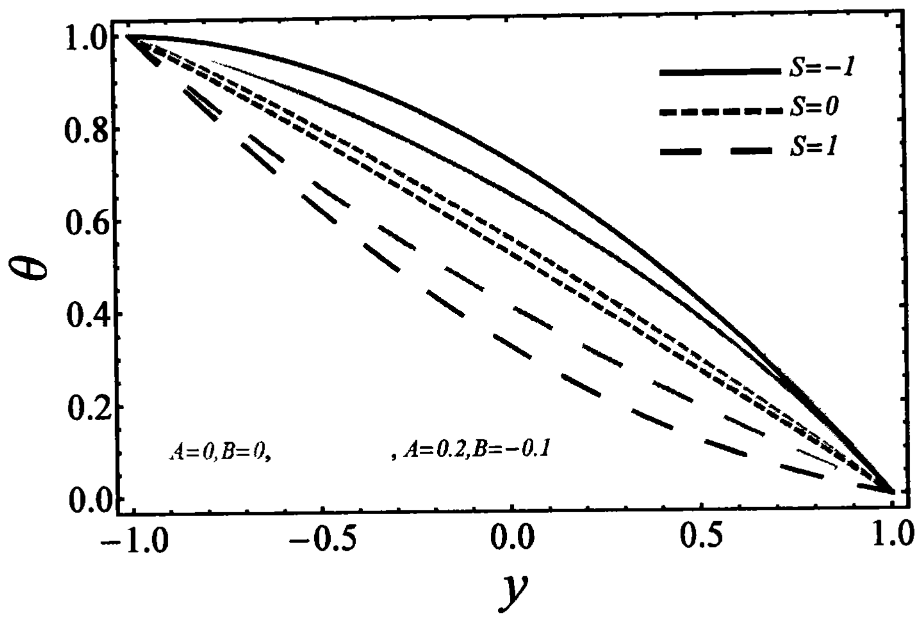

Figure 2.6(b): Impact of suction/injection at temperature.

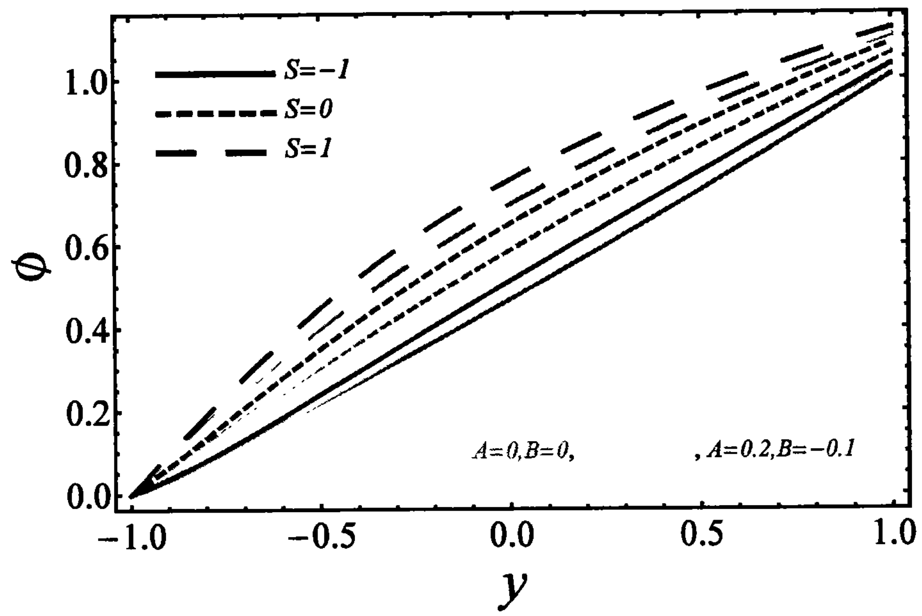

Figure 2.6(c): Impact of suction/injection at nanoparticle concentration.

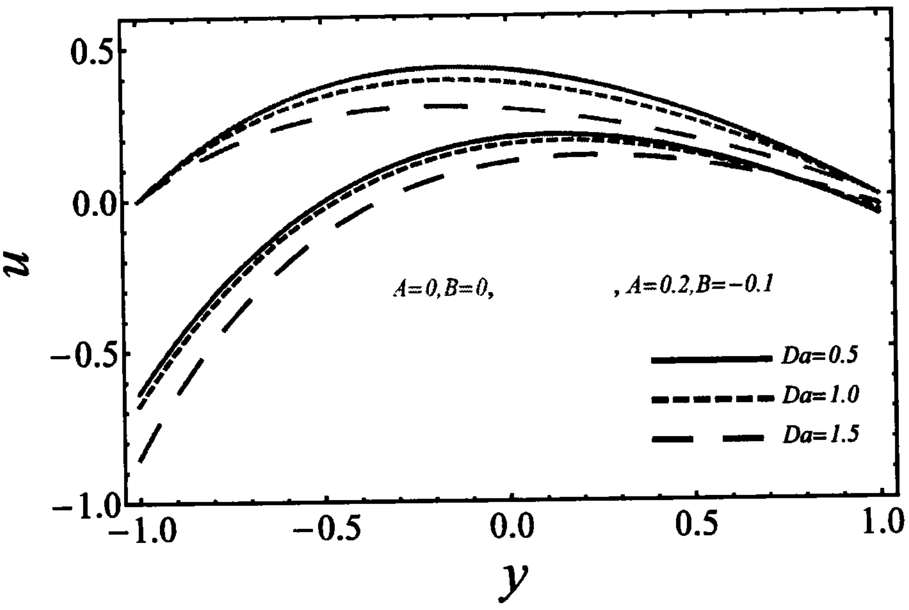

Figure 2.7: Impact of porosity parameter at velocity.

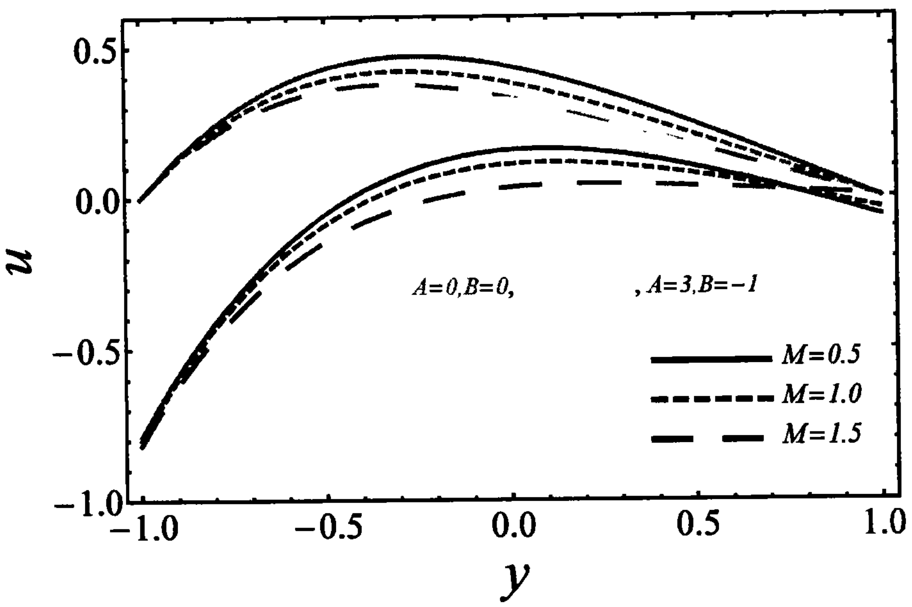

Figure 2.8(a): Impact of magnetic parameter at velocity.

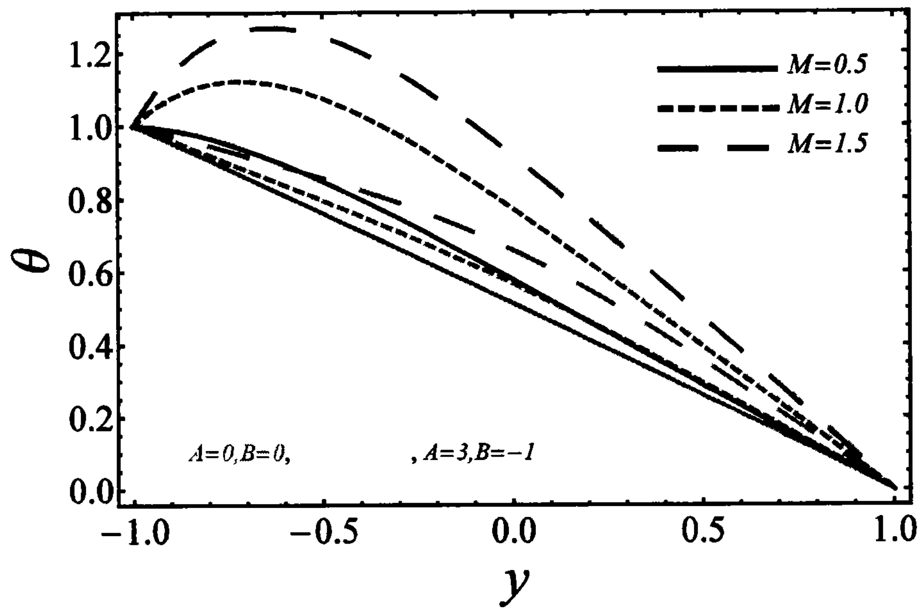

Figure 2.8(b): Impact of magnetic parameter at temperature.

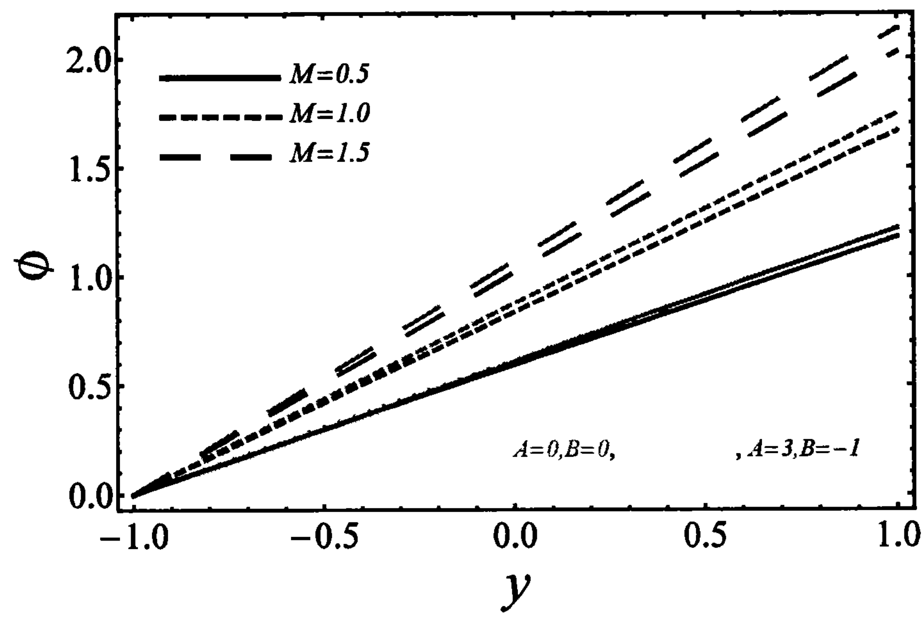

Figure 2.8(c): Impact of magnetic parameter at nanoparticle concentration.

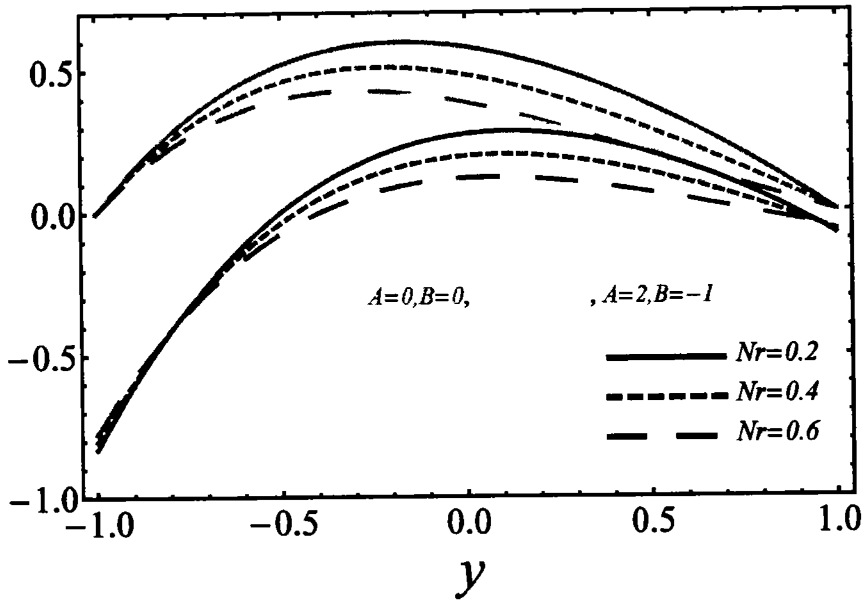

Figure 2.9: Impact of buoyancy ratio at velocity.

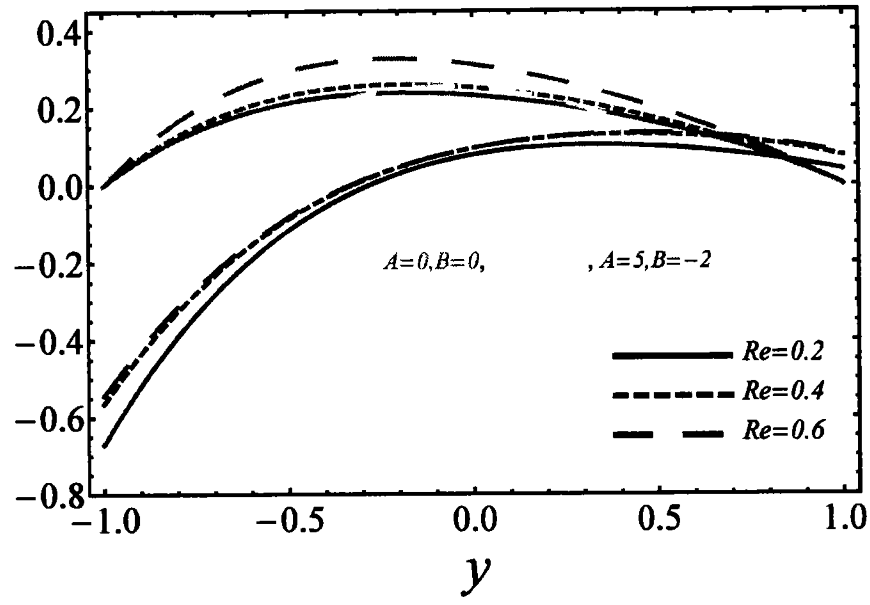

Figure 2.10(a): Impact of Reynolds number at velocity.

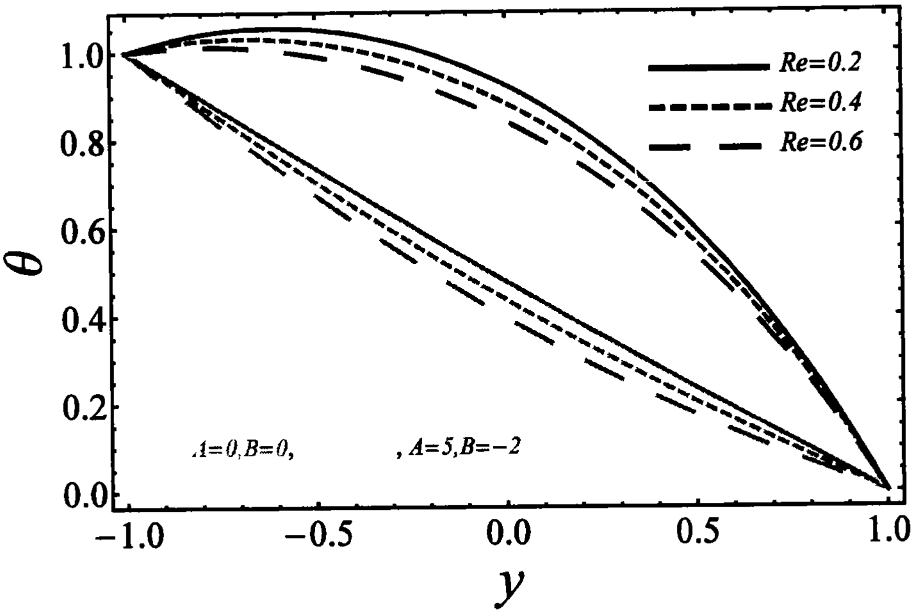

Figure 2.10(b): Impact of Reynolds number at temperature.

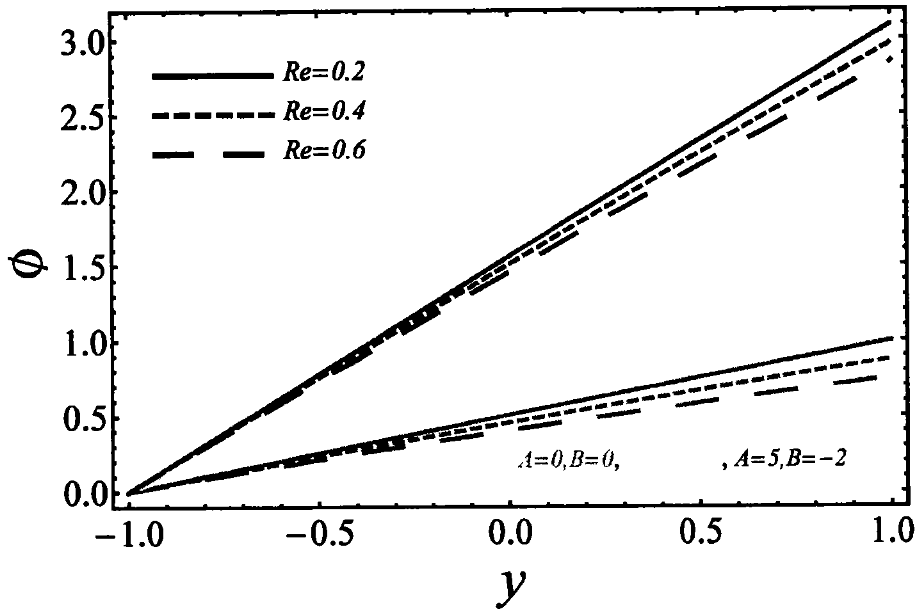

Figure 2.10(c): Impact of Reynolds number at nanoparticle concentration.

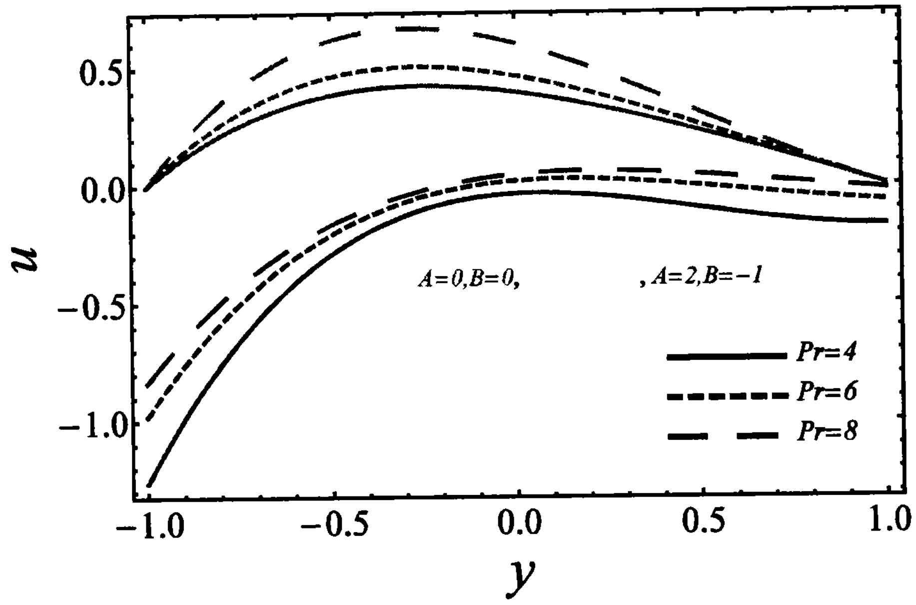

Figure 2.11(a): Impact of Pr at velocity.

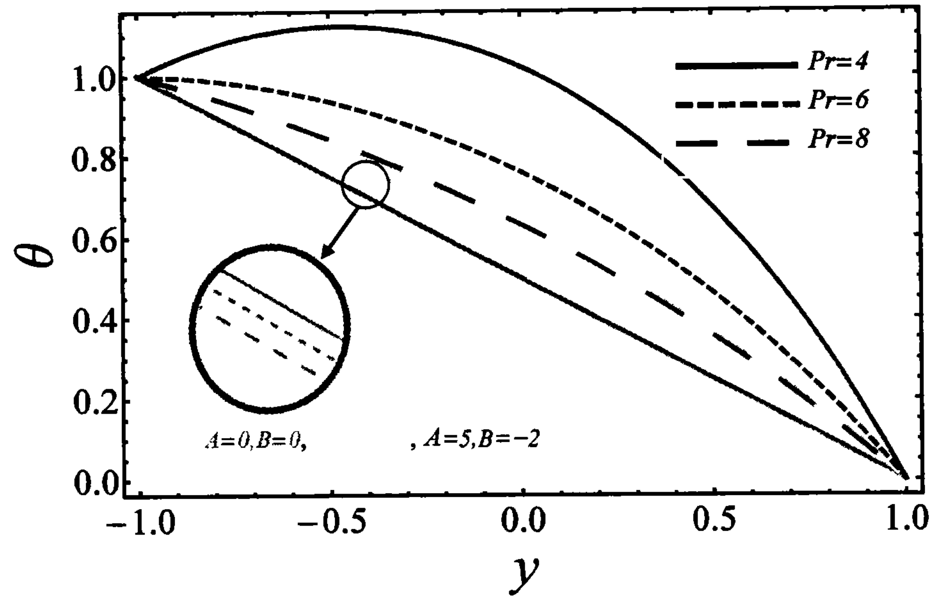

Figure 2.11(b): Impact of Pr at temperature.

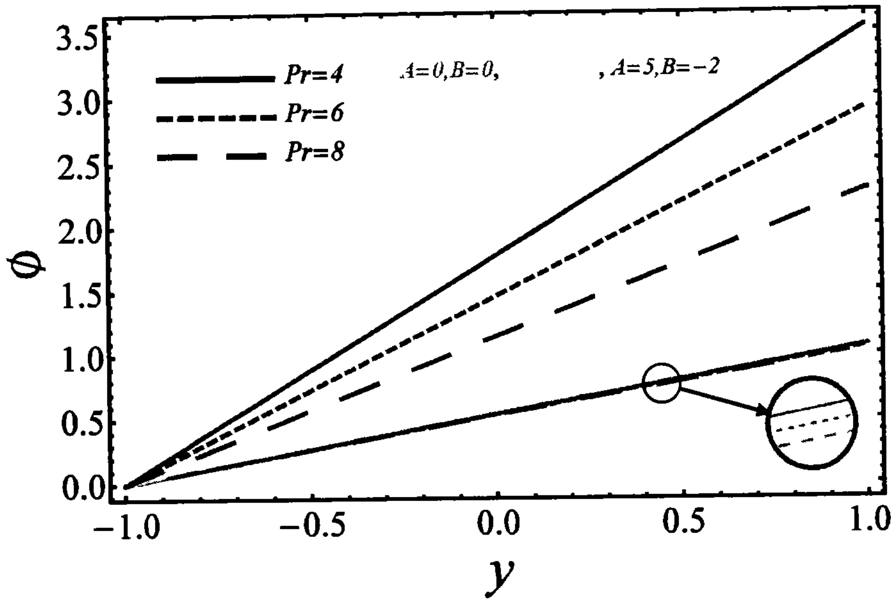

Figure 2.11(c): Impact of Pr at nanoparticle concentration.

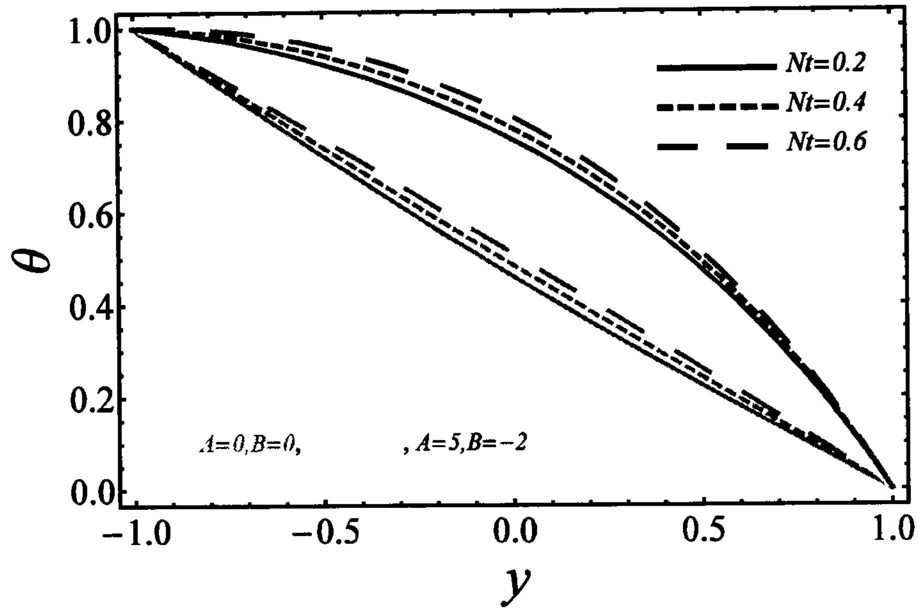

Figure 2.12(a): Impact of thermophoresis parameter at temperature.

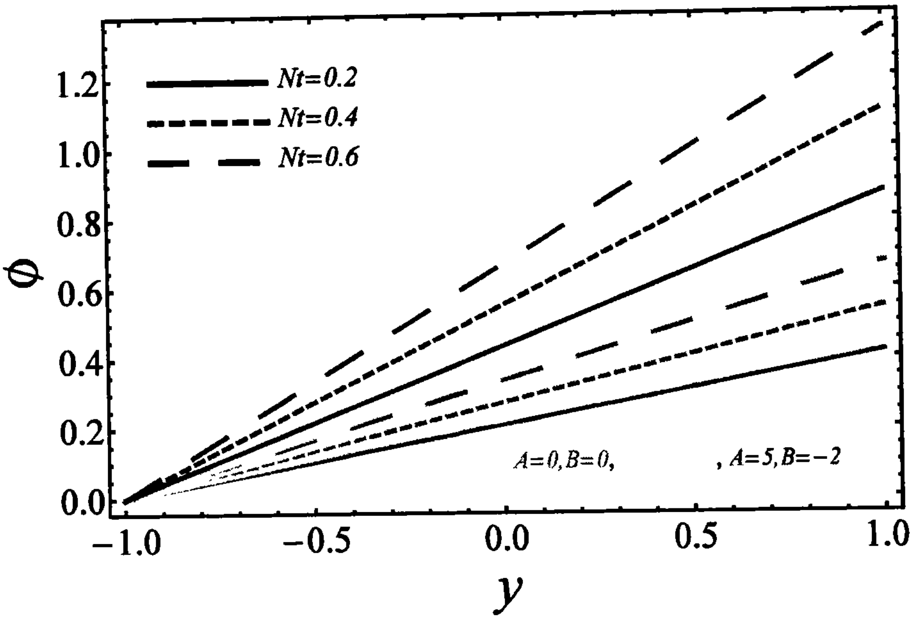

Figure 2.12(b): Impact of thermophoresis parameter at concentration.

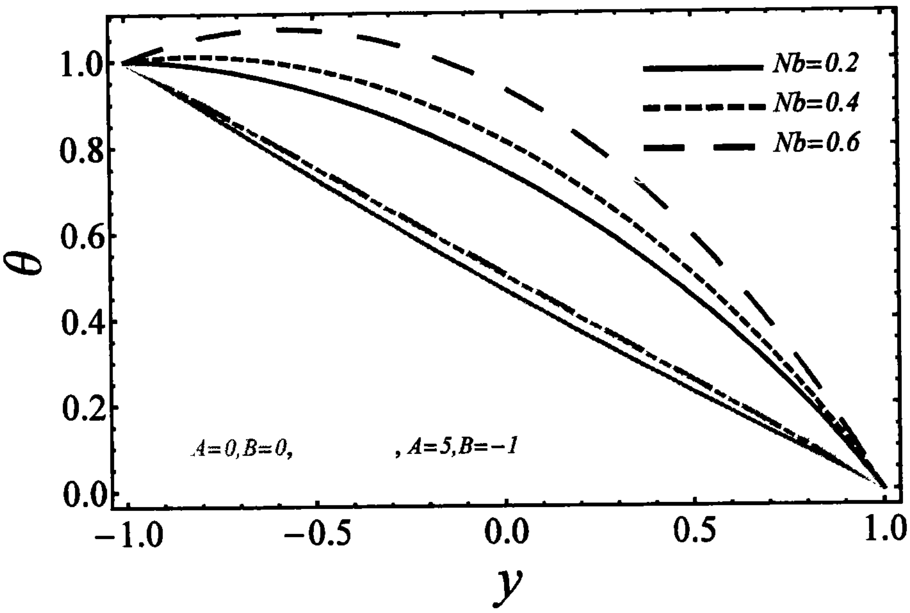

Figure 2.13(a): Impact of Brownian motion at temperature.

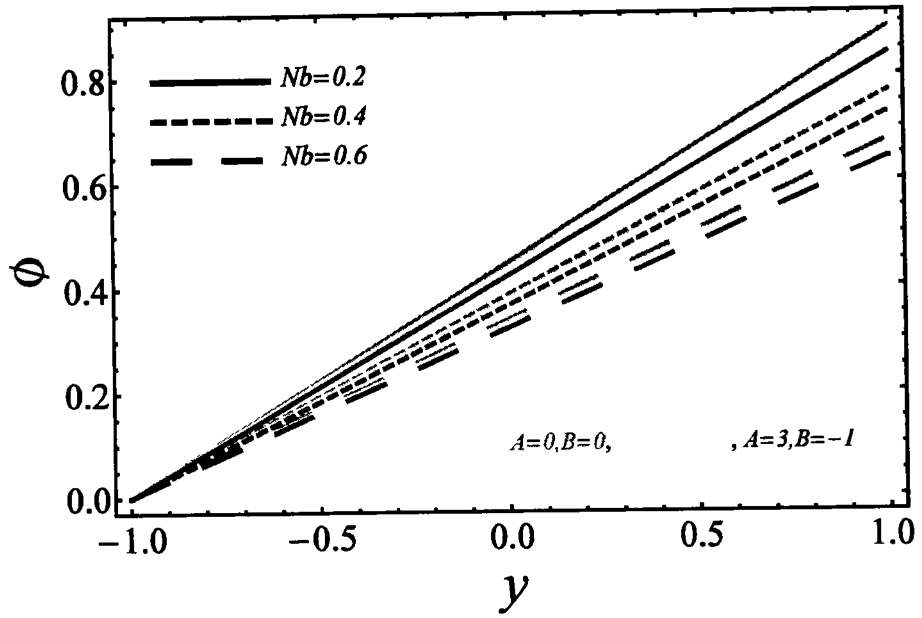

Figure 2.13(b): Impact of Brownian motion at nanoparticle concentration.

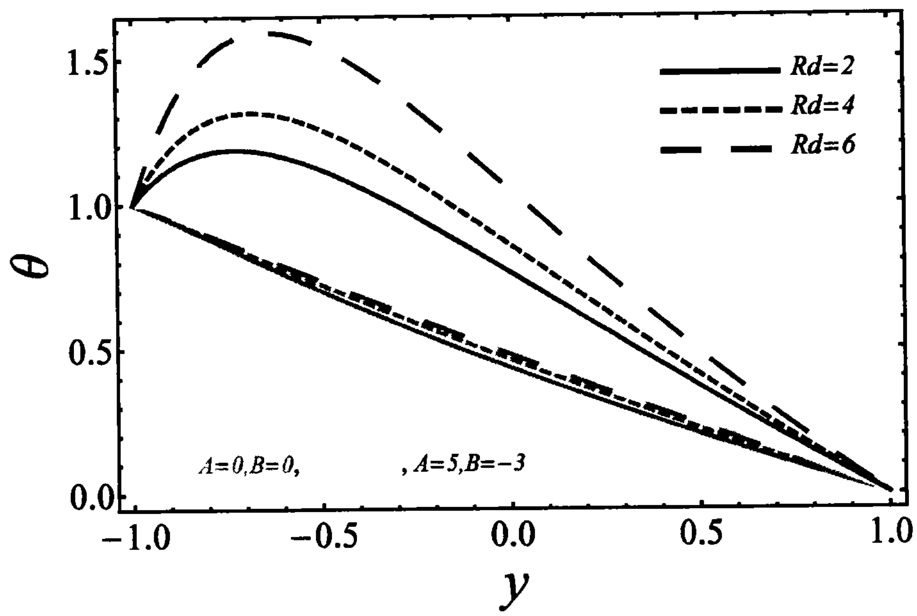

Figure 2.14: Impact of thermal radiation parameter at temperature.

Table 2.2: Skin friction coefficient at left and right walls.

					$A=0,\ B=0$		$A=2,\ B=0$		$A=5,\ B=-1$	
S	Pr	Re	M	S	$-u'(-1)$	$-u'(1)$	$-u'(-1)$	$-u'(1)$	$-u'(-1)$	$-u'(1)$
-1	6.8	0.3	0.5	0.5	-1.0345	0.7038	0.5932	-0.4149	0.1744	-0.4201
0					-0.9761	0.5456	0.5425	-0.3552	0.1863	-0.3313
1					-0.9240	0.4265	0.4540	-0.2868	0.1968	-0.2539
0.5	4				-1.1983	0.4168	0.6255	-0.3087	0.2730	-0.3990
	6				-0.9946	0.4678	0.5256	-0.3180	0.2081	-0.3113
	8				-0.8933	0.4940	0.4761	-0.3232	0.1755	-0.2682
		0.2			-1.1311	0.4548	0.6078	-0.3264	0.2482	-0.3802
		0.4			-0.8602	0.4933	0.4505	-0.3197	0.1641	-0.24 83
		0.6			-0.7865	0.5074	0.3964	-0.3105	0.1336	-0.2069
			0.5		-0.7672	0.3493	0.5023	-0.3204	0.1928	-0.2910
			1.0		-0.8662	0.4198	0.3622	-0.2083	0.1513	-0.2475
			1.5		-0.9469	0.4800	0.2470	-0.1259	0.1136	-0.2072
				0.5	-1.1820	0.6655	0.5023	-0.3204	0.1928	-0.2910
				1.0	-1.1076	0.6055	1.3071	-1.0554	0.3149	-0.4936
				1.5	-0.9469	0.4800	7.0663	-6.7302	0.4306	-0.7307

Table 2.3: Nusselt number at left and right walls.

M	Nt	Nb	Rd	Re	Pr	S	$A=0,\ B=0$		$A=2,\ B=0$		$A=5,\ B=-1$	
							$-\theta'(-1)$	$-\theta'(1)$	$-\theta'(-1)$	$-\theta'(1)$	$-\theta'(-1)$	$-\theta'(1)$
0.5	0.5	0.5	1.0	0.3	6.8	0.5	0.6064	0.4176	0.5730	0.4261	0.6172	0.4167
1.0							0.6090	0.4158	0.5414	0.4382	0.5670	0.4408
1.5							0.6147	0.4126	0.5315	0.4450	0.5612	0.4412
	0.2						0.5909	0.4317	0.5604	0.4400	0.6122	0.4242
	0.4						0.6015	0.4219	0.5692	0.4302	0.6158	0.4190
	0.6						0.6112	0.4135	0.5765	0.4224	0.6184	0.4146
		0.2					1.1739	0.2702	1.1175	0.2799	1.1345	0.2775
		0.4					0.6740	0.3863	0.6384	0.3943	0.6783	0.3879
		0.6					0.5659	0.4399	0.5337	0.4489	0.5807	0.4373
			2				0.5645	0.4420	0.5443	0.4483	0.5732	0.4415
			4				0.5358	0.4636	0.5246	0.4678	0.5417	0.4634
			6				0.5247	0.4735	0.5170	0.4766	0.5291	0.4734
				0.2			0.5140	0.4592	0.4556	0.4786	0.5206	0.4667
				0.4			0.6977	0.3832	0.6734	0.3884	0.7099	0.3793
				0.6			0.9189	0.3266	0.9010	0.3297	0.9325	0.3204
					4		0.5408	0.4495	0.5029	0.4630	0.5426	0.4563
					6		0.5873	0.4260	0.5536	0.4353	0.5959	0.4270
					8		0.6362	0.4059	0.6023	0.4136	0.6499	0.4025
						-1	0.2594	0.9129	0.2356	0.9410	0.2889	0.9087
						0	0.4272	0.5451	0.3962	0.5588	0.4450	0.5437
						1	0.9076	0.3240	0.8720	0.3288	0.9111	0.3231

Table 2.4: Sherwood number at left and right walls.

S	Re	Nb	Pr	M	Nt	$A=0,\ B=0$		$A=2,\ B=0$		$A=5,\ B=-1$	
						$-\phi'(-1)$	$-\phi'(1)$	$-\phi'(-1)$	$-\phi'(1)$	$-\phi'(-1)$	$-\phi'(1)$
-1	0.3	0.5	6.8	0.5	0.5	-0.1370	-0.9129	-0.1101	-0.9410	-0.1659	-0.9087
0						-0.4272	-0.5451	-0.3962	-0.5588	-0.4450	-0.5437
1						-1.1275	-0.3240	-1.0894	-0.3288	-1.1299	-0.3231
0.5	0.2					-0.5696	-0.4592	-0.5112	-0.4786	-0.5761	-0.4667
	0.4					-0.8240	-0.3832	-0.7989	-0.3884	-0.8359	-0.3793
	0.6					-1.1390	-0.3266	-1.1194	-0.3297	-1.1522	-0.3204
		0.2				-3.7227	-0.6755	-3.5677	-0.6996	-3.6139	-0.6937
		0.4				-0.9880	-0.4829	-0.9425	-0.4928	-0.9928	-0.4849
		0.6				-0.5312	-0.3666	-0.5042	-0.3741	-0.5434	-0.3644
			4			-0.6289	-0.4495	-0.5910	-0.4630	-0.6307	-0.4563
			6			-0.6756	-0.4260	-0.6417	-0.4353	-0.6842	-0.4270
			8			-0.7252	-0.4059	-0.6907	-0.4136	-0.7387	-0.4025
				0.5		-0.6950	-0.4176	-0.6612	-0.4261	-0.7056	-0.4167
				1.0		-0.6975	-0.4158	-0.6295	-0.4382	-0.6551	-0.4408
				1.5		-0.7031	-0.4126	-0.6196	0.4450	-0.6492	-0.4412
					0.2	-0.2022	-0.2018	-0.1905	-0.2062	-0.2118	-0.1986
					0.4	-0.5001	-0.3559	-0.4745	-0.3633	-0.5126	-0.3535
					0.6	-0.9270	-0.4703	-0.8840	-0.4799	-0.9333	-0.4716

2.4 Conclusions

A nanofluid through plane driven by sole contribution of pressure is investigated. Nanofluid flows through the gap of a symmetric channel with the application of different order slip. Temperature difference is also observed due to external source of heat at the boundary. The effects of various parameters are analyzed in tabular and graphical forms. The main findings are summarized as follows:

- The Stefan blowing/suction induces significant deceleration effects for velocity and temperature profiles whereas enhancement in nanoparticle concentrations is observed.
- Variation in porosity parameter declines the velocity.
- Momentum decreases subject to magnetic parameter, but reverse trend occurs in temperature distribution and nanoparticle concentrations.
- The buoyancy ratio corresponding to magnetism plays a dominant role on velocity, therefor buoyancy ratio has the same effect on velocity as observed for magnetic field.
- Thermophoresis, Brownian motion and radiation have same increasing effects on thickness of thermal boundary layer, but thickness of concentration boundary layer decreases with increase of Brownian motion.
- Nusselt number at left side of geometry channel has increasing phenomena but opposite trend at right side of geometry for Nb and Rd are noted.
- An increase in parameters Nt, S, $\Pr$ and Re decrease the Nusselt number at left wall but opposite behavior attain at right wall.
- Sherwood number increases with increase of S, Re and $\Pr$ at left wall, while decreases at right wall.

Chapter 3

3 Structural impact of Kerosene-Al_2O_3 nanoliquid on MHD Poiseuille flow with variable thermal conductivity: Application of cooling process

The fuel of rocket engine can improve the cooling of nozzle wall and chamber by means of Kerosene–Al_2O_3 nanofluid. In particular, this investigation is devoted to exploring the credible potential use of kerosene-Al_2O_3 nano-liquid for thrust chamber regenerative cooling in semi-cryogenic rocket engine due to its enhanced thermal properties. Poiseuille flow is analyzed by means of convective types of boundary condition. The contribution of inclined MHD and variable thermal conductivity are incorporated. The spherical shaped Alumina (Al_2O_3) nano-size particles with volume fraction (0.01, 0.02, 0.03 and 0.04) are suspended in kerosene oil carrier liquid. A set of nonlinear but mutually dependent differential equations describe the flow dynamic which are tackled by analytical technique. Effects of various important variables are examined graphically. The role of physical parameters of contemporary interest like Eckert number, Grashof number, thermal radiation, heat source/sink, rate of heat transfer and rate of shear stress are numerically investigated and provided in tabular form. Convergence of obtained series solutions has been deliberated by "$\hbar$" and the square error norm 2 curves are also presented in each case.

3.1 Problem formulation

3.1.1 Flow analysis

Let steady, laminar viscous liquid in plane Poiseuille boundary layer flow of nanofluid among two parallel walls at $\bar{y} = \pm a$ as shown in figure 3.1. Model considered into a rectangular coordinate system in which $\bar{x}$-axis along flow direction while $\bar{y}$-axis perpendicular to channel walls. Both walls of channel are kept fixed and sustained temperatures T_1 (heated left wall) and T_2 (cold right wall).

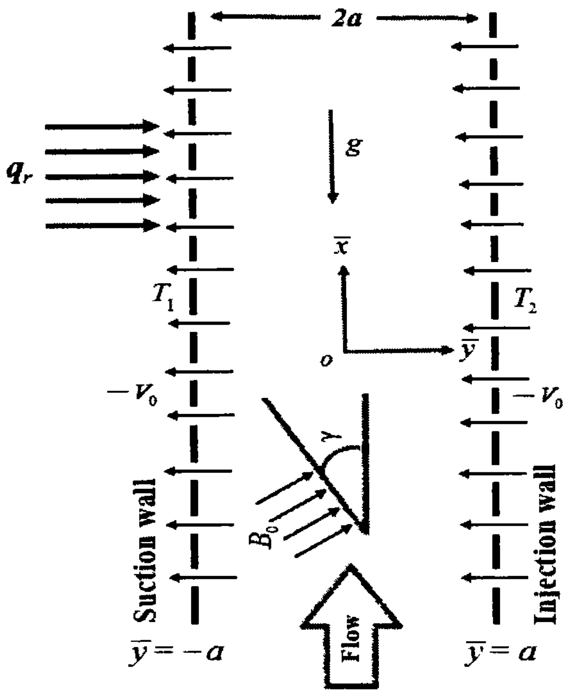

Figure 3.1: Geometry of flow model.

Liquid in enclosure is a Kerosene-based nanofluid with suspension of Alumina nanoparticles. It is supposed that there is no slip between base liquid (i.e., Kerosene oil) and the nanoparticles Alumina (Al_2O_3). Electric field and Hall current are assumed to be negligible in electrically conducting nanofluid for small Reynolds number.

3.1.2 Governing equations (Tiwari and Das's model)

According to the Tiwari and Das model, equations (1.18), (1.19) and (1.38) given in the chapter 1, for a steady state, incompressible nanofluid under the influence of inclined magnetic, buoyancy, radiative heat flux, heat source/sink, variation in thermal conductivity and viscous dissipation transporting through a channel consist of suction/injection walls are mathematically modeled with the application of boundary layer and Boussinesq's approximation as

$$\rho_{nf}\left(-V_0\frac{\partial \bar{u}}{\partial \bar{y}}\right)=-\frac{\partial \bar{p}}{\partial \bar{x}}+\mu_{nf}\left(\frac{\partial^2 \bar{u}}{\partial \bar{y}^2}\right)-\sigma_{nf}B_0^2\bar{u}+(\rho\beta)_{nf}(T-T^*)g, \tag{3.1}$$

$$(\rho C_p)_{nf}\left(-V_0\frac{\partial T}{\partial \bar{y}}\right)=k_{nf}^{\varepsilon}\left(\frac{\partial^2 T}{\partial \bar{y}^2}\right)-\left(\frac{\partial q_r}{\partial \bar{y}}\right)+Q_0(T-T^*)+\mu_{nf}\left(\frac{\partial \bar{u}}{\partial \bar{y}}\right)^2, \tag{3.2}$$

here, V_0 is the suction/injection velocity, Q_0 is volumetric heat source/sink and k_{nf}^{ε} represent the thermal conductivity with the variation of temperature of nanofluid.

Boundary conditions for plane-Poiseuille flow are

$$\left.\begin{array}{ll}\bar{u}=0,\ T=T_1 \text{ at } \bar{y}=-a & (\text{Left wall})\\ \bar{u}=0,\ T=T_2 \text{ at } \bar{y}=a & (\text{Right wall})\end{array}\right\}. \tag{3.3}$$

Consider following nondimensional terms

$$x=\frac{\bar{x}}{a},\ u=\frac{\bar{u}}{U_m},\ y=\frac{\bar{y}}{a},\ v=\frac{\bar{v}}{U_m},\ p=\frac{a^2\bar{p}}{\mu_{nf}U_m},\ \theta=\frac{T-T^*}{T_1-T^*},\ m^*=\frac{T_2-T^*}{T_1-T^*}. \tag{3.4}$$

Incorporating the equation (3.4) with radiative heat flux defined in equation (2.10), the governing equations (3.1) and (3.2) become

$$A_1\left(-P+\frac{\partial^2 u}{\partial y^2}\right)+A_2S_1\frac{\partial u}{\partial y}-A_3\bar{M}^2u+A_4\frac{Gr}{\mathrm{Re}}\theta=0, \tag{3.5}$$

$$\left(Rd + A_6\left(1+\varepsilon\theta\right)\right)\frac{\partial^2\theta}{\partial y^2} + A_5 S_1 \Pr\frac{\partial\theta}{\partial y} + A_6\varepsilon\left(\frac{\partial\theta}{\partial y}\right)^2 + A_1 Ec\Pr\left(\frac{\partial u}{\partial y}\right)^2 + Q\theta = 0. \quad (3.6)$$

The corresponding dimensionless boundary conditions

$$\left.\begin{array}{l} u=0,\ \theta=1 \quad \text{at } y=-1 \\ u=0,\ \theta=m^* \ \text{at } y=1 \end{array}\right\}, \quad (3.7)$$

where

$$\left.\begin{array}{l} Gr = \dfrac{\beta_f g a^3 (T_1 - T^*)}{\nu_f^{\,2}}, \Pr = \dfrac{\nu_f\left(\rho C_p\right)_f}{k_f},\ Ec = \dfrac{U_m^{\,2}}{\left(C_p\right)_f\left(T_1 - T^*\right)}, \nu_f = \dfrac{\mu_f}{\rho_f} \\ A_1 = \dfrac{\mu_{nf}}{\mu_f},\ A_2 = \dfrac{\rho_{nf}}{\rho_f},\ A_3 = \dfrac{\sigma_{nf}}{\sigma_f},\ A_4 = \dfrac{\left(\rho\beta\right)_{nf}}{\left(\rho\beta\right)_f},\ A_5 = \dfrac{\left(\rho C_p\right)_{nf}}{\left(\rho C_p\right)_f}, A_6 = \dfrac{k_{nf}}{k_f}, \\ Q = \dfrac{Q_0 a^2}{k_f},\ S_1 = \dfrac{\rho_f V_0 a}{\mu_f},\ M^2 = \dfrac{\sigma_f B_0^{\,2} a^2}{\mu_f},\ Rd = \dfrac{16\sigma^* T_m^{\,3}}{3k^* k_f},\ \text{Re} = \dfrac{\rho_f U_m a}{\mu_f} \end{array}\right\} \quad (3.8)$$

In this chapter, the physical thermal properties are used define in equations (1.3), (1.9), (1.10) and (1.11). The relation of thermal conductivity under variation with heat [95], defined as

$$k_{nf}^{\varepsilon} = k_{nf}\left(1+\varepsilon\theta\right), \quad (3.9)$$

here ε is parameter of variation in thermal conductivity, fluid flow is dependent on constant pressure gradient (i.e., $P = \frac{\partial p}{\partial x}$) and maximum velocity ($U_m = -\frac{a^2}{2\mu_f}\frac{\partial p}{\partial x}$) occurred between two walls. When the temperature of right and left walls extremely increase then the heat flux occurs and $\bar{M}$ is the inclined magnetic field with inclination γ, i.e., $\bar{M} = M\sin\gamma$. The dynamic viscosity of nanofluid from Brinkman model expressed in equation (1.3) and thermal conductivity of nanofluid from Maxwell model defined in equation (1.6) is used in current chapter. Expression of coefficient of skin friction defined in equation (1.54) and Nusselt number defined in equation (1.56) are transformed in view of equation (3.4) as

$$\left.\begin{array}{l}\operatorname{Re} C_f = 2A_1 u'(y)\,\big|_{y=-1,1}\\ Nu = -A_6\theta'(y)\big|_{y=-1,1}\end{array}\right\}. \tag{3.10}$$

3.2 Solution of the problem

To seek an approximated solution for equations (3.5) and (3.6) is found with the help of HAM procedure.

Zeroth–order solution

Consider, the following initial approximations $(u_0,\ \theta_0)$ which satisfy the linear operators $(\pounds_u,\ \pounds_\theta)$ and associated boundaries

$$u_0(y) = y^2 - 1,\ \theta_0(y) = \frac{(1-m^*)y - m^* - 1}{-2} \tag{3.11}$$

and

$$\pounds_u = \frac{d}{dy}\left(\frac{du}{dy}\right),\quad \pounds_\theta = \frac{d}{dy}\left(\frac{d\theta}{dy}\right). \tag{3.12}$$

The convergence control parameters $\hbar_u$, $\hbar_\theta$ with nonlinear operators N_u, N_θ of velocity and temperature along embedding parameter $\xi \in [0,\ 1]$, yields the following zeroth–order deformations respectively

$$\left.\begin{array}{l}(1-\xi)\pounds_u\left[u(y,\xi)-u_0(y)\right] = \xi\hbar_u N_u\left[u(y,\xi),\theta(y,\xi)\right]\\ (1-\xi)\pounds_\theta\left[\theta(y,\xi)-\theta_0(y)\right] = \xi\hbar_\theta N_\theta\left[u(y,\xi),\theta(y,\xi)\right]\end{array}\right\}, \tag{3.13}$$

with boundary conditions

$$\left.\begin{array}{l}u(y,\xi)=0,\ \ \theta(y,\xi)=m^*\ \text{ at } y=1\\ u(y,\xi)=0,\ \ \theta(y,\xi)=1\ \text{ at } y=-1\end{array}\right\} \tag{3.14}$$

and

$$\left.\begin{aligned}&N_u\left[u(y,\xi),\theta(y,\xi),\phi(y,\xi)\right]=A_1\left[-P+\frac{\partial^2 u}{\partial y^2}\right]+A_2S_1\frac{\partial u}{\partial y}-A_3\bar{M}^2u+A_4\frac{Gr}{\mathrm{Re}}\theta\\&N_\theta\left[u(y,\xi),\theta(y,\xi),\phi(y,\xi)\right]=\left[Rd+A_6(1+\varepsilon\theta)\right]\frac{\partial^2\theta}{\partial y^2}+A_5S_1\Pr\frac{\partial\theta}{\partial y}+A_6\varepsilon\left(\frac{\partial\theta}{\partial y}\right)^2\\&+A_1Ec\Pr\left(\frac{\partial u}{\partial y}\right)^2+Q\theta\end{aligned}\right\}. \quad (3.15)$$

***l* th–order solution**

The l th–order deformation for $u_l(y)$ and $\theta_l(y)$ are as follows

$$\left.\begin{aligned}\pounds_u\left[u_l(y)-\chi_l u_{l-1}(y)\right]=\hbar_u R_l^u(y)\\\pounds_\theta\left[\theta_l(y)-\chi_l\theta_{l-1}(y)\right]=\hbar_\theta R_l^\theta(y)\end{aligned}\right\}. \quad (3.16)$$

$$\left.\begin{aligned}u_l(y,\xi)=0,\ \theta_l(y,\xi)=1\ \text{ at } y=-1\\u_l(y,\xi)=0,\ \theta_l(y,\xi)=m^*\ \text{ at } y=1\end{aligned}\right\}, \quad (3.17)$$

$$\left.\begin{aligned}&R_l^u(y)=A_1\left[-P+u_l''\right]+A_2S_1u_l'-A_3\bar{M}^2u_l+A_4\frac{Gr}{\mathrm{Re}}\theta_l\\&R_l^\theta(y)=(Rd+A_6)\theta_l''+A_6\varepsilon\sum_{k=0}^{l}\theta_{l-k}\theta_k''+A_5S_1\Pr\theta_l'+A_6\varepsilon\sum_{k=0}^{l}\theta_k'\theta_{l-k}'+A_1Ec\Pr\sum_{k=0}^{l}u_k'u_{l-k}'+Q\theta_l\end{aligned}\right\}. \quad (3.18)$$

The solution can be described as of l th-order

$$\left.\begin{aligned}u(y)=u_0(y)+\sum_{k=1}^{l}u_k(y)\\\theta(y)=\theta_0(y)+\sum_{k=1}^{l}\theta_k(y)\end{aligned}\right\}. \quad (3.19)$$

Analytical solution expressions for velocity and temperature distributions at second order iterations are calculated with help of Mathematica package BVPh2.0 based on the HAM.

$$
\left.\begin{aligned}
u(y) = & -1 - 3\hbar_u - \hbar_u \frac{99Gr}{40} - \hbar_u^2 \frac{3}{2} - \hbar_u^2 \frac{99Gr}{80} + \hbar_u \hbar_\theta \frac{33Gr}{512} + \hbar_u \hbar_\theta \frac{539EcGr}{100} - \\
& \hbar_u \frac{5\bar{M}^2}{6} - \hbar_u^2 \frac{25\bar{M}^2}{24} - \hbar_u^2 \frac{33Gr\bar{M}^2}{64} - \hbar_u^2 \frac{61\bar{M}^4}{360} + \hbar_u \hbar_\theta \frac{33GrQ}{64} + \hbar_u^2 \frac{33GrS_1}{320} + \\
& \hbar_u \hbar_\theta \frac{231GrS_1}{64} + \hbar_u^2 \frac{S_1^2}{12} + \\
& \left(\begin{aligned} & -\hbar_u \frac{33Gr}{40} - \hbar_u^2 \frac{33Gr}{80} - \hbar_u^2 \frac{77Gr\bar{M}^2}{1600} + \hbar_u \hbar_\theta \frac{77GrQ}{1600} - \hbar_u \frac{2S_1}{3} - \hbar_u^2 \frac{5S_1}{6} - \\ & \hbar_u^2 \frac{33GrS_1}{80} - \hbar_u^2 \frac{33Gr}{80} - \hbar_u^2 \frac{17\bar{M}^2 S_1}{90} \end{aligned} \right) y + \\
& \left(\begin{aligned} & 1 + 3\hbar_u + \hbar_u \frac{99Gr}{40} + \hbar_u^2 \frac{3}{2} + \hbar_u^2 \frac{99Gr}{80} - \hbar_u \hbar_\theta \frac{99Gr}{1280} - \hbar_u \hbar_\theta \frac{231EcGr}{40} + \\ & \bar{M}^2 \hbar_u + \hbar_u^2 \frac{5\bar{M}^2}{4} + \hbar_u^2 \frac{99Gr\bar{M}^2}{160} + \hbar_u^2 \frac{5\bar{M}^4}{24} - \\ & \hbar_u \hbar_\theta \frac{99GrQ}{160} - \hbar_u^2 \frac{33GrS_1}{160} + \hbar_u \hbar_\theta \frac{693GrS_1}{160} + \hbar_u^2 \frac{S_1^2}{6} \end{aligned} \right) y^2 + \\
& \left(\begin{aligned} & \hbar_u \frac{33Gr}{40} + \hbar_u^2 \frac{33Gr}{80} + \hbar_u^2 \frac{11Gr\bar{M}^2}{160} - \hbar_u \hbar_\theta \frac{11GrQ}{160} + \hbar_u \frac{2S_1}{3} + \hbar_u^2 \frac{5S_1}{6} + \\ & \hbar_u^2 \frac{33GrS_1}{80} + \hbar_u^2 \frac{2\bar{M}^2 S_1}{9} \end{aligned} \right) y^3 + \\
& \left(\begin{aligned} & \hbar_u \hbar_\theta \frac{33Gr}{2560} - \hbar_u \frac{\bar{M}^2}{6} - \hbar_u^2 \frac{5\bar{M}^2}{24} - \hbar_u^2 \frac{33Gr\bar{M}^2}{320} - \hbar_u^2 \frac{\bar{M}^4}{24} + \hbar_u \hbar_\theta \frac{33GrQ}{320} - \\ & \hbar_u^2 \frac{33GrS_1}{320} - \hbar_u \hbar_\theta \frac{231GrS_1}{320} + \hbar_u^2 \frac{S_1^2}{12} \end{aligned} \right) y^4 + \\
& \left(-\hbar_u^2 \frac{33Gr\bar{M}^2}{1600} + \hbar_u \hbar_\theta \frac{33GrQ}{1600} - \hbar_u^2 \frac{\bar{M}^2 S_1}{30} \right) y^5 + \left(\hbar_u \hbar_\theta \frac{77EcGr}{200} + \hbar_u^2 \frac{\bar{M}^4}{360} \right) y^6.
\end{aligned}\right\}, \quad (3.20)
$$

$$
\left.\begin{aligned}
\theta(y) &= \frac{1}{2} - \frac{1}{16}\hbar_\theta - \hbar_\theta\frac{14Ec}{3} - \hbar_u\hbar_\theta\frac{231Gr}{40} - \hbar_\theta^2\frac{1}{32} - \hbar_\theta^2\frac{7Ec}{3} + \hbar_\theta^3\frac{5}{24576} + \hbar_\theta^3\frac{161Ec}{5760} + \\
&\hbar_\theta^3\frac{77Ec^2}{72} - \hbar_u\hbar_\theta\frac{91Ec\bar{M}^2}{45} - \hbar_\theta\frac{Q}{2} - \hbar_\theta^2\frac{89Q}{384} + -\hbar_\theta^2\frac{49EcQ}{45} + \hbar_\theta^3\frac{5Q}{1536} + \hbar_\theta^3\frac{161EcQ}{720} + \\
&\hbar_\theta^2\frac{5Q^2}{48} + \hbar_\theta^2\frac{13Q^2}{960} - \hbar_\theta^2\frac{Rd}{32} - \hbar_\theta^2\frac{7EcRd}{3} - \hbar_\theta^2\frac{QRd}{4} - \hbar_\theta\frac{7S_1}{2} - \hbar_\theta^2\frac{7S_1}{4} + \hbar_\theta^3\frac{35S_1}{1536} + \\
&\hbar_\theta^3\frac{1127EcS_1}{720} + \hbar_\theta^2\frac{7QS_1}{8} + \hbar_\theta^3\frac{35QS_1}{192} - \hbar_\theta^2\frac{7RdS_1}{4} + \hbar_\theta^3\frac{2457S_1^{\,2}}{384} + \\
&\left(\begin{aligned}
&\frac{1}{2} - \frac{1}{16}\hbar_\theta - \hbar_\theta\frac{14Ec}{3} - \hbar_u\hbar_\theta\frac{231QGr}{40} - \hbar_\theta^2\frac{1}{32} - \hbar_\theta^2\frac{7Ec}{3} + \hbar_\theta^3\frac{5}{24576} + \hbar_\theta^3\frac{161Ec}{5760} + \\
&\hbar_\theta^3\frac{77Ec^2}{72} - \hbar_u\hbar_\theta\frac{91Ec\bar{M}^2}{45} - \hbar_\theta\frac{Q}{2} - \hbar_\theta^2\frac{89Q}{384} + -\hbar_\theta^2\frac{49EcQ}{45} + \hbar_\theta^3\frac{5Q}{1536} + \hbar_\theta^3\frac{161EcQ}{720} - \\
&\hbar_\theta^2\frac{17\bar{M}^2S_1}{90} + \hbar_\theta^3\frac{35S_1}{1536} + \hbar_\theta^3\frac{1127EcS_1}{720}
\end{aligned}\right)y + \\
&\left(\begin{aligned}
&1 + \frac{4}{3}\hbar_\theta + \hbar_\theta\frac{99Ec}{120} + \hbar_\theta^2\frac{3Ec}{2} + \hbar_\theta^2\frac{99QGr}{80} - \hbar_u\hbar_\theta\frac{99Gr}{1580} - \hbar_u\hbar_\theta\frac{231EcQ}{160} + \hbar_\theta^2\frac{5\bar{M}^2}{4} + \\
&\hbar_\theta^2\frac{99Gr\bar{M}^2}{160} + \hbar_\theta^2\frac{5\bar{M}^4}{24} - \hbar_u\hbar_\theta\frac{99GrQ}{160} - \hbar_\theta^2\frac{33GrS_1}{160} + \hbar_u\hbar_\theta\frac{693GrS_1}{160} + \hbar_\theta^2\frac{S_1^{\,2}}{6}
\end{aligned}\right)y^2 + \\
&\left(\begin{aligned}
&\hbar_\theta\frac{33Gr}{40} + \hbar_\theta^2\frac{33Gr}{80} + \hbar_\theta^2\frac{11Gr\bar{M}^2}{160} + \hbar_\theta^2\frac{33\Omega Gr}{80} - \hbar_u\hbar_\theta\frac{99Gr}{1580} - \hbar_u\hbar_\theta\frac{11GrQ}{160} + \hbar_\theta\frac{2S_1}{3} + \\
&\hbar_\theta^2\frac{5S_1}{6} + \hbar_\theta^3\frac{5Q}{1536} + \hbar_\theta^3\frac{161EcQ}{720}
\end{aligned}\right)y^3 + \\
&\left(\begin{aligned}
&\hbar_u\hbar_\theta\frac{33Gr}{2560} - \hbar_\theta\frac{\bar{M}^2}{6} - \hbar_\theta^2\frac{5\bar{M}^2}{24} - \hbar_\theta^2\frac{33Gr\bar{M}^2}{320} - \hbar_\theta^2\frac{\bar{M}^4}{24} + \hbar_u\hbar_\theta\frac{33GrQ}{320} - \hbar_\theta^2\frac{33GrS_1}{320} - \\
&\hbar_u\hbar_\theta\frac{231GrS_1}{320} + \hbar_\theta^2\frac{S_1^{\,2}}{12}
\end{aligned}\right)y^4 + \\
&\left(\hbar_u\hbar_\theta\frac{231GrS}{320} - \hbar_\theta^2\frac{33Gr\bar{M}^2}{1600} + \hbar_u\hbar_\theta\frac{33GrQ}{1600} - \hbar_\theta^2\frac{7EcQ^2}{90} + \hbar_\theta^2\frac{5Q\bar{M}^2}{24} + \hbar_\theta^3\frac{QS_1^{\,2}}{480}\right)y^5 + \\
&\left(\hbar_\theta^3\frac{49Ec}{5760} - \hbar_u\hbar_\theta\frac{14Ec\bar{M}^2}{45} + \hbar_\theta^2\frac{7EcQ}{90} + \hbar_\theta^3\frac{49EcQ}{720} + \hbar_\theta^3\frac{Q^2}{2880} + \hbar_\theta^3\frac{343EcS_1}{7200}\right)y^6 \\
&\hbar_\theta^3\frac{EcQ}{48}y^7 + \hbar_\theta^3\frac{Ec^2}{24}y^8.
\end{aligned}\right\}. \tag{3.21}
$$

3.3 Discussion of results

3.3.1 Inspection of convergence

The equation (3.19) contain convergence control parameters $\hbar_u$ and $\hbar_\theta$. The optimal values of these parameters are chosen with the help of $\hbar$–curves, which are showing in figures 3.2 and 3.3 at 20th–order approximations. The best range of $\hbar_u$ and $\hbar_\theta$ are $-1.3 \le \hbar_u \le -0.4$ and $-1.3 \le \hbar_\theta \le -0.3$ respectively.

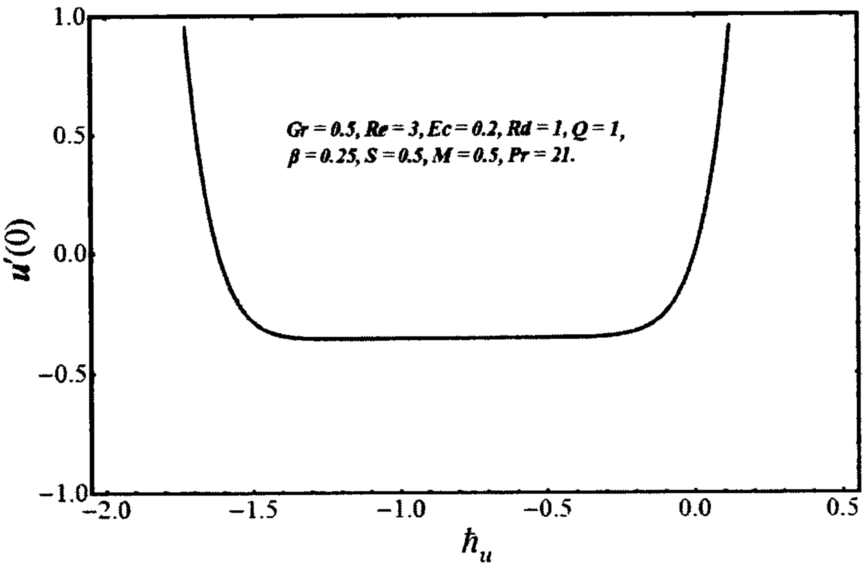

Figure 3.2: $\hbar_u$ – curve for velocity.

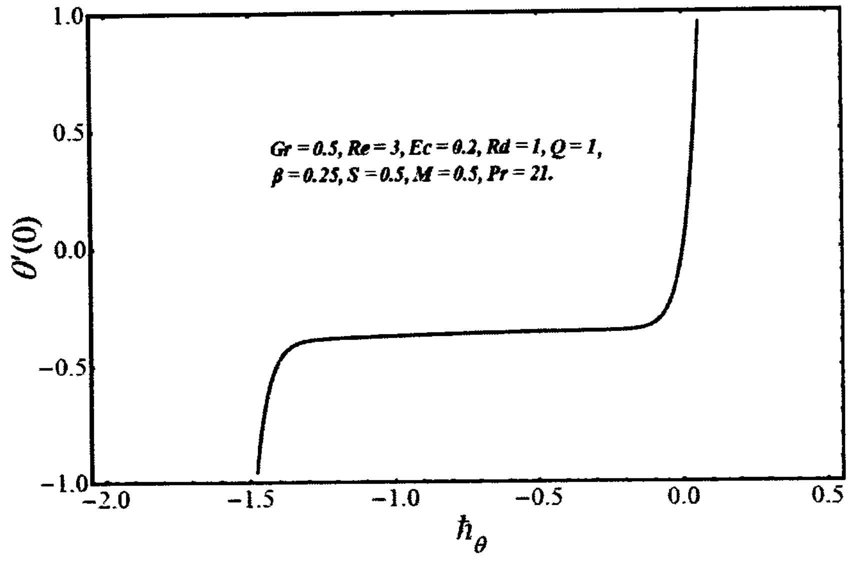

Figure 3.3: $\hbar_\theta$ – curve for temperature.

3.3.2 Residual error of norm 2

The best optimum values of $\hbar_u$ and $\hbar_\theta$ with help of residual errors were computed up to 20th –order approximation over an embedding parameter $\xi \in [0,\ 1]$ of velocity E_u and temperature E_θ by the succeeding formulas

$$E_u = \sqrt{\frac{1}{21}\sum_{i=0}^{20}\left(u(i/20)\right)^2},\ E_\theta = \sqrt{\frac{1}{21}\sum_{i=0}^{20}\left(\theta(i/20)\right)^2}. \tag{3.22}$$

The above residual formulas give the minimum error for velocity at $\hbar_u = -0.2$ and for temperature $\hbar_\theta = -0.3$, that are presented in figures 3.4 and 3.5. Table 3.1 gives an error for convergence of series solution up to the 20th–order approximation.

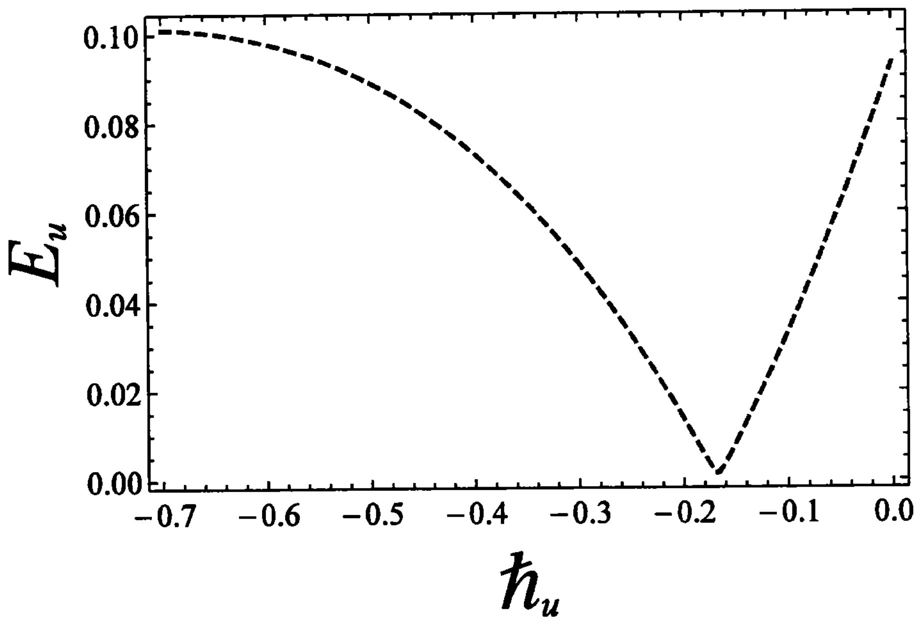

Figure 3.4: Residual error E_u −curve for velocity profile.

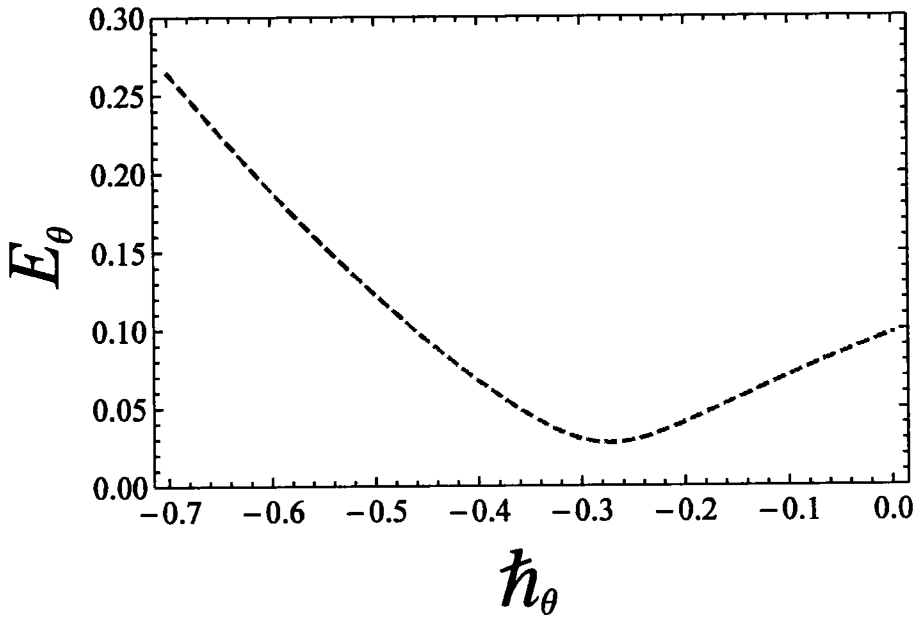

Figure 3.5: Residual error E_θ −curve for temperature profile.

Table 3.1. Residual error of analytic solutions when $Rd=1$, $Q=1$, $Gr=3$, $Ec=0.1$, $\varepsilon=0.25$, $S_1=0.5$, $\bar{M}=2$, $\Pr=21$ and $\varphi=1\%$.

Order of approximation	Time	E_u	E_θ
02	1.07793	9.2399×10^{-3}	1.1628×10^{-2}
06	3.4508	1.0496×10^{-4}	3.2529×10^{-4}
10	8.3315	1.8962×10^{-6}	1.8837×10^{-5}
14	15.3252	7.3379×10^{-8}	$1..37785\times10^{-6}$
20	30.8517	8.3321×10^{-10}	1.1296×10^{-8}

3.3.3 Illustration of graphical results

The study of thermal conductivity with temperature variation and magnetic field with inclination angle on steady plane Poiseuille flow with different flat walls temperature and suction/injection have been studied analytically and demonstrated for flow and heat distribution. The significances are elaborated through graphically in figures 3.6 to 3.13 for controlling parameters like suction parameter (S_1), variable thermal conductivity parameter (ε), Grashof number (Gr), Eckert number (Ec), thermal radiation (Rd), heat source/sink parameter (Q) and inclination angle (γ) in magnetic parameter ($\bar{M}$). Suction/injection (S_1) effects for different values on flow field is discussed in figure 3.6. The influence of magnetic parameter M under various inclination angle on the velocity w.r.t y shown in figure 3.7. Decreases results obtained for large inclination angle γ, velocity attains its maximum retardation when inclination is perpendicular between magnetic field and flow. In figure 3.8 effect of nanoparticles φ displayed. It is investigated that an increase in the fraction of particles velocity decreases. Manifestation of S_1 on temperature is exposed in figure 3.9. Effect of magnetic parameter M for different inclination angle on temperature against y portray in figure 3.10. It speculated that temperature rapidly increased when the inclination angle γ increased. Figure 3.11 respond to Rd at temperature, it investigated that for large Rd temperature is realized to be increased. Manifestation of Q at temperature is presented in figure 3.12. Here conclude from figure, when ($Q<0$) then heat reduces and when ($Q>0$) then heat enhance in the system. It is due generation in energy for system. Variation in thermal conductivity ε is given in figure 3.13.

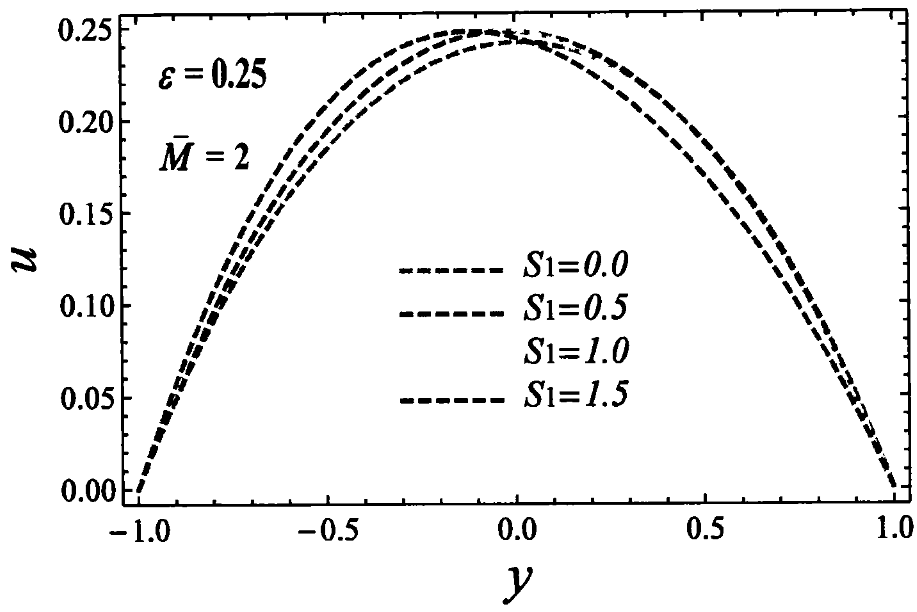

Figure 3.6: Influence of S_1 on u .

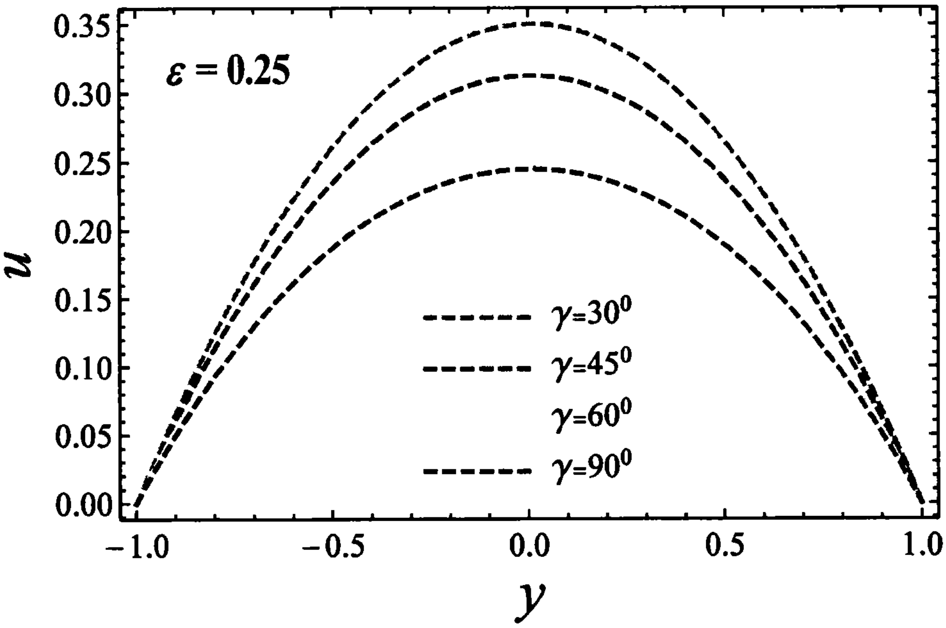

Figure 3.7: Influence of γ on u .

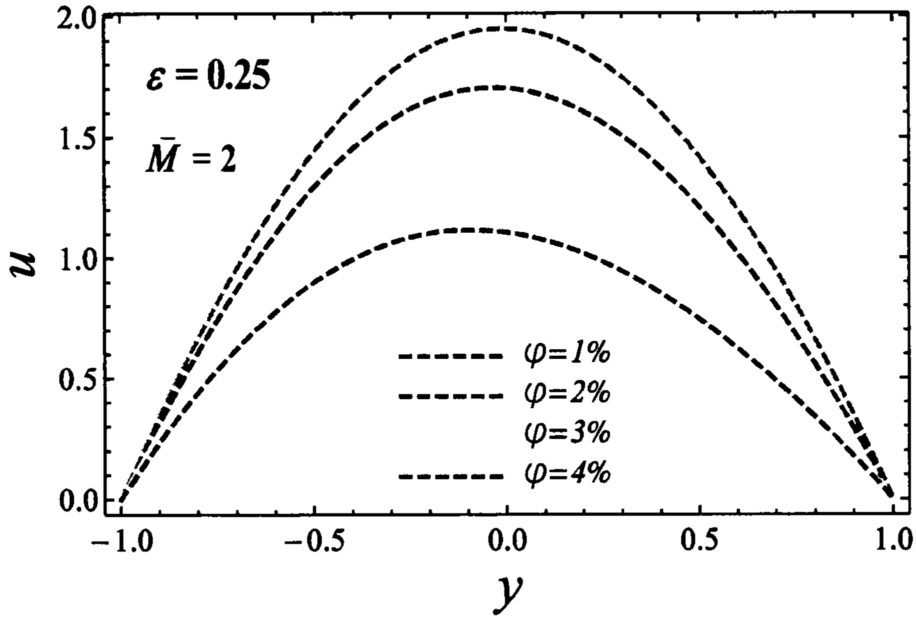

Figure 3.8: Influence of φ on u .

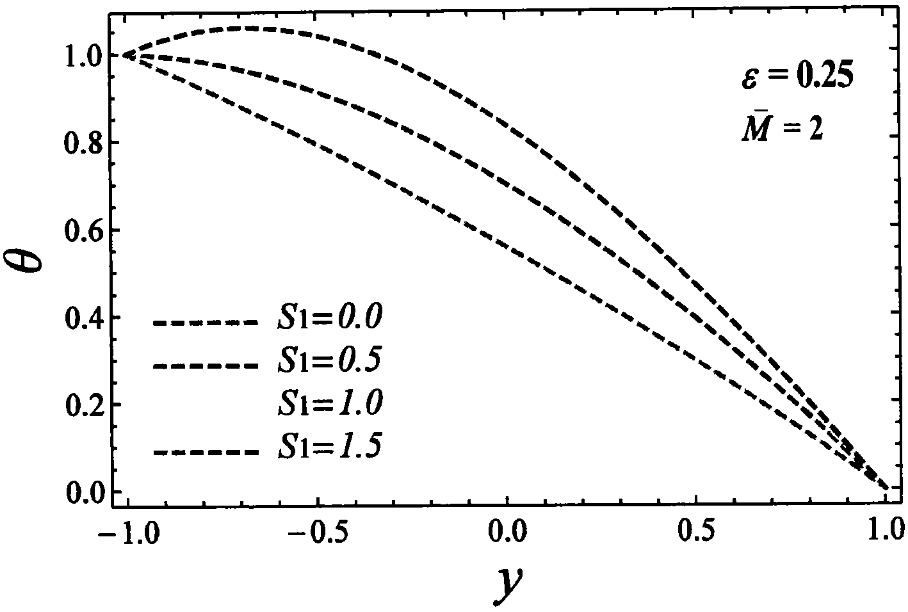

Figure 3.9: Influence of S_1 on θ.

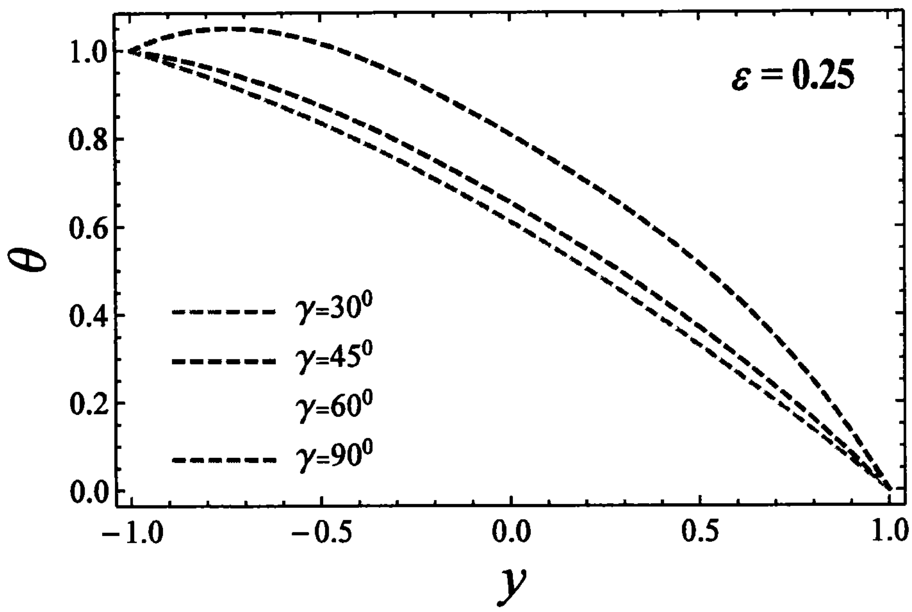

Figure 3.10: Influence of γ on θ.

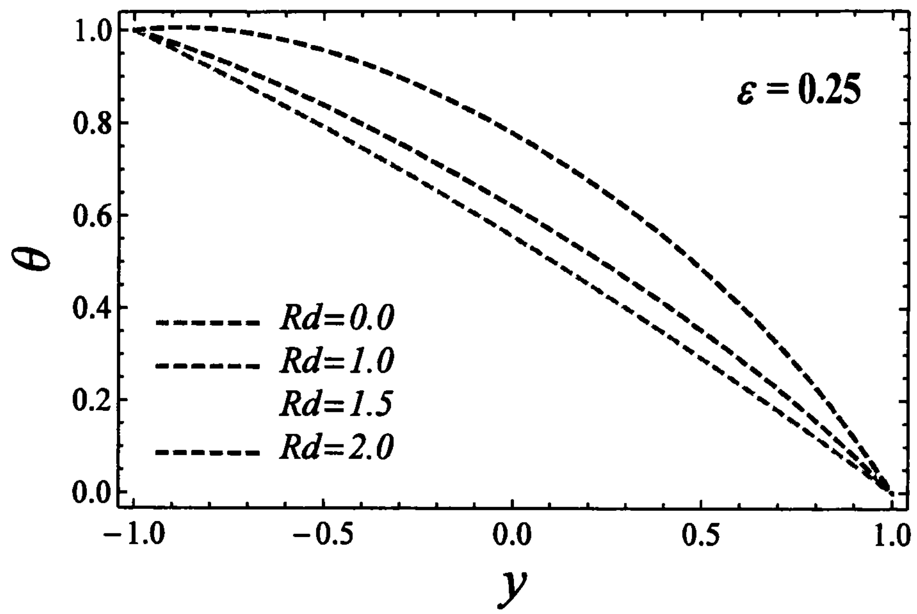

Figure 3.11: Influence of Rd on θ.

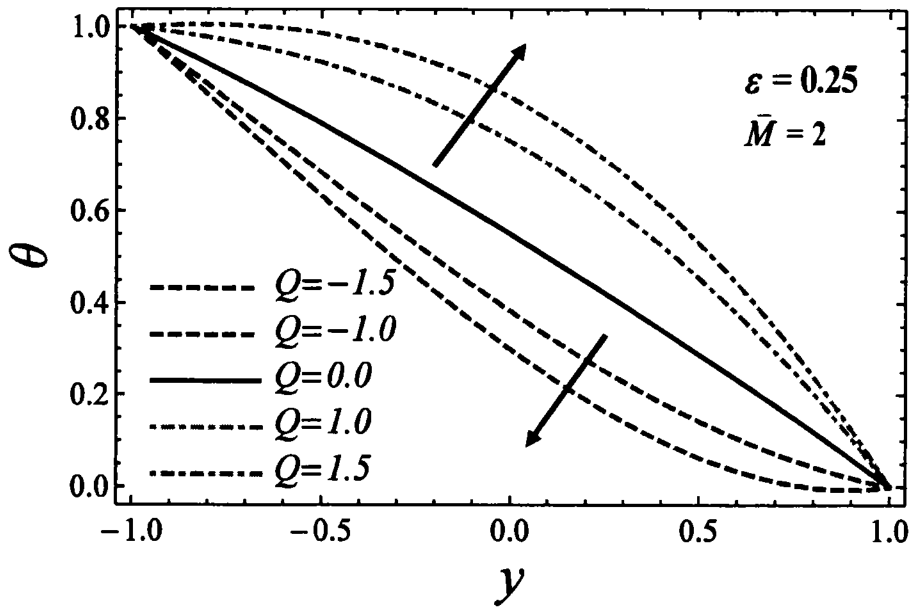

Figure 3.12: Influence of Q on θ.

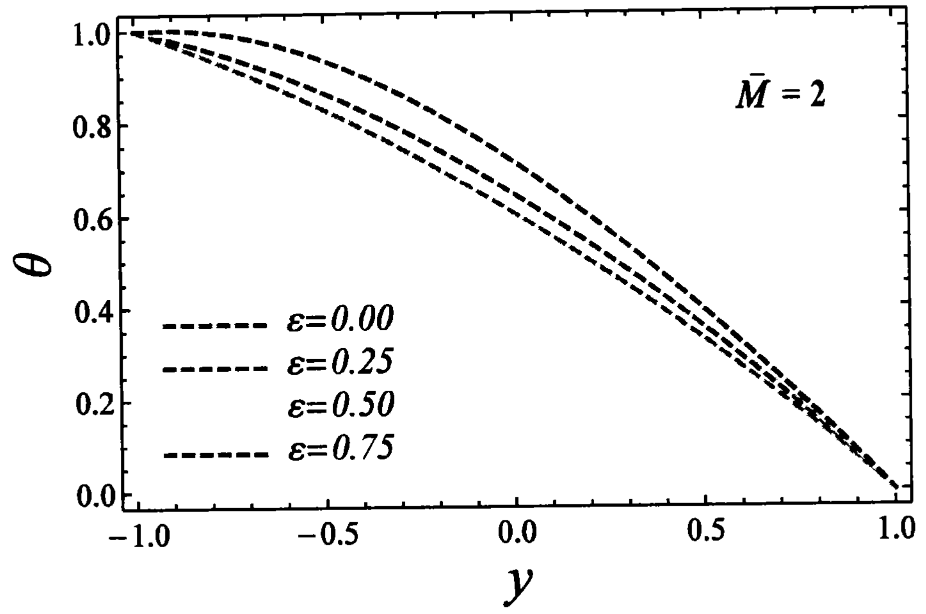

Figure 3.13: Influence of ε on θ.

The physical characteristics of Kerosene oil and Alumina (Al_2O_3) are mention in Table 1.2, whereas influence numerous parameters on C_f (Skin-friction) and Nu (Nusselt number) of Alumina Al_2O_3 nanoparticles suspended in Kerosene-based nanofluid are offered in Tables 3.1 and 3.2. The influence of variable thermal conductivity with particle volume fraction on C_f and Nu are given in Table 3.3. Nusselt number increases but Skin-friction coefficients decreases for increasing amount of particles.

Table 3.1: Effect of *Ec* and *Gr* on C_f and Nu when $Rd=1$, $Q=1$, $\varepsilon=0.25$, $S_1=0.5$, $M=2$, $\Pr=21$ and $\varphi=1\%$.

Ec	Gr	$Nu(-1)$	$Nu(1)$	$C_f(-1)$	$C_f(1)$
0.2	1	−1.6350	0.9293	−0.1790	0.2217
	2	−2.1978	1.3125	−1.0060	1.1490
	3	−2.7384	1.6577	−2.4830	2.7520
0.4	1	−3.5022	2.3119	−0.2792	0.3971
	2	−4.8700	3.3341	−1.2810	1.5240
	3	−6.1973	4.2851	−2.9590	3.3030
0.6	1	−5.7051	4.0740	−0.3469	0.5481
	2	−8.1213	5.9920	−1.5130	1.7540
	3	−10.4822	7.8105	−3.2642	3.6990
0.8	1	−8.2516	6.2257	−0.4631	0.6259
	2	−11.9605	9.2978	−1.6691	2.0260
	3	−15.6034	12.2467	−3.6520	4.1650

Table 3.2: Effect of thermal radiation, heat source/sink on Nusselt number and Skin-friction when $Gr = 3$, $Ec = 0.1$, $\varepsilon = 0.25$, $S_1 = 0.5$, $\bar{M} = 2$, $\Pr = 21$ and $\varphi = 1\%$.

Rd	Q	$Nu(-1)$	$Nu(1)$	$C_f(-1)$	$C_f(1)$
0.2	−1	−0.6641	0.1268	−1.1660	1.2992
	0	−2.0170	2.4370	−2.5361	2.9153
	1	−3.2450	5.1840	−4.2582	4.8231
0.4	−1	−1.0802	0.4182	−0.8476	1.0340
	0	−2.4120	2.7702	−2.1720	2.5171
	1	−3.6420	5.6010	−3.7363	4.3722
0.6	−1	−1.4340	0.7721	−0.5562	0.6627
	0	−2.7661	3.1240	−1.7750	2.1243
	1	−3.9110	5.9750	−3.2852	3.8420
0.8	−1	−1.7670	1.0631	−0.2117	1.2990
	0	−3.0991	3.5402	−1.4041	1.7231
	1	−4.2650	6.3710	−2.8082	3.3920

Table 3.3: Variation of Nusselt number, Skin- friction for nanoparticle volume fraction and variable thermal conductivity when $Gr = 3$, $Ec = 0.1$, $Rd = 1$, $Q = 1$, $S_1 = 0.5$, $\bar{M} = 2$ and $\Pr = 21$.

φ	ε	$Nu(-1)$	$Nu(1)$	$C_f(-1)$	$C_f(1)$
1%	0.25	−0.3632	1.1638	−0.5498	0.2614
	0.50	−0.3027	1.2903	−0.5467	0.2558
	0.75	−0.2398	1.3482	−0.5424	0.2498
2%	0.25	−0.3421	1.2414	−0.5829	0.2557
	0.50	−0.2788	1.3409	−0.5792	0.2498
	0.75	−0.2128	1.4307	−0.5750	0.2434
3%	0.25	−0.3204	1.3183	−0.6162	0.2502
	0.50	−0.2545	1.4207	−0.6122	0.2439

3.4 Conclusions

In the current study, kerosene is chosen as base fluid to form a nanofluid in a channel. Poiseuille flow is affected with inclined MHD, besides the thermal conductivity with the changing behavior. Analytic solution is vetted through graphs and some of the key results have been enlisted below:

- Close to heated wall velocity mounts up due to rapid process of suction/injection.
- Increasing suction/injection, increases velocity near to heated wall, while reverse effect near to the cold wall.
- It is detected that velocity of fluid decelerate by larger values of φ and velocity attain its minimum retardation when inclination is perpendicular between magnetic field and flow. Moreover, temperature profile is increased by increasing particle volume fraction, magnetic parameter with inclination and radiation.
- Suction/injection parameter increases temperature profiles near to the heated wall for ($S_1 > 0$), but the decreases near the cold wall for ($S_1 < 0$).
- The result of variable thermal conductivity enhance in temperature at cold wall, whereas reduction occurs at heated wall.
- Tabular results are determined, effects of particles on C_f and Nu. It is concluded that Skin-friction coefficient as compared with Nusselt number decreases for volume fraction of particles increases.
- Temperature of nanofluid inclines close to heated wall for heat source ($Q > 0$) but declines close to the cold wall for heat sink ($Q > 0$).
- C_f and Nu rise when Grashof number, Source/sink, suction/injection, Eckert number, thermal radiation and magnetic parameter with inclination are enlarged at right wall ($y = 1$), while they have opposite effect on the C_f and Nu at left wall ($y = -1$).

Chapter 4

4 Analysis of activation energy in Couette-Poiseuille flow of nanofluid in the presence of chemical reaction and convective boundary conditions

In the given chapter an MHD nanofluid is examined analytically. The role of constant pressure and radiation on the flow through a channel are also considered. Activation energy further increases thermal profile of nanofluid. For the mass flus density Buongiorno model is used. The governing flow problem is solved subject to convective boundary conditions by HAM which involved higher derivatives of mutually related nonlinear ODEs. The tabulated results are found in full agreement by performing parametric study in which the contribution of very significant dimensionless variables are demonstrated through graphs. And, it is established that concentration of particle rises with chemical reaction rate while Brownian and thermophoresis parameters reduce concentration.

4.1 Problem formulation

4.1.1 Flow analysis

In this chapter, consider steady fully developed laminar, Couette-Poiseuille flow of incompressible nanofluid is flowing in horizontal channel. The geometry of the channel consists of two parallel infinite walls as demonstrate in figure 4.1. Right wall is moving with constant velocity U^*, whereas left wall is stationary. In the geometry of the problem, the middle of the channel is taken at origin with position of left and right walls at $\bar{y}=-a$ and $\bar{y}=a$, respectively.

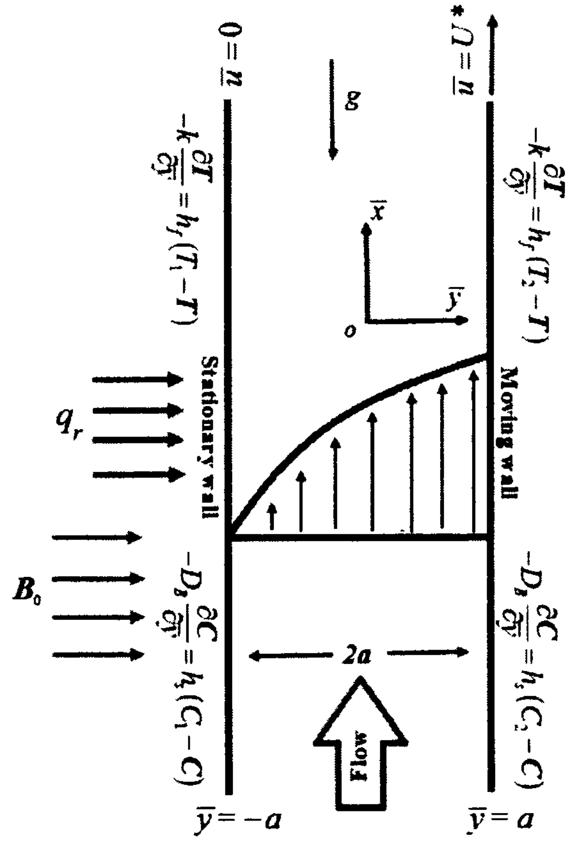

Figure 4.1: Sketch of flow model.

Convective boundary conditions are subject to left as well as right walls of model. Fluid is taken electrically conducted with applied magnetic field B_0 in the $\bar{y}$ -direction. The physical properties of nanofluid in this problem are supposed constant.

4.1.2 Governing equations (Buongiorno's model)

According to the Buongiorno's model, the equations (1.18), (1.19), (1.37) and (1.38) given in the chapter 1, for a steady state, incompressible nanofluid under the influence of magnetic, buoyancy, radiative heat flux, chemical reaction with activation energy, viscous and Ohmic dissipation transporting through a channel are mathematically modeled with the application of boundary layer and Boussinesq's approximation as

$$\frac{\partial \bar{p}}{\partial \bar{x}} = \mu_f\left(\frac{\partial^2 \bar{u}}{\partial \bar{y}^2}\right) - \sigma B_0^2 \bar{u} + \left[(1-C^*)\rho_f \beta g (T-T^*) - (\rho_p - \rho_f) g (C-C^*)\right], \quad (4.1)$$

$$(\rho c_p)_f \left(\bar{u}\frac{\partial T}{\partial \bar{x}}\right) = k_f\left(\frac{\partial^2 T}{\partial \bar{y}^2}\right) + (\rho c_p)_p \left[D_B\left(\frac{\partial C}{\partial \bar{y}}\frac{\partial T}{\partial \bar{y}}\right) + \frac{D_T}{T^*}\left(\frac{\partial T}{\partial \bar{y}}\right)^2\right] - \frac{\partial q_r}{\partial \bar{y}} + \mu_f\left(\frac{\partial \bar{u}}{\partial \bar{y}}\right)^2 + \sigma_f B_0^2 \bar{u}^2 \quad (4.2)$$

and

$$-D_B\left(\frac{\partial^2 C}{\partial \bar{y}^2}\right) = \frac{D_T}{T^*}\left(\frac{\partial^2 T}{\partial \bar{y}^2}\right) - K_r^2\left(\frac{T}{T^*}\right)^{n_1}(C-C^*)\exp\left(\frac{-E_a}{\kappa T}\right). \quad (4.3)$$

The appropriate Couette-Poiseuille and convective boundary conditions

$$\left.\begin{array}{l} \bar{u} = U^*,\ \bar{v} = 0,\ -k\dfrac{\partial T}{\partial \bar{y}} = h_f(T_2 - T),\ -D_B\dfrac{\partial C}{\partial \bar{y}} = h_s(C_2 - C)\ \text{at}\ \bar{y} = a \\ \bar{u} = 0,\ \bar{v} = 0,\ -k\dfrac{\partial T}{\partial \bar{y}} = h_f(T_1 - T),\ -D_B\dfrac{\partial C}{\partial \bar{y}} = h_s(C_1 - C)\ \text{at}\ \bar{y} = -a \end{array}\right\}. \quad (4.4)$$

Let us acquaint the following nondimensional quantities

$$\left.\begin{array}{l} x = \dfrac{\bar{x}}{a},\ u = \dfrac{\bar{u}}{U_m},\ y = \dfrac{\bar{y}}{a},\ v = \dfrac{\bar{v}}{U_m},\ p = \dfrac{a^2 \bar{p}}{\mu_f U_m}, U = \dfrac{U^*}{U_m}, \\ \theta = \dfrac{T - T^*}{T_1 - T^*},\ m^* = \dfrac{T_2 - T^*}{T_1 - T^*}, \phi = \dfrac{C - C^*}{C_1 - C^*}, n^* = \dfrac{C_2 - C^*}{C_1 - C^*} \end{array}\right\}. \quad (4.5)$$

Incorporating the equation (4.5) with radiative heat flux defined in equation (2.10), the governing equations (4.1) to (4.3) become

$$\frac{\partial^2 u}{\partial y^2} - M^2 u + \frac{Ra}{\operatorname{Re}\Pr}(\theta - Nr\phi) - P = 0, \quad (4.6)$$

$$(1+Rd)\frac{\partial^2 \theta}{\partial y^2} + Nb\frac{\partial \theta}{\partial y}\frac{\partial \phi}{\partial y} + Nt\left(\frac{\partial \theta}{\partial y}\right)^2 + Br\left(\frac{\partial u}{\partial y}\right)^2 + M^2 Br u^2 - \gamma_1 u = 0, \quad (4.7)$$

$$\frac{\partial^2 \phi}{\partial y^2} + \frac{Nt}{Nb}\left(\frac{\partial^2 \theta}{\partial y^2}\right) - S_c \operatorname{Re} Cr (1+\Omega\theta)^{n_1} \phi \exp\left(-\frac{E}{(1+\Omega\theta)}\right) = 0. \quad (4.8)$$

The corresponding dimensionless boundary conditions

$$\left.\begin{array}{l} u=U, v=0, \theta'(y)=-Bi(n^*-\theta(y)), \phi'(y)=-Nj(m^*-\phi(y)) \text{ at } y=1 \\ u=0,\ v=0,\ \theta'(y)=-Bi(1-\theta(y)),\ \phi'(y)=-Nj(1-\phi(y)) \text{ at } y=-1 \end{array}\right\}, \tag{4.9}$$

where

$$\left.\begin{array}{l} Ra=\dfrac{(1-C^*)(T_1-T^*)\beta g a^3}{\nu\alpha}, M^2=\dfrac{\sigma B_0^2 a^2}{\mu}, \mathrm{Re}=\dfrac{aU_m}{\nu_f}, \nu_f=\dfrac{\mu_f}{\rho_f}, \mathrm{Pr}=\dfrac{\nu_f}{\alpha_f}, Cr=\dfrac{K_r^2 a}{U_m}, \\ Br=\dfrac{\mu_f U_m^2}{k_f(T_1-T^*)}, Nb=\dfrac{\tau D_B(C_1-C^*)}{\alpha_f}, Nr=\dfrac{(\rho_p-\rho_f)(C_1-C^*)}{\rho_f\beta(T_1-T^*)(1-C^*)}, Rd=\dfrac{16\sigma^* T_1^3}{3k^* k_f}, \\ S_c=\dfrac{\nu_f}{D_B}, \Omega=\dfrac{T_1-T^*}{T^*}, E=\dfrac{E_a}{\kappa T^*}, Nt=\dfrac{\tau D_T(T_1-T^*)}{T^*\alpha_f}, \gamma_1=\dfrac{U_m a^2}{\alpha_f(T_1-T^*)}\dfrac{\partial T}{\partial x}=\text{constant}, \\ Bi=\dfrac{h_f a}{k_f}, Nj=\dfrac{h_s a}{D_B}, \tau=\dfrac{(\rho C_p)_p}{(\rho C_p)_f} \end{array}\right\}. \tag{4.10}$$

The formulations of coefficient of skin friction defined in equation (1.54), Nusselt number defined in equation (1.56) and Sherwood number defined in equation (1.58) are transformed in view of equation (4.5) as

$$\left.\begin{array}{l} \mathrm{Re}\,C_f=2u'(y)\ \big|_{y=-1,1} \\ Nu=-\theta'(y)\big|_{y=-1,1} \\ Sh=-\phi'(y)\big|_{y=-1,1} \end{array}\right\}. \tag{4.11}$$

4.2 Solution of the problem

For series solution, here we employed HAM technique for solving equations (4.6) to (4.8).

Zeroth–order solution

In the procedure of analytic solution, first we define initial guesses $(u_0,\ \theta_0,\ \phi_0)$ which satisfy the linear operators $(£_u,\ £_\theta,\ £_\phi)$ and associated boundaries

$$\left. u_0(y)=\frac{U(1+y)}{2},\ \theta_0(y)=\frac{-1+Bi(1-y)}{2Bi},\ \phi_0(y)=\frac{-1+Nj(1-y)}{2Nj}\right\} \tag{4.12}$$

and

$$£_u = \frac{d}{dy}\left(\frac{du}{dy}\right),\quad £_\theta = \frac{d}{dy}\left(\frac{d\theta}{dy}\right),\quad £_\phi = \frac{d}{dy}\left(\frac{d\phi}{dy}\right). \tag{4.13}$$

The convergence control parameters and nonlinear operators with embedding parameter $\xi \in [0,\ 1]$ are $\hbar_u$, $\hbar_\theta$, $\hbar_\phi$ and N_u, N_θ, N_ϕ for velocity, temperature, nanoparticle volume fraction respectively. Therefore, the zeroth-order deformations are

$$\left.\begin{aligned}(1-\xi)£_u\left[u(y,\xi)-u_0(y)\right] &= \xi\hbar_u N_u\left[u(y,\xi),\theta(y,\xi),\phi(y,\xi)\right]\\ (1-\xi)£_\theta\left[\theta(y,\xi)-\theta_0(y)\right] &= \xi\hbar_\theta N_\theta\left[u(y,\xi),\theta(y,\xi),\phi(y,\xi)\right]\\ (1-\xi)£_\phi\left[\phi(y,\xi)-\phi_0(y)\right] &= \xi\hbar_\phi N_\phi\left[u(y,\xi),\theta(y,\xi),\phi(y,\xi)\right]\end{aligned}\right\} \tag{4.14}$$

with corresponding boundary conditions

$$\left.\begin{aligned}&u=U, v=0, \theta'(y)=-Bi\left(n^*-\theta(y)\right), \phi'(y)=-Nj\left(m^*-\phi(y)\right) \text{ at } y=1\\ &u=0,\ v=0,\ \theta'(y)=-Bi\left(1-\theta(y)\right),\ \phi'(y)=-Nj\left(1-\phi(y)\right) \text{ at } y=-1\end{aligned}\right\}, \tag{4.15}$$

here

$$\left.\begin{aligned}N_u &= \frac{\partial^2 u(y,\xi)}{\partial y^2} - M^2 u(y,\xi) + \frac{Ra}{\operatorname{Re}\Pr}\left(\theta(y,\xi) - Nr\phi(y,\xi)\right) - P,\\ N_\theta &= (1+R_d)\frac{\partial^2\theta(y,\xi)}{\partial y^2} + Nb\frac{\partial\theta(y,\xi)}{\partial y}\frac{\partial\phi(y,\xi)}{\partial y} + Nt\left(\frac{\partial\theta(y,\xi)}{\partial y}\right)^2\\ &\quad + Br\left(\frac{\partial u(y,\xi)}{\partial y}\right)^2 + M^2 Br\left(u(y,\xi)\right)^2 - \gamma_1 u(y,\xi),\\ N_\phi &= \frac{\partial^2\phi(y,\xi)}{\partial y^2} - S_c \operatorname{Re} Cr\left(1+\Omega\theta(y,\xi)\right)^{n_1}\exp\left(-\frac{E}{\left(1+\Omega\theta(y,\xi)\right)}\right)\phi(y,\xi)\\ &\quad + \frac{Nt}{Nb}\frac{\partial^2\theta(y,\xi)}{\partial y^2}.\end{aligned}\right\}. \tag{4.16}$$

l th–order solution

The l th-order deformation expression for $u_l(y)$, $\theta_l(y)$ and $\phi_l(y)$ are

$$\left.\begin{aligned}&\pounds_u\left[u_l(y)-\chi_l u_{l-1}(y)\right]=\hbar_u R_l^u(y)\\&\pounds_\theta\left[\theta_l(y)-\chi_l\theta_{l-1}(y)\right]=\hbar_\theta R_l^\theta(y)\\&\pounds_\phi\left[\phi_l(y)-\chi_l\phi_{l-1}(y)\right]=\hbar_\phi R_l^\phi(y)\end{aligned}\right\} \tag{4.17}$$

with

$$\left.\begin{aligned}&u_l(y,\xi)=U,\theta_l'(y,\xi)=-Bi\left(n^*-\theta_l(y,\xi)\right),\phi_l'(y,\xi)=-Nj\left(m^*-\phi_l(y,\xi)\right)\text{ at } y=1\\&u_l(y,\xi)=0,\ \theta_l'(y,\xi)=-Bi\left(1-\theta_l(y,\xi)\right),\ \phi_l'(y,\xi)=-Nj\left(1-\phi_l(y,\xi)\right)\text{ at } y=-1\end{aligned}\right\} \tag{4.18}$$

and

$$\left.\begin{aligned}&R_l^u(y)=u_l''-M^2u_l+\frac{Ra}{RePr}(\theta_l-N_r\phi_l)-P\\&R_l^\theta(y)=(1+Rd)\theta_l''+Nb\sum_{k=0}^{l}\phi_k'\theta_{l-k}'+Nt\sum_{k=0}^{l}\theta_k'\theta_{l-k}'+Br\sum_{k=0}^{l}u_k'u_{l-k}'+\\&\qquad M^2Br\sum_{k=0}^{l}u_ku_{l-k}-\gamma_1u_l\\&R_l^\phi(y)=\phi_l''-S_c\,\mathrm{Re}\,Cr\sum_{k=0}^{l}(1+\Omega\theta_k)^{n_1}\exp\left(-\frac{E}{(1+\delta_D\theta_k)}\right)\phi_{l-k}+\frac{Nt}{Nb}\theta_l''\end{aligned}\right\}. \tag{4.19}$$

The solution can be described as of l th–order

$$\left.\begin{aligned}&u(y)=u_0(y)+\sum_{k=1}^{l}u_k(y)\\&\theta(y)=\theta_0(y)+\sum_{k=1}^{l}\theta_k(y)\\&\phi(y)=\phi_0(y)+\sum_{k=1}^{l}\phi_k(y)\end{aligned}\right\}. \tag{4.20}$$

The analytical solution for velocity, temperature and concentration at second order approximations are attained as below

$$u(y)=\frac{1}{2}+\frac{y}{2}+\hbar_u^2\left(\frac{254}{153}+\frac{2519y}{4590}-\frac{127y^2}{68}-\frac{1145y^3}{1836}+\frac{127y^4}{612}+\frac{229y^5}{3060}\right)+$$

$$\hbar_u\left(\begin{array}{l}\frac{127}{102}+\frac{229y}{306}-\frac{127y^2}{102}-\frac{229y^3}{306}+\\ \hbar_\theta\left(-\frac{6685}{3672}-\frac{155y}{612}+\frac{275y^2}{153}+\frac{25y^3}{102}+\frac{25y^4}{1224}+\frac{5y^5}{612}+\frac{5y^6}{1836}\right)+\\ \hbar_\phi\left(-\frac{13445}{19584}-\frac{12865y}{137088}+\frac{4405y^2}{6528}+\frac{1765y^3}{19584}+\frac{25y^4}{2176}+\frac{25y^5}{6528}+\frac{5y^6}{19584}+\frac{5y^7}{45696}\right)\end{array}\right), \tag{4.21}$$

$$\theta(y)=-\frac{1}{2}-\frac{y}{2}+\hbar_\theta^2\left(\frac{1237}{480}+\frac{23y}{40}-\frac{y^2}{16}+\frac{13y^3}{48}+\frac{13y^4}{96}-\frac{y^5}{80}\right)+$$

$$\hbar_\theta\left(\begin{array}{l}\frac{22}{3}+3y+\frac{y^2}{2}+\frac{y^3}{3}+\frac{y^4}{6}+\\ \hbar_u\left(\frac{127231}{36720}+\frac{34681y}{18360}+\frac{991y^2}{1224}+\frac{305y^3}{918}-\frac{533y^4}{7344}-\frac{991y^5}{6120}-\frac{229y^6}{4590}\right)+\\ \hbar_\phi\left(\frac{3079}{2560}+\frac{769y}{1280}+\frac{353y^2}{2560}+\frac{3y^3}{128}+\frac{5y^4}{512}+\frac{y^5}{1280}-\frac{y^6}{2560}\right)\end{array}\right), \tag{4.22}$$

$$\phi(y)=-\frac{1}{2}-\frac{y}{2}+\hbar_\phi^2\left(\begin{array}{l}\frac{1381}{100}-\frac{6057y}{1000}-\frac{8649y^2}{5120}-\frac{2981y^3}{5120}+\frac{45y^4}{2048}+\frac{549y^5}{51200}-\\ \frac{21y^6}{5120}+\frac{7y^7}{5120}+\frac{33y^8}{143360}-\frac{y^9}{20480}\end{array}\right)+$$

$$\hbar_\phi\left(\begin{array}{l}-\frac{881}{160}-\frac{353y}{160}-\frac{9y^2}{16}-\frac{5y^3}{16}-\frac{y^4}{32}+\frac{3y^5}{160}+\\ \hbar_\theta\left(\frac{14299}{1920}+\frac{3421y}{840}+\frac{3y^2}{2}+\frac{11y^3}{48}-\frac{41y^4}{192}-\frac{3y^5}{40}-\frac{y^6}{240}-\frac{y^7}{336}-\frac{y^8}{896}\right)\end{array}\right). \tag{4.23}$$

4.3 Discussion of results

4.3.1 Inspection of convergence

HAM is a powerful and reliable method to solve highly non-linear problems. Here the equation (4.20) involves the auxiliary parameters $\hbar_u$, $\hbar_\theta$ and $\hbar_\phi$ is a series solution. To choose the appropriate value of $\hbar_u$, $\hbar_\theta$ and $\hbar_\phi$. Figure 4.2 depicts $\hbar$–curves for

20th order approximations. The reliable values of the resulting solutions are lies in the range $-0.75 \le \hbar_u \le 0.2$, $-0.8 \le \hbar_\theta \le -0.1$ and $-0.55 \le \hbar_\phi \le 0.15$. The valid value of $\hbar$ in flat portion of these curves. Moreover, the series solutions are significant in the entire zone of y, when $\hbar_u = \hbar_\theta = \hbar_\phi = -0.4$.

4.3.2 Residual error of norm 2

The optimum values of $\hbar_u$, $\hbar_\theta$ and $\hbar_\phi$ with help of residual errors were computed up to 20th –order approximation over an embedding parameter $\xi \in [0, 1]$ of velocity E_u, temperature E_θ and concentration E_ϕ by the succeeding formulas

$$E_u = \sqrt{\frac{1}{21}\sum_{i=0}^{20}\left(u(i/20)\right)^2},\ E_\theta = \sqrt{\frac{1}{21}\sum_{i=0}^{20}\left(\theta(i/20)\right)^2},\ E_\phi = \sqrt{\frac{1}{21}\sum_{i=0}^{20}\left(\phi(i/20)\right)^2}. \quad (4.24)$$

The above residual formulas give the minimum error for velocity at $\hbar_u = -0.4$, for temperature $\hbar_\theta = -0.7$, and for nanoparticle concentration $\hbar_\phi = -0.18$ which presented in figures 4.3, 4.4 and 4.5 respectively. Table 4.1 shows the error for the convergence series solution up to the 20th-order approximation.

Table 4.1: Residual error of analytic solutions when $m^* = n^* = 0$, $E = 1$, $\Omega = 1$, $Rd = 1$, $Cr = 1$, $M = 2.0$, $Ra = 2$, $\mathrm{Re} = 0.3$, $Br = 1$, $Nt = 0.5$, $Nj = 0.5$, $Nr = 0.5$, $Nb = 0.5$, $n_1 = 0.5$, $Bi = 0.5$ and $\mathrm{Pr} = 7$.

Order of approximation	Time	E_u	E_θ	E_ϕ
02	1.07793	9.2399×10^{-3}	1.1628×10^{-2}	4.8973×10^{-3}
06	3.4508	1.0496×10^{-4}	3.2529×10^{-4}	2.2272×10^{-4}
10	8.3315	1.8962×10^{-6}	1.8837×10^{-5}	1.4287×10^{-5}
14	15.3252	7.3379×10^{-8}	$1..37785\times10^{-6}$	1.0896×10^{-6}
20	30.8517	8.3321×10^{-10}	1.1296×10^{-8}	1.1902×10^{-8}

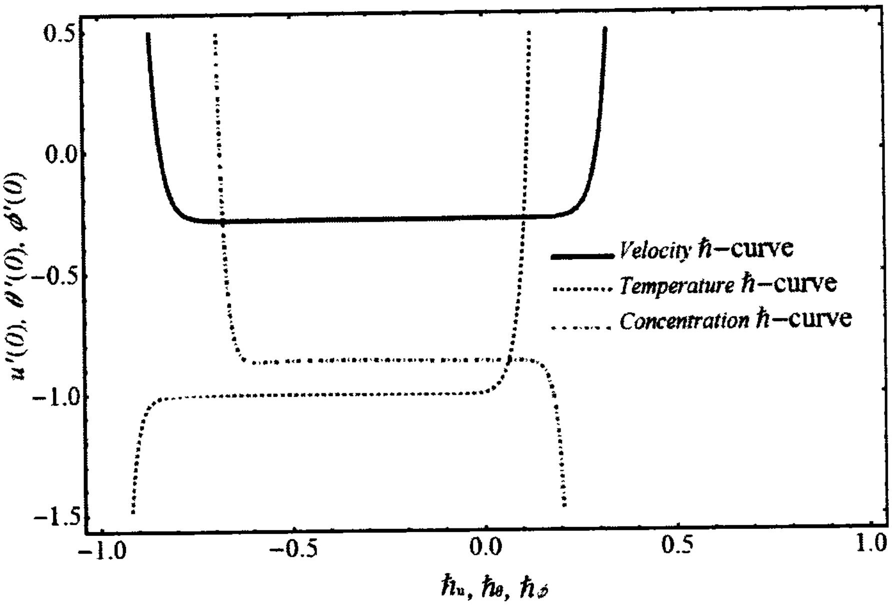

Figure 4.2: $\hbar$ – curves.

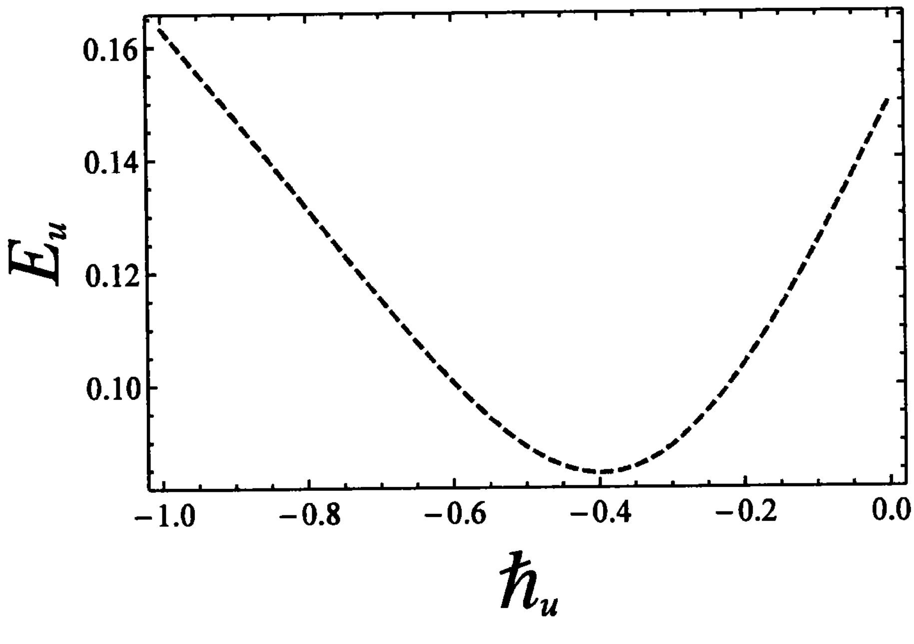

Figure 4.3: Residual error E_u –curve for velocity profile.

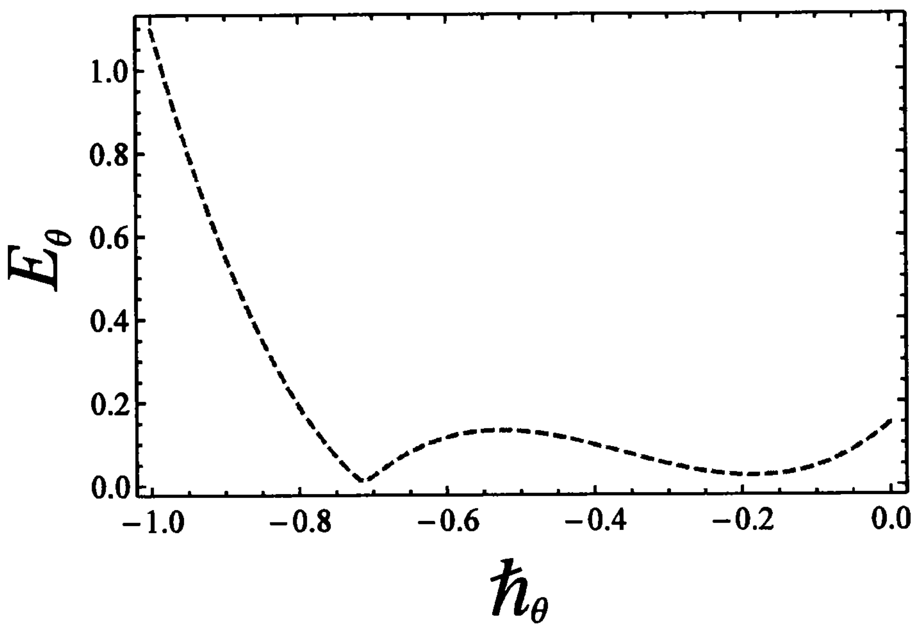

Figure 4.4: Residual error E_θ −curve for temperature profile.

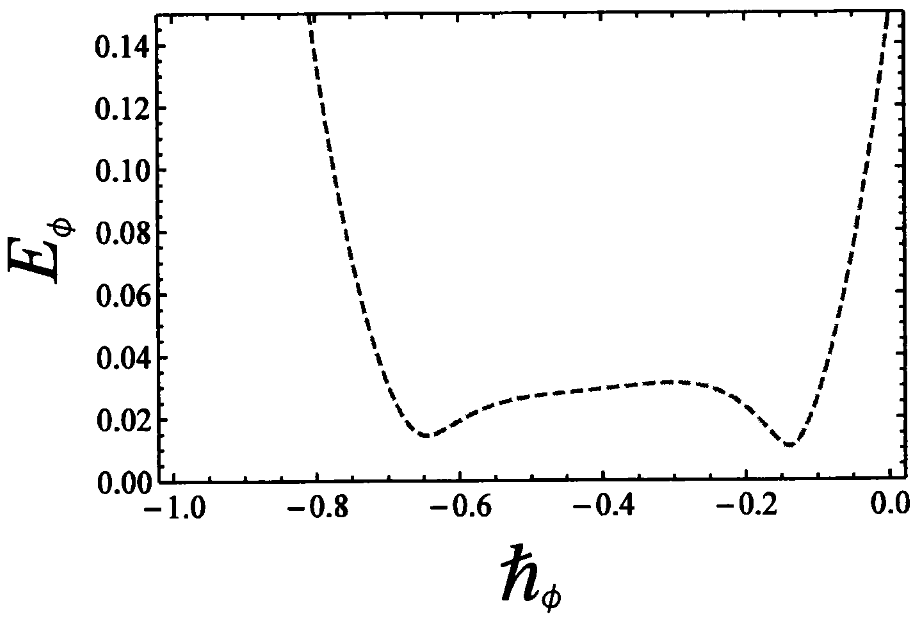

Figure 4.5: Residual error E_ϕ −curve for temperature profile.

In Table 4.2–4.4 represents the numerical results of magnetic field parameter, buoyancy ratio, Rayleigh number, radiation, Prandtl number, Brownian motion, Brinkman number, reaction rate, fitted rate constant, activation energy, thermophoresis parameter, Schmidt number, Biot number and convection-diffusion parameter on skin friction, Nusselt number and Sherwood number respectively. The increasing behavior of Skin friction and Nusselt number are detected for magnetic field parameter, whereas, activation energy is reversely influenced for the contribution of Sherwood number.

Table 4.2: Skin friction coefficient for several of M, Nr, Ra and Pr with $\text{Re}=0.3, Sc=10$ $Rd=Cr=E=\Omega=Br=1$, $n_1=Nt=Nb=Bi=Nj=0.5$ for both walls.

M	Nr	Ra	Pr	$-u'(-1)$	$-u'(1)$
0.0	0.5	2	7	-0.004573	0.004745
2.0				-0.004044	0.004606
4.0				-0.003453	0.004187
6.0				-0.002801	0.003489
	0.5			-0.004044	0.004606
	1.0			-0.004251	0.005911
	1.5			-0.004457	0.007216
	2.0			-0.004664	0.008522
		1		-0.005388	0.006848
		2		-0.004044	0.004606
		3		-0.002700	0.002364
		4		-0.001356	0.000122
			7	-0.004044	0.004606
			8	-0.004380	0.005166
			9	-0.004642	0.005602
			10	-0.004851	0.005951

Table 4.3: Nusselt number for several of M, Nt, Rd, Nb and Br with $\mathrm{Re}=0.3, Sc=10$, $\mathrm{Pr}=7$, $Ra=2$, $Cr=E=\Omega=1$, $n_1 = Nr = Bi = Nj = 0.5$ for both walls.

M	Nt	Rd	Nb	Br	$-\theta'(-1)$	$-\theta'(1)$
0.0	0.5	1	0.5	1	0.492929	0.504004
2.0					0.493246	0.504333
4.0					0.493493	0.504745
6.0					0.493810	0.505321
	0.5				0.493246	0.504333
	1.0				0.494116	0.506943
	1.5				0.494990	0.509565
	2.0				0.495869	0.512199
		1			0.493246	0.504333
		2			0.493262	0.504369
		3			0.493278	0.504406
		4			0.493293	0.504442
			0.5		0.493246	0.504333
			1.0		0.493848	0.506208
			1.5		0.494451	0.508085
			2.0		0.495055	0.509964
				0	0.492212	0.501538
				1	0.493246	0.504333
				5	0.494280	0.507129
				7	0.495314	0.509924

Table 4.4: Sherwood number for several of $\Lambda, E, n_1, \Omega, Sc$ and Rd with $\mathrm{Re}=0.3$, $Sc=10$, $\mathrm{Pr}=7$, $Ra=2$, $Nr=Bi=Nj=0.5$ for both walls.

Cr	E	n_1	δ_D	Sc	Rd	$-\phi'(-1)$	$-\phi'(1)$
0.0	2.0	0.5	1.0	10.0	1.0	-0.744148	2.330771
1.0						-0.870893	2.552822
2.0						-1.007160	2.795660
5.0						-1.153320	3.060250
	0.0					-0.124560	1.082631
	1.0					-0.241022	1.606220
	2.0					-0.870893	2.552820
	3.0					-1.842190	4.057940
		-1.0				-3.411570	6.359712
		0.0				-1.512590	3.509851
		0.5				-0.870893	2.552823
		1.0				-0.397690	1.851932
	1.0		0.0		0.5	0.052703	0.356023
	1.0		1.0			0.409739	0.715164
	1.0		2.0			2.652001	2.867631
	1.0		3.0			9.993070	9.019430
	1.0			1.0		5.312660	2.974801
	1.0			3.0		6.700660	4.696381
	1.0			5.0		8.257800	6.704832
	1.0			10.0		9.993070	9.019430

4.3.3 Illustration of graphical results

In this portion, the transmuted non-linear differential equations which are ODEs from equations (4.6) to (4.8) associated with convective boundary conditions equation (4.9) were analytically tackled using the best tool to obtain such solutions i.e., HAM. The role of significant flow parameters on flow field, temperature distribution and concentration profile are deliberated from figures 4.6 to 4.13. The following discussion and results are gained by using proper values of parameters, $m^* = n^* = 0$, $U = 1$, $n_1 = 0.5$, $E = 1$, $\Omega = 1$, $Sc = 10$, $M = 2.0$, $Ra = 2$, $Cr = 1$, $Rd = 1$, $\gamma_1 = 2$, $Nb = 0.5$, $Nt = 0.5$, $\Pr = 7$, $\text{Re} = 0.3$, $Br = 1$, $Nr = 0.5$, $Bi = 0.5$ and $Nj = 0.5$. Figures 4.6(a)-(b)-(c) illustrate the collective influence of M on velocity, temperature and concentration fields. As $M = 0$ leads hydrodynamic flow and $M \neq 0$ corresponds to hydromagnetic flow phenomena. It observed in figure 4.6(a) that velocity slow down M due to resistance in flow generated by Lorentz forces. It is also noted that temperature distribution is greater for hydromagnetic flow while compared to hydrodynamic flow case. Also Lorentz force caused an enhancement in the temperature distribution as shown in figure 4.6(b). A plot of concentration for M presented in figure 4.6(c). The increasing result occurs for concentration profile by M. The motion of fluid is reduce for Nr, shown in figure 4.7. Figure 4.8 is drawn to depict influence of Rd on temperature distribution. Increasing effect noted on the temperature distribution for Rd. Physically, this enhancement occurs when the radiative heat flux of the nanofluid increase in the channel. Figures 4.9(a)-(b)-(c) correspondingly show velocity, temperature and concentration profiles for diverse values of chemical reaction parameter Cr. The amount of velocity reduces due to the chemical reaction but near the surface it gain the maximum amplitude as compared to surface boundary. Moreover, it can also be seen that nanofluid temperature and concentration field are decelerated on increase of Cr. This behavior represents the weak effect of buoyancy force because of concentration gradient, which causes the reduction effect on concentration profile. The concentration field is a good agreement with outcomes found in case of Rout et al. [96]. Figure 4.10(a)-(c) shows with or without Biot number involvement in velocity figure (a), temperature figure (b) and concentration in figure (c). The velocity profile for with and without convection-diffusion parameter is revealed in figure 4.11(a). From said figure, concludes that when the convection-diffusion parameter is zero then the flow is smooth in the entire geometry, but when the values of convection-diffusion parameter increase then the velocity of nanofluid enhanced. The plots of temperature profile for different values convection-diffusion parameter Nj is exposed in figure 4.11(b). Result shows in said figure give the increasing effects in temperature with the increase of convection-diffusion parameter Nj. The influence of Nj on concentration is given in figure 4.11(c), a strong increase for concentration is accomplished with large values of Nj values. Figure 4.12 elucidates the increasing behavior in concentration profile due to greater values of E which gives large concentration of boundary layer thickness. Physically, higher activation energy and lower temperature lead to a lesser reaction rate, which slows down the chemical reaction. In figure 4.13(a)-(b) expose the results on concentration profile in reply to a variation in Nb and thermophoresis parameter Nt respectively. As for large Brownian motion, thickness of concentration boundary layer decrease, but performance of thermophoresis parameter on nanoparticle concentration gives a reverse pattern to that of Brownian motion parameter.

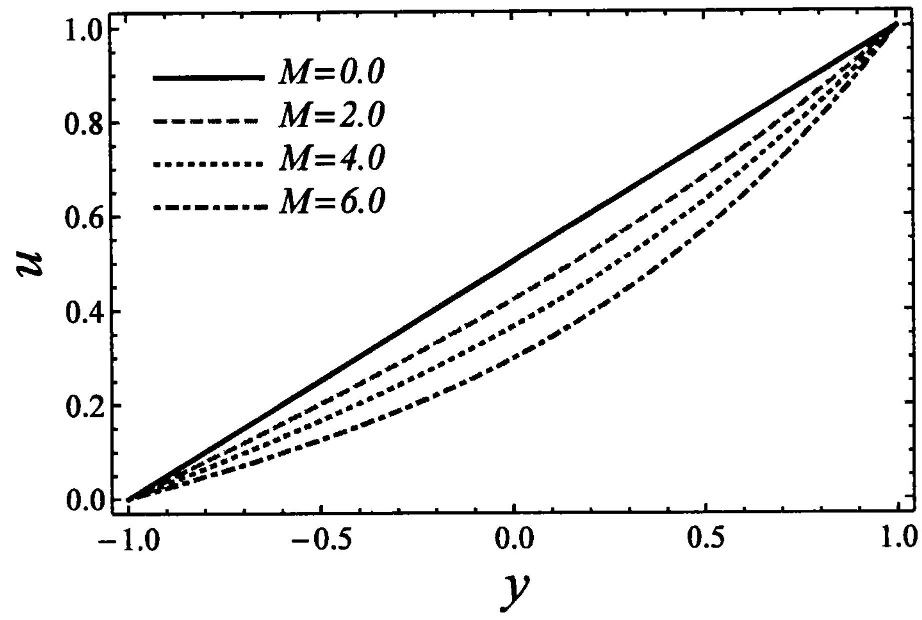

Figure 4.6(a): Appearance of M on velocity.

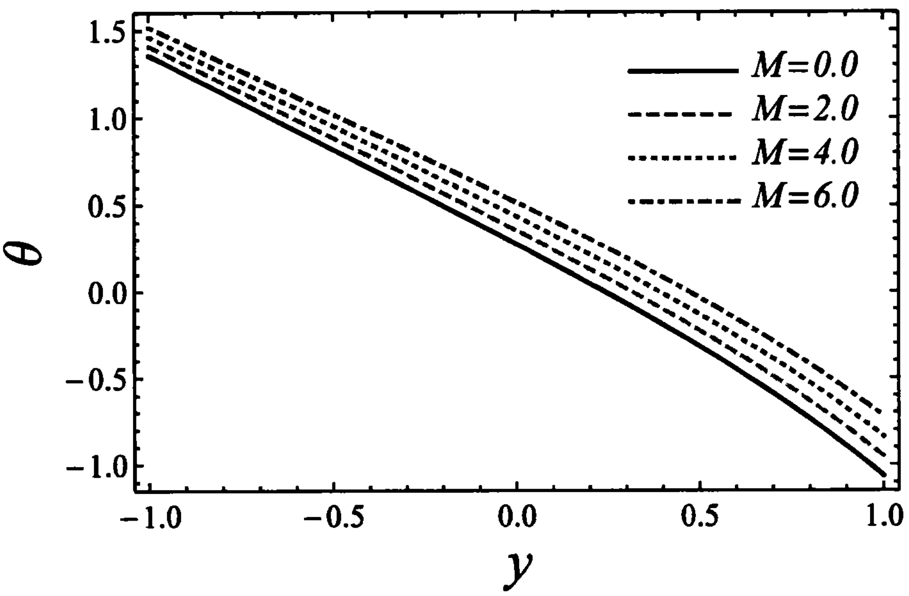

Figure 4.6(b): Appearance of M on temperature.

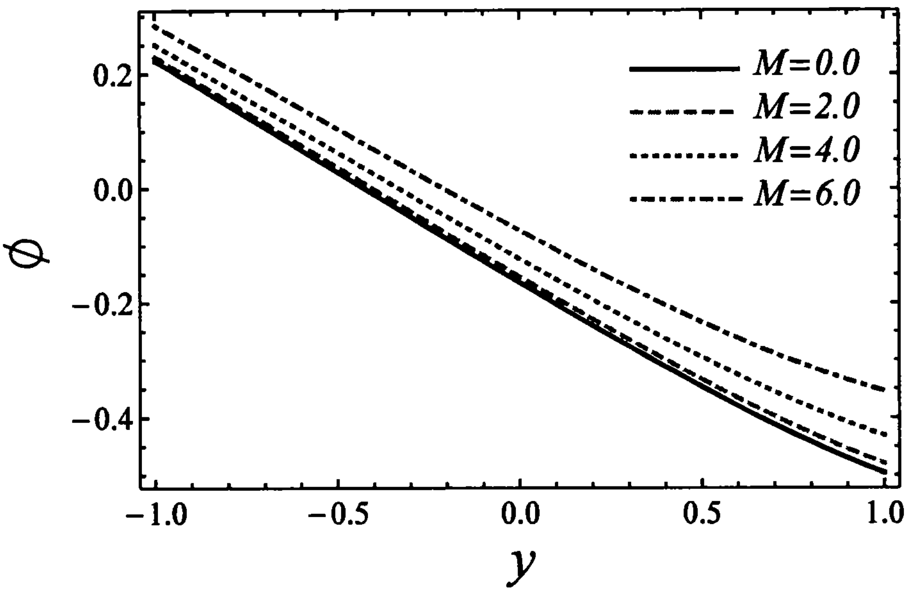

Figure 4.6(c): Appearance of M on concentration.

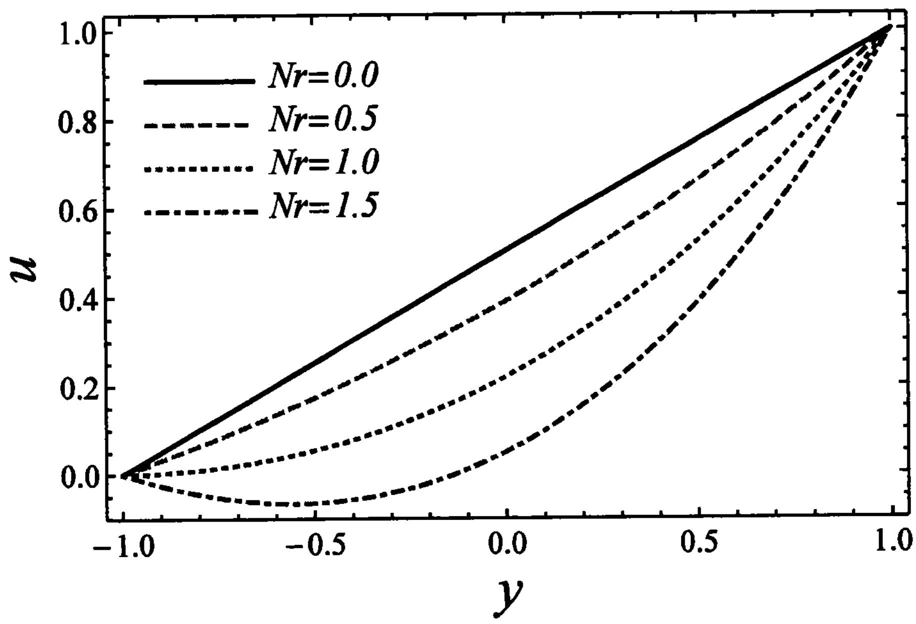

Figure 4.7: Appearance of Nr on velocity.

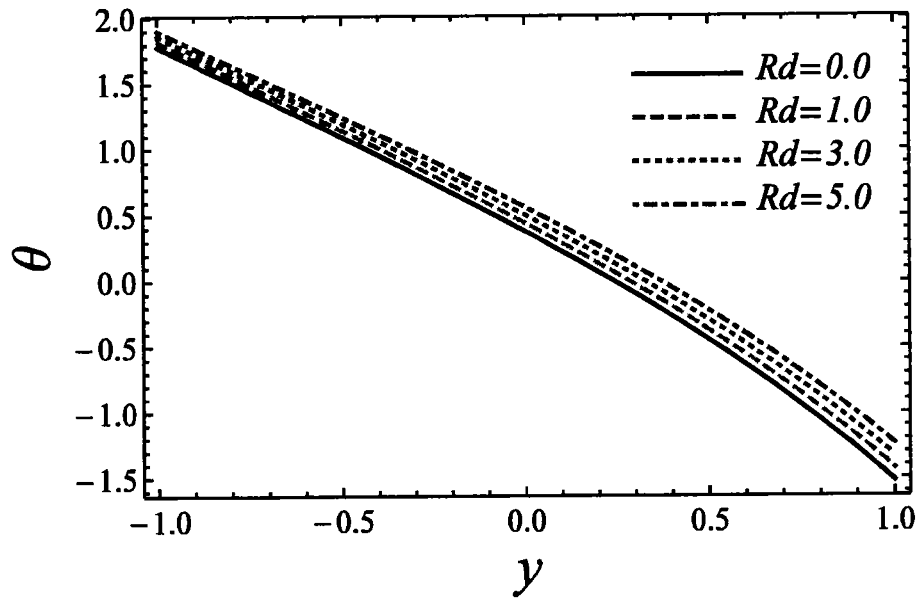

Figure 4.8: Appearance of Rd on temperature.

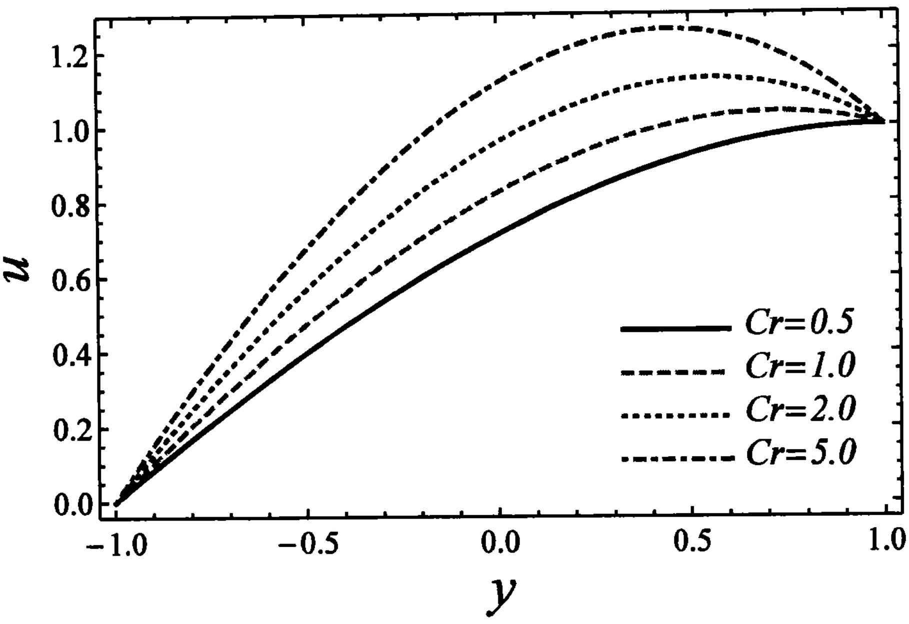

Figure 4.9(a): Appearance of Cr on velocity.

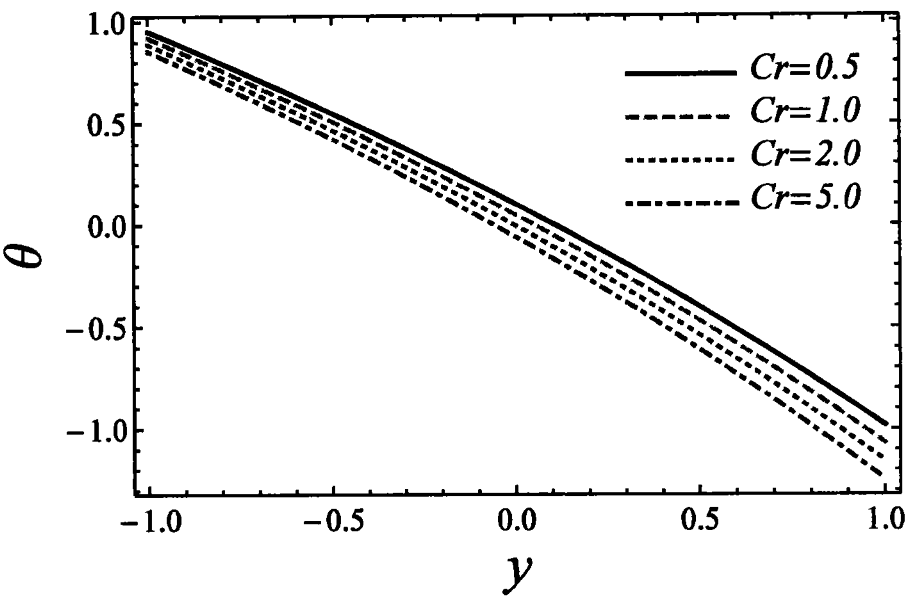

Figure 4.9(b): Appearance of Cr on temperature.

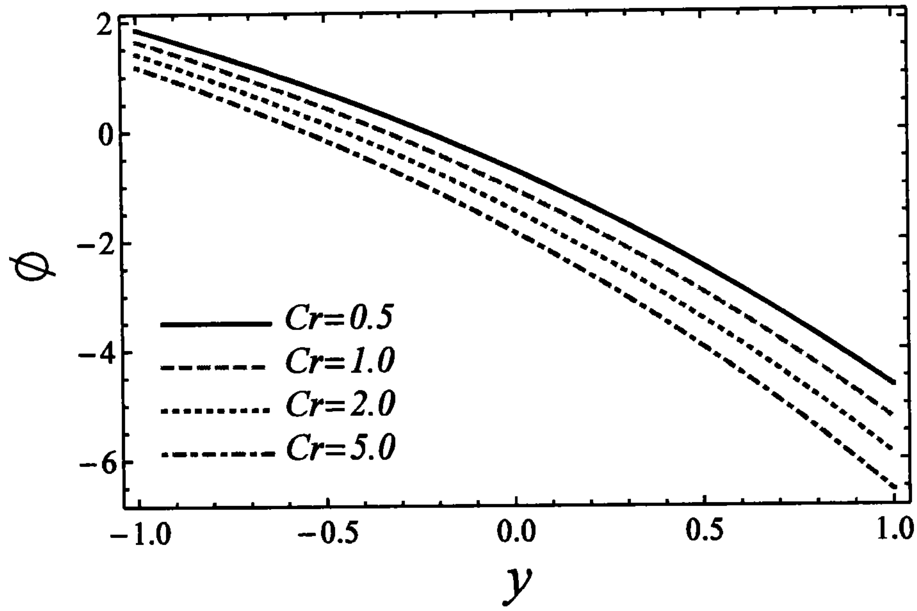

Figure 4.9(c): Appearance of Cr on concentration.

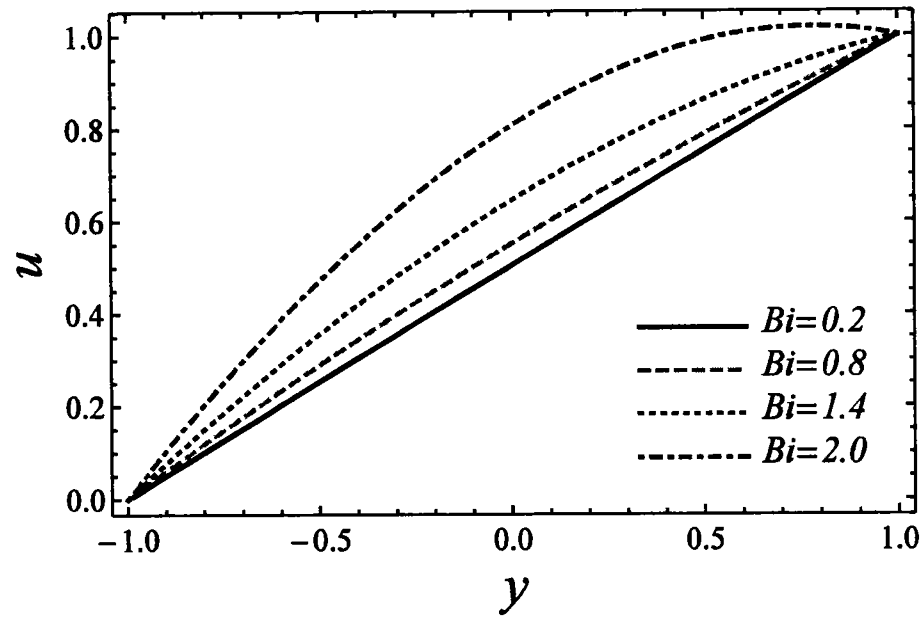

Figure 4.10(a): Appearance of Bi on velocity.

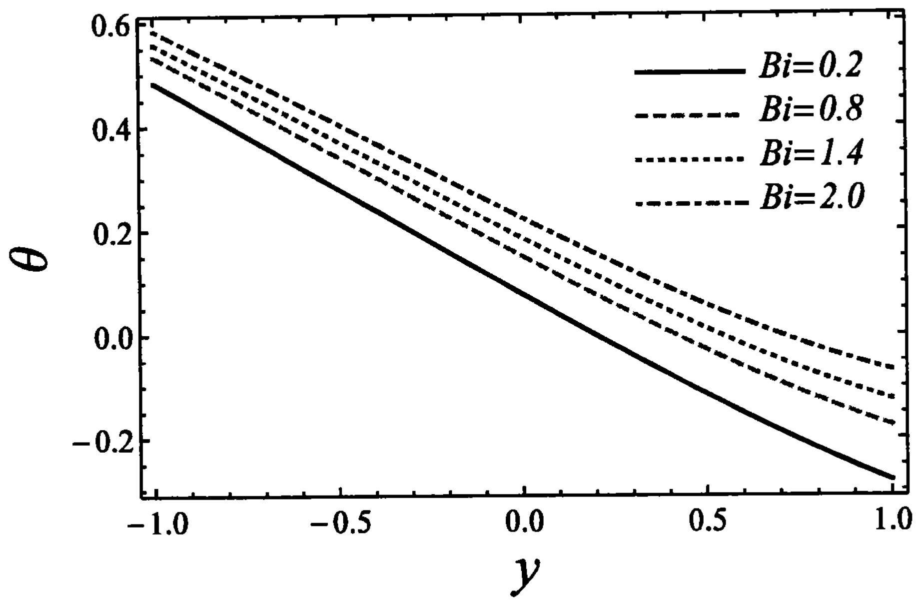

Figure 4.10(b): Appearance of Bi on temperature.

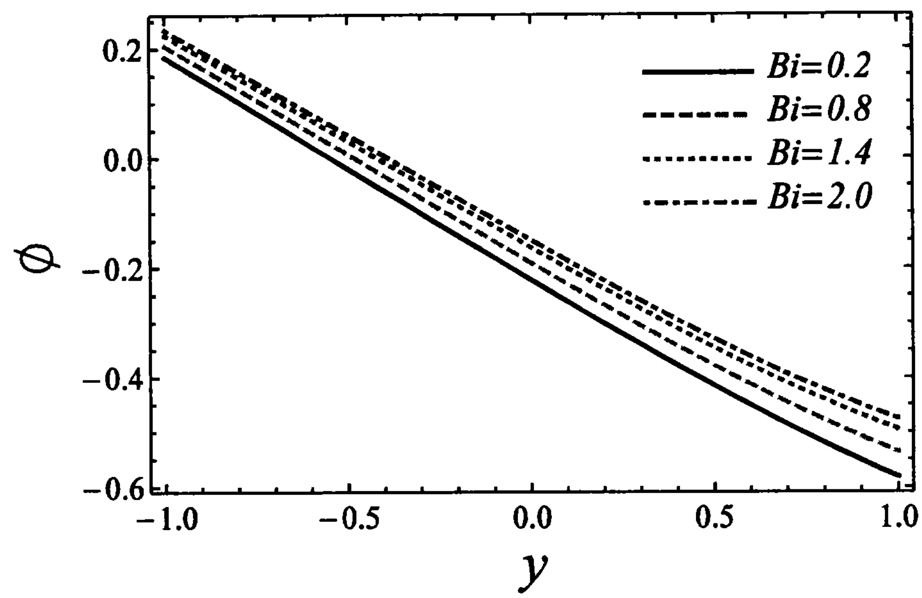

Figure 4.10(c): Appearance of Bi on concentration.

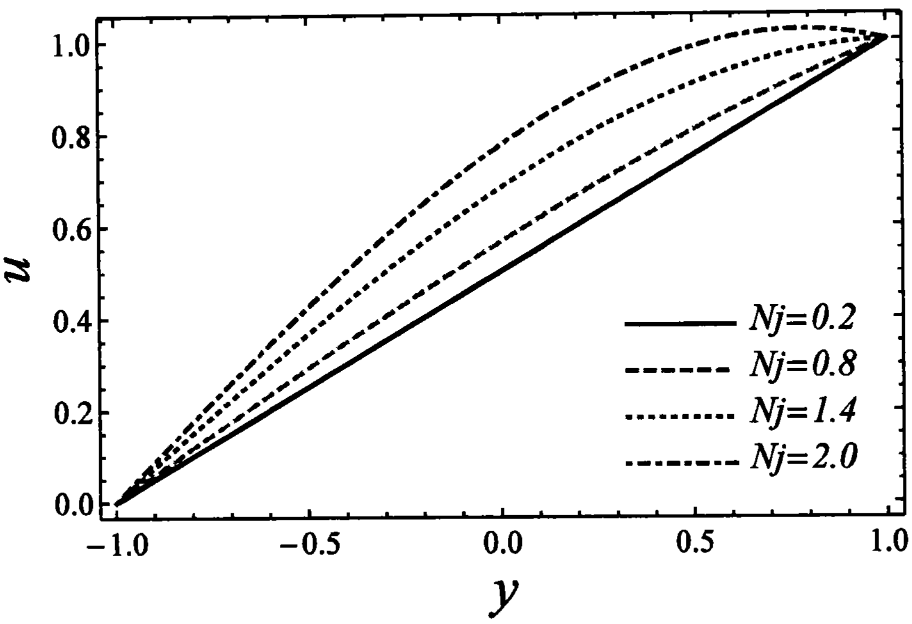

Figure 4.11(a): Appearance of Nj on velocity.

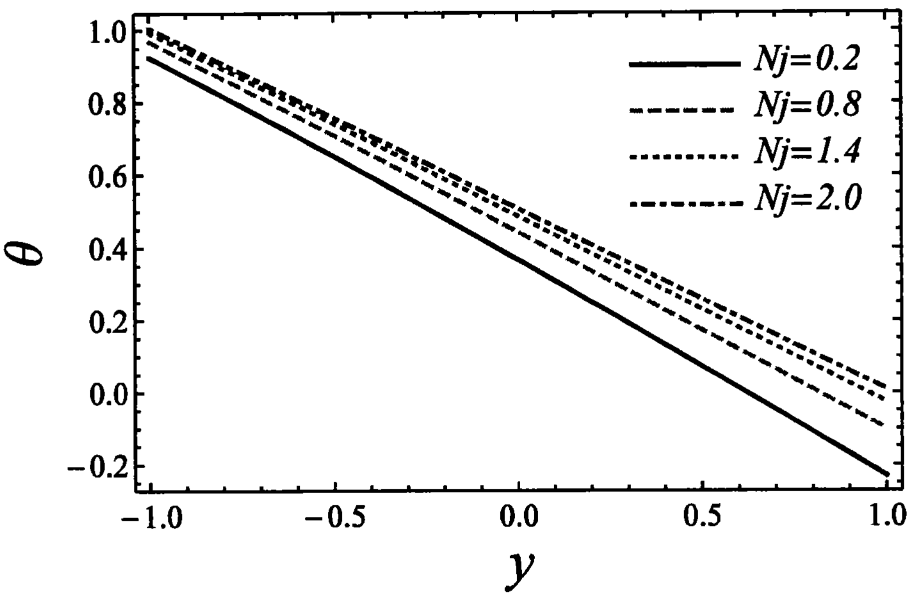

Figure 4.11(b): Appearance of Nj on temperature.

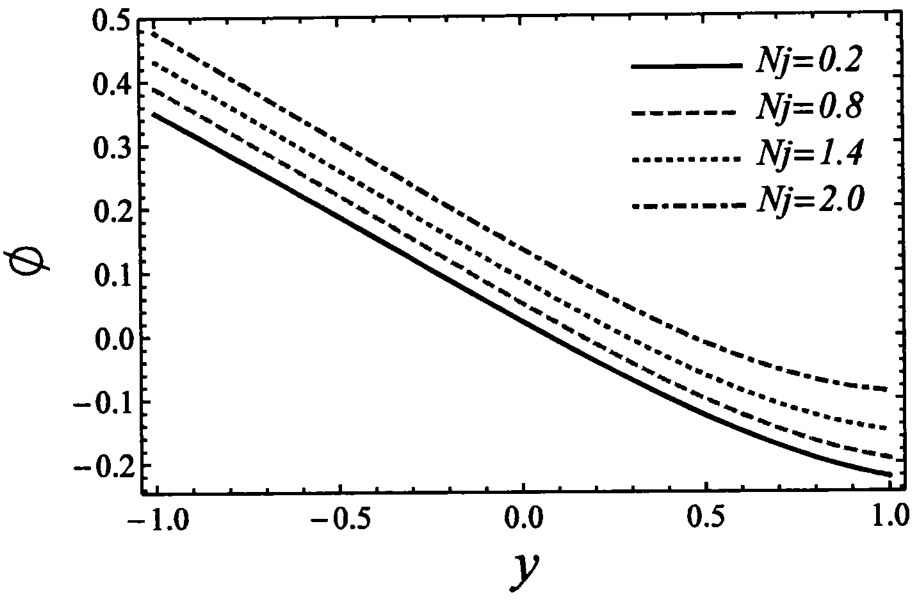

Figure 4.11(c): Appearance of Nj on concentration.

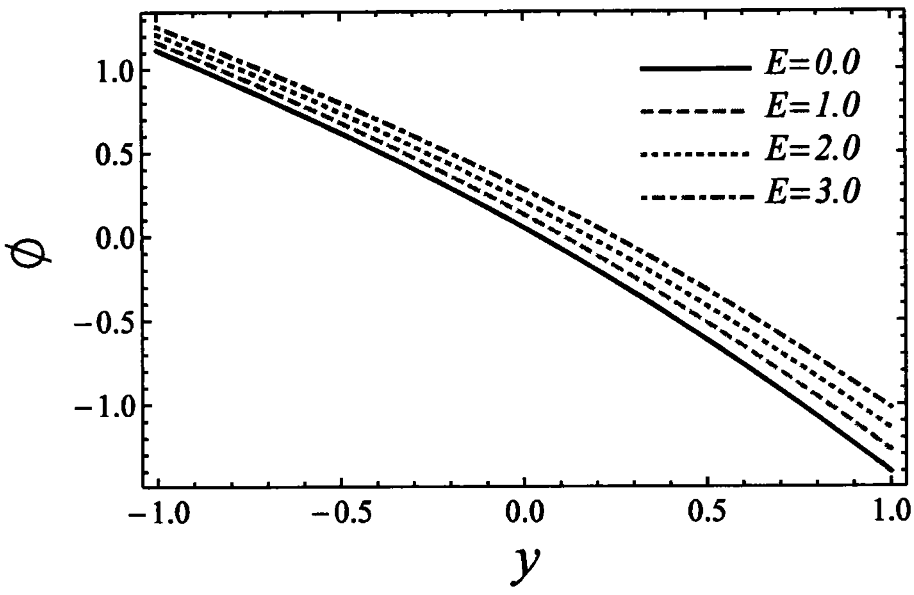

Figure 4.12: Appearance of E on concentration.

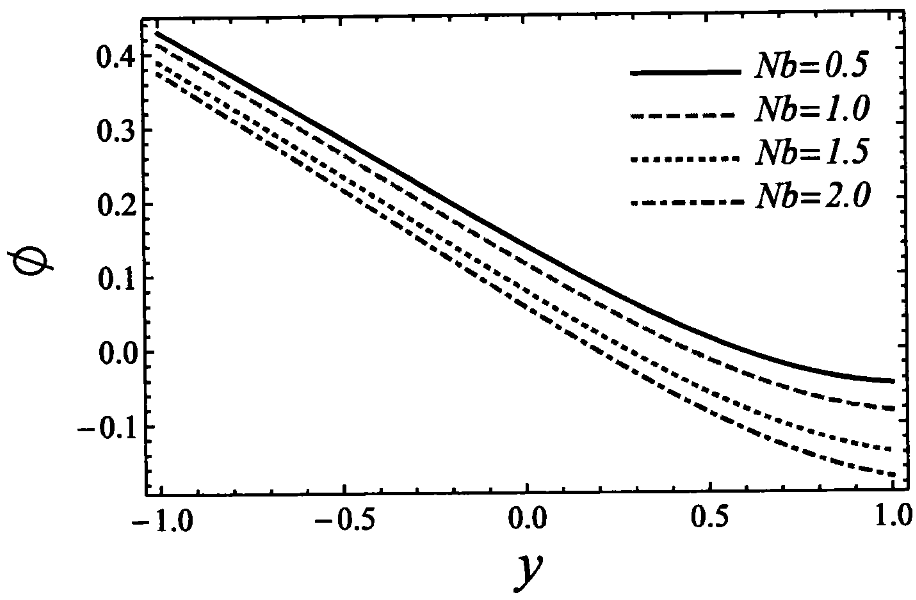

Figure 4.13(a): Appearance of Nb on concentration.

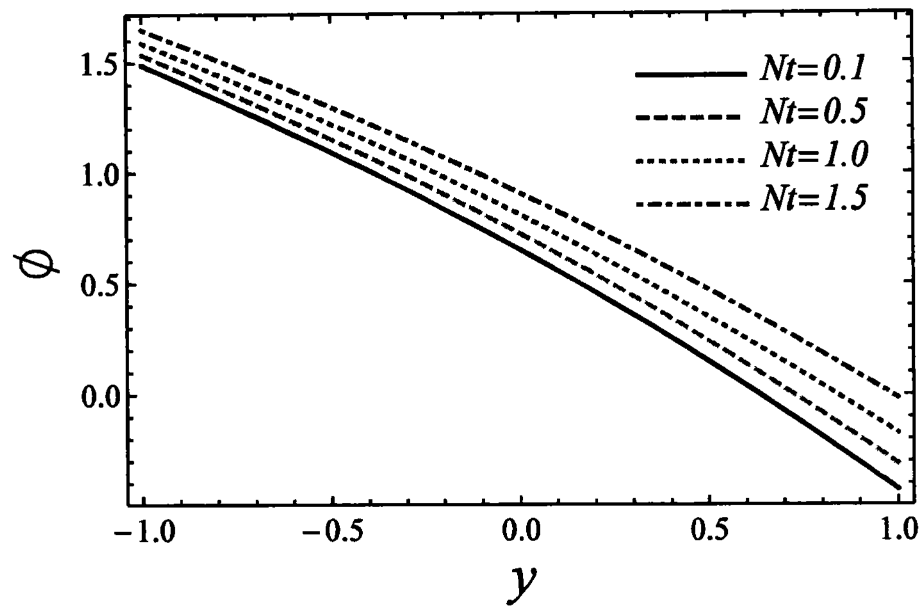

Figure 4.13(b): Appearance of Nt on concentration.

4.4 Conclusions

Couette-Poiseuille flow is the focus of this chapter. Buongiorno's model describes the flux density of the particles to form nanofluid through horizontal channel. The source of flow is smooth motion of the plate while stress is also generated by the constant pressure on the suspension. To further increase thermal process contribution of activation energy is added. Flow also experiences the Joule heating, radiation and viscous dissipation. Homotopy is used for the nonlinear problem and dimensionless variables are plotted to see their contribution. Some of most effective findings are listed as:

- Heat and mass distribution gives the proportionally effects with magnetic parameter as compare to flow field.
- Velocity decline of large magnetic parameter but concentration and temperature enhanced.
- Inverse behavior captured in heat and mass distribution with impact of chemical reaction.
- Activation energy gives the same agreement with the concentration field.
- Shear effects on both walls give the opposite effects due to rise in buoyancy ratio and magnetic parameter.
- The increasing effects of Heat transfer on both walls have detected with respect to thermophoresis and magnetic field parameter.
- Activation energy and chemical reaction give the opposite trend on channel walls for Sherwood number.

Chapter 5

5 Convective Poiseuille flow of Al_2O_3–EG nanofluid in a porous wavy channel with thermal radiation

In current chapter, convective boundary layer Poiseuille flow is presented. Ethylene glycol ($C_2H_6O_2$) serves as base liquid while aluminum oxide (Al_2O_3) are mixed to make a nanofluid to the investigation. Symmetric channel is of wavy type at the extreme containing porosity. External sources that influence the flow are Ohmic dissipation, two types of fields and radiation. Similarity variables are used before seeking an analytical solution via HAM. To make sure that the obtained solution is in full agreement with the physical expectations additional $\hbar$–curves and errors norm are plotted as well. The influence of numerous including parameters on flow, heat transfer, skin friction and Nusselt number are illustrated via graphs for better understanding.

5.1 Problem formulation

5.1.1 Flow analysis

Consider fully developed laminar, Poiseuille flow of incompressible nanofluid passing through a channel bounded by two wavy walls, as displayed in figure 5.1. The fluid is driven by a constant pressure gradient and Buoyancy force. Concerned problem is in Cartesian coordinate system, such that $\overline{x}$ -axis is taken along the channel wall, while $\overline{y}$ -axis is perpendicular to the channel and in a similar direction in which g affects. The middle of channel taken at origin and the configuration of the walls (left and right) with amplitude a_1, width d, length L of the walls and wavelength λ which is proportional to $2\pi/L$. The configuration of the left and right walls are defined as, respectively

$$H_1 = -d - a_1 \cos\left(\frac{2\pi}{L}\bar{x}\right), \quad H_2 = d + a_1 \cos\left(\frac{2\pi}{L}\bar{x}\right). \qquad (5.1)$$

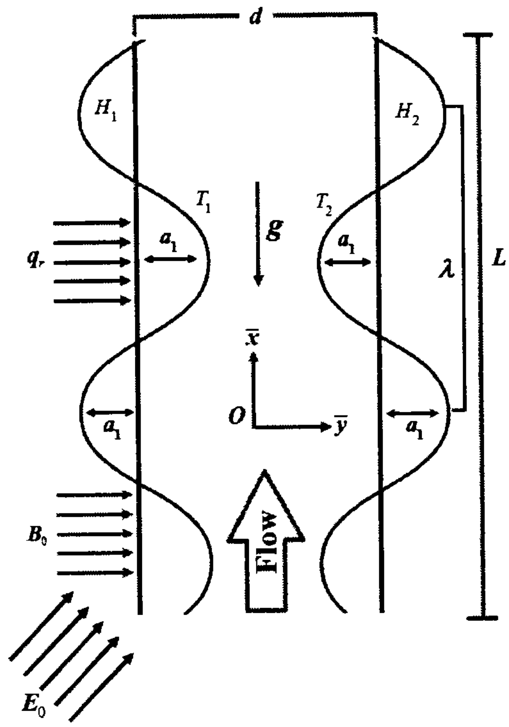

Figure 5.1: Flow model.

The uniform trend of B_0 is adopted in the $\bar{y}$ -direction and uniform electric field E_0 are applied normal to $\bar{y}$ -direction on the fluid.

5.1.2 Governing equations (Tiwari and Das's model)

According to the Tiwari and Das model, the governing equations (1.18), (1.19) and (1.38) given in the chapter 1, for a steady state, incompressible nanofluid with influence of electric, magnetic, buoyancy, radiative heat flux, viscous and Ohmic dissipation transporting through a porous medium are mathematically modeled. Boundary layer and Boussinesq's approximation are applied on the governing equations (1.18), (1.19) and (1.38), we get

$$\frac{\partial \bar{u}}{\partial \bar{x}}+\frac{\partial \bar{v}}{\partial \bar{y}}=0, \tag{5.2}$$

$$\rho_{nf}\left(\bar{u}\frac{\partial \bar{u}}{\partial \bar{x}}+\bar{v}\frac{\partial \bar{u}}{\partial \bar{y}}\right)=-\frac{\partial \bar{p}}{\partial \bar{x}}+\mu_{nf}\left(\frac{\partial^2 \bar{u}}{\partial \bar{x}^2}+\frac{\partial^2 \bar{u}}{\partial \bar{y}^2}\right)+\sigma_{nf}\left(E_0B_0-B_0^2\bar{u}\right)-\frac{\mu_{nf}}{K_1}\bar{u}+(\rho\beta)_{nf}\,g\left(\bar{T}-T^*\right), \tag{5.3}$$

$$\left(\rho C_p\right)_{nf}\left(\bar{u}\frac{\partial \bar{T}}{\partial \bar{x}}+\bar{v}\frac{\partial \bar{T}}{\partial \bar{y}}\right)=k_{nf}\left(\frac{\partial^2 \bar{T}}{\partial \bar{x}^2}+\frac{\partial^2 \bar{T}}{\partial \bar{y}^2}\right)+\mu_{nf}\left[\left(\frac{\partial \bar{u}}{\partial \bar{x}}\right)^2+\left(\frac{\partial \bar{u}}{\partial \bar{y}}\right)^2\right]+\sigma_{nf}\left(B_0\bar{u}-E_0\right)^2-\frac{\partial q_r}{\partial \bar{y}}. \tag{5.4}$$

The appropriate boundary conditions are

$$\left.\begin{array}{l}\bar{u}=0,\ \bar{v}=0,\ T=T_2\ \text{at}\ \bar{y}=H_2\\ \bar{u}=0,\ \bar{v}=0,\ T=T_1\ \text{at}\ \bar{y}=H_1\end{array}\right\}. \tag{5.5}$$

Let us acquaint the following nondimensional quantities

$$\left.\begin{array}{l}x=\dfrac{\bar{x}}{\lambda},\ y=\dfrac{\bar{y}}{d},\ u=\dfrac{\bar{u}}{U_m},\ v=\dfrac{\bar{v}}{U_m\delta},\ h_1=\dfrac{H_1}{d},\ h_2=\dfrac{H_2}{d},\\ p=\dfrac{d^2\bar{p}}{\mu_f U_m\lambda},\ \delta=\dfrac{d}{\lambda},\ \theta=\dfrac{T-T^*}{T_1-T^*},\ m^*=\dfrac{T_2-T^*}{T_1-T^*}\end{array}\right\}. \tag{5.6}$$

Using dimensionless quantities given in equation (5.6), then equations (5.2) to (5.4) are

$$\delta\frac{\partial u}{\partial x}+\frac{\partial v}{\partial y}=0, \tag{5.7}$$

$$A_2Re\delta\left(u\frac{\partial u}{\partial x}+v\frac{\partial u}{\partial y}\right)=A_1\left[\left(\delta^2\frac{\partial^2 u}{\partial x^2}+\frac{\partial^2 u}{\partial y^2}\right)-\frac{\partial p}{\partial x}\right]+A_3M^2\left(E_1-u\right)-\frac{A_1}{Da}u+A_4Gr\theta, \tag{5.8}$$

$$A_5 Re Pr\delta\left(u\frac{\partial\theta}{\partial x}+v\frac{\partial\theta}{\partial y}\right)=A_6\left(\delta^2\frac{\partial^2\theta}{\partial x^2}+\frac{\partial^2\theta}{\partial y^2}\right)+A_3 EcPrM^2\left(u-E_1\right)^2+A_1 EcPr\left(\frac{\partial u}{\partial y}\right)^2+Rd\left(\frac{\partial^2\theta}{\partial y^2}\right). \quad (5.9)$$

Using the long wavelength approximation, equations (5.7) to (5.9) take the form

$$-A_1 P+A_1\frac{\partial^2 u}{\partial y^2}+A_3 M^2\left(E_1-u\right)-\frac{A_1}{Da}u+A_4 Gr\theta=0\,, \quad (5.10)$$

$$\left(A_6+Rd\right)\frac{\partial^2\theta}{\partial y^2}+A_3 EcPrM^2\left(u-E_1\right)^2+A_1 EcPr\left(\frac{\partial u}{\partial y}\right)^2=0. \quad (5.11)$$

boundary conditions

$$\left.\begin{aligned} &u=0,\ \theta=m^*\ \text{at}\ y=h_2=1+\frac{a}{d}\mathrm{Cos}\left(\frac{2\pi\lambda}{L}x\right)\\ &u=0,\ \theta=1\ \ \text{at}\ y=h_1=-1-\frac{a}{d}\mathrm{Cos}\left(\frac{2\pi\lambda}{L}x\right)\end{aligned}\right\}, \quad (5.12)$$

where

$$\left.\begin{aligned} &Gr=\frac{(\rho\beta)_f gd^2\left(T_1-T^*\right)}{\mu_f U_m},\mathrm{Re}=\frac{\rho_f U_m d}{\mu_f},M^2=\frac{\sigma_f B_0^2 d^2}{\mu_f},E_1=\frac{E_0}{B_0 U_m}\\ &\mathrm{Pr}=\frac{\mu_f\left(\rho C_p\right)_f}{\rho_f k_f},Ec=\frac{U_m^2}{\left(C_p\right)_f\left(T_1-T^*\right)},Rd=\frac{16T^{*3}\sigma^*}{3k^*k_f},Da=\frac{K_1}{d^2}\\ &A_1=\frac{\mu_{nf}}{\mu_f},\ A_2=\frac{\rho_{nf}}{\rho_f},\ A_3=\frac{\sigma_{nf}}{\sigma_f},A_4=\frac{(\rho\beta)_{nf}}{(\rho\beta)_f},A_5=\frac{\left(\rho C_p\right)_{nf}}{\left(\rho C_p\right)_f},\ A_6=\frac{k_{nf}}{k_f}.\end{aligned}\right\}. \quad (5.13)$$

In this chapter, physical thermal properties are used defined in equations (1.3), (1.6), (1.9), (1.10) and (1.11). Expression of skin friction defined in equation (1.54) and Nusselt number defined in equation (1.56) are transformed in view of equation (5.6) as

$$\left.\begin{aligned} \operatorname{Re} C_f &= 2A_1 u'(y) \,\Big|_{y=h_1,h_2} \\ Nu &= -A_6 \theta'(y)\Big|_{y=h_1,h_2} \end{aligned}\right\}. \tag{5.14}$$

5.2 Solution of the problem

One of best suited analytical method is brought under consideration for equations (5.10) and (5.11) and that is "HAM".

Zeroth-order solution

we have picked out the following initial approximations $(u_0,\ \theta_0)$ which satisfy the linear operators $(£_u,\ £_\theta)$ and associated boundaries

$$\left.\begin{aligned} u_0(y) &= y^2 - (h_1+h_2)y + (h_1+h_2) \\ \theta_0(y) &= \frac{y-h_2}{h_1-h_2} \end{aligned}\right\} \tag{5.15}$$

and

$$£_u = \frac{d}{dy}\left(\frac{du}{dy}\right),\quad £_\theta = \frac{d}{dy}\left(\frac{d\theta}{dy}\right). \tag{5.16}$$

The convergence control parameters $\hbar_u$, $\hbar_\theta$ and nonlinear operators N_u, N_θ of velocity, temperature with embedding parameter $\xi \in [0,\ 1]$ yields the following zeroth-order homotopy respectively are

$$\left.\begin{aligned} (1-\xi)£_u\left[u(y,\xi)-u_0(y)\right] &= \xi\hbar_u N_u\left[u(y,\xi),\theta(y,\xi)\right] \\ (1-\xi)£_\theta\left[\theta(y,\xi)-\theta_0(y)\right] &= \xi\hbar_\theta N_\theta\left[u(y,\xi),\theta(y,\xi)\right] \end{aligned}\right\} \tag{5.17}$$

boundary conditions

$$\left.\begin{aligned} u(y,\xi) = 0,\ \theta(y,\xi) = m^* \quad \text{at}\ y = h_2 \\ u(y,\xi) = 0,\ \theta(y,\xi) = 1 \quad\ \ \text{at}\ y = h_1 \end{aligned}\right\} \tag{5.18}$$

and

$$\left.\begin{aligned} N_u &= A_1\left[-P+\frac{\partial^2 u(y,\xi)}{\partial y^2}\right]+A_3M^2\left(E_1-u(y,\xi)\right)-\frac{A_1}{Da}u(y,\xi)+A_4\frac{Gr}{\text{Re}}\theta(y,\xi) \\ N_\theta &= (Rd+A_6)\frac{\partial^2\theta(y,\xi)}{\partial y^2}+A_3EcPrM^2\left(u(y,\xi)-E_1\right)^2+A_1Ec\Pr\left(\frac{\partial u(y,\xi)}{\partial y}\right)^2 \end{aligned}\right\}. \tag{5.19}$$

l th–order solution

The l th–order deformation for $u_l(y)$ and $\theta_l(y)$ as follows

$$\left.\begin{aligned} \pounds_u\left[u_l(y)-\chi_l u_{l-1}(y)\right] &= \hbar_u R_l^u(y) \\ \pounds_\theta\left[\theta_l(y)-\chi_l\theta_{l-1}(y)\right] &= \hbar_\theta R_l^\theta(y) \end{aligned}\right\}, \tag{5.20}$$

$$\left.\begin{aligned} u_l(y,\xi)=0,\ \theta_l(y,\xi)=m^* \ \text{at}\, y=1 \\ u_l(y,\xi)=0,\ \theta_l(y,\xi)=1 \ \text{at}\, y=-1 \end{aligned}\right\}, \tag{5.21}$$

$$\left.\begin{aligned} R_l^u(y) &= A_1\left[-P+u_l''\right]+A_3M^2(E_1-u_l)-\frac{A_1}{Da}u_l+A_4\frac{Gr}{\text{Re}}\theta_l \\ R_l^\theta(y) &= (Rd+A_6)\theta_l''+A_3EcPrM^2(u_l-E_1)^2+A_1Ec\Pr\sum_{k=0}^{l}u_k'u_{l-k}' \end{aligned}\right\}. \tag{5.22}$$

The solution can be described as of l th-order

$$\left.\begin{aligned} u(y) &= u_0(y)+\sum_{k=1}^{l}u_k(y) \\ \theta(y) &= \theta_0(y)+\sum_{k=1}^{l}\theta_k(y) \end{aligned}\right\}. \tag{5.23}$$

The solutions at second-order iterations by utilizing the Mathematica package BVPh2.0 based on the HAM can be expressed for velocity and temperature as

$$
\left.
\begin{array}{l}
u=-1-\hbar_u\frac{63}{40}-\hbar_u\frac{97E_1M^2}{200}-\hbar_u\frac{4753GrM^2}{24000}-\hbar_u\frac{343Gr}{1600Da}+ \\
\hbar_u\frac{33271GrM^2}{600000}y+\hbar_u\frac{2401Gr}{40000Da}y+y^2+\hbar_u\frac{63}{40}y^2+ \\
\hbar_u\frac{97E_1M^2}{200}y^2+\hbar_u\frac{4753GrM^2}{20000}y^2+\hbar_u\frac{1029Gr}{4000Da}y^2- \\
\hbar_u\frac{4753GrM^2}{60000}y^3-\hbar_u\frac{343Gr}{4000Da}y^3-\hbar_u\frac{4753GrM^2}{120000}y^4- \\
\hbar_u\frac{343Gr}{8000Da}y^4+\hbar_u\frac{4753GrM^2}{200000}y^5+\hbar_u\frac{1029Gr}{40000Da}y^5
\end{array}
\right\}. \tag{5.24}
$$

$$
\left.
\begin{array}{l}
\theta=-\hbar_\theta\frac{7Ec}{2}-\hbar_\theta\frac{1067EcM^2}{300}-\hbar_\theta\frac{97E_1EcM^2}{12}-\hbar_\theta\frac{97E_1^2EcM^2}{20}- \\
\hbar_\theta\frac{Rd^2}{4}+\frac{1-y}{2}+\hbar_\theta\frac{Rd^2}{12}y+\hbar_\theta\frac{97EcM^2}{20}y^2+\hbar_\theta\frac{97E_1EcM^2}{10}y^2+ \\
\hbar_\theta\frac{97E_1^2EcM^2}{20}y^2+\hbar_\theta\frac{Rd^2}{4}y^2-\hbar_\theta\frac{Rd^2}{12}y^3+\hbar_\theta\frac{7Ec}{2}y^4- \\
\hbar_\theta\frac{97EcM^2}{60}y^4-\hbar_\theta\frac{97E_1EcM^2}{60}y^4+\hbar_\theta\frac{97EcM^2}{300}y^6
\end{array}
\right\}. \tag{5.25}
$$

5.3 Discussion of results

5.3.1 Inspection of Convergence

The hybrid genetic algorithm and Nelder-Mead approach (GANM) is used for approximation and the convergence region of $\hbar_u$ and $\hbar_\theta$. The hybrid scheme demonstrates its reliability, validity and ability to solve highly nonlinear problems in engineering and applied sciences by minimizing the residual error. To decide appropriate value of $\hbar_u$ and $\hbar_\theta$, figures 5.2 and 5.3 portray the $\hbar_u$ and $\hbar_\theta$-curves. The estimated ranges for $\hbar_u$ and $\hbar_\theta$ are $-1.3\le\hbar_u\le-0.1$ and $-1.4\le\hbar_\theta\le 0$.

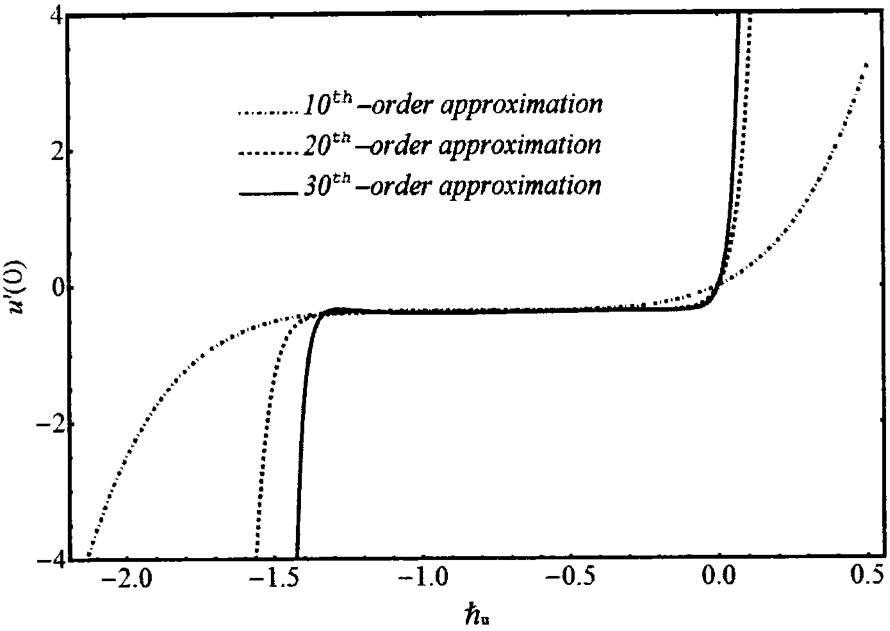

Figure 5.2: $\hbar_u$–curve for velocity.

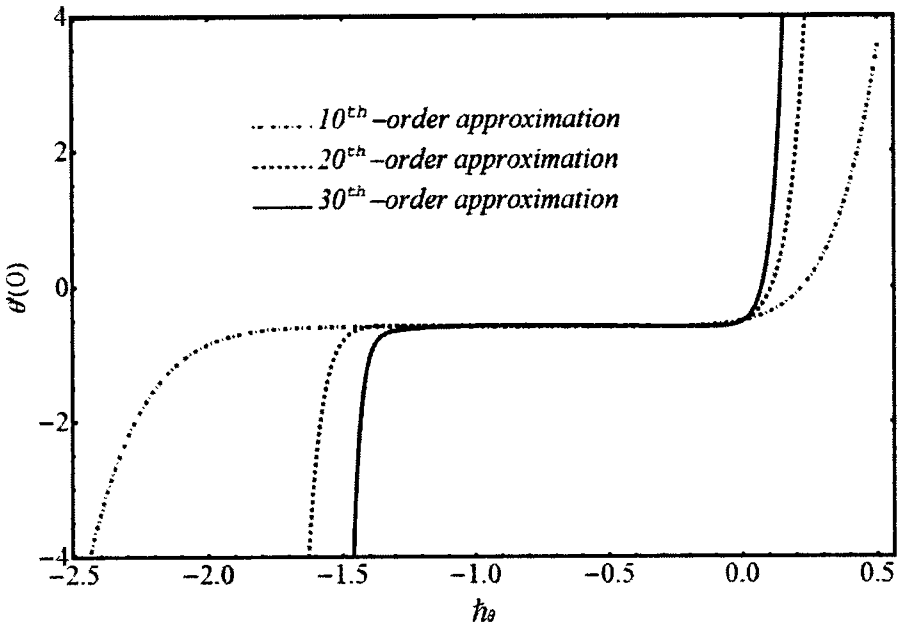

Figure 5.3: $\hbar_\theta$–curve for temperature.

5.3.2 Residual error of norm 2

Furthermore, the residual errors were computed up to 30th –order approximation over an embedding parameter $\xi \in [0, 1]$ of velocity E_u and temperature E_θ by the succeeding formulas

$$E_u = \sqrt{\frac{1}{31}\sum_{i=0}^{30}\left(u(i/30)\right)^2}, \quad E_\theta = \sqrt{\frac{1}{31}\sum_{i=0}^{30}\left(\theta(i/30)\right)^2}. \tag{5.26}$$

The minimum error for velocity at $\hbar_u = -0.5$ and temperature at $\hbar_\theta = -0.5$ are detected mention in Table 5.1. It is also very essential that $\hbar$ lie in convergent sort. A hybrid Genetic Algorithm (GA) and Nelder-Mead (NM) methodology [97] is employed to enhance the efficiency of HAM to find value appropriate value of $\hbar$. In Tables 5.1 to 5.2, given correlation between GANM and HAM.

Table 5.2: Correlation between homotopic solutions by $\hbar_u$ –curve and optimal series solution using GANM for velocity u.

						Series Solution (HAM)		Optimal Solution with GA & NM		
E_c	Gr	E_1	N	M	Da	Iteration	Error	Iteration	$\hbar_u$ –curves	Error
0.1	2	1	1	0.25	0.5	10	3.6×10^{-4}	10	-0.5732	3.7×10^{-5}
				0.50		20	2.8×10^{-6}	20	-0.6932	4.5×10^{-7}
				0.75		30	7.3×10^{-7}	30	-0.7833	6.3×10^{-9}
0.2	5	2	2	1.00	1.0	10	5.4×10^{-4}	10	-0.5847	7.5×10^{-5}
				1.25		20	3.4×10^{-6}	20	-0.6638	3.2×10^{-7}
				1.50		30	9.1×10^{-8}	30	-0.7384	4.7×10^{-9}
0.3	10	3	3	2.00	2.0	10	4.4×10^{-3}	10	-0.5278	8.5×10^{-5}
				2.25		20	6.6×10^{-5}	20	-0.6837	8.3×10^{-7}
				2.50		30	2.3×10^{-7}	30	-0.7973	1.3×10^{-9}

Table 5.2: Correlation between HAM solutions by $\hbar_\theta$ –curve and GANM solution θ.

						Series Solution (HAM)		Optimal Solution with GA & NM		
E_c	Gr	E_1	N	M	Da	Iteration	Error	Iteration	$\hbar_u$ –curves	Error
0.1	2	1	1	0.25	0.5	10	2.4×10^{-3}	10	-0.6973	8.7×10^{-4}
				0.50		20	3.3×10^{-5}	20	-0.7376	4.1×10^{-6}
				0.75		30	5.3×10^{-7}	30	-0.8638	3.4×10^{-7}
0.2	5	2	2	1.00	1.0	10	4.8×10^{-3}	10	-0.6385	3.2×10^{-4}
				1.25		20	7.5×10^{-5}	20	-0.7352	5.4×10^{-6}
				1.50		30	2.8×10^{-7}	30	-0.8851	2.2×10^{-8}
0.3	10	3	3	2.00	2.0	10	5.5×10^{-3}	10	-0.6249	1.3×10^{-4}
				2.25		20	6.3×10^{-5}	20	-0.7911	7.6×10^{-5}
				2.50		30	1.2×10^{-6}	30	-0.8122	5.1×10^{-8}

5.3.3 Illustration of graphical results

The governing equations are solved using HAM with GANM approach. The influence of numerous involving parameters on velocity, temperature, Nusselt number and Skin-friction is illustrated from figures 5.4 to 5.10. These figures are prepared for $\varphi = 2\%$ particle volume friction along with the constraint that heat is dominant in fluid. The nondimensional velocity profile u for several values of M is designed in figure 5.4(a). It observed that for magnetic parameter, velocity near center of geometry decreases with increase of M. It is due to, when magnetic field apply on walls then there produce a Lorentz force. By increasing the magnetic field parameter in response Lorentz force resist the fluid velocity. Velocity for Da is exposed in figure 5.4(b). It is perceived that for porosity parameter, velocity near center of channel increase with increase of Da. It is because, when Darcy number increase then permeability of medium increase. Therefore, fluid easily passes through channel. Velocity profile for E_1 is displayed in figure 5.4(c). It was perceived that as parameter rises then velocity increases. Due to

Lorentz force arising because of electric field in the system cause for large velocity. Dimensionless temperature profile θ for innumerable values of M is shown in figure 5.5(a). It observed that for magnetic parameter, temperature of liquid increase with rise of M. It is due to Lorentz force which resists flow speed and in response temperature of liquid rise. Temperature profile for Da is exposed in figure 5.5(b). It is perceived that for porosity parameter, temperature near middle of geometry decreases with increase of Da. It observed that as parameter increases in results velocity of fluid significant so heat transfer in the core region enhance and then overall temperature of fluid decrease. Thermal radiation Rd effects on temperature profile is connived in figure 5.5(c). It observed that as parameter increases temperature of fluid increases. The boundary layer thickness increased with increasing values of radiation factor. Temperature of nanofluid could also be controlled with radiation factor, because fluid temperature was very sensitive to Rd, which meant that the heat flux of channel walls would be as large as perceived. Effects of Ec and Gr on skin friction are shown in figures 5.6(left) and 5.6(right) for right and left walls respectively. The skin fiction increases with greater values of Ec and Gr at right wall of channel whereas skin fiction decreases for increase of Ec and Gr at left wall of channel. Influences of E_1 and M on skin friction are shown in figures 5.7(left) and 5.7(right) for right and left walls respectively. The skin fiction diminutions by increasing values of E_1 and M at right wall of channel whereas skin fiction rises with the increase of E_1 and M at left wall of channel. Impressions of Ec and Gr on Nusselt number are given in figures 5.8(left) and 5.8(right) for right and left walls respectively. Nusselt number increases by increasing values of Ec and Gr at right wall of channel whereas skin fiction decreases with increase of Ec and Gr at left wall of channel. Impacts of E_1 and M on Nusselt number are demonstrated in figures 5.9(left) and 5.9(right) for right and left walls respectively. Nusselt number increases by increasing values of E_1 and M at right wall of channel whereas Nusselt number decreases with increase of E_1 and M at left wall of channel. Figures 5.10(left) and 5.10(right) demonstrates the effects of Rd

and Da on Nusselt number. In figure 5.10(left), the Nusselt number gives decelerating behaviour for large thermal radiation along high permeability of porous media at right wall but in figure 5.10(right) a quite opposite behaviour is noted at left wall.

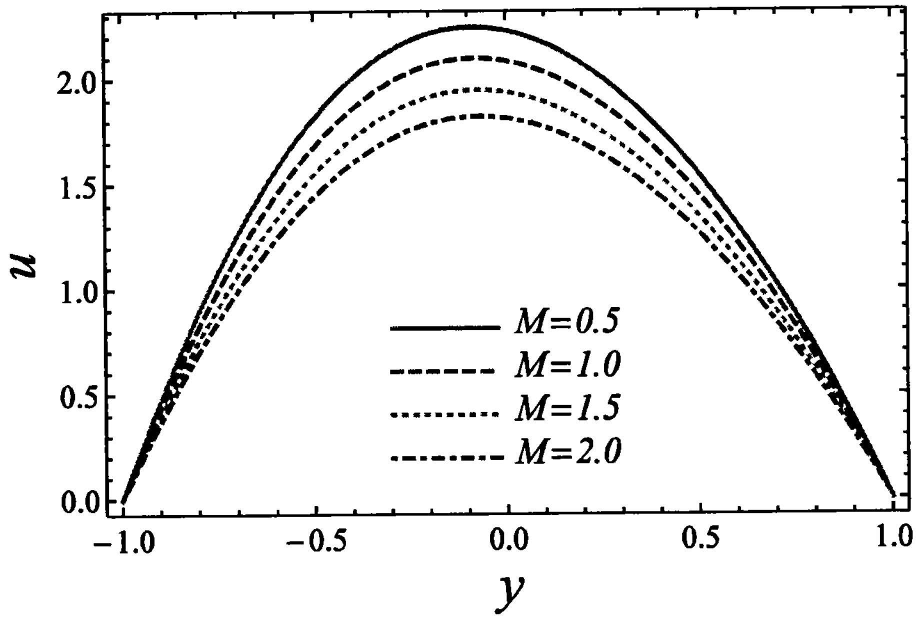

Figure 5.4(a): Impression of velocity corresponding to different M .

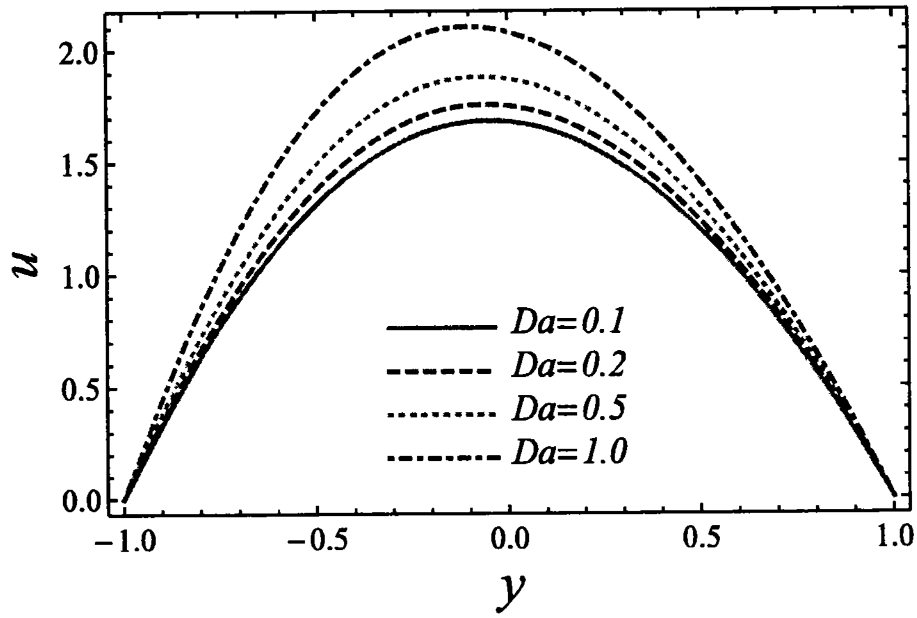

Figure 5.4(b): Impression of velocity corresponding to different Da.

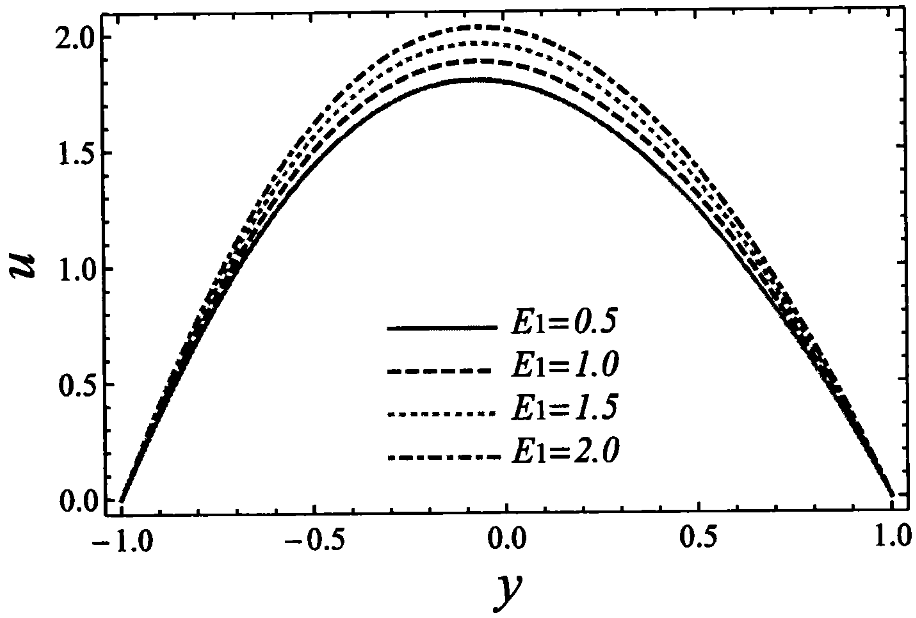

Figure 5.4(c): Impression of velocity corresponding to different E_1.

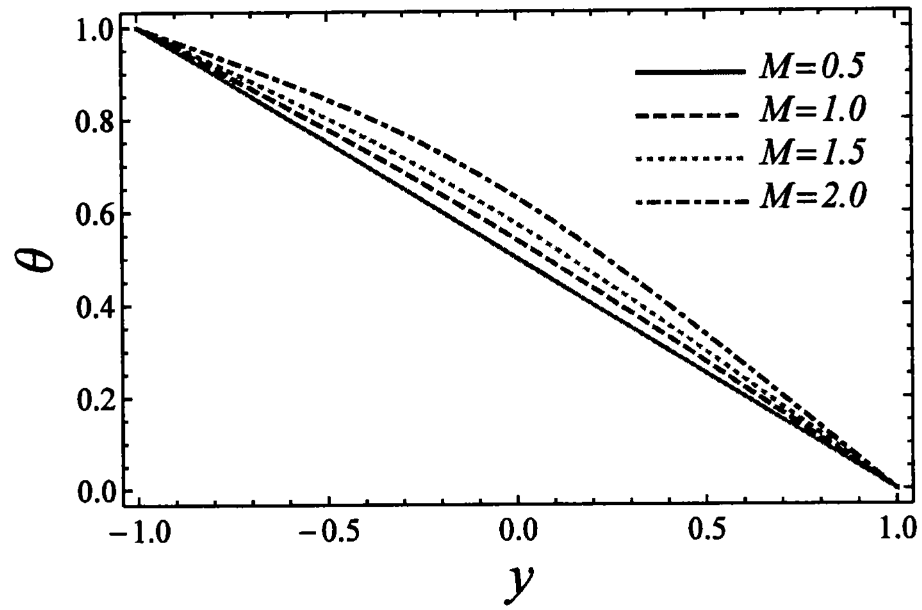

Figure 5.5(a): Impression of temperature profile corresponding to different M

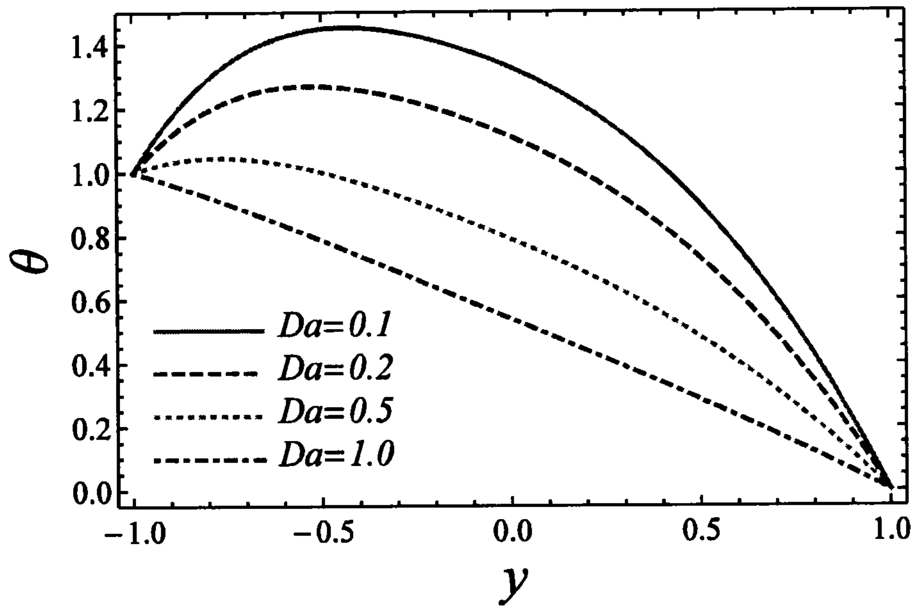

Figure 5.5(b): Impression of temperature profile corresponding to different Da.

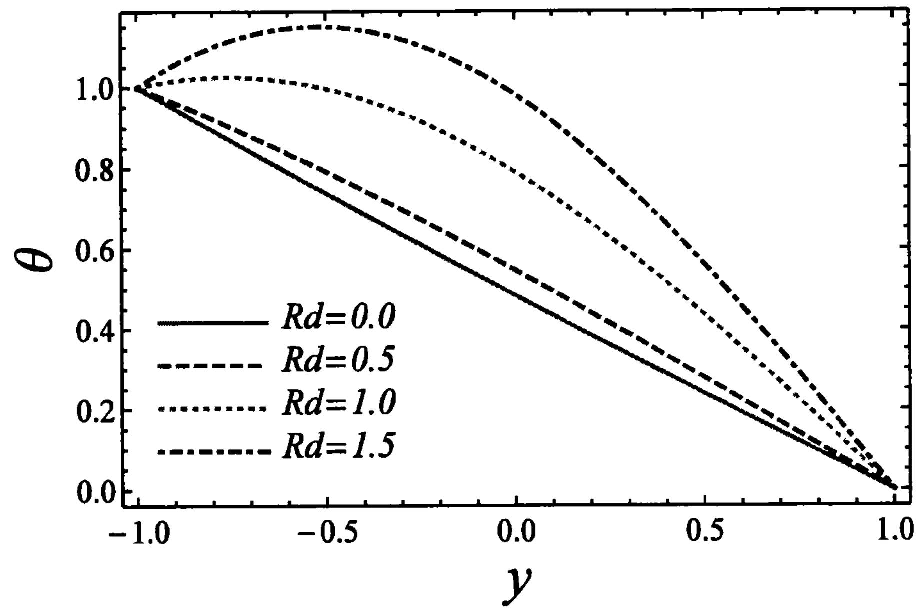

Figure 5.5(c): Impression of temperature profile corresponding to different Rd

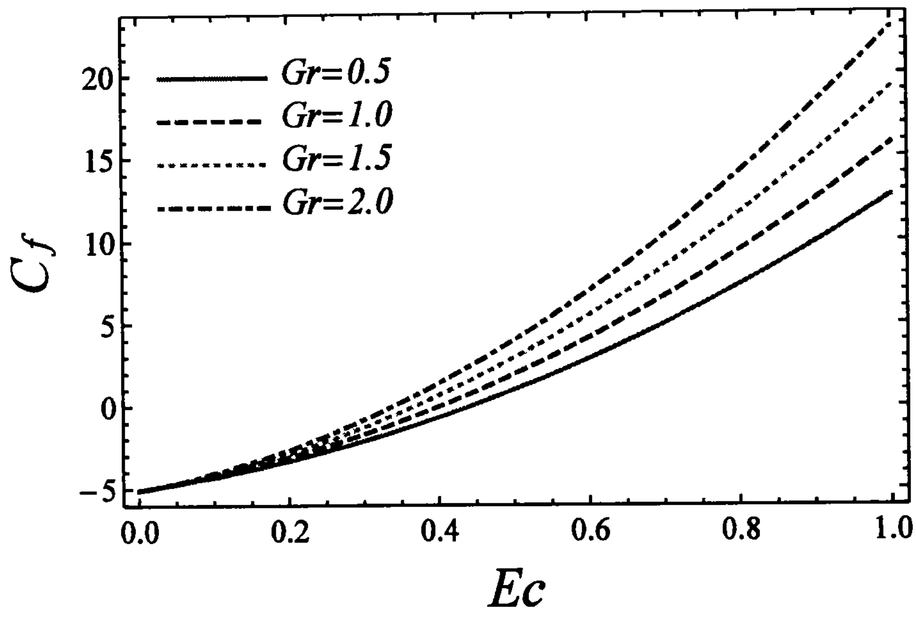

Figure 5.6(left): C_f plotted against Ec and Gr.

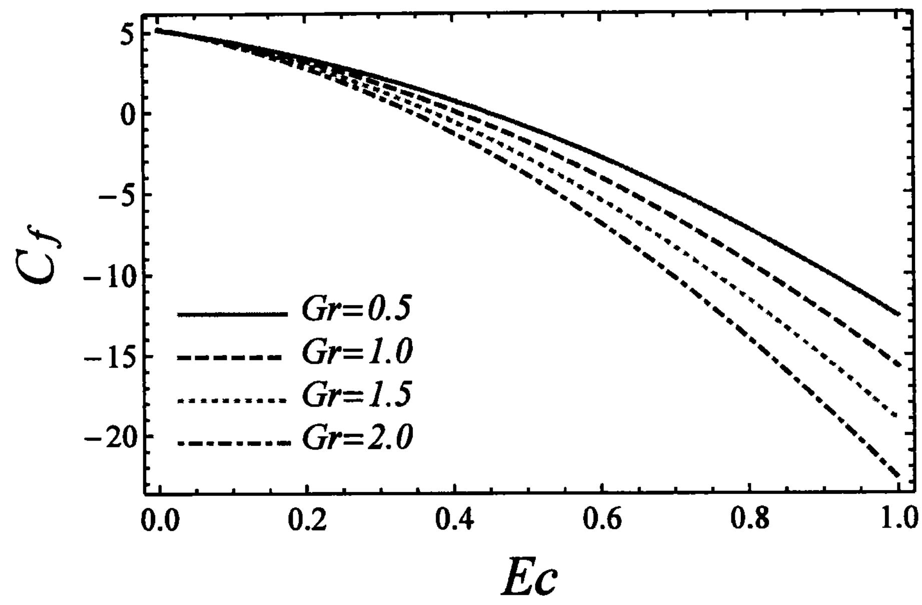

Figure 5.6(right): C_f plotted against Ec and Gr.

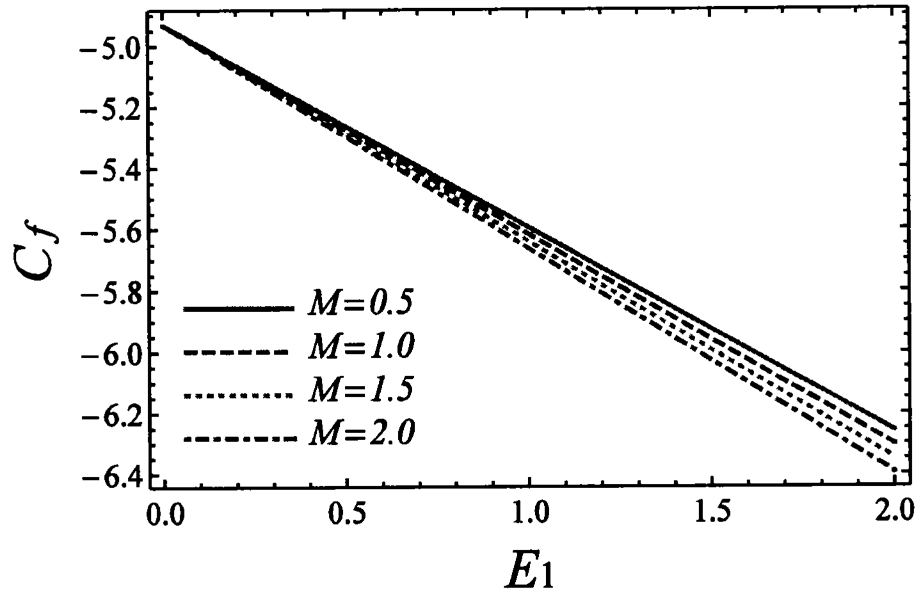

Figure 5.7(left): C_f plotted against E_1 and M .

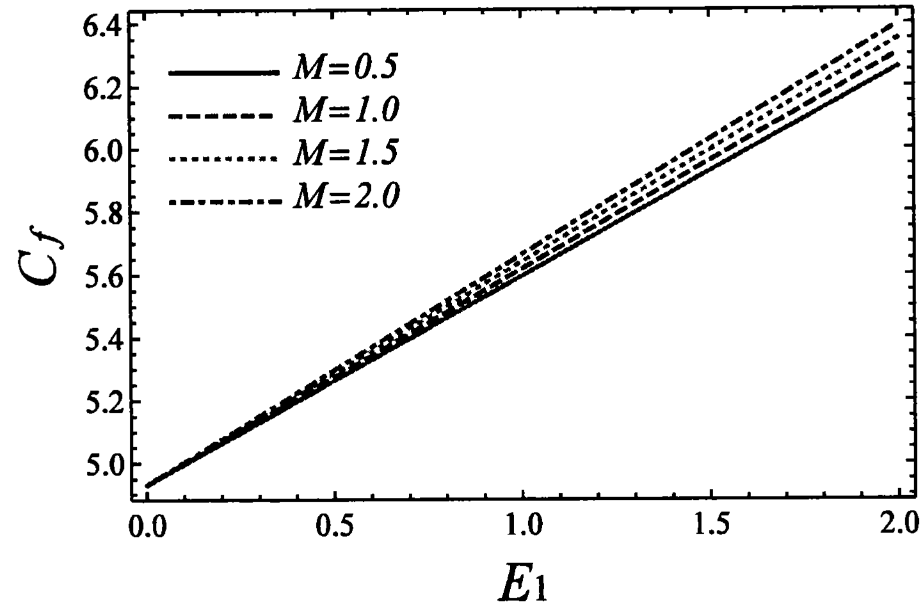

Figure 5.7(right): C_f plotted against E_1 and M .

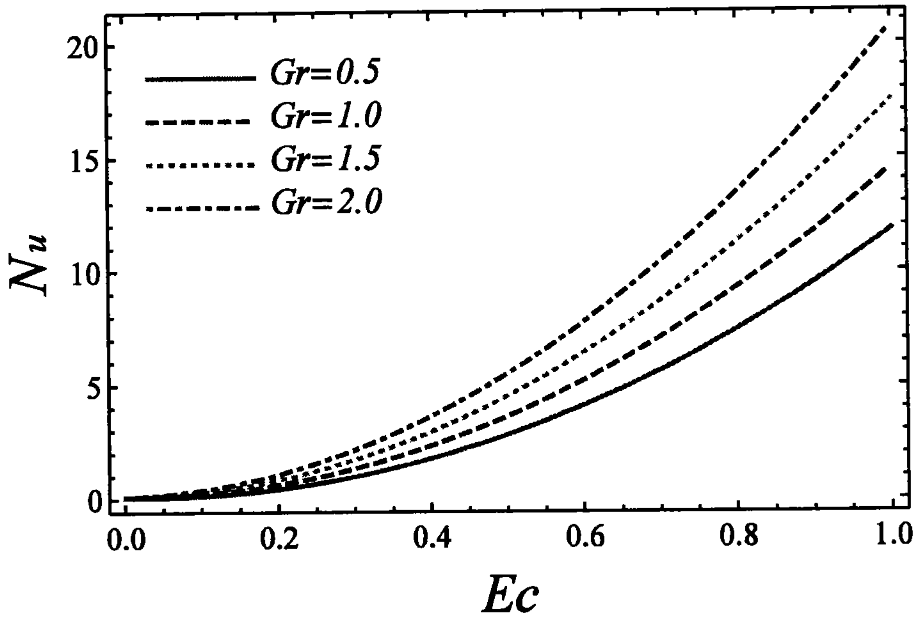

Figure 5.8(left): Nu plotted against Ec and Gr.

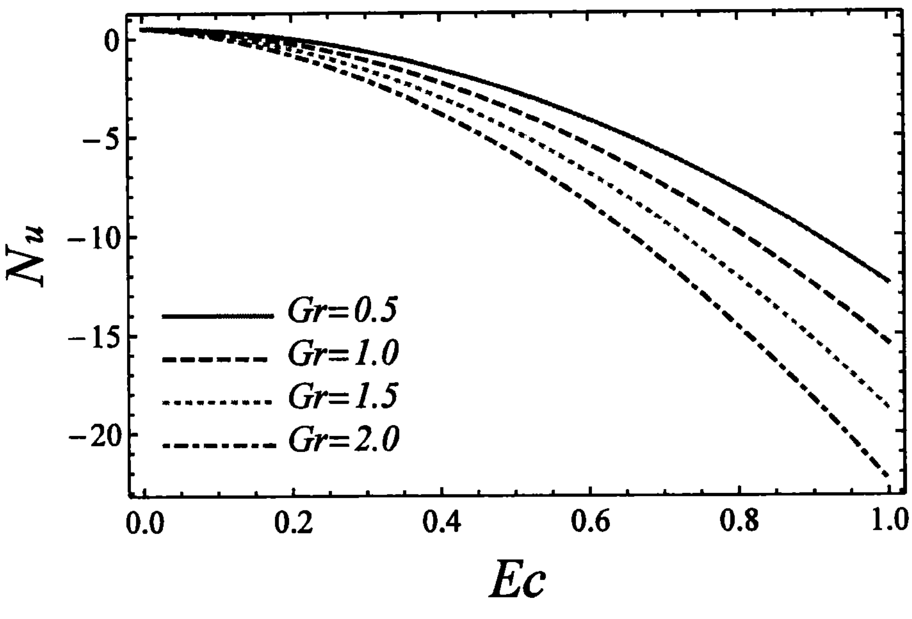

Figure 5.8(right): Nu plotted against Ec and Gr.

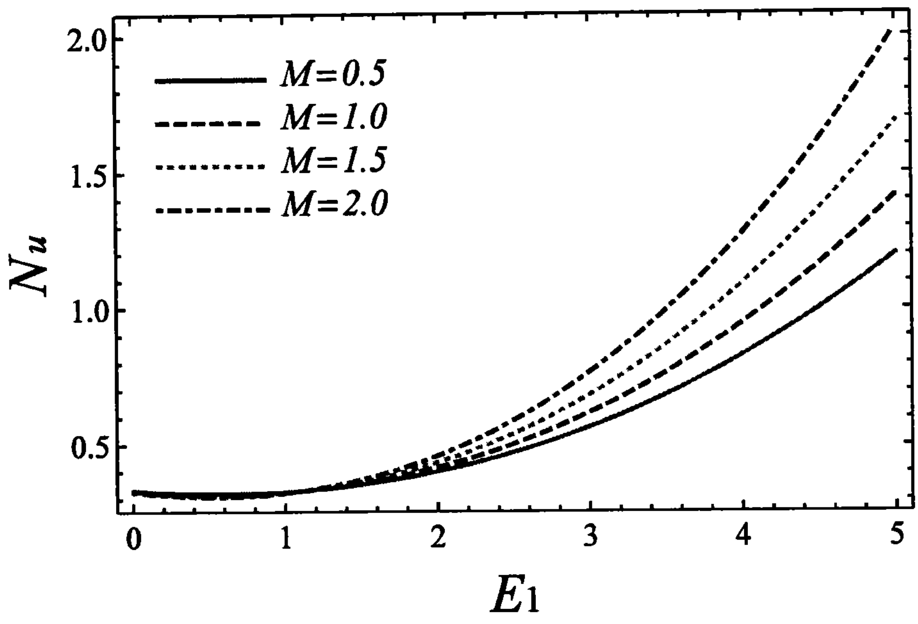

Figure 5.8(left): *Nu* plotted against E_1 and M .

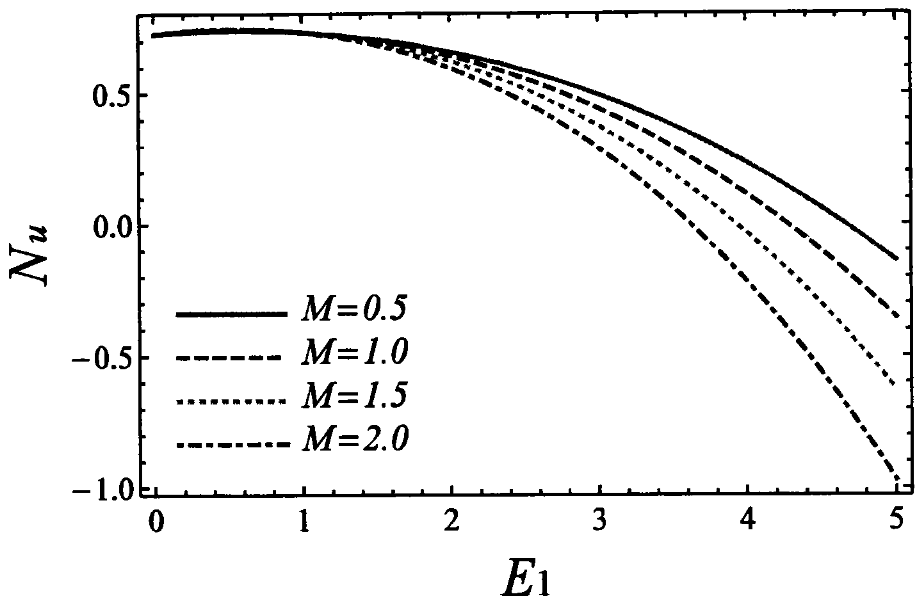

Figure 5.8(right): *Nu* plotted against E_1 and M .

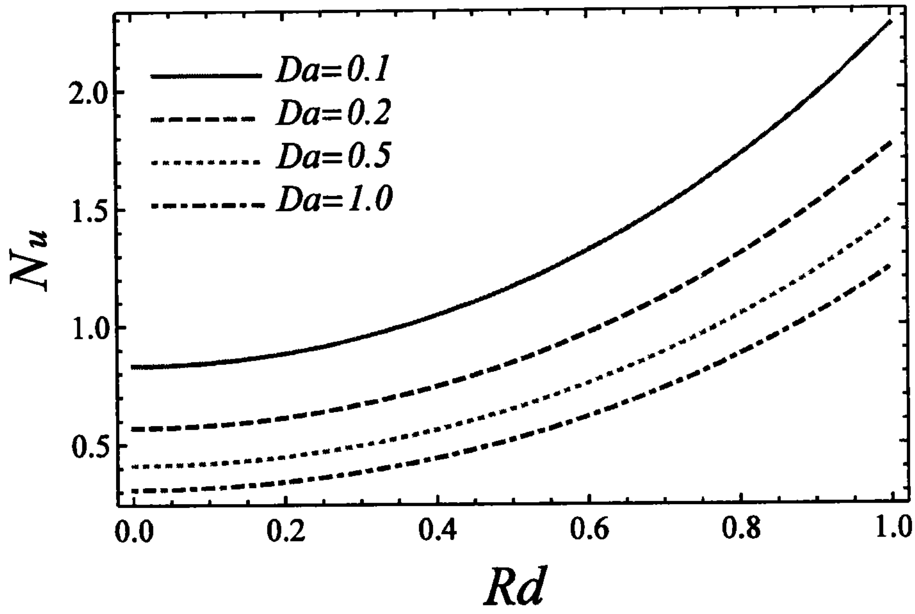

Figure 5.8(left): *Nu* plotted against *Rd* and *Da*.

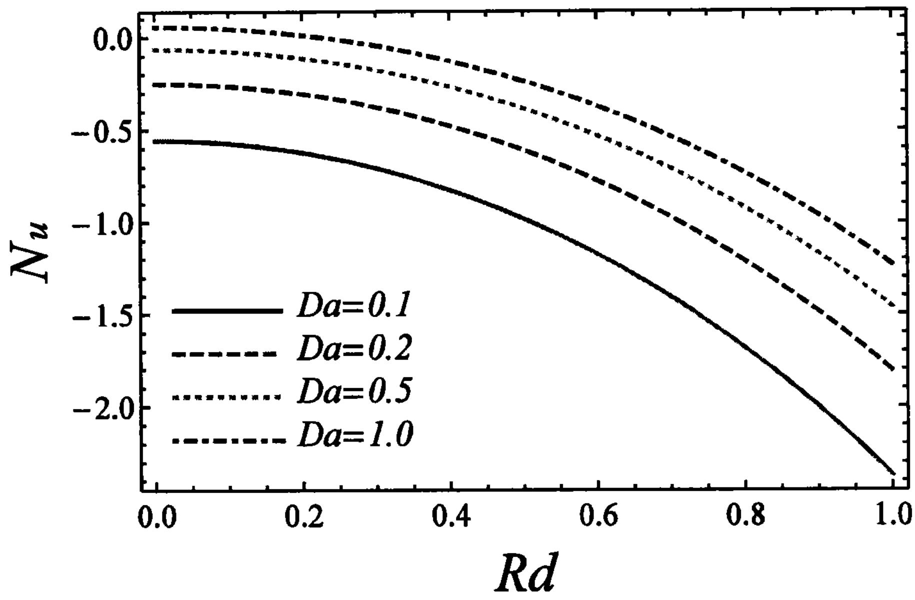

Figure 5.8(right): *Nu* plotted against *Rd* and *Da*.

5.4 Conclusions

This chapter successfully addresses the influence of heat on convective boundary layer flow. Flow is generated by solely the exertion of pressure on the fluid inside the wavy channel of some width. The role of parameter concern with momentum and heat along with particle flux are presented through figures in order to vet obtained results. Some such result are highlighted as:

- Velocity profile of nanofluid near center of channel decreases with increase of M , Da and Rd while it increases in the vicinity of walls.
- Temperature profiles of nanofluid enhance for large values of M , Da and Rd .
- Skin friction is rising for Gr and Ec at left wall while it decelerating at right wall.
- Skin friction declines with increase of M , E_1 , Da and Rd at the left of the channel while a quite contradictory results are noted at right wall.
- Nusselt number rises for large values of Gr , Ec , M and E_1 at left of channel whereas it decreases at right of the channel.
- Nusselt number is decreased for dissimilar values of Da and Rd at left of channel however opposite trend at right of channel.

Chapter 6

6 Modelling study on internal energy loss due to entropy generation for non-Darcy Poiseuille flow of silver-water nanofluid: An application of purification

In this paper, an analytical study of internal energy losses for the Forchheimer Poiseuille flow of Ag-H_2O nanofluid due to entropy generation in porous media is investigated. Spherical-shaped silver nanosize particles with volume fraction 0.3%, 0.6%, and 0.9% are utilized. Four illustrative models are considered: (i) heat transfer irreversibility (HTI), (ii) fluid friction irreversibility (FFI), (iii) Joule dissipation irreversibility (JDI), and (iv) non-Darcy porous media irreversibility (NDI). Basic governing equations are simplified by taking long wavelength approximations on the channel walls. The results represent nonlinear together with flow and heat differential coupled equations that are solved analytically with homotopy analysis method. It is shown that for minimum and maximum averaged entropy generation, 0.3% by vol and 0.9% by vol of nanoparticles, respectively, are observed. Also, a rise in entropy is evident due to an increase in pressure gradient. The current analysis provides an adequate theoretical estimate for low-cost purification of drinking water by silver nanoparticles in an industrial process.

6.1 Problem formulation

6.1.1 Flow analysis

Consider two-dimensional steady, laminar incompressible viscous Poiseuille flow nanofluid between two horizontal symmetric wavy walls (channels), as presented in figure 6.1. The middle of channel taken at origin and the configuration of the walls (left and right) with amplitude a_1, width d, length L of the walls and wavelength λ which is proportional to $2\pi/L$. The configuration of the left and right walls are defined as, respectively

$$H_1 = -d - a_1 \cos\left(\frac{2\pi}{L}\bar{x}\right), \quad H_2 = d + a_1 \cos\left(\frac{2\pi}{L}\bar{x}\right). \tag{6.1}$$

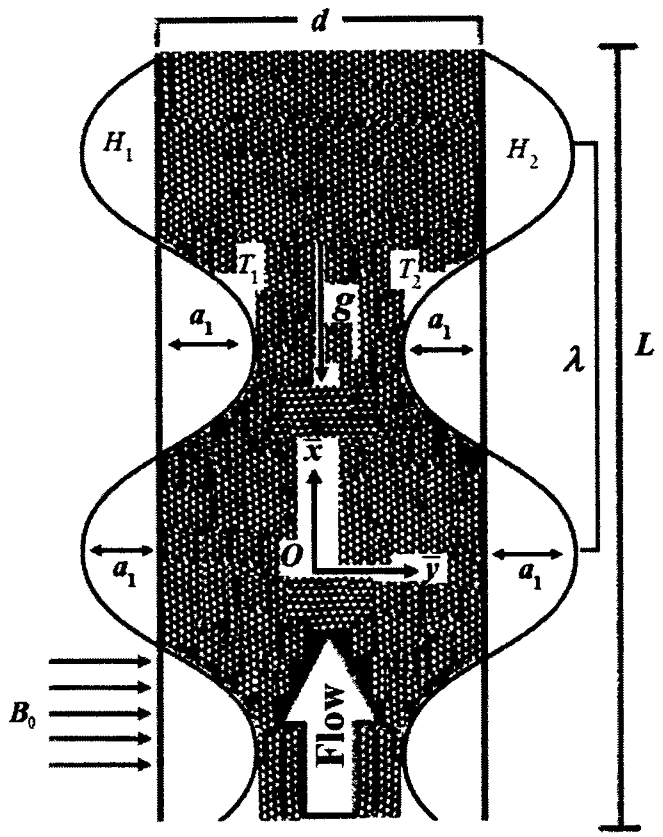

Figure 6.1: Geometry of the flow model.

6.1.2 Governing equations (Tiwari and Das's model)

According to said nanofluid model, the equations (1.18), (1.19) and (1.38) given in chapter 1, for a steady state, incompressible nanofluid with effect of electric, magnetic, buoyancy, viscous and Ohmic dissipation transporting through a porous medium with non-Darcy Forchheimer correction is mathematically modeled as

$$\frac{\partial \bar{u}}{\partial \bar{x}}+\frac{\partial \bar{v}}{\partial \bar{y}}=0, \tag{6.2}$$

$$\rho_{nf}\left(\bar{u}\frac{\partial \bar{u}}{\partial \bar{x}}+\bar{v}\frac{\partial \bar{u}}{\partial \bar{y}}\right)=-\frac{\partial \bar{p}}{\partial \bar{x}}+\mu_{nf}\left(\frac{\partial^2 \bar{u}}{\partial \bar{x}^2}+\frac{\partial^2 \bar{u}}{\partial \bar{y}^2}\right)-\sigma_{nf}B_0^2\bar{u}-\frac{\mu_{nf}}{K_1}\bar{u}-\rho_{nf}F_c\bar{u}^2+(\rho\beta)_{nf}\,g\left(\bar{T}-T^*\right), \tag{6.3}$$

$$\left(\rho C_p\right)_{nf}\left(\bar{u}\frac{\partial T}{\partial \bar{x}}+\bar{v}\frac{\partial T}{\partial \bar{y}}\right)=k_{nf}\left(\frac{\partial^2 T}{\partial \bar{x}^2}+\frac{\partial^2 T}{\partial \bar{y}^2}\right)+(\mu)_{nf}\left[\left(\frac{\partial \bar{u}}{\partial \bar{x}}\right)^2+\left(\frac{\partial \bar{u}}{\partial \bar{y}}\right)^2\right]+\sigma_{nf}B_0^2\bar{u}^2. \tag{6.4}$$

The appropriate boundary conditions are

$$\left.\begin{array}{l}\bar{u}=0,\ \bar{v}=0,\ T=T_2\ \text{at}\ \bar{y}=H_2\\ \bar{u}=0,\ \bar{v}=0,\ T=T_1\ \text{at}\ \bar{y}=H_1\end{array}\right\}. \tag{6.5}$$

Let us acquaint the following nondimensional quantities

$$\left.\begin{array}{l}x=\dfrac{\bar{x}}{\lambda},\ y=\dfrac{\bar{y}}{d},\ u=\dfrac{\bar{u}}{U_m},\ v=\dfrac{\bar{v}}{U_m\delta},\ h_1=\dfrac{H_1}{d},\ h_2=\dfrac{H_2}{d},\\ p=\dfrac{d^2\bar{p}}{\mu_f U_m\lambda},\ \delta=\dfrac{d}{\lambda},\ \theta=\dfrac{T-T^*}{T_1-T^*},\ m^*=\dfrac{T_2-T^*}{T_1-T^*}\end{array}\right\}. \tag{6.6}$$

Hence, governing equations (6.2) to (6.4) become

$$\delta\frac{\partial u}{\partial x}+\frac{\partial v}{\partial y}=0, \tag{6.7}$$

$$A_2 Re\delta\left(u\frac{\partial u}{\partial x}+v\frac{\partial u}{\partial y}\right)=A_1\left[-\frac{\partial p}{\partial x}+\left(\delta^2\frac{\partial^2 u}{\partial x^2}+\frac{\partial^2 u}{\partial y^2}\right)\right]-A_3M^2u-\frac{A_1}{Da}u-A_2F*u^2+A_4Gr\theta, \quad (6.8)$$

$$A_5 RePr\delta\left(u\frac{\partial \theta}{\partial x}+v\frac{\partial \theta}{\partial y}\right)=A_6\left(\delta^2\frac{\partial^2 \theta}{\partial x^2}+\frac{\partial^2 \theta}{\partial y^2}\right)+A_3EcPrM^2u^2+A_1EcPr\left(\frac{\partial u}{\partial y}\right)^2. \quad (6.9)$$

By applying the theory of long wavelength approximation, equations (6.7) to (6.9) become

$$-A_1P+A_1\frac{\partial^2 u}{\partial y^2}-A_3M^2u-\frac{A_1}{Da}u-A_2F*u^2+A_4Gr\theta=0, \quad (6.10)$$

$$A_6\frac{\partial^2 \theta}{\partial y^2}+A_3BrM^2u^2+A_1Br\left(\frac{\partial u}{\partial y}\right)^2=0. \quad (6.11)$$

Boundary conditions are

$$\left.\begin{array}{l} u=0,\ \theta=m^*\ \text{ at } y=h_2=1+\frac{a}{d}\text{Cos}\left(\frac{2\pi\lambda}{L}x\right) \\ u=0,\ \ \theta=1\ \ \text{ at } y=h_1=-1-\frac{a}{d}\text{Cos}\left(\frac{2\pi\lambda}{L}x\right) \end{array}\right\}, \quad (6.12)$$

where

$$\left.\begin{array}{l} Gr=\frac{(\rho\beta)_f gd^2(T_1-T^*)}{\mu_f U_m}, \text{Re}=\frac{\rho_f U_m d}{\mu_f}, M^2=\frac{\sigma_f B_0^2 d^2}{\mu_f}, Da=\frac{K_1}{d^2}, Br=\Pr Ec \\ \Pr=\frac{\mu_f(\rho C_p)_f}{\rho_f k_f}, Ec=\frac{U_m^2}{(C_p)_f(T_1-T^*)}, Rd=\frac{16T^{*3}\sigma^*}{3k^*k_f}, F^*=\frac{\rho_f F_c d^2 U_m}{\mu_f} \\ A_1=\frac{\mu_{nf}}{\mu_f},\ A_2=\frac{\rho_{nf}}{\rho_f},\ A_3=\frac{\sigma_{nf}}{\sigma_f}, A_4=\frac{(\rho\beta)_{nf}}{(\rho\beta)_f}, A_5=\frac{(\rho C_p)_{nf}}{(\rho C_p)_f},\ A_6=\frac{k_{nf}}{k_f} \end{array}\right\}. \quad (6.13)$$

The physical thermal properties using in above system of equations are define in equations (1.9), (1.10) and (1.11). The nanofluid viscosity μ_{nf} and thermal conductivity k_{nf} at minimum value of concentration (0.3, 0.6, and 0.9%) with temperature between 323 K and 363 K are defined in equations (1.4) and (1.7).

Expression of coefficient of skin friction defined in equation (1.54) and Nusselt number defined in equation (1.56) are transformed in view of equation (6.6) as

$$\left.\begin{aligned} \operatorname{Re} C_f &= 2A_1 u'(y)\,\big|_{y=h_1,h_2} \\ Nu &= -A_6\theta'(y)\big|_{y=h_1,h_2} \end{aligned}\right\}. \tag{6.14}$$

6.1.3 Entropy generation analysis

For non-Darcy porous media, energy loss due to entropy generation for the case of heat in the presence of a magnetic field is described as

$$E_G = \underbrace{\frac{k_{nf}}{T^{*2}}\left(\frac{\partial T}{\partial y}\right)^2}_{\text{entropy due to heat transfer}} + \underbrace{\frac{\mu_{nf}}{T^*}\left(\frac{\partial \bar{u}}{\partial y}\right)^2}_{\text{entropy due to fluid friction}} + \underbrace{\frac{\sigma_{nf} B^2{}_0 \bar{u}^2}{T^*}}_{\text{entropy due to magnetic field}} + \underbrace{\frac{1}{T^*}\left(\frac{\mu_{nf}}{K} + \rho_{nf} F_c\, \bar{u}\right)\bar{u}^2}_{\text{entropy due to non-Darcy porous media}}. \tag{6.15}$$

Equation (6.15) comprises four parts, the first term on the right-hand side is entropy generation due to the contribution of thermal irreversibility that is due to axial conduction from the wavy surface, the second term describes how friction resists the flow, the third term denotes the movement of electrically conducting fluid under the consideration of magnetic field induces an electric current that circulates in the fluid, and the last one is energy loss due to non-Darcy porous media, which occurs due to the flow rate in porous media. The entropy generation number is similar to the entropy generation rate, which shows the ratio between the local entropy generation rate and the characteristic entropy generation rate E_{G_0}. Mathematically, one can write it as

$$E_{G_0} = \frac{k_{nf}\,(T_1 - T^*)^2}{d^2 T^{*2}}, \tag{6.16}$$

$$N_G = \frac{E_G}{E_{G_0}}, \tag{6.17}$$

where N_G is the dimensional entropy generation

$$N_G = \frac{d^2 T^{*2}}{k_{nf}\left(T_1 - T^*\right)^2} \times \left[\frac{k_{nf}}{T^{*2}}\left(\frac{\partial \bar{T}}{\partial \bar{y}}\right)^2 + \frac{\mu_{nf}}{T^*}\left(\frac{\partial \bar{u}}{\partial \bar{y}}\right)^2 + \frac{1}{T^*}\left(\frac{\mu_{nf}}{K} + \rho_{nf} F_c\, \bar{u}\right)\bar{u}^2 \right], \tag{6.18}$$

hence, the dimensionless entropy generation number N_G is obtained as

$$N_G = \left(\frac{\partial \theta}{\partial y}\right)^2 + \frac{A_1}{A_6}\frac{Br}{\Omega}\left(\frac{\partial u}{\partial y}\right)^2 + \frac{A_3}{A_6}\frac{MBr}{\Omega}u^2 + \frac{A_1}{A_6}\frac{Br}{\Omega Da}u^2 + \frac{A_2}{A_6}\frac{F^* Br}{\Omega}u^3, \tag{6.19}$$

where

$$\Omega = \frac{T_1 - T^*}{T^*}, \quad Br = \frac{\mu_f U_m^2}{k_f\left(T_1 - T^*\right)}. \tag{6.20}$$

The dominance of the entropy procedure is essential due to the feebleness of the entropy generation number, so the Bejan number Be is employed to comprehend the possible mechanism. Mathematically, it can be defined as follows

$$Be = \frac{\text{Entropy generation due to heat transfer}}{\text{Total entropy generation}}, \text{ i.e., } Be = \frac{HTI}{HTI + FFI + JDI + NDI}, \tag{6.21}$$

$$HTI = \left(\frac{\partial \theta}{\partial y}\right)^2, FFI = \frac{A_1}{A_6}\frac{Br}{\Omega}\left(\frac{\partial u}{\partial y}\right)^2, JDI = \frac{A_3}{A_6}\frac{MBr}{\Omega}u^2, NDI = \frac{A_1}{A_6}\frac{Br}{\Omega Da}u^2 + \frac{A_2}{A_6}\frac{F^* Br}{\Omega}u^3. \tag{6.22}$$

In view of equation (6.6), the equation (6.21) becomes

$$Be = \frac{\left(\frac{\partial \theta}{\partial y}\right)^2}{\left(\frac{\partial \theta}{\partial y}\right)^2 + \frac{A_1}{A_6}\frac{Br}{\Omega}\left(\frac{\partial u}{\partial y}\right)^2 + \frac{A_3}{A_6}\frac{MBr}{\Omega}u^2 + \frac{A_1}{A_6}\frac{Br}{\Omega Da}u^2 + \frac{A_2}{A_6}\frac{F^* Br}{\Omega}u^3}. \tag{6.23}$$

It is understood from equation (6.22) that $Be \in [0,1]$. When the Bejan number = zero, the heat transfer irreversibility is negligible. When the Bejan number < 0.5, irreversibility by viscous effects dominates. In the case where the Bejan number = 0.5, the sum of fluid friction, Joule dissipation, and non-Darcy porous media irreversibility is double the heat transfer irreversibility. When the Bejan number > 0.5, the entropy due to heat transfer leads to dominance over entropy due to fluid friction, magnetic field, and non-Darcy porous media irreversibility. When the Bejan number = 1, then HTI is considered as like viscous effects. The average entropy generation number is computed by following dimensionless relation

$$N_{G\_avg} = \frac{1}{\forall}\int_{\forall} N_G \, d\forall = \frac{1}{\forall}\int_z\int_y\int_x N_G \, dx\, dy\, dz, \tag{6.24}$$

here

$$N_{G\_avg} = \frac{1}{\forall}\int_{h_1}^{h_2} N_G \, dy, \tag{6.25}$$

or

$$N_{G\_avg} = \frac{1}{\forall}\int_{h_1}^{h_2} (HTI + FFI + JDI + NDI)\, dy, \tag{6.26}$$

where $\forall$ denotes the area of geometry. The volume triple integral (equation (6.24)) reduces to a line integral due to unidirectional flow. The average energy loss due to entropy generation from fluid flow and heat transfer components can be calculated for a large finite domain, but in this scenario, we obtained average entropy generation in the domain h_1 and h_2, as shown by equation (6.26).

6.2 Solution of the problem

To get an analytic solution, a homotopy technique is utilized to solve equations (6.10) and (6.11).

Zeroth–order solution

Assume, initial guesses $u_0(y)$, $\theta_0(y)$ and supplementary linear operators $\pounds_u$, $\pounds_\theta$ for velocity and temperature are

$$\left.\begin{aligned} u_0(y) &= y^2-(h_1+h_2)y+(h_1h_2) \\ \theta_0(y) &= \frac{y-h_2}{h_1-h_2} \end{aligned}\right\} \tag{6.27}$$

and

$$\pounds_u=\frac{d}{dy}\left(\frac{du}{dy}\right),\quad \pounds_\theta=\frac{d}{dy}\left(\frac{d\theta}{dy}\right). \tag{6.28}$$

The convergence control parameters $\hbar_u$, $\hbar_\theta$ and nonlinear operators N_u, N_θ of velocity, temperature with embedding parameter $\xi\in[0,\ 1]$ yields the following zeroth-order deformations respectively are

$$\left.\begin{aligned} (1-\xi)\pounds_u\left[u(y,\xi)-u_0(y)\right] &= \xi\hbar_u N_u\left[u(y,\xi),\theta(y,\xi)\right] \\ (1-\xi)\pounds_\theta\left[\theta(y,\xi)-\theta_0(y)\right] &= \xi\hbar_\theta N_\theta\left[u(y,\xi),\theta(y,\xi)\right] \end{aligned}\right\} \tag{6.29}$$

with boundary conditions

$$\left.\begin{aligned} u(y,\xi)=0,\ \theta(y,\xi)=m^* \quad & \text{at } y=h_2 \\ u(y,\xi)=0,\ \theta(y,\xi)=1 \quad & \text{at } y=h_1 \end{aligned}\right\} \tag{6.30}$$

and

$$\left.\begin{aligned} N_u &= A_1\left[-P+\frac{\partial^2 u(y,\xi)}{\partial y^2}\right]-A_3M^2u(y,\xi)-\frac{A_1}{Da}u(y,\xi)-A_2F^*u^2(y,\xi)+A_4\frac{Gr}{\mathrm{Re}}\theta(y,\xi) \\ N_\theta &= A_6\frac{\partial^2\theta(y,\xi)}{\partial y^2}+A_3BrM^2u^2(y,\xi)+A_1Br\left(\frac{\partial u(y,\xi)}{\partial y}\right)^2 \end{aligned}\right\}. \tag{6.31}$$

l th–order solution

The l th –order deformation expression for $u_l(y)$ and $\theta_l(y)$ as follows

$$\left.\begin{aligned} \pounds_u\left[u_l(y)-\chi_l u_{l-1}(y)\right] &= \hbar_u R_l^u(y) \\ \pounds_\theta\left[\theta_l(y)-\chi_l\theta_{l-1}(y)\right] &= \hbar_\theta R_l^\theta(y) \end{aligned}\right\}, \tag{6.32}$$

$$\left.\begin{array}{l} u_l(y,\xi)=0,\ \ \theta_l(y,\xi)=m^*\ \text{ at } y=1 \\ u_l(y,\xi)=0,\ \ \theta_l(y,\xi)=1\ \text{ at } y=-1 \end{array}\right\}, \tag{6.33}$$

$$\left.\begin{array}{l} R_l^u(y)=A_1\left[-P+u_l''\right]-A_3M^2u_l-\dfrac{A_1}{Da}u_l-A_2F^*u_l^2+A_4Gr\theta_l \\ R_l^\theta(y)=A_6\theta_l''+A_3BrM^2u_l^2+A_1Br\sum\limits_{k=0}^{l}u_k'u_{l-k}' \end{array}\right\}. \tag{6.34}$$

The solution can be described as of l th–order

$$\left.\begin{array}{l} u(y)=u_0(y)+\sum\limits_{k=1}^{l}u_k(y) \\ \theta(y)=\theta_0(y)+\sum\limits_{k=1}^{l}\theta_k(y) \end{array}\right\}. \tag{6.35}$$

The solutions at second-order iterations by utilizing the Mathematica package BVPh2.0 based on the HAM can be expressed for velocity and temperature as

$$u(y)=C_1+C_2y+C_3y^2+C_4y^3+C_5y^4+C_6y^5+C_7y^6+C_8y^7+C_9y^8+C_{10}y^{10}, \tag{6.36}$$

$$\theta(y)=D_1+D_2y+D_3y^2+D_4y^3+D_5y^4+D_6y^5+D_7y^6+D_8y^7+D_9y^8+D_{10}y^{10}. \tag{6.37}$$

Coefficients of polynomial equation (6.40) are

$$\begin{aligned} C_1 = {} & -1-3A_1\hbar_u-\frac{5A_1}{6Da}\hbar_u+\frac{11A_2F^*}{15}\hbar_u-\frac{A_4Gr}{2}\hbar_u+\frac{7A_1A_2BrGr}{45}\hbar_u\hbar_\theta-\frac{3A_1^2}{2}\hbar_u^2-\frac{61A_1^2}{360Da^2}\hbar_u^2- \\ & \frac{25A_1^2\hbar_u^2}{24Da}+\frac{22A_1A_2F^*\hbar_u^2}{15}+\frac{25A_1A_2F^*\hbar_u^2}{56Da}-\frac{4919A_2^2F^*\hbar_u^2}{18900}-\frac{A_1A_4Gr\hbar_u^2}{4}-\frac{5A_1A_4Gr\hbar_u^2}{48Da}+A_3M^2\hbar_u^2 \\ & \frac{11A_2A_4F^*Gr\hbar_u^2}{60}+\frac{739A_3A_4BrGrM^2}{5040}\hbar_u\hbar_\theta+\frac{A_1A_3M^2\hbar_u^2}{2}+\frac{5A_1A_3M^2}{24Da}\hbar_u^2-\frac{11A_2A_3F^*M^2}{30}\hbar_u^2, \end{aligned}$$

$$C_2=\frac{1}{6}A_4Gr\hbar_u+\frac{1}{12}A_1A_4Gr\hbar_u^2+\frac{7A_1A_4Gr}{720Da}\hbar_u^2-\frac{19A_2A_4F^*Gr}{1260}\hbar_u^2,$$

$$\begin{aligned} C_3 = {} & 1+3A_1\hbar_u+\frac{A_1}{Da}\hbar_u-A_2F^*\hbar_u+\frac{1}{2}A_4Gr\hbar_u-\frac{1}{6}A_1A_4BrGr\hbar_u\hbar_\theta+\frac{3}{2}A_1^2\hbar_u^2+\frac{5A_1^2}{24Da^2}\hbar_u^2- \\ & \frac{5A_1^2}{4Da}\hbar_u^2-2A_1A_2F^*\hbar_u^2-\frac{3A_1A_2F^*}{5Da}\hbar_u^2+\frac{11}{30}A_2^2F^{*2}\hbar_u^2+\frac{1}{4}A_1A_4Gr\hbar_u^2+\frac{1}{4}A_1A_4F^*Gr\hbar_u^2- \\ & A_3M^2F^*\hbar_u-\frac{11}{60}A_3A_4BrGrM\hbar_u\hbar_\theta-\frac{1}{2}A_1A_3M^2\hbar_u^2-\frac{1}{4Da}A_1A_3M^2\hbar_u^2+\frac{1}{2}A_2A_3F^*M^2\hbar_u^2, \end{aligned}$$

$$C_4 = -\frac{1}{6}A_4 Gr\hbar_u,$$

$$C_5 = -\frac{A_1^2}{24Da}\hbar_u^2 - \frac{5A_1^2}{24Da}\hbar_u^2 - \frac{2}{3}A_1A_2F^*\hbar_u^2 + \frac{7A_1A_2F^*}{36Da}\hbar_u^2 - \frac{13}{90}A_2^2F^{*2}\hbar_u^2 - \frac{A_1A_4Gr}{48Da}\hbar_u^2 +$$
$$\frac{1}{12}A_4A_2F^*Gr\hbar_u^2 + \frac{1}{24}A_3A_4BrGrM^2\hbar_u\hbar_\theta + \frac{1}{24Da}A_1A_3M^2\hbar_u^2 - \frac{1}{6}A_3A_2F^*M^2\hbar_u^2,$$

$$C_6 = \frac{A_4A_1Gr}{240Da}\hbar_u^2 - \frac{1}{60}A_4A_2F^*Gr\hbar_u^2,$$

$$C_7 = A_2F^*\hbar_u + \frac{1}{90}A_1A_4BrGr\hbar_u\hbar_\theta + \frac{A_1^2}{360Da^2}\hbar_u^2 - \frac{2}{15}A_1A_2F^*\hbar_u^2 - \frac{2A_1A_2F^*}{45Da}\hbar_u^2 + \frac{2A_2^2}{45}F^{*2}\hbar_u^2 -$$
$$\frac{1}{60}A_4A_2F^*\hbar_u^2 - \frac{1}{180}A_3A_4GrBrM^2\hbar_u\hbar_\theta + \frac{1}{30}A_3A_2F^*M^2\hbar_u^2,$$

$$C_8 = \frac{1}{252}A_4A_2F^*Gr\hbar_u^2,\ C_9 = \frac{A_1A_2F^*}{280Da}\hbar_u^2 - \frac{A_2^2}{140}F^{*2}\hbar_u^2 + \frac{1}{1680}A_3A_4BrGrM^2\hbar_u\hbar_\theta,$$
$$C_{10} = \frac{A_2^2}{1350}F^{*2}\hbar_u^2.$$

Coefficients of polynomial equation (6.41) are

$$D_1 = \frac{1}{2} - \frac{2}{3}A_1Br\hbar_\theta - \frac{1}{3}A_1A_6Br\hbar_\theta^2 - \frac{13A_1^2Br}{45Da}\hbar_u\hbar_\theta + \frac{163A_1A_2BrF^*}{630}\hbar_u\hbar_\theta - \frac{11}{55}A_3BrM^2\hbar_u -$$
$$\frac{1}{6}A_1A_4BrGr\hbar_u\hbar_\theta - \frac{11}{30}A_3A_6BrM^2\hbar_\theta^2 - \frac{23}{30}A_1A_3BrM^2\hbar_u\hbar_\theta - \frac{1511}{5040Da}A_1A_3BrM^2\hbar_u\hbar_\theta +$$
$$A_1^2Br\hbar_u\hbar_\theta + \frac{4919}{18900}A_2A_3BrF^*M^2\hbar_u\hbar_\theta - \frac{11}{60}A_4A_3BrGrM^2\hbar_u\hbar_\theta + \frac{11}{30}A_3^2BrM^2\hbar_u\hbar_\theta,$$

$$D_2 = -\frac{1}{2} + \frac{1}{180}A_1A_4BrGrM^2\hbar_u\hbar_\theta + \frac{19}{1260}A_3A_4BrGrM^2\hbar_u\hbar_\theta,$$

$$D_3 = +A_3BrM^2\hbar_\theta + \frac{1}{2}A_3A_6BrM^2\hbar_\theta^2 + \frac{3}{2}A_3A_1BrM^2\hbar_u\hbar_\theta + \frac{5}{12Da}A_3A_1BrM^2\hbar_u\hbar_\theta -$$
$$\frac{11}{30}A_3A_2BrF^*M^2\hbar_u\hbar_\theta + \frac{1}{4}A_3A_4BrGrM^2\hbar_u\hbar_\theta - \frac{1}{2}A_3^2BrM^4\hbar_1\hbar_2,$$

$$D_4 = \frac{1}{18}A_1A_4BrGr\hbar_u\hbar_\theta - \frac{1}{36}A_3A_4BrGrM^2\hbar_u\hbar_\theta,$$

$$D_5 = +\frac{2}{3}A_1Br\hbar_\theta + \frac{1}{3}A_1A_6Br\hbar_\theta^2 + \frac{1}{3Da}A_1^2Br\hbar_1\hbar_2 - \frac{1}{3}A_1A_2BrF*\hbar_u\hbar_\theta + \frac{1}{6}A_1A_4BrGr\hbar_u\hbar_\theta -$$
$$\frac{1}{3}A_3BrM^2\hbar_\theta - \frac{1}{6}A_3A_6BrM^2\hbar_\theta^2 - \frac{5}{6}A_1A_3BrM^2\hbar_u\hbar_\theta + A_1^2Br\hbar_1\hbar_2 - \frac{11}{72Da}A_1A_3BrM^2\hbar_u\hbar_\theta +$$
$$\frac{13}{90}A_2A_3BrF*M^2\hbar_u\hbar_\theta - \frac{1}{12}A_3A_4BrGrM^2\hbar_u\hbar_\theta + \frac{1}{6}A_3^2BrM^4\hbar_1\hbar_2,$$

$$D_6 = -\frac{1}{20}A_1A_4BrGr\hbar_u\hbar_\theta + \frac{1}{60}A_3A_4BrGrM^2\hbar_u\hbar_\theta,$$
$$D_7 = -\frac{2}{45}A_1^2Br\hbar_1\hbar_2 + \frac{4}{45}A_1A_2BrF*\hbar_u\hbar_\theta + \frac{1}{30}A_3A_6BrM^2\hbar_\theta^2 + \frac{7}{180Da}A_1A_3BrM^2\hbar_u\hbar_\theta +$$
$$\frac{1}{10}A_1A_3BrM^2\hbar_u\hbar_\theta - \frac{2}{45}A_3A_2BrF*M^2\hbar_u\hbar_\theta + \frac{1}{15}A_3BrM^2\hbar_\theta + \frac{1}{60}A_3A_4BrGrM^2\hbar_u\hbar_\theta -$$
$$\frac{1}{30}A_3^2BrM^4\hbar_1\hbar_2,$$

$$D_8 = -\frac{1}{252}A_3A_4BrGrM^2\hbar_u\hbar_\theta,$$
$$D_9 = -\frac{1}{70}A_1A_2BrF*\hbar_u\hbar_\theta - \frac{1}{336}A_1A_3BrM^2\hbar_u\hbar_\theta + \frac{1}{140}A_3A_2BrF*M^2\hbar_u\hbar_\theta,$$
$$D_{10} = -\frac{1}{1350}A_3A_2BrF*M^2\hbar_u\hbar_\theta.$$

6.3 Discussion of results

6.3.1 Inspection of convergence

The admissible convergence range of both auxiliary parameters $\hbar_u$ and $\hbar_\theta$ that arises in equation (6.35) is very important for an analytic solution. The suitable range for $\hbar-$curves are found at 20th-order of approximations. The range for best values of $\hbar_u$ and $\hbar_\theta$ are estimated as $-1.3 \le \hbar_u \le -0.4$ and $-1.3 \le \hbar_\theta \le -0.3$, respectively.

6.3.2 Residual error of norm 2

The residual error of velocity E_u and temperature distribution E_θ at two successive approximations over embedding parameter $\xi \in [0, 1]$ up to the 20th-order approximations is computed by the following mathematical relations

$$E_u = \sqrt{\frac{1}{21}\sum_{i=0}^{20}\left(u(i/20)\right)^2}, \quad E_\theta = \sqrt{\frac{1}{21}\sum_{i=0}^{20}\left(\theta(i/20)\right)^2}. \tag{6.38}$$

The above residual formulas give the minimum error at $\hbar_u = -0.7$ for velocity and $\hbar_\theta = -0.6$ for temperature distribution at $\hbar_\theta = -0.6$, which are displayed in figures 6.2 and 6.3, respectively. Table 6.1 shows residual error for the convergence series solution up to the 20th-order approximation.

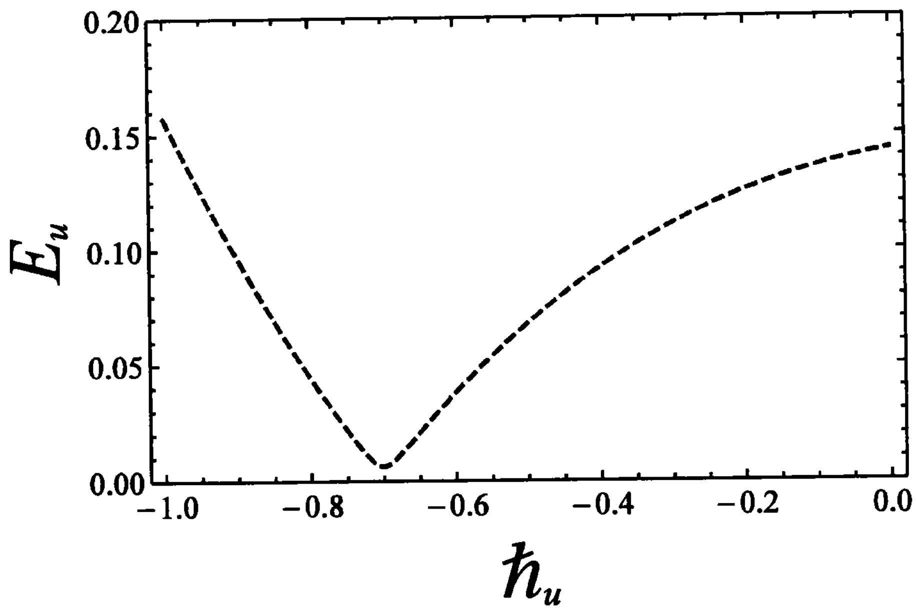

Figure 6.2: Residual error E_u −curve for velocity profile.

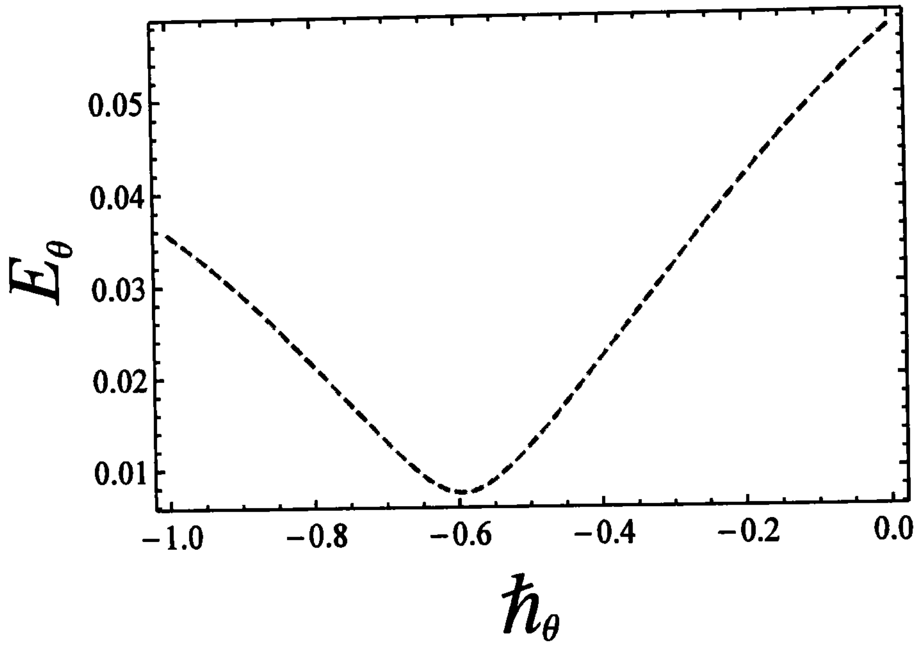

Figure 6.3: Residual error E_θ −curve for temperature profile.

Table 6.1: Residual error (RE) of series solutions when $Gr = 0.5$, $Br = 1$, $F^* = 1$, $Da = 2$, and $M = 0.2$.

Order of approximation	Time	E_u	E_θ
05	8.2651	1.3340×10^{-3}	2.3980×10^{-3}
10	35.1732	7.4001×10^{-5}	3.2385×10^{-6}
15	67.9793	1.5624×10^{-8}	3.5705×10^{-9}
20	187.6291	1.6199×10^{-12}	4.7723×10^{-14}
25	296.1218	1.7193×10^{-16}	1.7037×10^{-17}

6.3.3 Illustration of graphical results

This section describes the role of various parameters on nanoparticle volume fraction, MHD parameter, entropy generation, Darcy number, non-Darcy parameter, Brinkman number, group parameter, Eckert number, Grashof number, Reynolds number, Prandtl number, Bejan number, skin friction, and Nusselt number. Figures 6.4 to 6.7 represent the impact of M, Da, F^*, and Br on velocity as well as temperature. Moderately high temperature is used to perform the simulations. The temperature at the right and left walls is assumed to be 323 K and 363 K, respectively, in this study. Moreover, high temperature in the range of 323 K to 363 K is used in the inlet section of the channel according to the Godson nanofluid model. In figure 6.4(a)-(b), the manifestation of M on velocity and temperature is shown. The Lorentz force is developed by inflicting a vertical magnetic field on the electrically conducting nanofluid. The resultant Lorentz force has the ability to reduce the fluid velocity in confined geometry and causes an increase in temperature. Hence, values of M directly affect thermal boundary layer thickness, but velocity in flow direction decreases. In figure 6.5(a)-(b), the manifestation of Da on velocity and temperature is elaborated. The performance of the non-Darcy (Forchheimer) number F^* on velocity and temperature is shown in figure 6.6(a)-(b). It is detected that larger values of the Forchheimer number lead to a stronger thermal boundary layer and weaker momentum boundary layer thickness. In figure 6.7(a)-(b), the impact of the Brinkman number Br on velocity and temperature is shown. The impression of Br on velocity in figure 6.7(a) and at temperature in figure 6.7(b) are displayed.

Figures 6.8–6.11 represent the impact of M, Da, F^*, and $Br\Omega^{-1}$ on energy loss due to entropy generation and the Bejan number. In figure 6.8(a)-(b), the impression of M on entropy generation NG and the Bejan number Be is shown. Energy loss occurs in the system when Lorentz or drag force is created between the fluid and M. In figure 6.8(a), it is perceived that the influence of M energy loss is maximum at both walls and gradually decreases toward the center of the channel. Energy loss in the middle of the channel is almost zero, so it is detected that M is a major source of energy loss in the system, while the Bejan number gives the dominant decision about fluid friction, magnetic field, and non-Darcy porous media entropy over heat transfer entropy in the system and vice versa. Performance of the magnetic parameter M on Be is depicted in figure 6.8(b). It is perceived that the Bejan number at the center of channel becomes the extreme value when the magnetic field is neglected. In figure 6.9(a)-(b), the impact of Da on NG and Be is shown. A large increase in entropy generation is detected at the left wall as related to the right wall, with increase of Darcy number in figure 6.9(a). Also, the impact of Da the Bejan number is displayed in figure 6.9(b). It is perceived that the Bejan number at the center of the channel attained the extreme value when Da increased. The influence of the non-Darcy (Forchheimer) number F^* on entropy generation N_G in figure 6.10(a) and the Bejan number Be in figure 6.10(b) is presented. The same large increment in entropy generation is noticed at both left and right walls for different values of F^*, but also noticed is that the energy loss is zero nearby the middle of geometry for large values of Forchheimer parameter. The Bejan number for F^* can be observed in figure 6.10(b). It is analyzed that for Forchheimer number and Bejan number nearby the middle of geometry increases with the corresponding values of F^*. In figure 6.11(a)-(b) controlling effects of $Br\Omega^{-1}$ on energy loss due to N_G and Be is observed. As entropy is a function of the group parameter $Br\Omega^{-1}$, it contains the ratio of Br and Ω. The behavior of $Br\Omega^{-1}$ when $Br = 2$ and a mixed convection parameter $Gr = 0.5$ on energy loss is displaced in figure 6.11(a), which describes that increasing values of group parameter cause an enhancement of the buoyancy force in the system, and in response to this a large increase in entropy generation is detected at left wall as compared to right wall. Result of the group parameter with $Br = 2$ and $Gr = 0.5$ on the Bejan number is clearly elaborated in figure 6.11(b). The Bejan number attains its maximum value 1 at $y = 0.2$ due to enhanced in HTI with absence of the group parameter, but gradually decreases and has a value less than 1 toward both walls. This energy loss only occurs due to fluid heat transfer in a particular cross-section of the channel. Non-Darcy porous media irreversibility is introduced in average entropy generation for first time.

Figures 6.12–6.16 represent, in bar charts, the impact of φ, M, Da, F^*, and $Br\Omega^{-1}$ on average energy loss due to entropy generation. These bar charts are drawn at different pressure gradients ($P = -0.5$ and $P = -1.0$). In figure 6.12(a)-(b), it is seen that average entropy at both pressure gradients is gradually reduced with large amount of ϕ. In the case of a low concentration of silver nanoparticle sustained in the base fluid, when $\phi = 0.3\%$, the average entropy of the whole system is 0.4603 at $P = -0.5$ and 2.1762 at $P = -1.0$. Gradually, when the amount of silver nanoparticles increases in base fluid, it is clearly observed that the average energy loss due to entropy generation is increased. Nanoparticle concentration directly affects the fluid friction, Joule dissipation, and non-Darcy irreversibility, therefore FFI, JDI, and NDI are increased with dense ϕ. The average breakdown in entropy generation due to MHD directly affects Joule dissipation irreversibility, as given figure 6.13(a)-(b). It is realized in both figures that when the magnetic parameter M is zero, the Joule dissipation irreversibility vanishes, but as the magnetic parameter increases its values, the Joule dissipation irreversibility boosts up speedily. Observed that FFI is diminished for large values of the magnetic parameter at different pressure gradients. Non-Darcy porous media irreversibility depends on the Darcy number Da and the non-Darcy (Forchheimer) parameter $F*$, as given in figure 6.14(a)-(b) and 6.15(a)-(b). The Darcy number gives the opposite behavior of its increasing values via NDI. As the Darcy number increases, the average entropy and non-Darcy porous media irreversibility of the system decrease, while fluid friction, heat transfer, and Joule dissipation irreversibility boost up quickly for both pressure gradient cases. However, in figure 6.15(a)-(b), the non-Darcy (Forchheimer) parameter $F*$ gives the same trend for non-Darcy porous media irreversibility as the Darcy number in figure 6.14(a)-(b), because when the Darcy number is large, the flow tends to behave as a non-Darcy flow. For $Br = 1$, the variation of four group parameters $Br\Omega^{-1}$ on average entropy generation is given figure 6.16(a)-(b). Concluded that when $Br\Omega^{-1} = 0$, then 100% entropy loss occurs in heat transfer irreversibility, while there is no entropy loss in fluid friction, Joule dissipation, and non-Darcy porous media irreversibility. The magnitude of the average entropy generation rate is higher for higher values of $Br\Omega^{-1}$. The effects of concerned parameters are presented in Tables 6.2 and 6.3. It observed that C_f at both left as well as right walls arw decreases with increase of Da and $F*$, while Nu increases at right wall, but reduction is shown at left wall. Similar results for Gr and Br are deducted for Nusselt number at both walls, but C_f decreases at right wall while increasing at left. The behavior of C_f and Nu via magnetic field parameter M and φ are revealed in Tables 6.4 and 6.5, respectively. The prominent increase in φ and magnetic field parameter is noticed, whereas Nu and C_f decrease at right, while the opposite trend occurs at left.

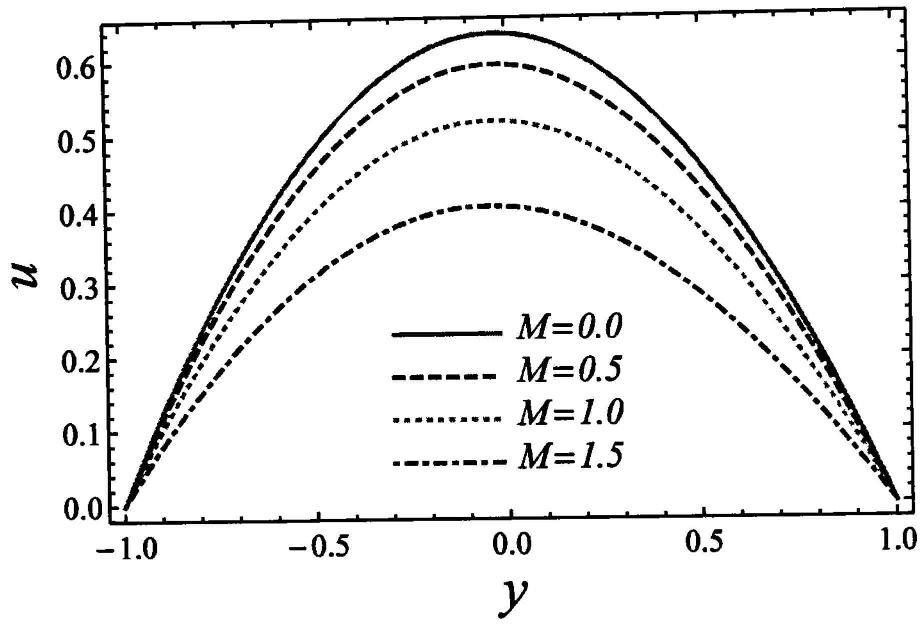

Figure 6.4(a): Manifestation of M on u .

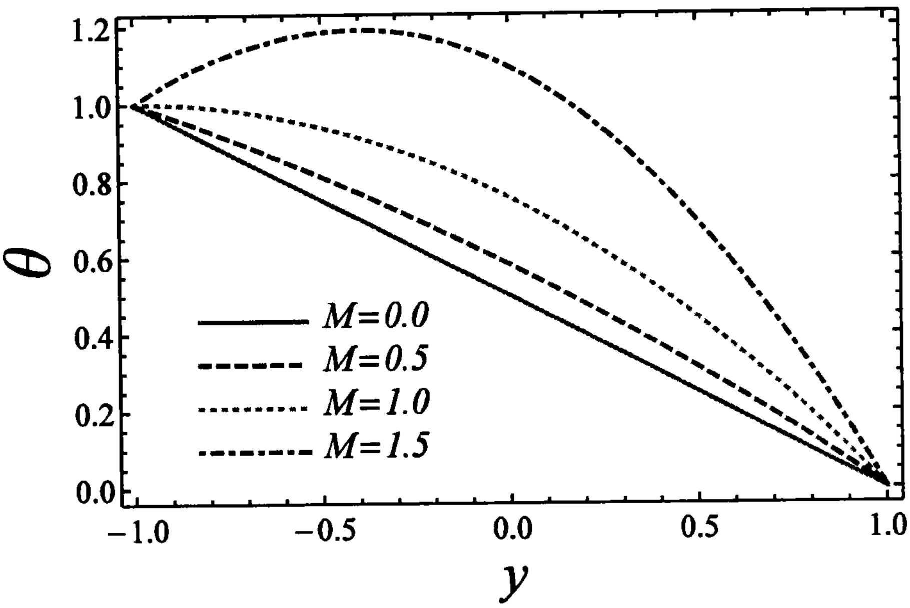

Figure 6.4(b): Manifestation of M on θ .

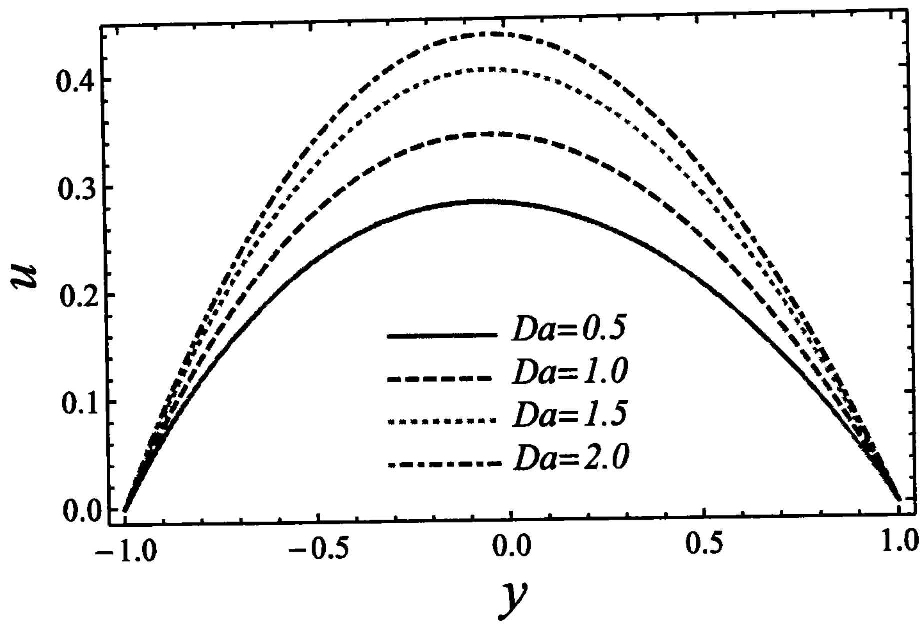

Figure 6.5(a): Manifestation of Darcy number on u .

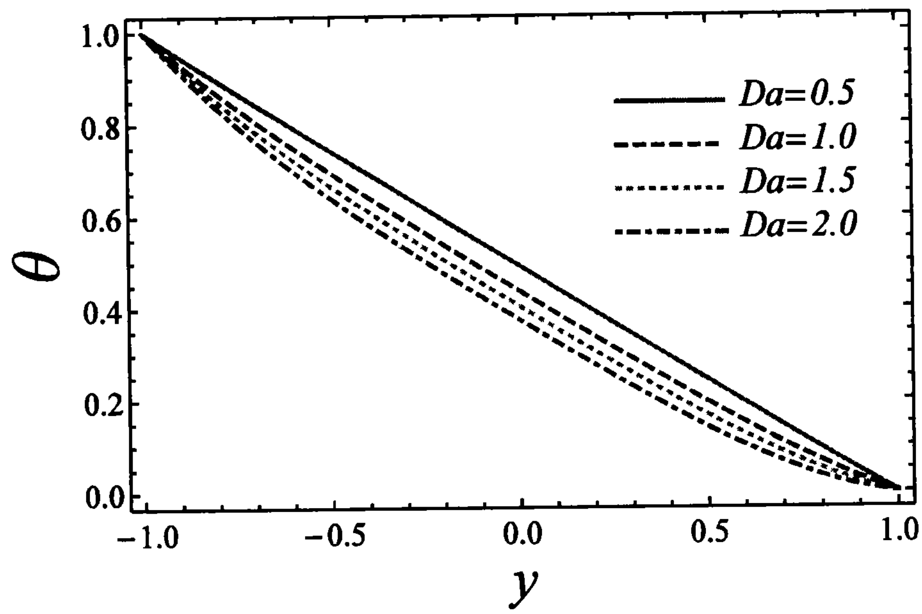

Figure 6.5(b): Manifestation of Darcy number on θ .

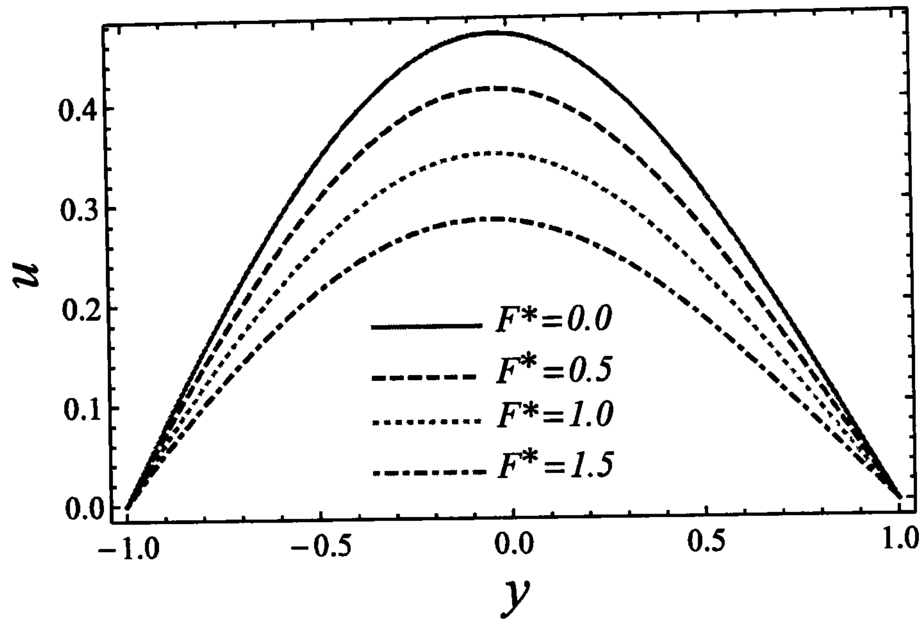

Figure 6.6(a): Manifestation of Forchheimer parameter on u .

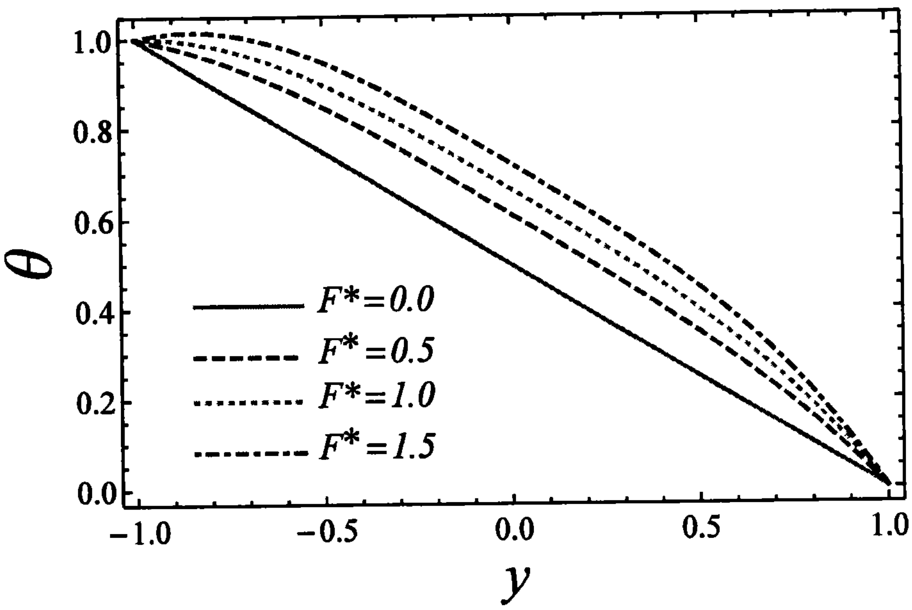

Figure 6.6(b): Manifestation of Forchheimer parameter on θ .

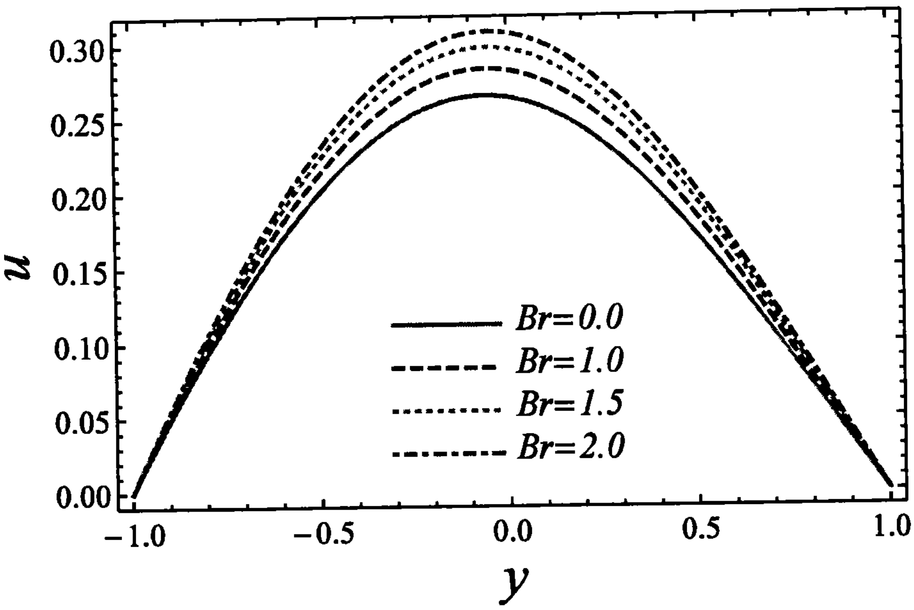

Figure 6.7(a): Manifestation of Brinkman number on u .

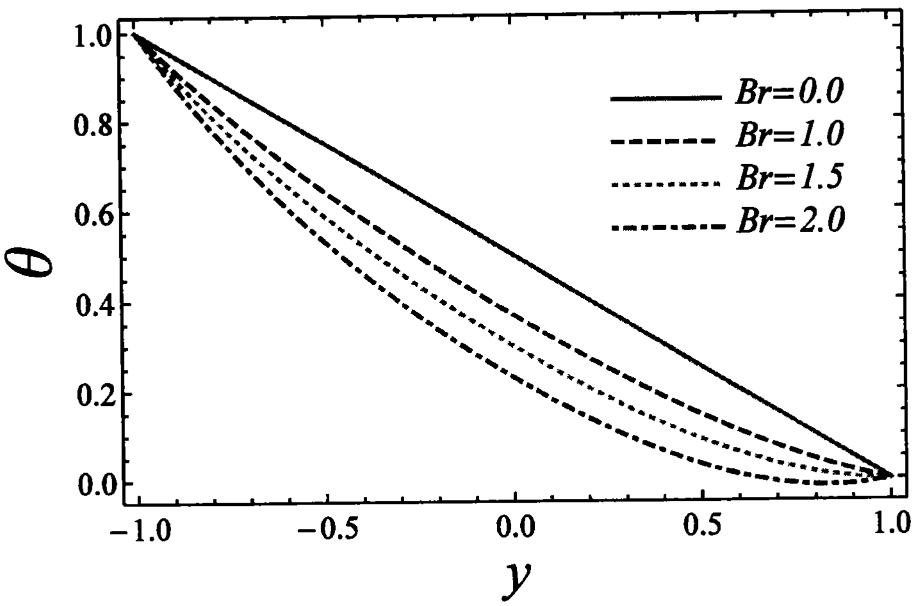

Figure 6.7(b): Manifestation of Brinkman number on θ .

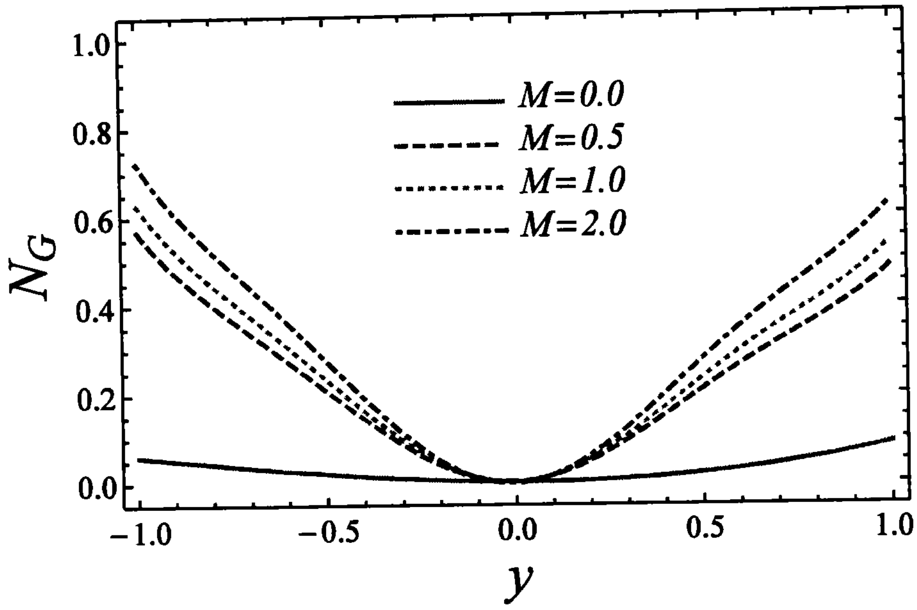

Figure 6.8(a): Manifestation of M on N_G.

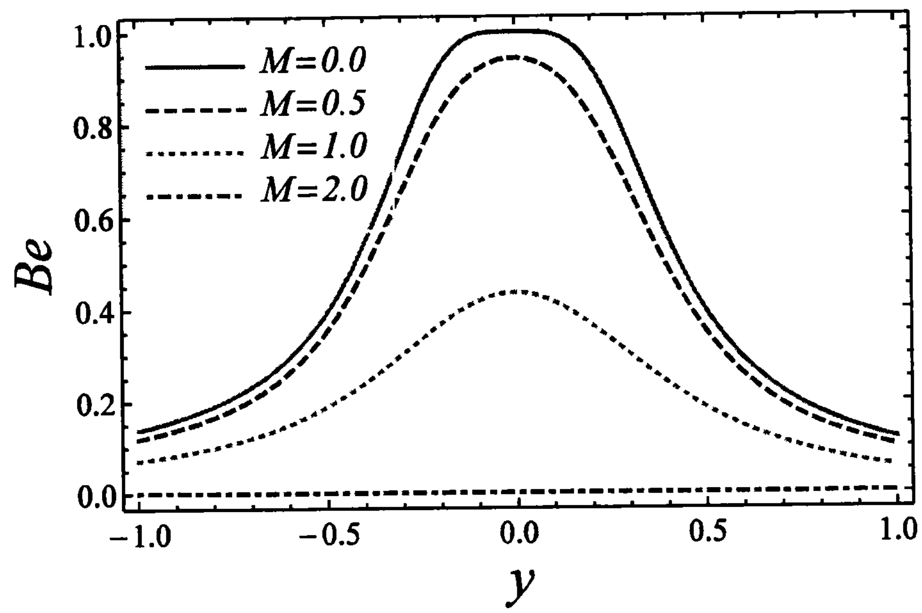

Figure 6.8(b): Manifestation of M on Be.

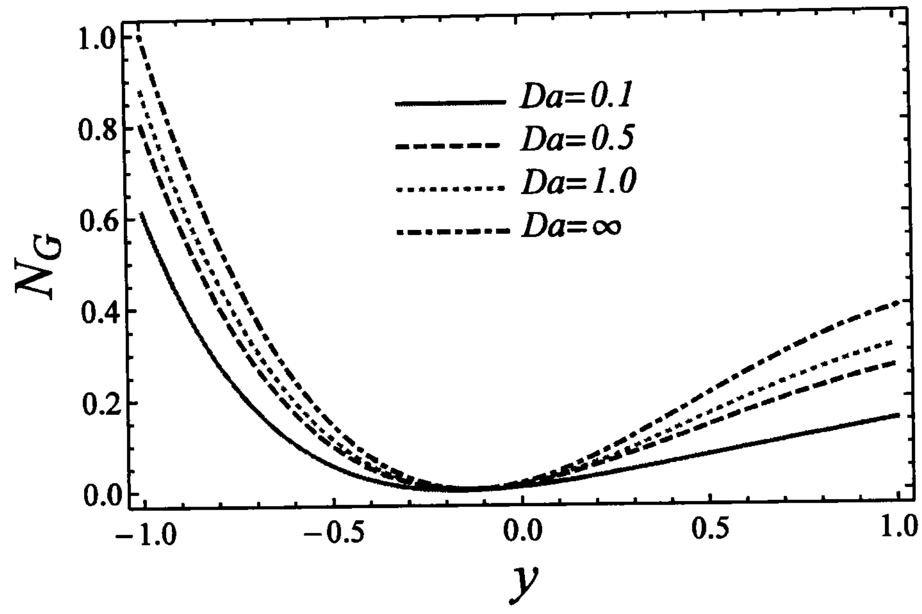

Figure 6.9(a): Manifestation of Darcy number on NG.

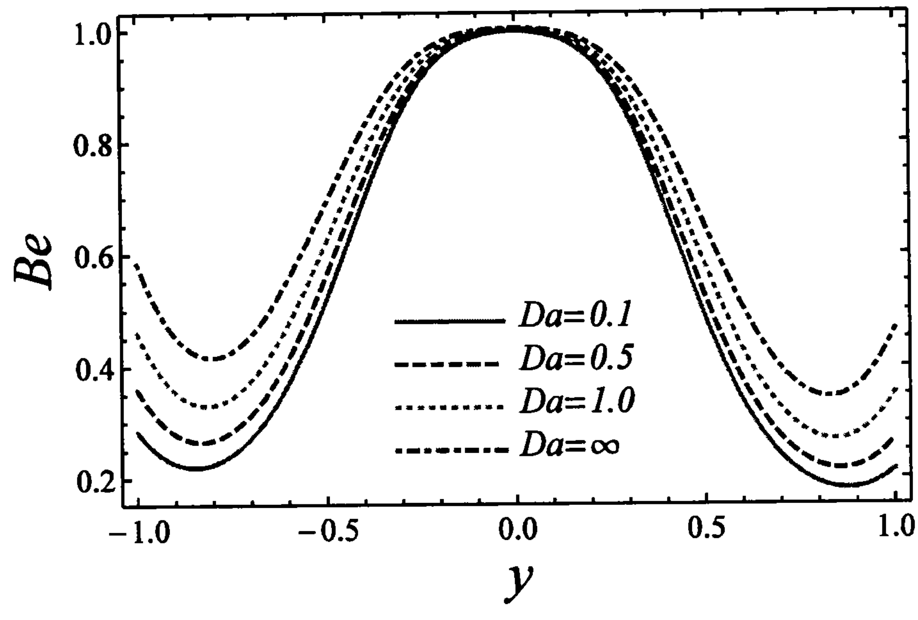

Figure 6.9(b): Manifestation of Darcy number on Be.

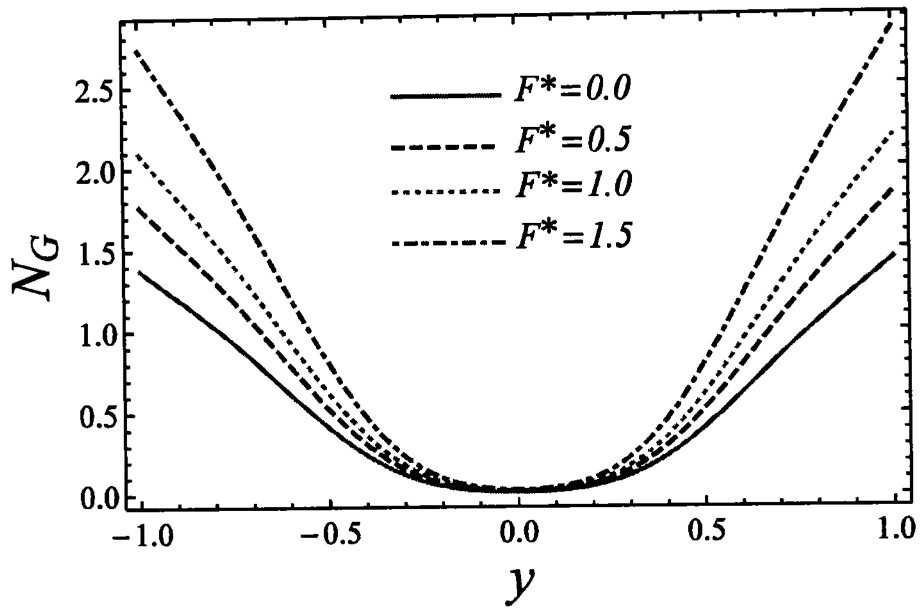

Figure 6.10(a): Manifestation of Forchheimer parameter on N_G.

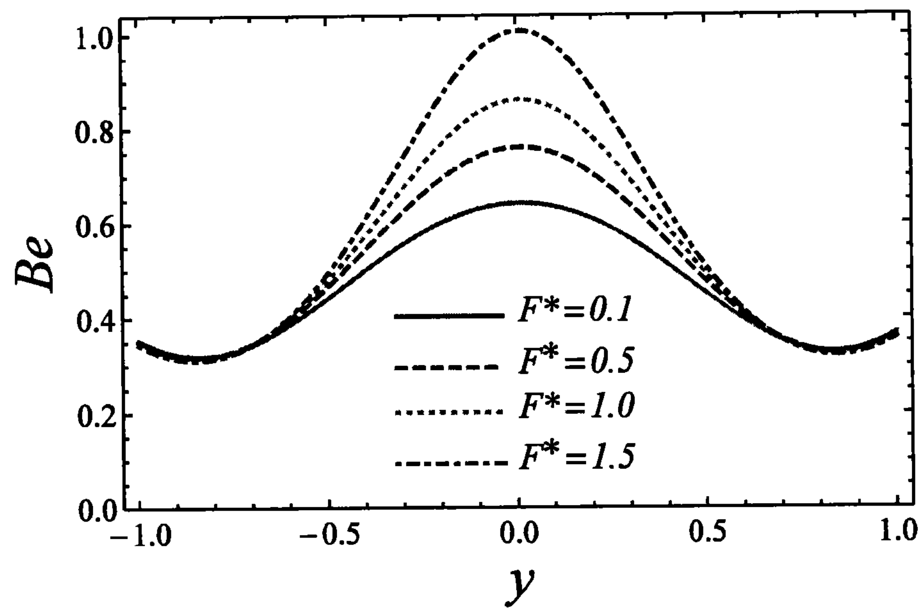

Figure 6.10(b): Manifestation Forchheimer parameter on Be.

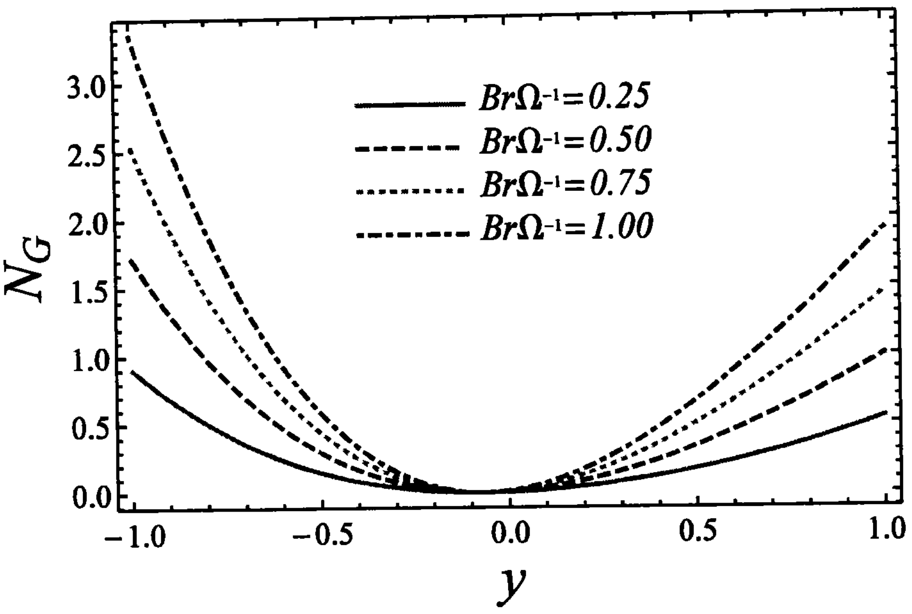

Figure 6.11(a): Manifestation of $Br\Omega^{-1}$ on N_G.

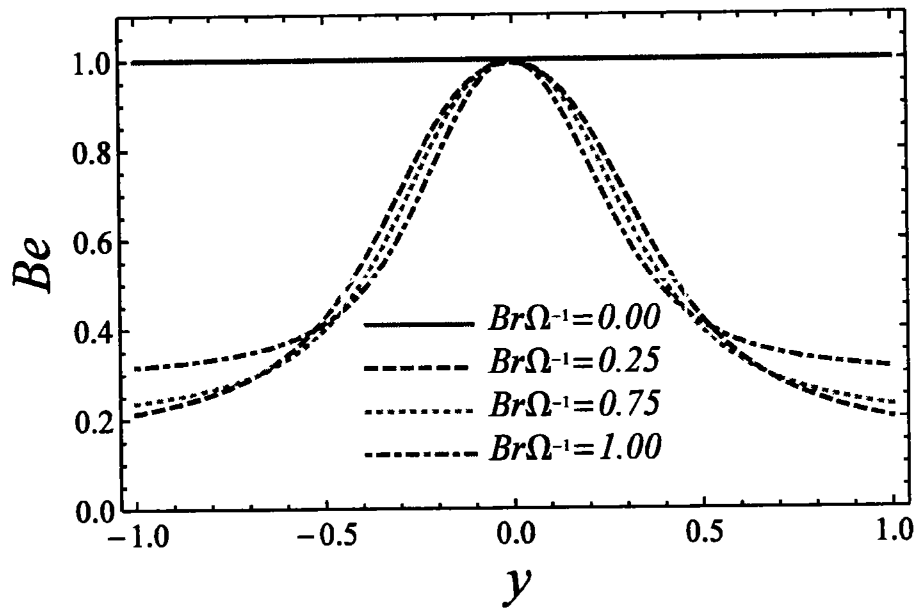

Figure 6.11(b): Manifestation of $Br\Omega^{-1}$ on Be.

***P* = - 0.5**

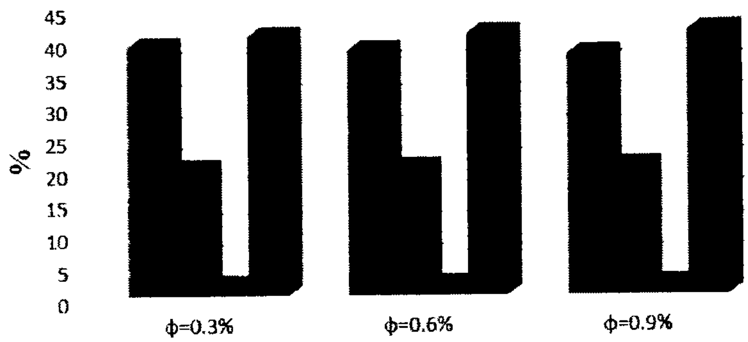

	φ=0.3% NG_Ave=0.4603	φ=0.6% NG_Ave=0.4622	φ=0.9% NG_Ave=0.4638
■ HTI	38.6238	37.9972	37.3705
■ FFI	19.6107	19.7949	19.9789
■ JDI	1.5759	1.603	1.6303
■ NDI	40.1896	40.6049	41.0202

(a)

***P* = - 1.0**

	φ=0.3% NG_Ave=2.1762	φ=0.6% NG_Ave=2.2051	φ=0.9% NG_Ave=2.2337
■ HTI	34.9551	34.6456	34.3353
■ FFI	20.3496	20.4174	20.4852
■ JDI	1.6443	1.6625	1.6807
■ NDI	43.051	43.2745	43.4988

(b)

Figure 6.12: Average breakdown in entropy generation for different φ at (**a**) $P = -0.5$ and (**b**) $P = -1.0$.

P = - 0.5

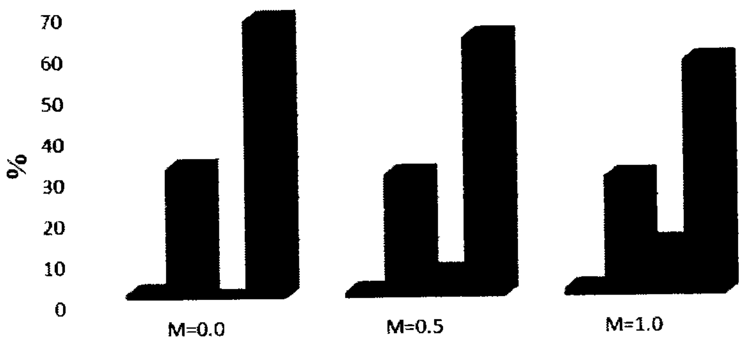

	M=0.0 NG_Ave=0.0237	M=0.5 NG_Ave=0.2760	M=1.0 NG_Ave=0.4067
■HTI	1.2472	1.4565	1.9358
■FFI	31.6332	29.8264	28.8126
■JDI	0	6.0299	12.6438
■NDI	67.1196	62.6872	56.6078

(a)

P = - 1.0

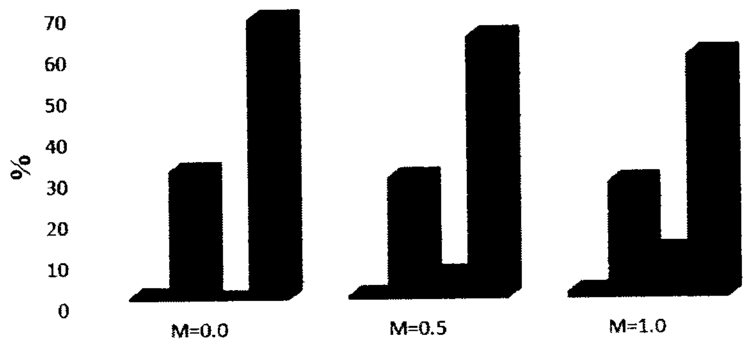

	M=0.0 NG_Ave=0.1746	M=0.5 NG_Ave=0.6532	M=1.0 NG_Ave=0.8477
■HTI	0.7596	0.9467	1.6549
■FFI	31.3251	29.5869	28.2101
■JDI	0	5.9639	11.4139
■NDI	67.9153	63.5025	58.7211

(b)

Figure 6.13: Average breakdown in entropy generation due to M at (**a**) $P = -0.5$ and (**b**) $P = -1.0$.

***P* = - 0.5**

	Da=0.2 NG_Ave=0.3175	Da=0.5 NG_Ave=0.1494	Da=1.0 NG_Ave=0.0429
■ HTI	24.6809	31.2898	41.8372
■ FFI	29.8981	33.7317	37.9138
■ JDI	2.2389	2.7088	2.7566
■ NDI	43.1821	32.2697	17.4924

(a)

***P* = - 1.0**

	Da=0.2 NG_Ave=0.6419	Da=0.5 NG_Ave=0.5791	Da=1.0 NG_Ave=0.0943
■ Series1	0.9519	16.9967	30.7967
■ Series2	30.6757	36.6348	42.0068
■ Series3	2.4742	3.6089	3.3909
■ Series4	65.8982	42.7596	23.8056

(b)

Figure 6.14: Average breakdown in entropy generation due to Da at **(a)** $P=-0.5$ and **(b)** $P=-1.0$.

P = - 0.5

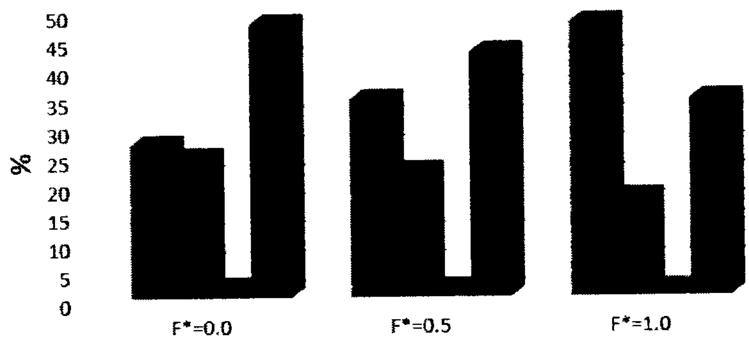

	F*=0.0 NG_Ave=0.3052	F*=0.5 NG_Ave=0.0929	F*=1.0 NG_Ave=0.0675
■ HTI	26.4314	34.1657	47.4623
■ FFI	24.3219	21.8068	17.1544
■ JDI	1.9104	1.6919	1.2956
■ NDI	47.3363	42.3356	34.0877

(a)

P = - 1.0

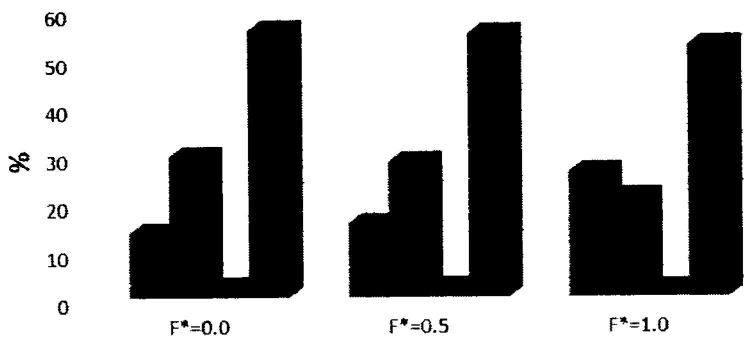

	F*=0.0 NG_Ave=0.8278	F*=0.5 NG_Ave=0.2482	F*=1.0 NG_Ave=0.2442
■ HTI	13.3551	15.3144	25.7766
■ FFI	29.1173	27.9893	20.5982
■ JDI	2.2317	2.1552	1.6908
■ NDI	55.2959	54.5411	51.9344

(b)

Figure 6.15: Average breakdown in entropy generation due to F^* at **(a)** $P = -0.5$ and **(b)** $P = -1.0$.

P = - 0.5

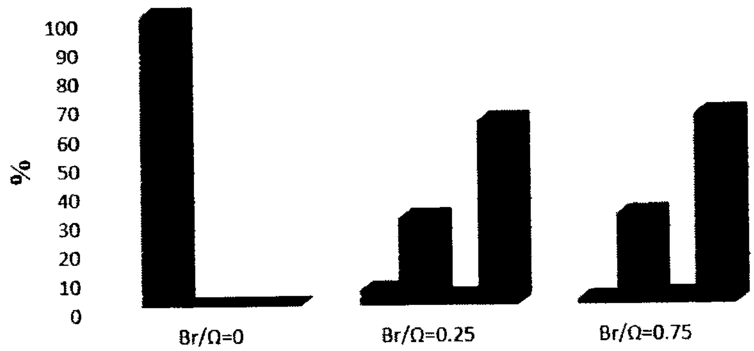

	Br/Ω=0 NG_Ave=0.0049	Br/Ω=0.25 NG_Ave=0.1013	Br/Ω=0.75 NG_Ave=0.2940
■ HTI	100	4.8647	1.6759
■ FFI	0	29.7357	30.7324
■ JDI	0	2.4011	2.4816
■ NDI	0	62.9985	65.1101

(a)

P = - 1.0

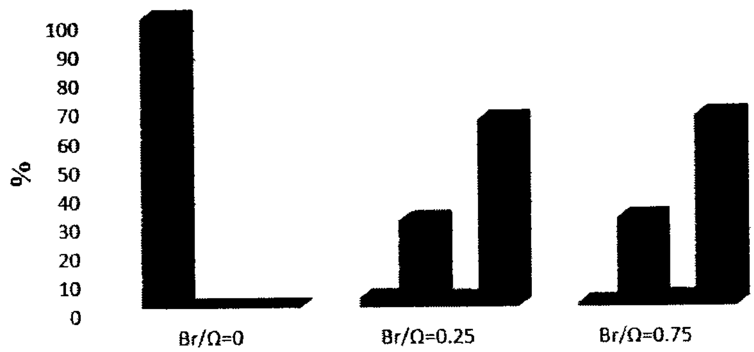

	Br/Ω=0 NG_Ave=0.0064	Br/Ω=0.25 NG_Ave=0.2118	Br/Ω=0.75 NG_Ave=0.6225
■ HTI	100	3.0357	1.0328
■ FFI	0	29.8807	30.4979
■ JDI	0	2.4061	2.4558
■ NDI	0	64.6775	66.0135

(b)

Figure 6.16: Average breakdown in entropy generation for $Br\Omega^{-1}$ at (**a**) $P = -0.5$ and (**b**) $P = -1.0$.

Table 6.2: Variation of Da and non-Darcy (Forchheimer) parameter F^* on Nu and C_f when $Gr = 0.5$, $Br = 1$, $M = 0.5$, and $\varphi = 0.3\%$.

Da	F^*	$Nu(-1)$	$Nu(1)$	$C_f(-1)$	$C_f(1)$
0.5	0.0	0.3111	0.6329	1.3898	−1.069
	0.5	0.3836	0.5634	1.2572	−0.9680
	1.0	0.3928	0. 5483	1.0021	−0.7155
	1.5	0.5067	0. 4428	0.7424	−0.4595
1.0	0.0	0.6497	0.3028	1.5772	−1.2715
	0.5	0.6854	0.2655	1.5600	−1.2552
	1.0	0.8509	0.0987	1.6243	−1.3209
	1.5	1.1791	−0.2298	1.9714	−1.6666
2.0	0.0	0.7814	0.1738	1.7266	−1.4126
	0.5	0.9048	0.0496	1.8225	−1.5089
	1.0	1.1602	−0.2057	2.1024	−1.7891
	1.5	1.5454	−0.5894	2.7338	−2.4202
10.0	0.0	0.9064	0.0517	1.8619	−1.5410
	0.5	1.0892	−0.1309	2.0655	−1.7442
	1.0	1.3881	−0.4285	2.5071	−2.1850
	1.5	1.7725	−0.8098	3.2985	−2.9743

Table 6.3: Variation of Gr and Br on Nu and C_f when $Da = 10$, $F^* = 1$, $M = 0.5$, and $\varphi = 0.3\%$.

Gr	Br	$Nu(-1)$	$Nu(1)$	$C_f(-1)$	$C_f(1)$
0.2	0	0.4768	0.4768	1.9264	−1.8003
	1	1.1824	−0.2266	1.8695	−1.7435
	2	1.8639	−0.9062	1.8104	−1.6846
	3	2.5192	−1.5601	1.7491	−1.6234
0.5	0	0.4768	0.4768	2.2683	−1.9541
	1	1.1602	−0.2057	2.1024	−1.7891
	2	1.7575	−0.8043	1.9234	−1.6110
	3	2.2464	−1.3067	1.7315	−1.4199
0.7	0	0.4768	0.4768	2.4907	−2.0519
	1	1.1301	−0.1795	2.2375	−1.8004
	2	1.6391	−0.6957	1.9601	−1.5246
	3	1.9802	−1.0481	1.6583	−1.2244
1.0	0	0.4768	0.4768	2.8159	−2.1914
	1	1.0622	−0.1220	2.4125	−1.7912
	2	1.3923	−0.4735	1.9632	−1.3449
	3	1.4183	−0.5289	1.4679	−0.8527

6.4 Conclusions

In this paper, entropy for non-Darcy porous media in Poiseuille (different pressure gradient) nanofluid flow through a wavy channel is analyzed. The momentum (flow), energy (heat), and entropy generation (energy loss) equations are transformed by using a similarity transformation to obtain nonlinear ordinary differential equations (ODEs). Homotopy analysis method is implemented to tackle nonlinear ODEs along suitable boundary conditions. Results of nanoparticle volume fraction, magnetic field parameter, Darcy number, non-Darcy (Forchheimer) parameter, Brinkman number, entropy generation, Bejan number, skin friction, Nusselt number, and average energy loss due to entropy generation on velocity and temperature were determined numerically as well as graphically by using Mathematica software. The major findings investigated during the study are as follows:

- It is perceived that velocity gives reduction flow map with large values of magnetic field and non-Darcy (Forchheimer) parameter, while velocity increases for large values of Darcy and Brinkman number.
- Temperature distribution increases with M and F^*. Instead, the temperature profile reduces for various values of Da and Br.
- Energy loss due to entropy generation becomes stronger along the walls of the channel for M and F^*, and near the center of the channel, energy loss becomes zero for said parameters.
- Energy loss due to entropy generation becomes weaker at left wall as related to right wall of channel for Da, and $Br\Omega^{-1}$ is also negligible near middle of channel.
- The Bejan number at center of geometry attained maximum value when the magnetic field was neglected and Be gained extreme value when group parameter was zero. Moreover, the Bejan number accelerated at boundaries with a large value of Darcy number and at the center of the channel increased with non-Darcy (Forchheimer) parameter.
- Average energy loss due to NDI was enhanced with enhancing nanoparticle volume fraction ϕ, non-Darcy (Forchheimer) parameter F^*, and group parameter $Br\Omega^{-1}$, but the reduction in non-Darcy porous media irreversibility was due to M and Da.
    - Increase in entropy is associated with the rise in pressure gradient.

Chapter 7

7 Effect of radiative electro magnetohydrodynamics diminishing internal energy of pressure-driven flow of titanium dioxide-water nanofluid due to entropy generation

The internal average energy loss caused by entropy generation (E_G) for steady natural and forced convective Poiseuille flow of a nanofluid, suspended with titanium dioxide (TiO_2) particles in water, and passed through a wavy channel, was examined. The models of viscosity as well as thermal conductivity of titanium dioxide of 21 nm size particles with a volume concentration at temperature reaching from 15 °C to 35°C were utilized. The characteristics of the working fluid were dependent on electro-magnetohydrodynamics (EMHD) and thermal radiation. The governing equations were first modified by taking long wavelength approximations, which were then solved by a homotopy technique, whereas for numerical computation, the software package BVPh2.0 was utilized. The results for the leading parameters, like as electric field, nanoparticle volume fraction and radiation parameters for three different temperatures scenarios were examined graphically. The minimum energy loss at the middle of the wavy channel due to the rise in the electric field parameter was noted. However, an increase in entropy was observed due to the change in the pressure gradient from low to high.

7.1 Problem formulation

7.1.1 Flow analysis

An incompressible, electrically conducting, steady-state laminar TiO_2-water nanofluid flowing between horizontal wavy channels is taken, as displayed in figure 7.1. The middle of channel taken at origin and the left and right walls of channel having a length L with amplitude a_1, width d and wavelength λ that proportional to $2\pi/L$ consider. The configuration of the left and right walls are defined as, respectively

$$H_1 = -d - a_1 \cos\left(\frac{2\pi}{L}\bar{x}\right), \quad H_2 = d + a_1 \cos\left(\frac{2\pi}{L}\bar{x}\right). \tag{7.1}$$

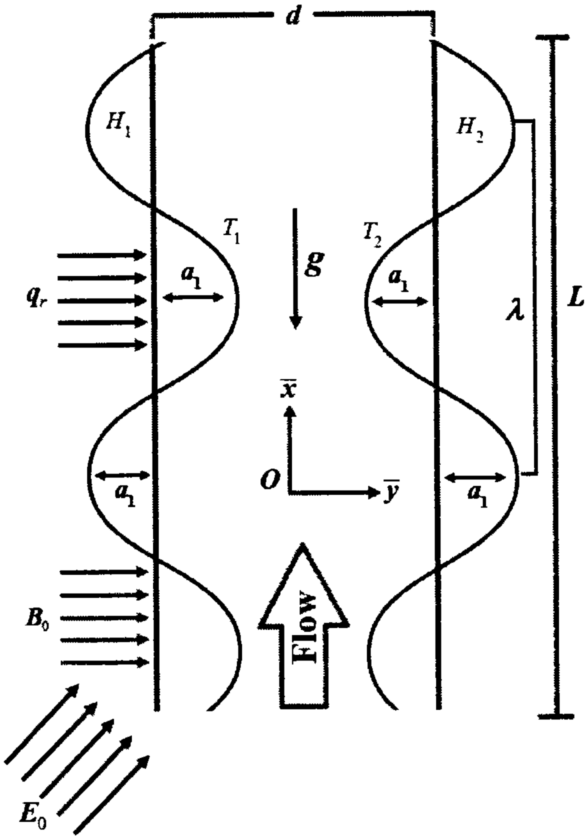

Figure 7.1: Geometry of the flow model.

7.1.2 Governing equations (Tiwari and Das's model)

According to said nanofluid model, the equations (1.18), (1.19) and (1.38) given in chapter 1, for a steady state, incompressible nanofluid with effect of electric, magnetic, buoyancy, thermal radiation, viscous and Ohmic dissipation transporting through symmetric wavy walls are modeled mathematically as

$$\frac{\partial \bar{u}}{\partial \bar{x}}+\frac{\partial \bar{v}}{\partial \bar{y}}=0, \tag{7.2}$$

$$\rho_{nf}\left(\bar{u}\frac{\partial \bar{u}}{\partial \bar{x}}+\bar{v}\frac{\partial \bar{u}}{\partial \bar{y}}\right)=-\frac{\partial \bar{p}}{\partial \bar{x}}+\mu_{nf}\left(\frac{\partial^2 \bar{u}}{\partial \bar{x}^2}+\frac{\partial^2 \bar{u}}{\partial \bar{y}^2}\right)+\sigma_{nf}\left(E_0B_0-B_0^2\bar{u}\right)+\left(\rho\beta\right)_{nf}g\left(\bar{T}-T^*\right), \tag{7.3}$$

$$\left(\rho C_p\right)_{nf}\left(\bar{u}\frac{\partial T}{\partial \bar{x}}+\bar{v}\frac{\partial T}{\partial \bar{y}}\right)=k_{nf}\left(\frac{\partial^2 T}{\partial \bar{x}^2}+\frac{\partial^2 T}{\partial \bar{y}^2}\right)+\mu_{nf}\left[\left(\frac{\partial \bar{u}}{\partial \bar{x}}\right)^2+\left(\frac{\partial \bar{u}}{\partial \bar{y}}\right)^2\right]+\sigma_{nf}\left(B_0\bar{u}-E_0\right)^2-\frac{\partial q_r}{\partial \bar{y}}. \tag{7.4}$$

Boundary conditions

$$\left.\begin{array}{l}\bar{u}=0,\ \bar{v}=0,\ T=T_2\ \text{at}\ \bar{y}=H_2\\ \bar{u}=0,\ \bar{v}=0,\ T=T_1\ \text{at}\ \bar{y}=H_1\end{array}\right\}. \tag{7.5}$$

Let us acquaint the following nondimensional quantities

$$\left.\begin{array}{l}x=\dfrac{\bar{x}}{\lambda},\ y=\dfrac{\bar{y}}{d},\ u=\dfrac{\bar{u}}{U_m},\ v=\dfrac{\bar{v}}{U_m\delta},\ h_1=\dfrac{H_1}{d},\ h_2=\dfrac{H_2}{d},\\ p=\dfrac{d^2\bar{p}}{\mu_f U_m\lambda},\ \delta=\dfrac{d}{\lambda},\ \theta=\dfrac{T-T^*}{T_1-T^*},\ m^*=\dfrac{T_2-T^*}{T_1-T^*}\end{array}\right\}. \tag{7.6}$$

Using the variables which have ho dimensions, defined in equation (7.6), the governing equations (7.2) to (7.4) become

$$\delta\frac{\partial u}{\partial x}+\frac{\partial v}{\partial y}=0, \tag{7.7}$$

$$A_2Re\delta\left(u\frac{\partial u}{\partial x}+v\frac{\partial u}{\partial y}\right)=A_1\left[\left(\delta^2\frac{\partial^2 u}{\partial x^2}+\frac{\partial^2 u}{\partial y^2}\right)-\frac{\partial p}{\partial x}\right]+A_3M^2\left(E_1-u\right)+A_4Gr\theta,, \tag{7.8}$$

$$A_5RePr\delta\left(u\frac{\partial \theta}{\partial x}+v\frac{\partial \theta}{\partial y}\right)=A_6\left(\delta^2\frac{\partial^2\theta}{\partial x^2}+\frac{\partial^2\theta}{\partial y^2}\right)+A_1EcPr\left(\frac{\partial u}{\partial y}\right)^2+A_3EcPrM^2\left(u-E_1\right)^2+Rd\left(\frac{\partial^2\theta}{\partial y^2}\right). \tag{7.9}$$

Under the long wavelength approximation, equations (7.7) to (7.9) along with linked boundary in dimensionless form are renewed as

$$-A_1 P + A_1 \frac{\partial^2 u}{\partial y^2} + A_3 M^2 (E_1 - u) + A_4 Gr\theta = 0, \tag{7.10}$$

$$(A_6 + Rd)\frac{\partial^2 \theta}{\partial y^2} + A_1 Br\left(\frac{\partial u}{\partial y}\right)^2 + A_3 BrM (u - E_1)^2 = 0, \tag{7.11}$$

$$\left.\begin{aligned} &u = 0,\ \theta = m^* \ \text{at}\ y = h_2 = 1 + \frac{a}{d}\text{Cos}\left(\frac{2\pi\lambda}{L}x\right) \\ &u = 0,\ \ \theta = 1 \quad \text{at}\ y = h_1 = -1 - \frac{a}{d}\text{Cos}\left(\frac{2\pi\lambda}{L}x\right) \end{aligned}\right\}. \tag{7.12}$$

Parameters defined in equation (7.10) and (7.11) are

$$\left.\begin{aligned} &Gr = \frac{(\rho\beta)_f g d^2 (T_1 - T^*)}{\mu_f U_m}, \text{Re} = \frac{\rho_f U_m d}{\mu_f}, M^2 = \frac{\sigma_f B_0^2 d^2}{\mu_f}, Br = \text{Pr}\, Ec \\ &\text{Pr} = \frac{\mu_f (\rho C_p)_f}{\rho_f k_f}, Ec = \frac{U_m^2}{(C_p)_f (T_1 - T^*)}, Rd = \frac{16T^{*3}\sigma^*}{3k^* k_f}, E_1 = \frac{E_0}{B_0 U_m} \\ &A_1 = \frac{\mu_{nf}}{\mu_f}, A_2 = \frac{\rho_{nf}}{\rho_f}, A_3 = \frac{\sigma_{nf}}{\sigma_f}, A_4 = \frac{(\rho\beta)_{nf}}{(\rho\beta)_f}, A_5 = \frac{(\rho C_p)_{nf}}{(\rho C_p)_f}, A_6 = \frac{k_{nf}}{k_f} \end{aligned}\right\}. \tag{7.13}$$

The physical thermal properties using in above resulting equations (7.10) and (7.11) are define in equations (1.9), (1.10) and (1.11). The viscosity as well as thermal conductivity of Titanium dioxide-water nanofluid explain in equations (1.5) and (1.8) are used for this chapter respectively.

Expression of coefficient of skin friction defined in equation (1.54) and Nusselt number defined in equation (1.56) are transformed in view of equation (7.6) as

$$\left.\begin{aligned} \text{Re}\, C_f &= 2A_1 u'(y)\ \big|_{y=h_1,h_2} \\ Nu &= -A_6 \theta'(y)\big|_{y=h_1,h_2} \end{aligned}\right\}. \tag{7.14}$$

7.1.3 Entropy generation analysis

The entropy generation E_G in a nanofluid with effective influences of electro-magnetohydrodynamics (EMHD) and thermal radiation is described in the subsequent relation as

$$E_G=\underbrace{\frac{1}{T^{*2}}\left[k_{nf}\left(\frac{\partial \bar{T}}{\partial \bar{y}}\right)^2-q_r\left(\frac{\partial \bar{T}}{\partial \bar{y}}\right)\right]}_{\text{energy loss via heat transfer}}+\underbrace{\frac{\mu_{nf}}{T^*}\left(\frac{\partial \bar{u}}{\partial \bar{y}}\right)^2}_{\text{energy loss via fluid friction}}+\underbrace{\frac{\sigma_{nf}\left(B_0\bar{u}-E_0\right)^2}{T^*}}_{\text{energy loss via Joule dissipation and electric field}}. \tag{7.15}$$

The entropy generation rate E_{G_0} is determined by

$$E_{G_0}=\frac{k_{nf}\left(T_1-T^*\right)^2}{d^2T^{*2}}. \tag{7.16}$$

Entropy generation number N_G is defined as

$$N_G=E_G/E_{G_0}. \tag{7.17}$$

Such that

$$N_G=\frac{d^2T^{*2}}{k_{nf}\left(T_1-T^*\right)^2}\times\left[\frac{1}{T^{*2}}\left[k_{nf}\left(\frac{\partial T}{\partial \bar{y}}\right)^2-q_r\left(\frac{\partial T}{\partial \bar{y}}\right)\right]+\frac{\mu_{nf}}{T^*}\left(\frac{\partial \bar{u}}{\partial \bar{y}}\right)^2+\frac{1}{T^*}\sigma_{nf}\left(B_0\bar{u}-E_0\right)^2\right] \tag{7.18}$$

Hence, the total entropy generation is

$$N_G=\left(1+\frac{4}{3}Rd\right)\left(\frac{\partial \theta}{\partial y}\right)^2+\frac{1}{A_6}\frac{Br}{\Omega}\left[A_1\left(\frac{\partial u}{\partial y}\right)^2+A_3M^2\left(u-E_1\right)^2\right], \tag{7.19}$$

where

$$\Omega=\frac{T_1-T^*}{T^*},\quad Br=\frac{\mu_f U_m^2}{k_f\left(T_1-T^*\right)}. \tag{7.20}$$

The Bejan number Be can be made as

$$Be=\frac{HTI}{HTI+FFI+JDEI}, \tag{7.21}$$

$$HTI=\left(\frac{\partial \theta}{\partial y}\right)^2, FFI=\frac{A_1}{A_6}\frac{Br}{\Omega}\left(\frac{\partial u}{\partial y}\right)^2, JDEI=\frac{A_3}{A_6}\frac{Br}{\Omega}M^2\left(u-E_1\right)^2. \tag{7.22}$$

From equations (7.6) and (7.13), it follows that

$$Be=\frac{\left(1+\frac{4}{3}Rd\right)\left(\frac{\partial\theta}{\partial y}\right)^2}{\left(1+\frac{4}{3}Rd\right)\left(\frac{\partial\theta}{\partial y}\right)^2+\frac{1}{A_6}\frac{Br}{\Omega}\left[A_1\left(\frac{\partial u}{\partial y}\right)^2+A_3M^2\left(u-E_1\right)^2\right]}. \tag{7.23}$$

Average entropy generation can be calculated by

$$NG_{\_avg}=\frac{1}{\forall}\int_{\forall}NG\,d\forall. \tag{7.24}$$

Here

$$NG_{\_avg}=\frac{1}{\left(d\times L\right)}\int_{h_1}^{h_2}NG\,dy, \tag{7.25}$$

or

$$NG_{\_avg}=\frac{1}{\left(d\times L\right)}\int_{h_1}^{h_2}(HTI+FFI+JDEI)\,dy. \tag{7.26}$$

7.2 Solution of the problem

To get an analytic solution, a homotopy technique is utilized to solve equations (7.10) and (7.11).

Zeroth-order solution

Consider, the initial approximations $u_0(y)$, $\theta_0(y)$ and supplementary linear operators $\pounds_u$, $\pounds_\theta$ for velocity and temperature are

$$\left.\begin{aligned}u_0(y)&=y^2-(h_1+h_2)y+(h_1h_2)\\ \theta_0(y)&=\frac{y-h_2}{h_1-h_2}\end{aligned}\right\} \tag{7.27}$$

and

$$\pounds_u=\frac{d}{dy}\left(\frac{du}{dy}\right),\quad \pounds_\theta=\frac{d}{dy}\left(\frac{d\theta}{dy}\right). \tag{7.28}$$

The convergence control parameters $\hbar_u$, $\hbar_\theta$ and nonlinear operators N_u, N_θ of velocity, temperature with embedding parameter $\xi\in[0,\ 1]$ yields the following zeroth-order deformations respectively are

$$\left.\begin{aligned}(1-\xi)\pounds_u\left[u(y,\xi)-u_0(y)\right]=\xi\hbar_u N_u\left[u(y,\xi),\theta(y,\xi)\right]\\(1-\xi)\pounds_\theta\left[\theta(y,\xi)-\theta_0(y)\right]=\xi\hbar_\theta N_\theta\left[u(y,\xi),\theta(y,\xi)\right]\end{aligned}\right\},\tag{7.29}$$

with boundary conditions

$$\left.\begin{aligned}u(y,\xi)=0,\ \theta(y,\xi)=m^*\ \text{ at } y=h_2\\u(y,\xi)=0,\ \theta(y,\xi)=1\ \text{ at } y=h_1\end{aligned}\right\}\tag{7.30}$$

and

$$\left.\begin{aligned}N_u&=-A_1P+A_1\frac{\partial^2u(y,\xi)}{\partial y^2}+A_3M^2\left[E_1-u(y,\xi)\right]+A_4Gr\theta(y,\xi)\\N_\theta&=(A_6+Rd)\frac{\partial^2\theta(y,\xi)}{\partial y^2}+A_1Br\left(\frac{\partial u(y,\xi)}{\partial y}\right)^2+A_3BrM^2\left(u(y,\xi)-E_1\right)^2\end{aligned}\right\}.\tag{7.31}$$

l th–order solution

The l th–order deformation expression for $u_l(y)$ and $\theta_l(y)$ as follows

$$\left.\begin{aligned}\pounds_u\left[u_l(y)-\chi_l u_{l-1}(y)\right]=\hbar_u R_l^u(y)\\\pounds_\theta\left[\theta_l(y)-\chi_l\theta_{l-1}(y)\right]=\hbar_\theta R_l^\theta(y)\end{aligned}\right\}.\tag{7.32}$$

$$\left.\begin{aligned}u_l(y,\xi)=0,\ \theta_l(y,\xi)=m^*\ \text{ at } y=1\\u_l(y,\xi)=0,\ \theta_l(y,\xi)=1\ \text{ at } y=-1\end{aligned}\right\}\tag{7.33}$$

$$\left.\begin{aligned}R_l^u(y)&=A_1\left[-P+u_l''\right]-A_3M^2(E_1-u_l)+A_4Gr\theta_l\\R_l^\theta(y)&=(A_6+Rd)\theta_l''+A_3BrM^2(u_l-E_1)^2+A_1Br\sum_{k=0}^{l}u_k'u_{l-k}'\end{aligned}\right\}.\tag{7.34}$$

The solution can be described as of l th–order

$$\left.\begin{aligned}u(y)=u_0(y)+\sum_{k=1}^{l}u_k(y)\\\theta(y)=\theta_0(y)+\sum_{k=1}^{l}\theta_k(y)\end{aligned}\right\}.\tag{7.35}$$

7.3 Discussion of results

7.3.1 Inspection of convergence

The velocity and temperature results in equation (7.35) hold $\hbar_u$ and $\hbar_\theta$, respectively. In homotopy analysis method, a faster convergence can be achieved by the optimum selection of the involved auxiliary parameters. Figure 7.2 portrays the $\hbar$ –curves at thirtieth–order approximations for u and θ, to estimate accurate range of convergence, that visibly predicts admissible ranges for $\hbar_u$ and $\hbar_\theta$ to lie between −2.0 to 0.5 and −1.5 to 0.5.

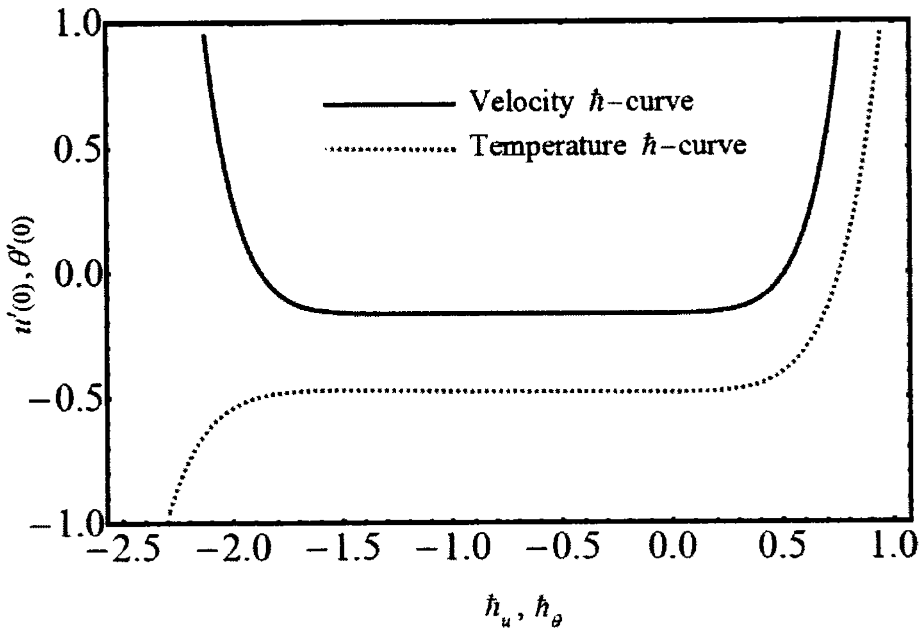

Figure 7.2: $\hbar$ –curves for velocity and temperature profile.

7.3.2 Residual error of norm 2

The residual error of velocity E_u and temperature distribution E_θ at two successive approximations over embedding parameter $\xi \in [0, 1]$ up to the 30th-order approximations is computed by the following mathematical relations

$$E_u = \sqrt{\frac{1}{31}\sum_{i=0}^{30}\left(u(i/30)\right)^2},\quad E_\theta = \sqrt{\frac{1}{31}\sum_{i=0}^{30}\left(\theta(i/30)\right)^2}. \tag{7.36}$$

The above residual formulas give minimum error for velocity at $\hbar_u = -0.7$ and for temperature distribution at $\hbar_\theta = -0.6$, which are displayed in figures 7.3 and 7.4, correspondingly. Table 7.1 shows residual error for the convergence series solution up to the 30th-order approximation.

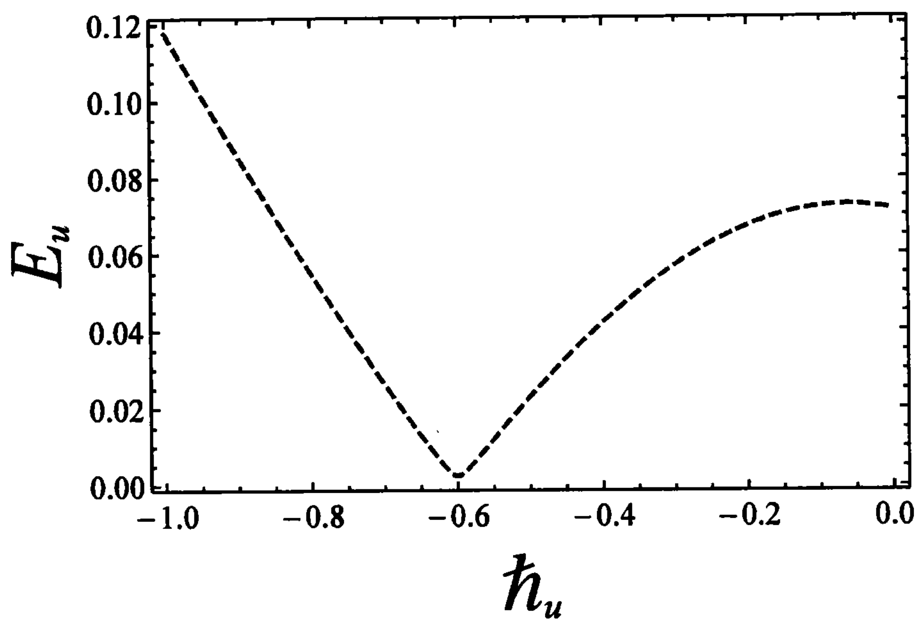

Figure 7.3: Residual error E_u –curve for velocity profile.

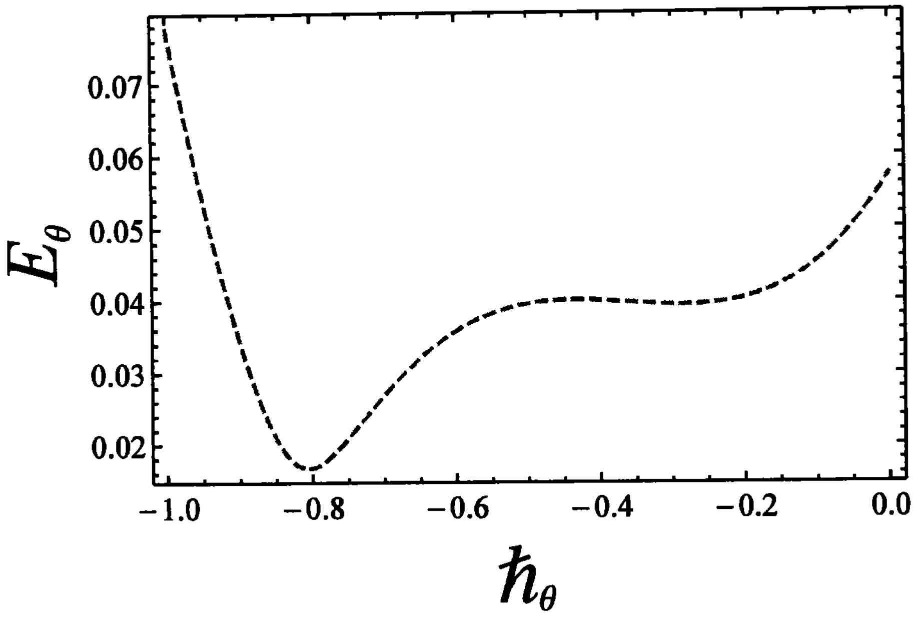

Figure 7.4: Residual error E_θ–curve for temperature profile.

Table 7.1. Residual error estimation when $M = 0.25$, $E_1 = 1.0$, $Gr = 2.0$, $Rd = 0.5$, and $\Pr = 7.0$.

Order of Approximation	Time	E_u	E_θ
05	5.3818	4..4073 × 10^{-4}	2.8357 × 10^{-6}
10	9.7290	2.8199 × 10^{-8}	4.6835 × 10^{-9}
15	16.7899	4.0554 × 10^{-14}	5.0418 × 10^{-14}
20	26.9812	1.0687 × 10^{-17}	1..0454 × 10^{-17}
30	40.6344	1.3593 × 10^{-22}	7.9903 × 10^{-22}

7.3.3 Illustration of graphical results

The sketches of the key factors, such as the electric field, nanoparticle volume fraction, radiation and group parameter are presented for temperatures at (15 °C, 25 °C, 35 °C). Figures 7.5–7.8 signify the impressions of E_1, φ and Rd on velocity (u) and temperature (θ) profiles. The plots of electric field parameter E_1 on velocity and temperature distributions are shown in figures 7.5 and 7.6. Figure 7.5, identified that velocity gradually increased by an upturn of E_1, whereas the combined effects of the electro-magnetohydrodynamics (EMHD) produced Lorentz forces to resist the fluid velocity. Also, the size of the boundary layer increased with the rise of E_1. However, in figure 7.6, the opposite behavior for the fluid temperature was noted, which was due to the applied electric field. The effects of the nanoparticle volume fraction ϕ on the fluid flow are shown in figure 7.7. It could easily be examined that when the volume fraction of the nanoparticle upsurges in the base fluid, the base fluid's density increased. Subsequently, the fluid became denser, so the suspension of particles in fluid resulted in a reduction in nanofluid velocity. In figure 7.8, the temperature distribution of the nanofluid against the radiation parameter Rd is displayed. The temperature of nanofluid could also be controlled with the radiation factor, because the fluid temperature was very sensitive to Rd, which meant that the heat flux of channel walls would be as large as perceived.

Figures 7.9–7.14 portray the effects of E_1, $Br\Omega^{-1}$ and Rd on NG and Be. Figures 7.9 and 7.10 show the behaviors of the electric field parameter E_1 on NG and Be. The entropy generation rate near the walls increased with rise of the electric field parameter, as exposed in figure 7.9, while at the left wall, the entropy loss was greater as compared to the right wall. It is further noted that near the center of the channel, energy loss was at a minimum, between $y=-0.3$ and $y=0.2$. This was due to the combined effects of the electro-magnetohydrodynamics, which produced Lorentz forces to resist the fluid flow. In figure 7.10, The Bejan number near to the center of the channel with a large electric parameter value gradually accelerated and approached to 1, but near to the walls, a reduction in the Bejan number against large values of electric field parameter was detected. The impacts of group parameters $Br\Omega^{-1}$ on NG and Be are shown in figures 7.11 and 7.12. The entropy generation rate escalated with large vales of $Br\Omega^{-1}$, as exposed in figure 7.11. The upshot $Br\Omega^{-1}$ was visible in figure 7.12. Here Be attained an extreme value, almost at $y=-0.1$, because of the escalation of the heat transfer irreversibility for $Br\Omega^{-1}=0.2$, but gradually decreased for large value of the group parameter values. The influence of Rd on entropy generation rate are displayed in figure 7.13. Here, the entropy generation are seen by the nice curved shape and almost symmetrical profiles for all values of Rd. A small change in Rd caused a large variation of NG, as perceived in figure 7.13. It could also be found that the energy loss entropy generation rate around the center of the channel was approximately zero, but as one proceeded towards the channel walls, entropy occurred. Figure 7.14 shows the same increasing results for the radiation parameter Rd on Be, as shown in the case of entropy generation. The Bejan number near center of channel was about to attain its extreme position for low radiation evolvement, but near the vicinity of the walls, the Bejan number increased with the growing radiation factor. The increasing results suggested that heat transfer irreversibility plays a dominant role in energy loss.

Figures 7.15(a)–(d) and 7.16(a)–(d) depict the effects of M, E_1, φ and Rd on average HTI: heat transfer irreversibility, average FFI: fluid friction irreversibility, average JDEI: joule dissipation and electric field irreversibility by using Duangthongsuk and Wongwises model at $T = 25^{\circ}C$. In figure 7.15(a), phi diagrams are displayed against the magnetic parameter for different M. In figure 7.15(b), the phi diagrams show the performance of the electric field for different E_1. In figure 7.15(c), the phi drawings deal with the nanoparticle volume fraction for different φ. In figure 7.15(d), the phi drawings describe the radiation parameter for different values of Rd. The effects of energy loss for M are plotted in the phi diagrams, as revealed in figure 7.16(a), whereas figure 7.16(b), show phi diagrams against the electric field parameter for diverse values of E_1. In figure 7.16(c), the phi diagrams depict energy loss for diverse values of φ, while figure 7.16(d), demonstrates the Rd involvments in energy loss via phi diagrams. In all phi diagrams, it was determined that when the pressure gradient increased, the average entropy loss and consequently entropy generation increased in the system. Thus, one can say that the reported results about electro-magnetohydrodynamics (EMHD), thermal radiation and entropy generation on Poiseuille flow with Titanium dioxide nanoparticles are very effective to reduce the energy losses and escalate the heat transfer in wavy surfaces. The said analysis is very informative for food industries, as in the presence of titanium dioxide in the consumer packaging, which helps to preserve food for a considerable time period.

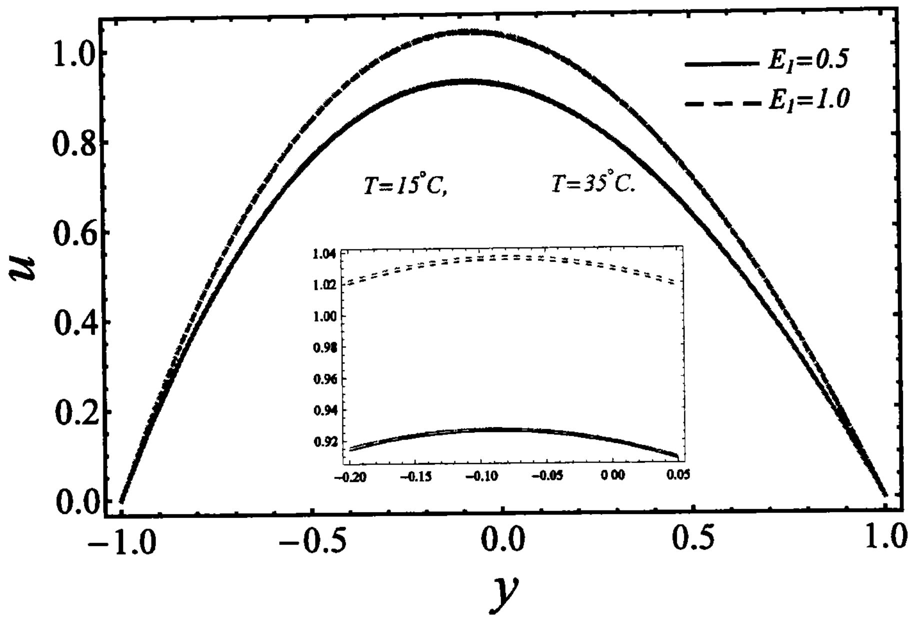

Figure 7.5: Manifestation of E_1 on u .

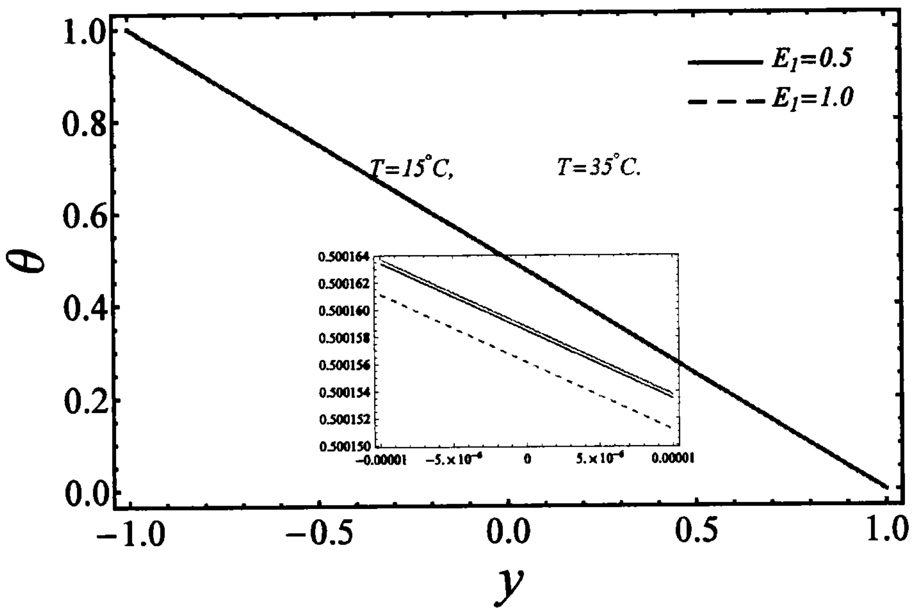

Figure 7.6: Manifestation of $Br\Omega^{-1}$ on θ .

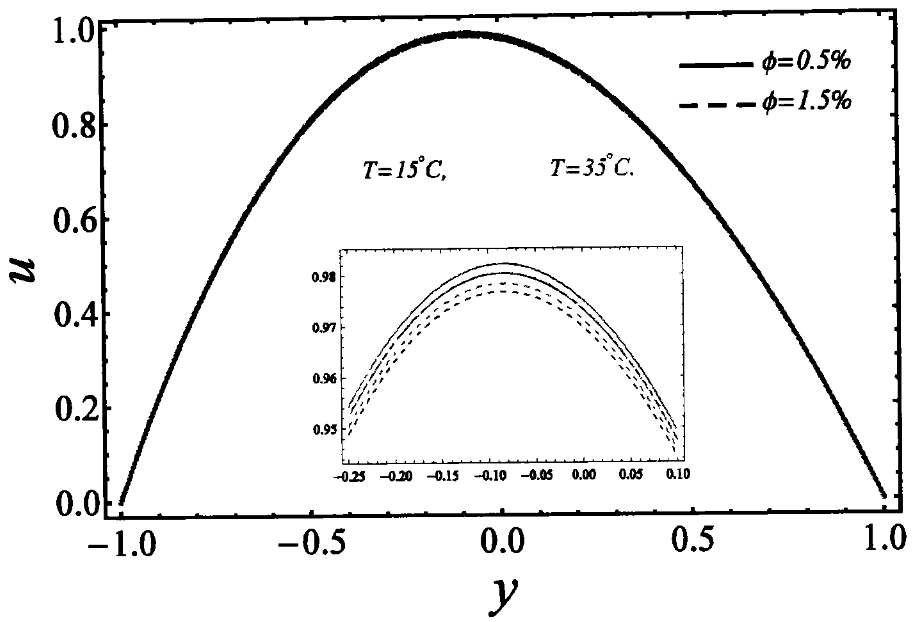

Figure 7.7: Manifestation of φ on u .

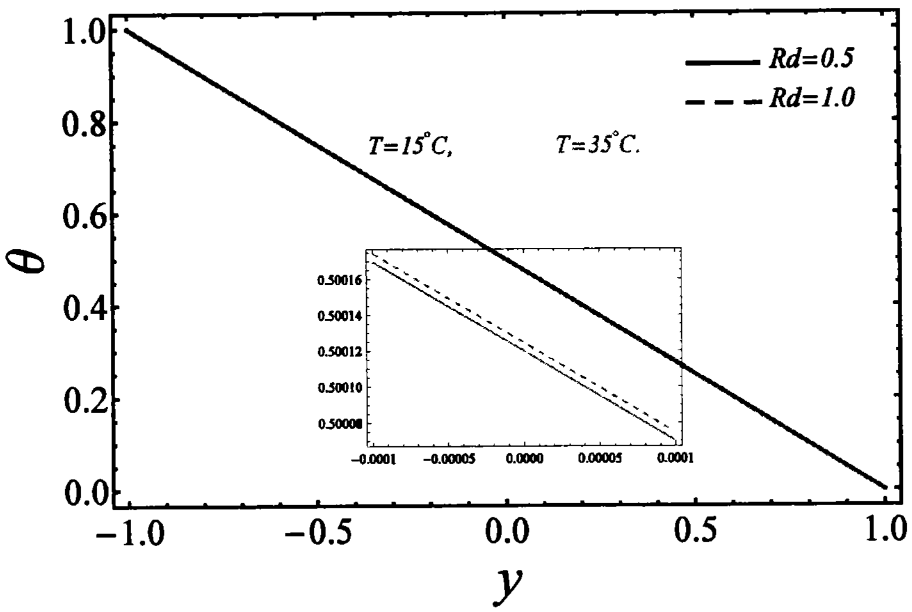

Figure 7.8: Manifestation of Rd on θ .

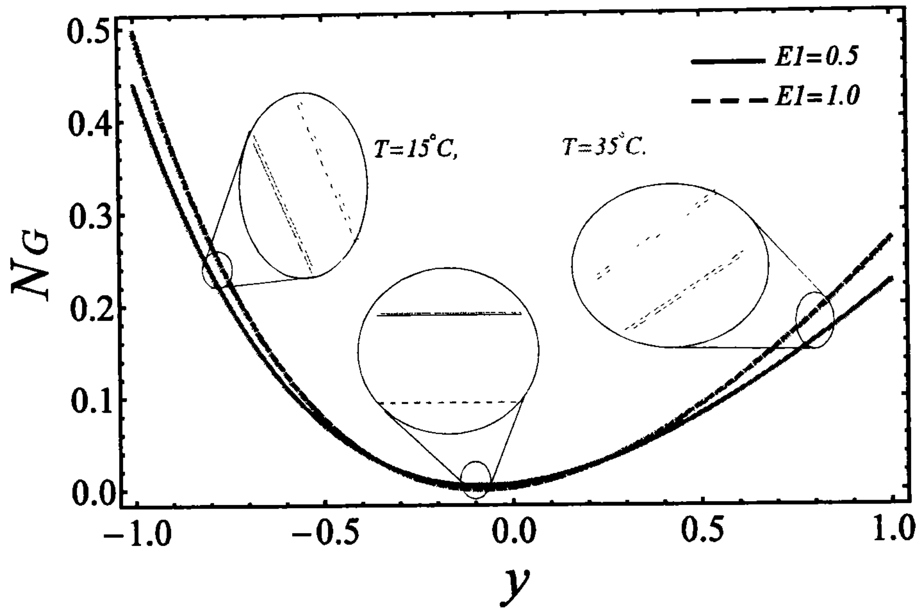

Figure 7.9: Manifestation of E_1 on NG.

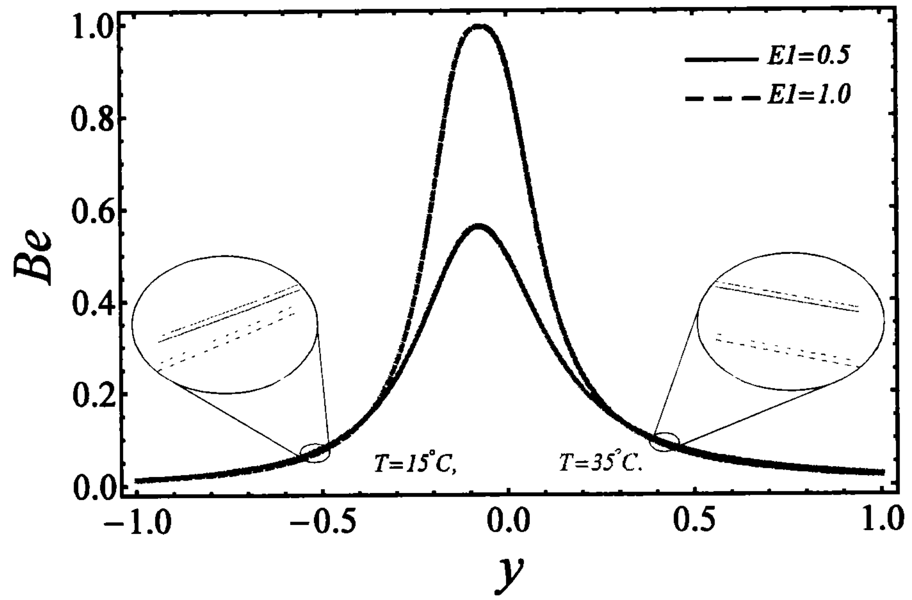

Figure 7.10: Manifestation of E_1 on Be.

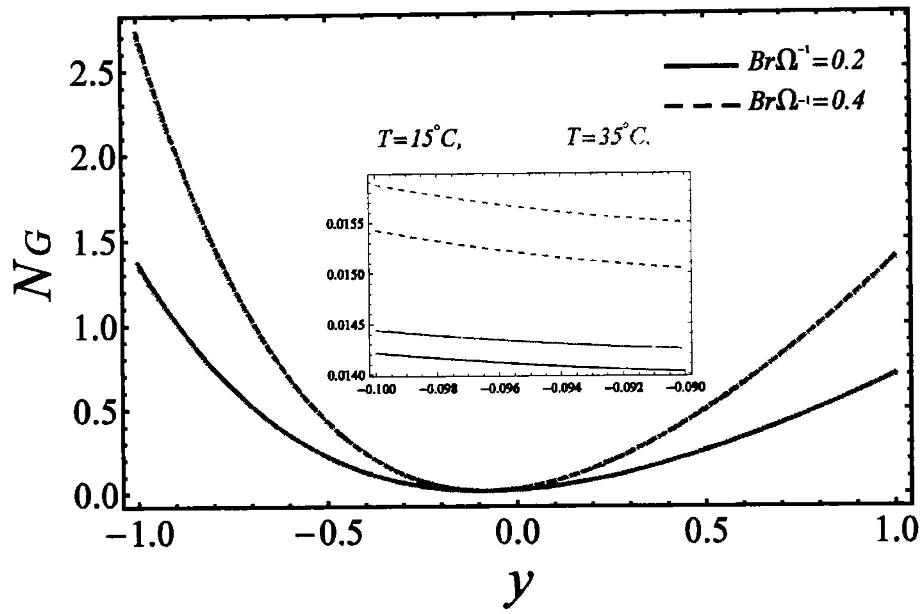

Figure 7.11: Manifestation of $Br\Omega^{-1}$ on NG.

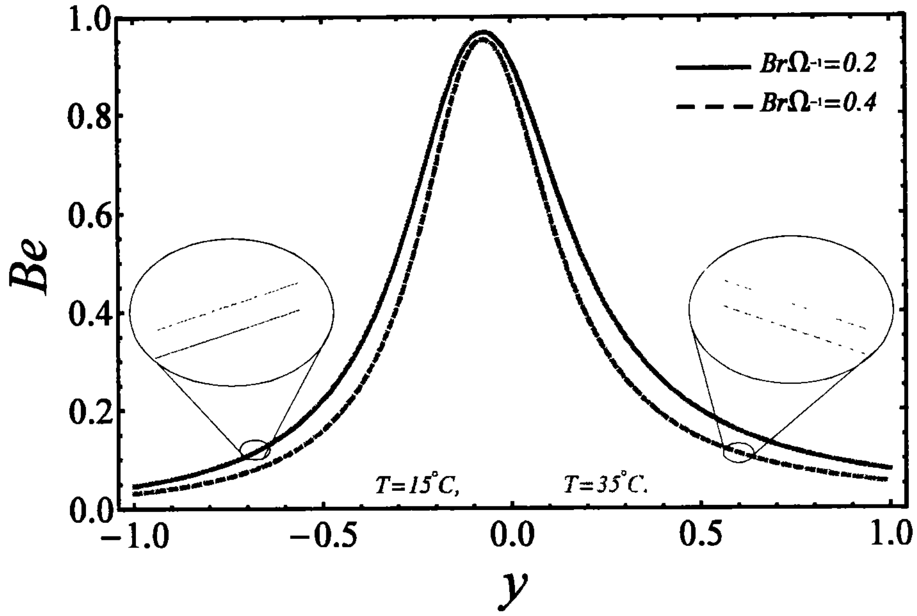

Figure 7.12: Manifestation of $Br\Omega^{-1}$ on Be.

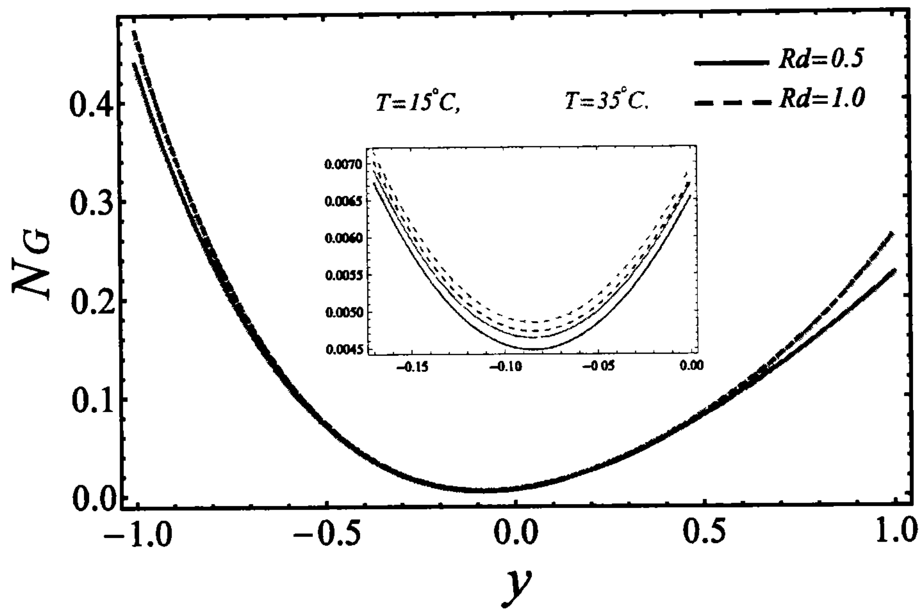

Figure 7.13: Manifestation of *Rd* on *NG*.

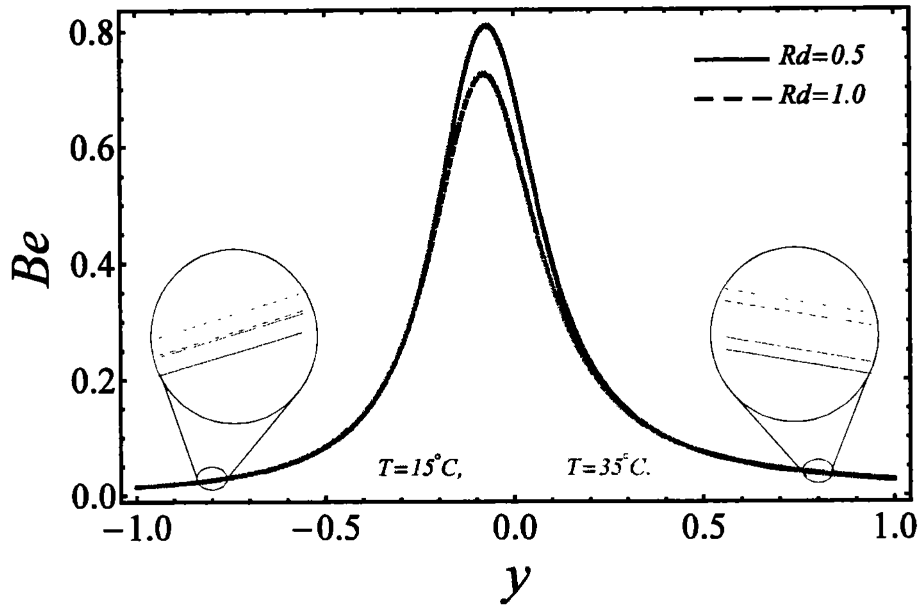

Figure 7.14: Manifestation of *Rd* on *Be*.

The numeric features of C_f and Nu on both opposite walls w.r.t three different temperature conditions, as suggested by Duangthongsuk and Wongwises against different values of φ , E_1 and M are calculated in Tables 7.2 and 7.3, respectively. It could be noted that C_f reduced at right wall, with increasing values of φ , E_1 and M , while the opposite effects occurred at left wall of the concerned parameters. In heat transfer phenomena, heat rate increased at right wall but decreased at left wall, for large values of φ , E_1 and M .

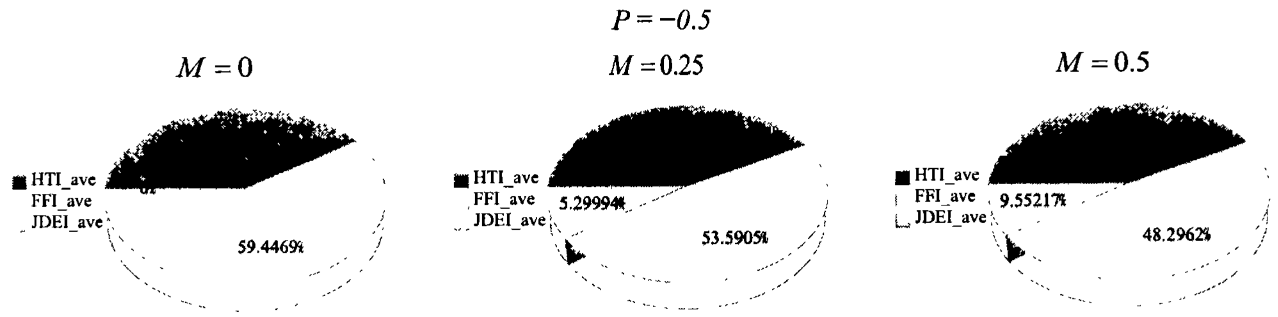

Figure 7.15: (**a**) Phi diagrams showing effects of magnetic parameter by keeping other parameters as fixed.

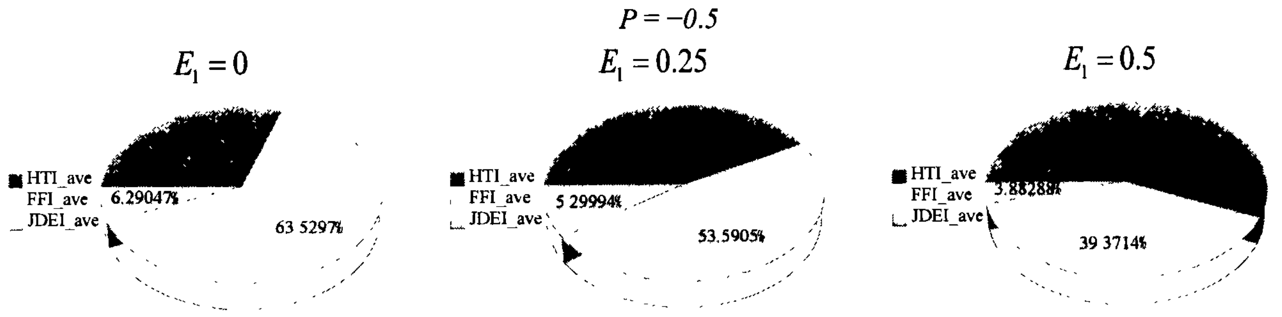

Figure 7.15: (**b**) Phi diagrams showing effects of electric field parameter by keeping other parameters as fixed.

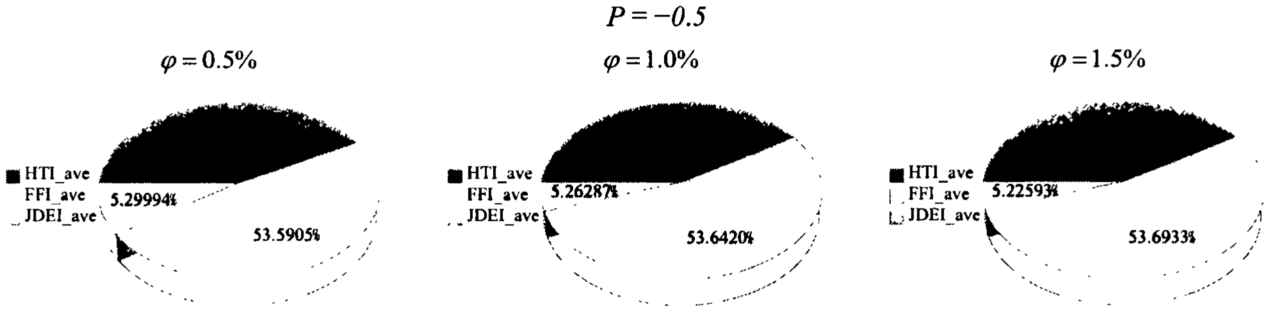

Figure 7.15: (**c**) Phi diagrams showing effects of φ by keeping other parameters as fixed.

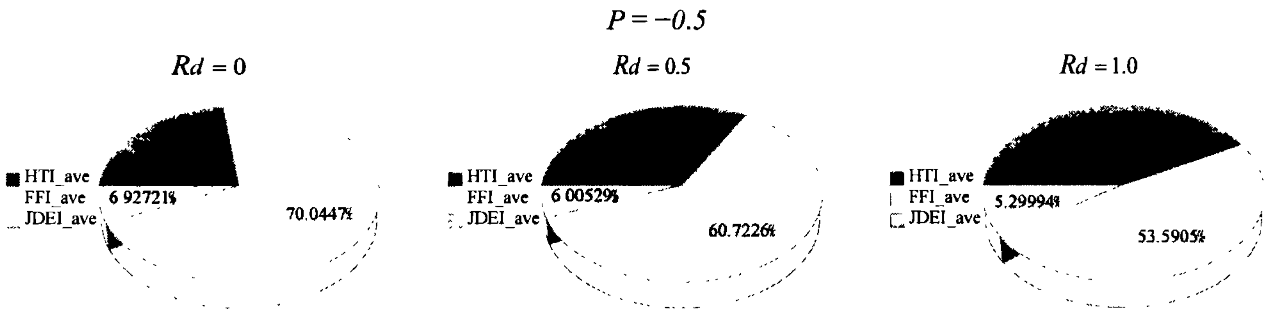

Figure 7.15: (**d**) Phi diagrams showing effects of radiation parameter by keeping other parameters as fixed.

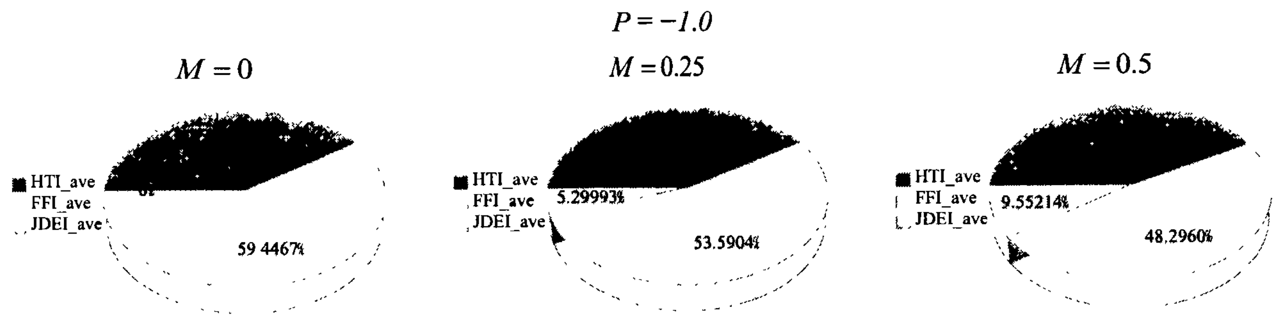

Figure 7.16: (**a**) Phi diagrams showing effects of magnetic parameter by keeping other parameters as fixed.

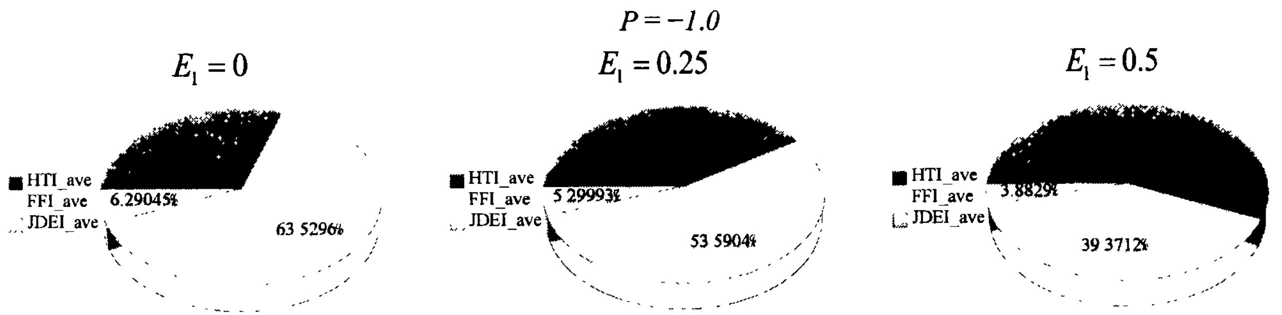

Figure 7.16: (**b**) Phi diagrams showing effects of electric field parameter by keeping other parameters as fixed.

$P = -1.0$

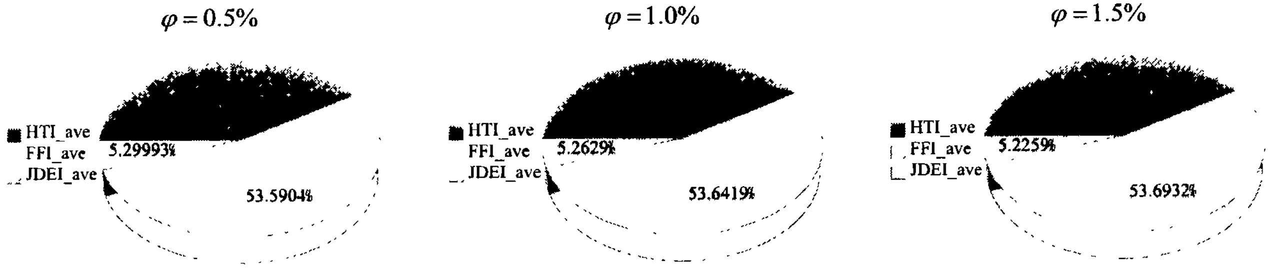

Figure 7.16: **(c)** Phi diagrams showing effects of φ by keeping other parameters as fixed.

$P = -1.0$

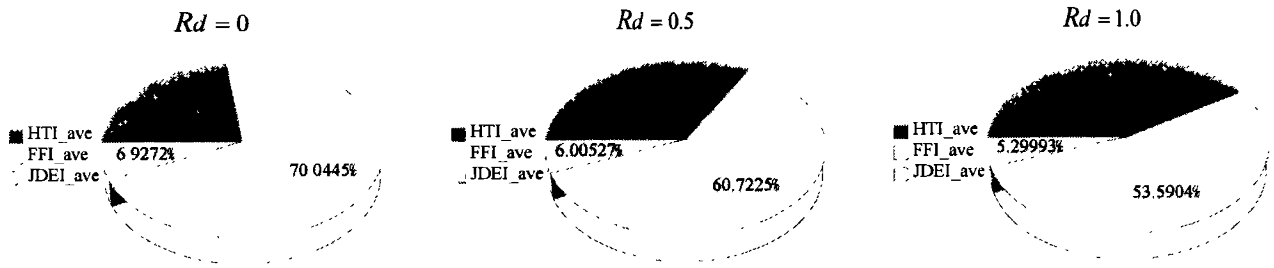

Figure 7.16: **(d)** Phi diagrams showing effects of radiation parameter by keeping other parameters as fixed.

Table 7.2: Numeric attributes of C_f on opposite walls with respect to three different temperature conditions against different points of ϕ , E_1 and M when $Gr = 2.0$ and $Rd = 1.0$.

φ	E_1	M	$T = 15^{\circ}C$		$T = 25^{\circ}C$		$T = 35^{\circ}C$	
			$C_f(-1)$	$C_f(1)$	$C_f(-1)$	$C_f(1)$	$C_f(-1)$	$C_f(1)$
		0.00	3.80765	−2.41647	3.79748	−2.40690	3.80302	−2.41211
	0.0	0.25	3.56943	−2.19941	3.55835	−2.18901	3.56439	−2.19466
		0.50	3.36696	−2.01740	3.35512	−2.00632	3.36157	−2.01235
		0.00	3.80765	−2.41647	3.79748	−2.40690	3.80302	−2.41211
0.5%	0.5	0.25	3.79915	−2.42912	3.78789	−2.41854	3.79402	−2.42430
		0.50	3.79582	−2.44626	3.78342	−2.43462	3.79017	−2.44096
		0.00	3.80765	−2.41647	3.79748	−2.40690	3.80302	−2.41211
	1.0	0.25	4.02891	−2.65888	4.01746	−2.64812	4.02370	−2.65398
		0.50	4.22474	−2.87519	4.21177	−2.86298	4.21883	−2.86962
		0.00	3.79649	−2.41100	3.78657	−2.40167	3.79221	−2.40697
	0.0	0.25	3.56060	−2.19602	3.54979	−2.18588	3.55594	−2.19164
		0.50	3.35987	−2.01553	3.34833	−2.00473	3.35489	−2.01086
		0.00	3.79649	−2.41100	3.78657	−2.40167	3.79221	−2.40697
1.0%	0.5	0.25	3.78872	−2.42414	3.77774	−2.41382	3.78398	−2.41968
		0.50	3.78594	−2.44161	3.77386	−2.43026	3.78073	−2.43671
		0.00	3.79649	−2.41100	3.78657	−2.40167	3.79221	−2.40697
	1.0	0.25	4.01688	−2.65231	4.00572	−2.64181	4.01207	−2.64777
		0.50	4.21208	−2.86774	4.19945	−2.85586	4.20663	−2.86261
		0.00	3.78532	−2.40553	3.77565	−2.39643	3.78140	−2.40183
	0.0	0.25	3.55174	−2.19262	3.54122	−2.18273	3.54747	−2.18860
		0.50	3.35275	−2.01363	3.34151	−2.00311	3.34818	−2.00935
		0.00	3.78532	−2.40553	3.77565	−2.39643	3.78140	−2.40183
1.5%	0.5	0.25	3.77827	−2.41915	3.76758	−2.40909	3.77393	−2.41506
		0.50	3.77605	−2.43693	3.76429	−2.42589	3.77127	−2.43244
		0.00	3.78532	−2.40553	3.77565	−2.39643	3.78140	−2.40183
	1.0	0.25	4.00485	−2.64573	3.99398	−2.63550	4.00044	−2.64157
		0.50	4.19941	−2.86030	4.18712	−2.84873	4.19442	−2.85559

Table 7.3: Numeric attributes of Nu on opposite walls with respect to three different temperature conditions against different points of φ, E_1 and M when $Gr = 2.0$ and $Rd = 1.0$.

φ	E_1	M	$T = 15^{\circ}C$		$T = 25^{\circ}C$		$T = 35^{\circ}C$	
			$Nu(-1)$	$Nu(1)$	$Nu(-1)$	$Nu(1)$	$Nu(-1)$	$Nu(1)$
		0.00	0.510991	0.511551	0.509936	0.510495	0.506687	0.507244
	0.0	0.25	0.511011	0.511534	0.509955	0.510479	0.506707	0.507228
		0.50	0.511032	0.511517	0.509976	0.510461	0.506728	0.507211
		0.00	0.510991	0.511551	0.509936	0.510495	0.506687	0.507244
0.5%	0.5	0.25	0.510989	0.511553	0.509934	0.510497	0.506685	0.507247
		0.50	0.510987	0.511555	0.509932	0.510499	0.506683	0.507249
		0.00	0.510991	0.511551	0.509936	0.510495	0.506687	0.507244
	1.0	0.25	0.510962	0.511613	0.509872	0.510556	0.506623	0.507306
		0.50	0.510863	0.511672	0.509809	0.510616	0.506560	0.507365
		0.00	0.511061	0.511618	0.510000	0.510556	0.506752	0.507306
	0.0	0.25	0.511081	0.511601	0.510019	0.510540	0.506771	0.507289
		0.50	0.511101	0.351158	0.510040	0.510523	0.506791	0.507272
		0.00	0.511061	0.511618	0.510000	0.510556	0.506752	0.507306
1.0%	0.5	0.25	0.511059	0.511620	0.509998	0.510558	0.506749	0.507308
		0.50	0.511057	0.511622	0.509996	0.510560	0.506747	0.507310
		0.00	0.511061	0.511618	0.510000	0.510556	0.506750	0.507306
	1.0	0.25	0.510997	0.511679	0.509936	0.510617	0.506688	0.507367
		0.50	0.510934	0.511738	0.509873	0.510676	0.506625	0.507425
		0.00	0.511131	0.511685	0.510000	0.510617	0.506816	0.507367
	0.0	0.25	0.511150	0.511668	0.510083	0.510601	0.506835	0.507351
		0.50	0.511171	0.511651	0.510103	0.510584	0.506855	0.507334
		0.00	0.511131	0.511685	0.510064	0.510617	0.506816	0.507367
1.5%	0.5	0.25	0.511129	0.511687	0.510062	0.510619	0.506814	0.507369
		0.50	0.511126	0.511689	0.510060	0.510621	0.506811	0.507371
		0.00	0.511131	0.511685	0.510064	0.510617	0.506816	0.507428
	1.0	0.25	0.511067	0.511746	0.510000	0.510678	0.506752	0.507428
		0.50	0.511004	0.511804	0.509938	0.510736	0.506690	0.507486

7.4 Conclusions

The electro-magnetohydrodynamics (EMHD) and entropy analysis are investigated here. The most vital findings were:

- The electric field E_1 applied in a tangential direction to the fluid affected both velocity and temperature distributions, which produced a reduction in the temperature and rise in the velocity.
- The amount of nanoparticles φ in base fluid affected a slowdown in nanofluid velocity.
- The thermal boundary layer increased against the growing radiation parameter Rd, which was why an increase in temperature was observed.
- The entropy generation near the boundary of the channel prolonged, while was very insufficient at the vicinity of the center for the electric field E_1.
- Initially, Be attained a high impact near the middle of channel, but gradually it fell for a large value of the electric field parameter near the walls.
- The energy loss for $Br\Omega^{-1}$ and radiation parameter Rd at the intermediate of the channel was approximately zero, while an enhancement was noted near the walls.
- The average energy loss was due to a rise in the pressure gradient.

References

[1] Sarpkaya, T. (1966). Experimental determination of the critical Reynolds number for pulsating Poiseuille flow. *Journal of Basic Engineering*, **88** (3), 589-598.

[2] Loyalka, S. K., Storvick, T. S. and Park, H. S. (1976). Poiseuille flow and thermal creep flow in long, rectangular channels in the molecular and transition flow regimes. *Journal of Vacuum Science and Technology*, **13** (6), 1188-1192.

[3] Ziarani, A. S. and Mohamad, A. A. (2006). A molecular dynamics study of perturbed Poiseuille flow in a nanochannel. *Microfluidics and Nanofluidics*, **2** (1), 12-20.

[4] Fetecau, C., and Fetecau, C. (2005). Starting solutions for some unsteady unidirectional flows of a second grade fluid. *International Journal of Engineering Science*, **43** (10), 781-789.

[5] Fetecau, C., Zierep, J., Bohning, R., and Fetecau, C. (2010). On the energetic balance for the flow of an Oldroyd-B fluid due to a flat plate subject to a time-dependent shear stress. *Computers and Mathematics with Applications*, **60** (1), 74-82.

[6] Valanis, K. C. and Sun, C. T. (1969). Poiseuille flow of a fluid with couple stress with applications to blood flow. *Biorheology*, **6** (2), 85-97.

[7] Golibersuch, D. C. (1973). Observation of aspherical particle rotation in Poiseuille flow via the resistance pulse technique: I. Application to human erythrocytes. *Biophysical Journal*, **13** (3), 265-280.

[8] Chaturani, P. and Biswas, D. (1984). A comparative study of Poiseuille flow of a polar fluid under various boundary conditions with applications to blood flow. *Rheologica Acta*, **23** (4), 435-445.

[9] Pirofsky, B. (1953). The determination of blood viscosity in man by a method based on Poiseuille's law. *The Journal of Clinical Investigation*, **32** (4), 292-298.

[10] Sorensen, E. N., Burgreen, G. W., Wagner, W. R. and Antaki, J. F. (1999). Computational simulation of platelet deposition and activation: II. Results for Poiseuille flow over collagen. *Annals of Biomedical Engineering*, **27** (4), 449-458.

[11] Choi, S. U. S. (1995). Enhancing Thermal Conductivity of Fluids with Nanoparticles. *ASME-Publications-Fed*, **231**, 99–106.

[12] Vajravelu, K., and Prasad, K. V. (2012). Natural and mixed convection heat transfer in nanofluids. *Reviews in Nanoscience and Nanotechnology*, **1** (2), 142-151.

[13] Vajravelu, K., Prasad, K. V., and Ng, C. O. (2013). The effect of variable viscosity on the flow and heat transfer of a viscous Ag-water and Cu-water nanofluids. *Journal of Hydrodynamics*, **25** (1), 1-9.

[14] Naz, R., Mahomed, F. M., and Mason, D. P. (2008). Comparison of different approaches to conservation laws for some partial differential equations in fluid mechanics. *Applied Mathematics and Computation*, **205** (1), 212-230.

[15] Magan, A. B., Mason, D. P., and Mahomed, F. M. (2016). Analytical solution in parametric form for the two-dimensional free jet of a power-law fluid. *International Journal of Non-Linear Mechanics*, **85**, 94-108.

[16] Akbar, N. S., Khalique, C. M., and Khan, Z. H. (2017). Double diffusion effects on magnetohydrodynamic non-newtonian fluid nanoparticles. *Journal of Computational and Theoretical Nanoscience*, **14** (1), 694-703.

[17] Hussain, S., Aziz, A., Aziz, T., and Khalique, C. M. (2016). Slip flow and heat transfer of nanofluids over a porous plate embedded in a porous medium with temperature dependent viscosity and thermal conductivity. *Applied Sciences*, **6** (12), 376.

[18] Darcy, H. *Les Fontaines Publiques de la Ville de Dijon: Exposition et Application*; Victor Dalmont. 1856.

[19] Forchheimer, P. Wasserbewegung durch boden. *Z. Ver. Dtsch. Ing.* **1901**, *45*, 1782–1788.

[20] Lee, S. and Yang, J. (1997). Modeling of Darcy–Forchheimer drag for fuid flow across a bank of circular cylinders. *Internal Journal of Heat and Mass Transfer,* **40** (13), 3149–3155.

[21] Turkyilmazoglu, M. (2019). MHD natural convection in saturated porous media with heat generation/absorption and thermal radiation: closed-form solutions. *Archives of Mechanics*, **70** (1), 49-64.

[22] Turkyilmazoglu, M. (2011). Numerical and analytical solutions for the flow and heat transfer near the equator of an MHD boundary layer over a porous rotating sphere. *International Journal of Thermal Sciences*, **50** (5), 831-842.

[23] Ahmed, S. and Pop, I. (2010). Mixed convection boundary layer flow from a vertical flat plate embedded in a porous medium filled with nanofluids, *International Communications in Heat and Mass transfer*, **37** (8), 987-991.

[24] Eastman, J. A., Choi, S. U. S., Li, S., Yu, W. and Thompson. L.J. (2001). Anomalously increased effective thermal conductivities of ethylene glycol based nanofluids containing copper nanoparticles, *Applied Physics Letters,* **78** (6), 718–720.

[25] Pak, B.C. and Cho, Y.L. (1998). Hydrodynamics and heat transfer study of dispersed fluids with submicron metallic oxide particles. *Experimental Heat Transfer*, **11** (2), 151–170

[26] Agarwal, D. K., Vaidyanathan, A. and Kumar, S. S. (2013). Synthesis and characterization of kerosene–alumina nanofluids. *Applied Thermal Engineering*, **60** (1-2), 275–284.

[27] Feng, Q.L., Wu, J., Chen, G., Cui, F., Kim, T. and Kim, J. A. (2000) mechanistic study of the antibacterial effect of silver ions on Escherichia coli and Staphylococcus aureus. *Journal* of *Biomedical Materials. Research Banner*, **52** (4), 662–668.

[28] Brown, J. and Sobsey, M.D. (2010). Microbiological effectiveness of locally produced ceramic filters for drinking water treatment in Cambodia. *Journal of Water and Health,* **8** (1), 1–10.

[29] Van Halem, D., Van der Laan, H., Heijman, S., Van Dijk, J. and Amy, G. (2009). Assessing the sustainability of the silver-impregnated ceramic pot filter for low-cost household drinking water treatment. *Physics and Chemistry of the Earth, Parts A/B/C*, **34** (1-2), 36–42.

[30] Shahverdi, A.R., Fakhimi, A., Shahverdi, H.R. and Minaian, S. (2007). Synthesis and effect of silver nanoparticles on the antibacterial activity of different antibiotics against Staphylococcus aureus and Escherichia coli. *Nanomedicine: Nanotechnology, Boilogy and Medicine*, **3** (2), 168–171.

[31] Godson, L., Raja, B., Mohan Lal, D. and Wongwises, S. (2010). Experimental investigation on the thermal conductivity and viscosity of silver-Deionized water nanofluid. *Experimental Heat Transfer*, **23** (4), 317–332.

[32] Bhatti, M. M. and Rashidi, M. M. (2016). Effects of thermo-diffusion and thermal radiation on Williamson nanofluid over a porous shrinking/stretching sheet, *Journal of Molecular Liquids*, **221**, 567-573.

[33] Xu, H., Fan, T. and Pop I. (2013). Analysis of mixed convection flow of a nanofluid in a vertical channel with the Buongiorno mathematical model. *International Communications in Heat and Mass Transfer*, **44**, 15-22.

[34] Bestman, A. R. (1990). Natural convection boundary layer with suction and mass transfer in a porous medium. *International Journal of Energy Research*, **14** (4), 389-96.

[35] Sheikholeslami, M. (2017). Magnetic field influence on CuO–H2O nanofluid convective flow in a permeable cavity considering various shapes for nanoparticles. *International Journal of Hydrogen Energy*, **42** (31), 19611-21.

[36] Bhatti, M. M, Rashidi, M. M and Pop, I. (2017). Entropy Generation with nonlinear heat and Mass transfer on MHD Boundary Layer over a Moving Surface using SLM. *Nonlinear Engineering Modeling and Application*, **6** (1), 43-52.

[37] Rashidi, M. M., Abelman, S. and Mehr, N. F. (2013). Entropy generation in steady MHD flow due to a rotating porous disk in a nanofluid. *International Journal of Heat and Mass Transfer*, **62**, 515-25.

[38] Sheikholeslami, M. and Bhatti, M. M. (2017). Forced convection of nanofluid in presence of constant magnetic field considering shape effects of nanoparticles. *International Journal of Heat and Mass Transfer*, **111**, 1039-49.

[39] Mahmud, S. and Fraser, R. A. (2002). Analysis of mixed convection—Radiation interaction in a vertical channel: Entropy generation. *Exergy, An International Journal*, **2** (4), 330–339.

[40] Rashidi, M. M., Abelman, S. and Mehr, N. F. (2013). Entropy generation in steady MHD flow due to a rotating porous disk in a nanofluid. *International Journal of Heat and Mass Transfer*, **62**, 515–525.

[41] Cho, C. C. and Chen, C. L. (2013). Natural convection heat transfer and entropy generation in wavy-wall enclosure containing water-based nanofluid. *International Journal of Heat and Mass Transfer*, **61**, 749–758.

[42] Ranjit, N. K. and Shit, G. C. (2017). Entropy generation on electro-osmotic flow pumping by a uniform peristaltic wave under magnetic environment. *Energy*, **128**, 649–660.

[43] Sheremet, M. A., Grosan, T. and Pop, I. (2017). Natural convection and entropy generation in a square cavity with variable temperature side walls filled with a nanofluid: Buongiorno's mathematical model. *Entropy*, **19** (7), 337-356.

[44] Jamalabadi, M. Y. A., Safaei, M. R., Alrashed, A. A. A. A., Nguyen, T. K. and Filho, E. P. B. (2017). Entropy generation in thermal radiative loading of structures with distinct heaters. *Entropy*, **19** (10), 506-522.

[45] Darbari, B., Rashidi, S. and Esfahani, J. A. (2016). Sensitivity analysis of entropy generation in nanofluid flow inside a channel by response surface methodology. *Entropy*, **18** (2), 52-68.

[46] Liao, S. J. (1992). The proposed homotopy analysis technique for the solution of nonlinear problems (Doctoral dissertation, PhD thesis, Shanghai Jiao Tong University).

[47] Zhao, Y., and Liao, S. (2012). On the HAM-based mathematica package BVPh for coupled nonlinear ODEs. In AIP Conference Proceedings, **1479** (1), 1842-1844.

[48] Van Gorder, R. A., and Vajravelu, K. (2009). On the selection of auxiliary functions, operators, and convergence control parameters in the application of the homotopy analysis method to nonlinear differential equations: a general approach. *Communications in Nonlinear Science and Numerical Simulation,* **14** (12), 4078-4089.

[49] Liao, S. (2005). Comparison between the homotopy analysis method and homotopy perturbation method. *Applied Mathematics and Computation*, **169** (2), 1186-1194.

[50] Smits, A. J. (2018). *A Physical Introduction to Fluid Mechanics*, (2nd Ed.) Princeton University.

[51] Acheson, D. J. (1990). *Elementary Fluid Dynamics*, Oxford University Press.

[52] Batchelor, G. K. (1967). *An Introduction to Fluid Dynamics*, Cambridge University Press.

[53] Holman, J. P. (1981). *Heat Transfer*, New York McGraw-Hill.

[54] Jaluria, Y. (1988). *Computer Methods for Engineering*, Allyn Bacon Inc., Boston.

[55] Maxwell, J. C. (1881). *A Treatise on Electricity and Magnetism*, Oxford Clarendon Press, **1** (2).

[56] Mudunkotuwa, I. A. and Grassian, V. H. (2011). Impact of surface structure and surface energetics on understanding the behavior of nanomaterials in the environment, *Journal of Environmental Monitoring*, **13** (5), 1135-1144.

[57] Masuda, H., Ebata, A., Teramae, K. and Hishinuma, N. (1993) Alteration of thermal conductivity and viscosity of liquid by dispersing ultrafine particles (dispersions of Al2O3, SiO2, and TiO2 ultrafine particles), *Japan Society of Thermophysical Properties*, **7** (4), 227-233.

[58] Jang, S.P. and Choi, S. U. S. (2004). Role of Brownian motion in the enhanced thermal conductivity of nanofluids. *Applied Physics Letters*, **84** (21), 4316–4318.

[59] Einstein, A. (1906). A new determination of the molecular dimensions. *Annalen der Physik*, **19** (2), 289-306.

[60] Brinkman, H. C. (1952). The viscosity of concentrated suspensions and solution, *the Journal of Chemical Physics*, **20** (4), 571-581.

[61] Hwang, K. S., Jang, S. P. and Choi, S. U. S. (2009). Flow and convective heat transfer characteristics of water-based Al_2O_3 nanofluids in fully developed laminar flow regime, *International Journal of Heat and Mass Transfer*, **52** (1-2), 193-199.

[62] Godson, L., Mohan Lal, D., and Wongwises, S. (2010). Measurement of thermo physical properties of metallic nanofluids for high temperature applications. *Nanoscale and Microscale Thermophysical Engineering*, 14(3), 152-173.

[63] Duangthongsuk, W. and Wongwises, S. (2009). Measurement of temperature-dependent thermal conductivity and viscosity of TiO_2-water nanofluids. *Experimental Thermal and Fluid Science*, **33** (4), 706–714.

[64] Maxwell, J. C. (1892). *A Treatise on Electricity and Magnetism*, Oxford University Press, **1** (3).

[65] Godson, L., Deepak, K., Enoch, C., Jefferson, B., and Raja, B. (2014). Heat transfer characteristics of silver/water nanofluids in a shell and tube heat exchanger. *Archives of Civil and Mechanical Engineering*, **14** (3), 489-496.

[66] Duangthongsuk, W., and Wongwises, S. (2010). Comparison of the effects of measured and computed thermophysical properties of nanofluids on heat transfer performance. *Experimental Thermal and Fluid Science*, **34** (5), 616-624.

[67] Einstein, A. (1906). The theory of the Brownian motion, *Annalen der Physik*, **19** (2), 371-381.

[68] Li, C. H., and Peterson, G. P. (2006). Experimental investigation of temperature and volume fraction variations on the effective thermal conductivity of nanoparticle suspensions (nanofluids). *Journal of Applied Physics*, **99** (8), 084314.

[69] Einstein, A. (1911). Correction of my work: A new determination of the molecular dimensions. *Annalen der Physik*, **34** (3), 591-592.

[70] Zhang, X., Gu, H., & Fujii, M. (2007). Effective thermal conductivity and thermal diffusivity of nanofluids containing spherical and cylindrical nanoparticles. *Experimental Thermal and Fluid Science*, **31** (6), 593-599.

[71] Askari, S., Lotfi, R., Rashidi, A. Koolivand, M. H. and Koolivand-Salooki, M. (2016). Rheological and thermophysical properties of ultra-stable kerosene-based Fe_3O_4 /grapheme nanofluids for energy conservation. *Energy Conversion and Management*, **128** 134–144.

[72] Oyanedel-Craver, V.A. and Smith, J.A. (2007). Sustainable colloidal-silver-impregnated ceramic filter for point-of-use water treatment. *Environmental Science ans Technology*, **42** (3), 927–933.

[73] Buongiorno, J. (2006). Convective transport in nanofluids. *Journal of Heat Transfer*, **128** (3), 240–250.

[74] Tiwari, R. K. and Das, M. K. (2007). Heat transfer augmentation in a two-sided lid-driven differentially heated square cavity utilizing nanofluids, *International Journal of Heat and Mass Transfer*, **50** (9-10) 2002-18.

[75] Dandapat, B. S. and Mukhopadhyay, A. 2003. Finite amplitude long wave instability of a film of conducting fluid flowing down an inclined plane in presence

of electromagnetic field. *International Journal of Applied Mechanics and Engineering*, **8** (3), 379–93.

[76] Nield, D. A. and Bejan, A. (2017). *Convection in Porous Media*. New York: Springer.

[77] Arrhenius, S. (1889). Über die Dissociationswärme und den Einfluss der Temperatur auf den Dissociationsgrad der Elektrolyte. Zeitschrift für physikalische Chemie, **4** (1), 96-116.

[78] Nayfeh, A. H. and Mook, D. T. (1979). *Nonlinear Oscillations*. New York: John Willey and Sons.

[79] He, J. H. (2006). Some asymptotic methods for strongly nonlinear equations. *International Journal of Modern Physics B*, **20** (10), 1141-1199.

[80] Wazwaz, A. M. (2004). The Tanh method for generalized forms of nonlinear heat conduction and Burger's-Fisher equations. *Applied Mathematics and Computation*, **152** (1), 403-413.

[81] Fu, Z., Liu, S. and Zhao, Q. (2001). New Jacobi elliptic function expansion and new periodic solutions of nonlinear wave equations. *Physics Letters A*, **290** (1-2), 72-76.

[82] Adomian, G. (1998). A review of the decomposition method in applied mathematics. *Journal of Mathematical Analysis and Applications*, **135** (2), 501-544.

[83] Sen, S. (1983). Topology and geometry for physicists, *Florida: Academic Press*.

[84] Liao, S. J. (1997). An approximate solution technique which does not depend upon small parameters (Part2): an application in fluid mechanics. *International Journal of Non-Linear Mechanics*, **32** (5), 815–22.

[85] Liao, S. (2003). *Beyond perturbation: introduction to the homotopy analysis method*. Chapman and Hall/CRC.

[86] Karniadakis, R. K. G., Beskok, A. and Aluru, N. (2005). *Microflows and Nanoflows: Fundamentals and Simulation*. New York: Springer.

[87] Fang, T. (2014). Flow and mass transfer for an unsteady stagnation-point flow over a moving wall considering blowing effects. *Journal of Fluids Engineering*, **136** (7). 71-103.

[88] Uddin, M. J., Alginahi,Y., Beg, O. A. and Kabir, M. N. (2016). Numerical solutions for gyrotactic bioconvection in nanofluid-saturated porous media with Stefan blowing and multiple slip effects. *Computers and Mathematics with Applications*. **72** (10), 2562-2581.

[89] Beskok, A. and Karniadakis, G.E. (1994). Simulation of heat and momentum transfer in complex micro-geometries. *Journal of Thermophysics and Heat Transfer*, **8** (4), 355–370.

[90] Rosca, A. V. and Pop, I. Flow and heat transfer over a vertical permeable stretching/shrinking sheet with a second order slip. *International Journal of Heat and Mass Transfer*, **60** (2013), 355-364.

[91] Rahman, M. M., Rosca, A. V. and Pop, I. (2014). Boundary layer flow of a nanofluid past a permeable exponentially shrinking/stretching surface with second-order slip using Buongiorno's model. *International Journal of Heat and Mass Transfer*, **77**, 1133-1143.

[92] Roseland, S. (1931). *Astrophysik und Atom-Theoretische Grundlagen*, Springer Verlag, Berlin, 41-44.

[93] Sinha, A. and Shit, G. C. (2015). Electromagnetohydrodynamic flow of blood and heat transfer in a capillary with thermal radiation. *Journal of Magnetism and Magnetic Materials*, **378**, 143-151.

[94] Ibrahim, W. and Shankar. B. (2013). MHD boundary layer flow and heat transfer of a nanofluid past a permeable stretching sheet with velocity, thermal and solutal slip boundary conditions. *Computers and Fluids*, **75**, 1-10.

[95] Arunachalam, M. and Rajappa, N. R. (1978). Forced Convection in liquid metals with variable thermal conductivity and capacity. *Acta Mechanica*, **31** (1-2), 25-31.

[96] Rout, B. R., Parida, S. K and Pattanayak, H. B. (2014). Effect of radiation and chemical reaction on natural convective MHD flow through a porous medium with double diffusion. *Journal of Engineering Thermophysics*, **23** (1), 53–65.

[97] Mastorakis, N. E. (2005). Numerical solution of non-linear ordinary differential equations via collocation method (Finite elements) and Genetic algorithms. *Proceedings of the 6th WSEAS Int, Confer. on Evolu. Comput*, Lisbon, Portugal.

Turnitin Originality Report

Study of Internal Poiseuille Flows of Nano Fluids by Nasir Shehzad

From PhD Thesis (PhD Mathematics-1)

turnitin

- Processed on 05-Dec-2019 12.23 PKT
- ID: 1227566097
- Word Count: 36481

Similarity Index
16%
Similarity by Source

Internet Sources:
9%
Publications:
8%
Student Papers:
11%

Shakeel Ahmed
Superintendent
International Islamic University
Islamabad

sources:

1 1% match (student papers from 05-Dec-2019)
Class: PhD Mathematics-1
Assignment: PhD Thesis
Paper ID: 1227564124

2 1% match (Internet from 23-Nov-2018)
https://doaj.org/article/cd91e76950da4d0eb3a667811d6754c1

3 1% match (publications)
Rahmat Ellahi, Ahmed Zeeshan, Kambiz Vafai, Hafiz U Rahman. "Series solutions for magnetohydrodynamic flow of non-Newtonian nanofluid and heat transfer in coaxial porous cylinder with slip conditions", Proceedings of the Institution of Mechanical Engineers, Part N: Journal of Nanoengineering and Nanosystems, 2011

4 1% match (Internet from 03-May-2019)
https://www.mdpi.com/1099-4300/21/3/236

5 < 1% match (Internet from 06-Mar-2019)
https://www.mdpi.com/1099-4300/21/3

6 < 1% match (student papers from 20-Oct-2019)
Submitted to Higher Education Commission Pakistan on 2019-10-20

7 < 1% match (Internet from 29-Aug-2014)
http://ftp.ihcdstore.org/Yoshi's%20Book%20Files/book%20INDD%20files/kc2.indd

8 < 1% match (student papers from 20-May-2015)
Submitted to Higher Education Commission Pakistan on 2015-05-20

9 < 1% match (student papers from 14-Dec-2018)
Class: PhD Mathematics
Assignment: Thesis
Paper ID: 1056936089

10 < 1% match (Internet from 02-Oct-2019)
https://www.tandfonline.com/doi/full/10.1080/25765299.2018.1511079

11 < 1% match (student papers from 28-Feb-2014)
Submitted to Universiti Teknologi Petronas on 2014-02-28

12 < 1% match (student papers from 27-Jun-2016)
Submitted to Indian Institute of Technology, Madras on 2016-06-27

13 < 1% match (student papers from 13-Dec-2018)
Class: PhD Mathematics
Assignment: Thesis
Paper ID: 1056270579

< 1% match (student papers from 06-May-2015)